Investigation Using Polymer Additives to Mitigate Erosion in Multiphase Turbulent Pipe Flow

by

Rafat Jami

A thesis submitted in partial fulfillment of the requirements for the degree of

Master of Science

Department of Mechanical Engineering
University of Alberta

Abstract

Long chained polymers were evaluated for their impact on reducing pipe erosion during two-phase flow. The research study was compartmentalized into three categories. One of the components of this study investigated the erosion of different materials in an attempt to find a faster eroding substitute to carbon steel. This would allow for faster testing times and thus a larger amount of tests during the timespan of this study. The initial two materials that were proposed as substitutes included Al-6061 T6 allow and a polyurethane (PU) coating along with the baseline A106 carbon steel (CS). A Toroid Wheel tester (TWT) allowed screening of materials before moving to the Saskatchewan Research Council (SRC) recirculating pipe flow loop. The PU coated samples did not exhibit similar behavior; polyvinylchloride (PVC) was used as a replacement. Each material was subjected to a 300 hour test of recirculating slurry at SRC. Mass measurements were taken before and after the test to calculate the average wear rate of each pipe material. The PVC and CS showed a linear increase in wear rate in respect to the solids frictional pressure loss. The Al 6061 data did not show a consistent trend and was ruled out as a substitute. PVC proved to be a viable substitute material to CS for wear testing.

The second stage of the study investigated the effect of chemical properties such as anionic charge and molecular weight on the drag reduction (DR) performance of polyacrylamides (PAM). A small apparatus was required to run screening tests quickly in order to find ideal polymeric solutions. An in-house designed Taylor Couette device (TCD) was built. The PAM based solutions, ranging from 10% to 50% anionicity, showed a peak DR at 20-30% for multiple molecular weights in pipe flow tests. To compare the TCD and pipe loop tests, a large sweep of operating speeds of both devices was carried out and compared using one consistent PAM solution. It was found, that the turbulent length scale of pipe flow was lower than the TCD tests and allowed for the polymers to fully stretch and distinguish performance differences which was not possible in the TCD due to a lower wall shear stress and a lower degree of turbulence.

The final segment of this study utilized the PAM polymers in the SRC flow loop. In order to account for polymer degradation, an injection system was utilized to hold the DR percentage constant. The DR at both diameter test sections were in agreement at 25%, and wear reduction of 40 to 70% was witnessed in all three materials. It was concluded that polymer additives reduces the amount of wear in the pipes.

Preface

This thesis study was completed under the supervision of Dr. Sina Ghaemi and Dr. Sean Sanders from the Department of Mechanical Engineering at the University of Alberta.

The experimental setup for the wear tests (in Chapter 3.1) was owned by the Saskatchewan Research Council. Dr. Ryan Spelay supervised all experiments conducted at SRC Pipe Flow Centre. The pipe loop was operated by Piti Srisukvatananan.

The Taylor Couette device (in Chapter 3.3) was designed, and developed under the supervision of Dr. Sina Ghaemi and Dr. Sean Sanders. The device was assembled at the Mechanical Engineering Shop at the University of Alberta.

The in-house recirculating pipe loop facility (in Chapter 3.4) is owned by Dr. Sina Ghaemi and Dr. Sean Sanders, and 40% of the experimental data in Chapter 5.1 were conducted by Sadek Shaban.

The Toroid Wheel tester used for the analogous material testing (Chapter 4.1) was located in Chemical Engineering at the University of Alberta and is owned by the PTP research group under the supervision of Dr. Sean Sanders.

The polymer additives used for this study were provided by SNF Floerger.

Acknowledgements

I would like to start by expressing my sincerest gratitude towards my supervisor Dr. Sina Ghaemi, and co-supervisor Dr. Sean Sanders. Both of them have provided me with an immense amount of their time, effort and guidance. Their help in my experimental design, test matrix, project objectives and theory provided a smooth process throughout the entirety of my program. Their insight and mentorship allowed me to find new ways to problem solve and be innovative, and I find this to be invaluable for the rest of career as an engineer and researcher. I would also like to thank Shell, CNRL and NSERC for the financial support they have provided for this project; none of this could have been possible without it.

Thank you to all my friends and family for the support they have given me for the last two years during my Master's program. Specifically I want to thank my parents for always providing me moral support and further guidance throughout these last few years. My colleague, Daren Wilkinson, has always been there for help in support both in my education. In addition, it was a pleasure to work with David Serrano; he encouraged me to always commit to my hobbies. He became a close friend and someone who always helped me keep a balance between the stress of my program and taking downtime.

I want to also give special thanks to Mohammad Mohammadtabar and Sadek Shaban for providing me with understanding and assistance in all lab procedures. They both have a detailed understanding of pipe flow and the effect of polymers and they gladly shared their knowledge in a respectful manner. Finally I want to thank all members of the LTF and PTP group for always providing valuable comments and feedback that allowed me to grow as a researcher and individual. I would like to sincerely give my thanks to the personnel at Saskatchewan Research Council, specifically Ryan Spelay and Piti Srisukvatananan for their expertise and help throughout the project.

I would like to thank SNF for their polymer products and many meetings to give the project direction. I thank the Mechanical Engineering shop, specifically Roger Marchand and Andrew Campbell for manufacturing the Taylor Couette Device. Finally a special thanks to Terry Runyon and Jim Skwarok for assistance with orders and other important administrative tasks.

Table of Contents

List of Tables

List of Figures

1 Thesis Introduction

1.1 Project Motivation

Multiple industries in Canada are interested in what is known as particle-laden flow. It is a type of flow in which two phases are present; both a liquid and solid particles; often this is given the name slurry. The main reason these flows are so crucial is because of their ability to transport solids and liquid as a suspension mixture. In fact, slurry pipelines are the most efficient above land means of transport for raw solids in large quantities [1]. One of the main industries that use slurry pipelines as a means of transportation is the Alberta Oil Sands [2]. This type of hydrotransport utilizes one of the most intensive applications of slurry pipeline technology in the world [3]. Despite this, there are large issues involving wear which have led to unsatisfactory performance of pipelines reported by oil sand extraction plants [3].

One of the main concerns with these pipelines is the amount of wear that is caused within the pipe. Pipelines typically operate at high solid concentrations and high velocities resulting in significant material wear through the phenomenon known as erosion [2, 4]. The erosion due to these flows affects the life of the pipes and other equipment such as the pumps; and thus raise the capital costs of projects [5]. On average, the wear rates of these slurry pipelines in hydrotransport are approximately 1 cm/year of pipe thickness loss and consequently leads to a pipe life less than a year [2]. Pipe replacements, inspections, and maintenance results in costs up to $1 billion in the Alberta Oil Sands industry [6]. As a means of mitigating wear reliability costs, some conservative maintenance approaches have been used; such as premature pipe section replacement to prolong the life of the rest of the pipe. Unfortunately, due to unexpected retirement of pipeline sections, the plant operating costs increase instead [7].

In an attempt to reduce costs from pipeline wear, extensive studies have been conducted to understand this phenomenon [8]. However, the knowledge is still limited due to the complex nature of the erosion process [5]. An accurate model of wear has to be created in order to predict the life of a pipe depending on the conditions of the flow [3, 5, 6, 8]. This study tackles this challenge by looking at methods of reducing the wear rate for pipelines. Specifically, polymer additives, known as drag reducing agents, are widely used in industrial applications for reducing pumping and other input power costs. Due to the ability of these polymeric solutions to reduce drag, it was

hypothesized that they may have an ability to reduce the overall erosion within a pipe as well. The reduction of the pipe wear could minimize the costs spent associated with maintenance and replacement. Secondly, to reduce the long testing times for wear measurements, a suitable substitute to carbon steel pipes for erosion experiments are explored. A weaker substitute material allows faster testing times; typically steel coupons require testing times over 100 hours in a pipe loop before a sizable mass loss is detected.

Common experimental setups used for wear and drag reduction tests are pilot-scale recirculating loops. These setups have a high initial cost, a large space requirement, and require lengthy testing times with a major contribution of labor work. A testing apparatus such as a rotary device that simulates Taylor-Couette flow has a much smaller scale than a pipe flow loop. This results in faster test times, lower volume within the lab and slurry during experimentation. The effectiveness of small scale apparatuses in following similar results as pipe flow is important before they can be used as a cost and time saving method to study polymer drag reduction and wear mechanisms.

1.2 Overview

The objectives of this study can be broken into three distinct components. The first part involves an analogous material experiment at different flow conditions. The objective of this test is to compare the wear characteristics of several materials to carbon steel in an attempt to find a suitable substitute for erosion tests. A suitable substitute should have equivalent susceptibility to specific flow conditions as carbon steel. The erosion experiments are conducted in a pilot scale flow loop in order to fully simulate the conditions of industrial pipelines. In addition, a small scale wear tester, the Toroid wheel, is also used as screening device to verify the usability of materials before they are tested in the larger loop.

The second phase of the testing involves the use of polymer additives in both a small testing apparatus, known as a Taylor Couette (TC) device, and a pilot scale flow loop. The TC device is utilized to run faster tests to evaluate a multitude of polymers in single phase flow. The drag reduction characteristics of the polymers will be compared between the TC device and pilot scale flow loop to verify the device as a screening tool. If the verification is successful, the TC device can then be used to evaluate the performance of polymer additives within fine clay suspensions, a common type of slurry within the tailings of oil sand extraction processes. This step of the testing will also investigate the effect of anionic charge of polyacrylamides (PAMs) in both TC and pipe

flow conditions. Ultimately, these tests should provide insight on which anionic charge displays the highest drag reduction performance, and whether the TC device is an appropriate screening test setup.

The final phase of this study involves a combination of the first two phases in which erosion tests will be conducted with the addition of the PAM polymers. The purpose of this experiment is to assess if PAM causes wear reduction in slurry flow. It is known prior to these experiments that polymers have the ability to reduce drag, which correspond to savings in pumping costs.

1.3 Objectives

The objectives of the project can be broken into three sections:

1. Analyzing polymer drag reduction performance between Taylor Couette and pipe flow.
2. Finding a substitute material for steel during erosion testing.
3. The effect of polymer additives on the wear rate of pipe materials.

1.4 Thesis Outline

The following thesis has been broken down into five main chapters:

Chapter 2: Literature Review

The literature review covers topics about erosion; such as the characteristics of slurry flow, the mechanisms of wear, the Two Layer model developed at Saskatchewan Research Council (SRC), and types of wear measurement apparatuses. It also covers the basics of the drag reduction phenomenon using polymers including: the elastic theory of polymer stretching, polymer degradation, and different types of polymers.

Chapter 3: Experimental Facilities

There are four experimental setups used in the entirety of this study, two for erosion tests, the Toroid wheel tester used for initial material comparisons, and the large scale recirculating flow loop for conditions that mimic industrial pipelines. The other two experimental setups are used for drag reduction tests for polymers in single phase flow, the Taylor Couette device and a small scale recirculating pipe loop.

Chapter 4: Analogous Material Testing

This chapter consists of a study in two different experimental setups that analyze the erosive trends of multiple materials and compares their responses to the change in different flow characteristics. The objective of this section is to find a suitable substitute to carbon steel during wear tests to save costs and time.

Chapter 5: Performance of Polymer Additives in Single Phase Flow

This chapter focuses on the drag reduction performance of different polymer additives. In this section they are used only in single phase flow and compared against one another at different flow conditions to see which chemical properties improve their overall effectiveness.

Chapter 6: Performance of Polymer Additives in Slurry Flow

This section of the thesis combines the work of chapters 4 and 5 in an attempt to find the effect of polymer additives on erosion. The study focuses on previous flow conditions from chapter 4, which was composed of slurry flow, and applies polymers previously tested in chapter 5.

Chapter 7: Conclusions and Future Works

This chapter highlights all main conclusions from every segment of the study. It also focuses on different strategies and tests that are required to further understand the effect of polymer additives on the wear mechanisms exhibited by different pipe materials.

2 Literature Review

This section covers three areas of background information required to understand the basis of the study. Firstly the pipeline erosion caused from slurry flow and ways to measure this erosion through different experimental techniques is discussed. Secondly, the explanation of the mechanism behind the drag reduction phenomenon from polymer additives within a flow is provided. Lastly, the Taylor-Couette flow is conceptually explained.

2.1 Erosion and Wear Modelling

In this section the impact of slurry flow conditions on erosion will be explored. A slurry is characterized based on flow conditions such as its velocity and pressure loss, and composition such as its concentration and viscosity. The Two-Layer model implements these characteristics to describe attributes of the two phase flow. This model will be reviewed in depth and utilized in further sections to explain the wear observed in the materials. In addition, different types of pilot scale erosion testing apparatuses are listed with their advantages and weaknesses.

2.1.1 Slurry Characterization

In order to correlate the wear rate as a function of the operating condition, a wear model must be applied. Many of the wear models that exist today are empirically derived and do not work in all situations. Many wear models have parameters that cannot be measured during pipeline wear tests such as the particle impact speed and angle of the impact. Additionally, many wear models do not focus on the target material, and the ones that do, do not provide empirically derived coefficients for all materials. Due to the lack of robust models, it has been difficult to predict the exact wear rates of pipelines. Before the wear rates can be related to the slurry, the parameters of the slurry must be defined.

The slurry can be characterized based on its physical properties which consist of two phases: the liquid phase and solid phase. Both the liquid and solid phases have different densities, however, when flowing as a mixture, the bulk density of the mixture is

$$\rho_m = (1 - C_s)\rho_f + C_s\rho_s \qquad (2\text{-}1)$$

where C_s = volumetric concentration of the solid phase.

The volumetric concentration of the solid phase can be defined in two ways. Gillies and Shook [10] defined the average particle concentration within the pipe cross section as the in-situ concentration, C_r. This however is not equal to the delivered volumetric concentration of the particles, C_v, which is averaged based on the amount of particles per volume flow of slurry.

The in-situ and delivered volumetric concentrations can be defined as follows:

$$C_r = \frac{1}{A}\int_A c dA \qquad (2\text{-}2)$$

$$C_v = \frac{1}{AV}\int_A c v_s dA \qquad (2\text{-}3)$$

where c = local particle volume concentration, v_s = local time-averaged particle velocity (m/s), and A and V are the cross sectional area and average velocity of the slurry .

The in-situ concentration for pipe loop tests can be measured by weighing the total quantity of solids that have been charged into the pipeline [10]. Due to the simplicity of this measurement, the in-situ concentration is used for the analysis in this study. Typically, the delivered concentration of the mixture will be slightly less than the in-situ, this is because the solids typically have a lower velocity than the liquid phase [11].

Apart from the mixture density, the mean particle size is also an important parameter that must be known. Typically, the mean particle size is denoted as the d_{50}. There are different ways of calculating the particle size; averaging techniques can be area based, volume based or diameter based.

Once the in-situ concentration, particle diameter, mixture density, and particle velocity is known, it can be used in the Two-Layer model and in empirical equations to predict wear of a material shown in the next few sections.

2.1.2 Wear Parameters

Material wear is defined as the amount of material loss based on shear that is exerted from a fluid traveling against the corresponding material surface and particles impacting the surface directly. There are multiple parameters that dictate the wear rate within a material and are broken down into sections below.

1. **Velocity:** increased slurry velocity results in higher impact velocities, thus a larger amount of energy is transferred from the particle to the wall to cause fracture. Hutchings [12] reported that velocity had a power-law relationship,

$$Wear\ Rate\ \propto (v_s)^n, \tag{2-4}$$

to the resulting wear rates using pipe loop experiments. Hutchings stated based on his recirculating flow loop tests that the sensitivity exponent for velocity was in the range of 0.85 to 4.5, with an average of value of 3 [12]. However, it is very difficult to predict the wear rate due to this wide range of n values.

2. **Particle Concentration:** Higher concentration of particles increases the probability of impacts between the particle and the wall. The relationship of the wear rate to the concentration,

$$Wear\ Rate\ \propto (C_v)^n, \tag{2-5}$$

was found to be exponential to the resulting wear found in early works by Elkholy et al. [13]. Elholy predicted that the wear rate was proportional to the concentration with a sensitivity exponent of 0.682, however this can change between experimental setups, and therefore cannot directly predict wear rate.

3. **Flow Regime:** Different types of flow regimes dictate how the particles behave within the flow, for example in a sliding bed regime, a larger amount of wear may occur on the bottom of the pipe due to the effect of gravity on denser particles. This can be explained using the Two-Layer model, and will be discussed in depth in a later section.

4. **Viscosity:** The viscosity of the carrier fluid, and also bulk viscosity of the slurry affects the wear rate in pipelines. Based on early works in 1987 by Levy and Hickey [14] showed a 67% reduction in mass loss of 321SS steel coupons when the viscosity was increased 0.70 cP to 1.10 cP. Therefore, the viscosity increase of a suspension typically leads increased wear rate.

5. **Impact Angle:** The impact angle, θ, is defined as the angle at which the particle collides with the wall. Based on a threshold angle, α_{max}, the type of erosion is distinguished into two separate mechanisms. The first of which occurs at $\theta < \alpha_{max}$, where the particle causes plowing or cutting of a material. At these conditions, scratches and cuts can be seen at the wall's surface. At $\theta > \alpha_{max}$, brittle deformation or removal of a chunk of the material occurs. Desale, Gandhi and Jain [15] showed that the maximum cutting angle,

$$\alpha_{max} = 0.55(H_T)^{0.69}, \quad (2\text{-}6)$$

changes with the hardness of the target material. However, this exponential relationship may change in a different operating condition, and therefore each setup would have different exponential constants. It is very difficult to accurately find a correlation between hardness and α_{max} directly.

6. **Particle Size:** Size of the particle changes the type of wear mechanism that might be present, the main two wear mechanisms are cutting, and impacts. Desale, Jain and Gandhi [15] reported that the erosion rate typically,

$$Wear\ Rate \propto (particle\ size)^m, \quad (2\text{-}7)$$

increases as the particle size increases. However, the effect of particle size is widely debated with sensitivity exponents (m) ranging from 0.3 to 2.0 [17]. Elholy [13] conducted experiments in which he reported $m = 0.616$ whereas Gupta et al. [18] reported $m = 0.344$ and $m = 0.291$ for steel and brass respectively, thus indicating that the target material also contributes to the effect. These values of m may be subject to change at different conditions.

7. **Particle Shape:** Greater particle angularity (more sharp and jagged sides and angles) can penetrate the pipe surface deeper causing faster cutting wear rates. Levy and Chik [19] conducted experiments that showed the differences that particle sharpness had in erosion. Desale et al. [20] refined this theory and produced a formula that determines the shape factor of a particle,

$$SF = \frac{4\pi A}{P^2}, \tag{2-8}$$

where *SF* is the shape factor, *A* is the projected area of the particle, and *P* is the projection perimeter. This shape factor is used in wear models in order to relate the effect of particle shape to the wear rate.

8. **Particle Hardness and Pipe Material:** Particles that are harder do not degrade and round off as quickly therefore cause cutting wear for a longer period of time. In addition, the material's ability to resist microscopic plastic deformation determines its effectiveness at resisting wear; this property is defined as the hardness of the material. It was first shown in 1983 by Elkholy et al. [13] that the greater the ratio of particle hardness to the hardness of the target material,

$$Hardness\ Ratio = \frac{H_P}{H_T}, \tag{2-9}$$

the greater the amount of erosion. Using this parameter, Desale, Gandhi and Jain [21] produced an empirical coefficient known as *K*,

$$K_{(H_P/H_T)} = 0.42, \quad for \frac{H_P}{H_T} \leq 6, \tag{2-10}$$

$$K_{(H_P/H_T)} = 1.0, \quad for \quad 6 \leq \frac{H_P}{H_T} \leq 12.3, \tag{2-11}$$

$$\text{and } K_{(H_P/H_T)} = 1.83, \quad for \frac{H_P}{H_T} \geq 12.3 \tag{2-12}$$

to describe the effect that the hardness ratio had on the wear rate. This coefficient K, was a function of the hardness ratio, defined by Elkholy [13]. K may change based on the experimental setup or hydrodynamics of the flow, therefore, cannot be used directly.

9. **Pipe Material Strength:** Harder materials typically do not fracture from particle impact as easily as softer materials. Secondly, the amount of toughness of the material is also important, as it determines the amount of energy a surface can absorb before it fractures. Oka et al. [22] and Huang et al. [5] provided an independent particle wear model that involved the target materials strength in order to predict the wear rate.

Overall, it should be noted that these empirical correlations have factors that change between different flow setups, and have a large level of uncertainty. Due to this, wear rates cannot be directly correlated to properties.

2.1.3 Wear Mechanisms

There are two mechanisms that cause the type of wear that is seen in materials in pipe flow conditions. The first type of mechanism is known as erosive wear; this mechanism consists of plowing or hitting the target material and removing a set amount of mass from the surface [17]. Typically this type of wear mechanism leads to scarring on the material surface and small craters indicating areas where particles collided and removed pipe material. Depending on the impact angle and hardness of the material surface; the effect is either impact craters or plowed material loss [23]. An example of an impact crater chip caused by a high impact particle to wall collision can be seen below in Figure 1.

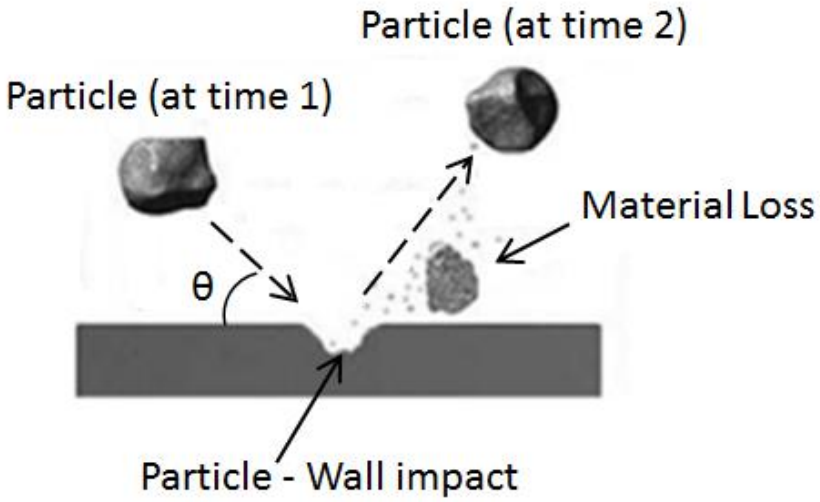

Figure 1: Erosive wear mechanism from high angle impact from a particle-wall collision [17].

The second type of wear mechanism is known as abrasion. This occurs when sharp particles slide against the pipe walls and cause scratching which eventually leads to the loss of pipe mass [17]. This type of wear mechanism should not be interchanged with the plowing effect, which is categorized as an impact driven wear at low angles. However, in slurry pipelines at high velocities, the dominant type of wear is erosive; which includes both plowing and impact depending on the target material and slurry flow conditions [17].

As mentioned before the erosive wear is broken into two types, the impact and plowing wear depending on the particles impact angle, θ. The frictional wear from a sliding bed, also referred to as the coulombic friction causes what is known as abrasive wear. All components of pipeline wear is illustrated by Figure 2 below.

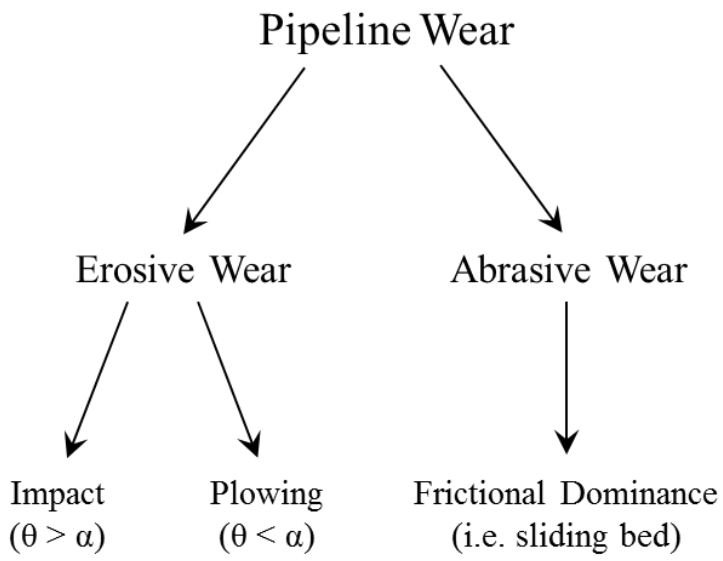

Figure 2: Componential breakdown of wear mechanisms.

Based on the experimentations done by Okonkwo et al. [23], different types of wear mechanisms effected the API X42 steel pipes. The study utilized a sand-blaster to shoot silica particles at a perpendicular rotating sheet of API X42 steel. After the wear test was complete, microscopic imaging was conducted to identify the erosion profile. It was stated by Okonkwo et al. that small fragments of these particles were embedded within the steel. Overtime further particles impacted the embedded particles driving them through the steel to create a secondary plowing effect.

It was suggested by Okonkwo et al. [23] and previous researchers that harder metals, ones with martensitic microstructures undergo the highest erosion at 90° impact angles. Ductile steels with pearlite microstructures have lower hardness values which cause them to have crack growth and micro fractures, and are more susceptible to impact wear from 15° to 45°. Based on Okonkwo et al. the microstructure of the metal determines the hardness property, which in turn results in the effectiveness of a material to resist impact wear.

Antonov et al. [24] performed wear experiments on different types of materials to compare their wear resistance. A wide range of materials were tested such as plastics, ceramics, rubber, soft metals, and hard metals. Different particle sizes, angles and speeds were observed on all the different types of materials. It was seen that in the hard metals such as carbide alloys and zirconia (a very hard ceramic), the main type of wear was caused by fine erodent particles (less than 120 microns) that became embedded within the metal's surface causing deformation over time.

Antonov's [24] experiments showed a few different conclusions. Firstly, both aluminum and steel were very susceptible to plowing wear caused by the particles impacting the metal at an angle lower than 45 degrees. The main difference between the two metals was the fact that the erosive scarring of the aluminum alloy was larger than that of the steel which is expected based on the conclusion that harder materials are less susceptible to wear. Plastics showed that the dominant mechanism was impact based on the presence of large craters of missing material.

Softer metals such as aluminum and untreated steel had the most wear from coarse particles that were larger than 600 microns, and were not very sensitive to the impacting particles that were 120 microns and smaller [24]. Materials with a lower hardness value such as rubber showed larger craters on the specimens compared to materials with a higher hardness (such as Hardox 400). Steels experienced a plowing mechanism which was not shown in softer materials such as plastics (also observed by Okonkwo et al. [23]). Based on the results of previous researchers, the sensitivity of the erosion to particle size is based on the material's strength properties.

The most susceptible wear mechanism for a material is greatly impacted by its malleable characteristics. According a model presented by Neilson and Gilchrist [25], wear of ductile materials occurred the most at impact angles of particle-wall collisions around 20°. This was demonstrated by the first combined ductile and brittle erosion model created by Neilson and Gilchrist [25] in 1968, shown in Figure 3.

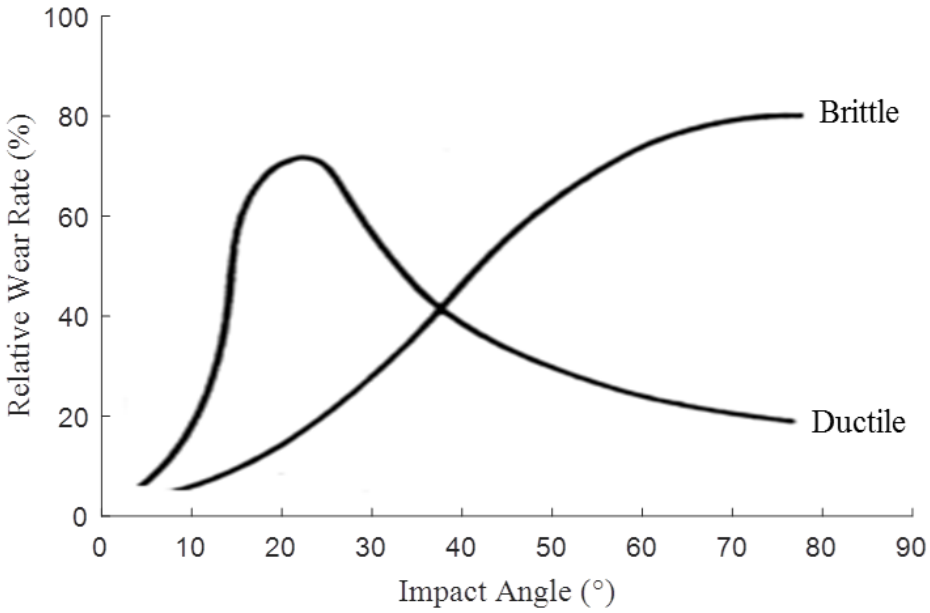

Figure 3: Erosion against Impact angles based on Neilson and Gilchrist Model [26].

This model suggests that ductile materials are vulnerable to wear at impact angles of 20°, whereas brittle materials tend to be show the most erosion at 90° particle-wall impacts. It should be noted that the ductility of a material is described by its elongation of plastic deformation before fracturing.

The Neilson and Gilchrist [25] model has agreement with the data in Antonov's [24] experiments in which metals such as steel and aluminum saw high levels of cutting erosion, whereas brittle plastics showed susceptibility to impact wear. Therefore, it can be expected that ductile materials are prone to low impact wear.

2.1.4 SRC Two-Layer Model

Types of Frictional Loss

An analytical model must be applied to provide a relationship between the erosion rate of a material and the slurry parameters that have been defined. The Two-Layer model is used in this study for this purpose. The model is robust since it accounts for all important parameters that are associated with slurry pipe flow. Additionally, the model was created directly from pipe flow rather than an empirical model from non-pipe flow measurements of wear.

The Two-Layer model splits the total frictional loss in the pipe into different components. Essentially there are two types of friction that is found during heterogeneous slurry flows as stated by Gillies et al. [27]:

a) Kinematic friction is caused by motion of the fluid-phase against the walls of the pipe; an additional component is from the particles dispersive stress. Both of these components of kinematic friction is velocity dependent, and as a result the kinematic friction increases with respect to velocity. However, another phenomenon known as the near wall lift of particles, can reduce the overall dispersive stress, but is only significant at very high velocity conditions [27].

b) Coulombic friction is the result of an incomplete suspension of the particles, this causes a portion of the particles immersed weight to be supported by the pipe wall that is in contact with this sliding phase. Typically, coulombic friction is higher when the velocity is closer to the deposition velocity of the system. At higher velocities, larger concentrations of particles are suspended reducing the coulombic friction [27].

Horizontal pipe flow forces

The Two-Layer model suggests that there are two sections in which a different type of friction is predominant. Both of these layers have distinctly different bulk velocities and particle concentrations [27].

A representation of the two distinct layers of flow in terms of the cross sectional area of a pipe is shown with Figure 4. The upper layer is the source of the kinematic friction, whereas the lower layer is the source of coulombic friction. It should be stated that kinematic friction is still present within the lower layer. The angle beta angle, β, is used to define the height of each layer.

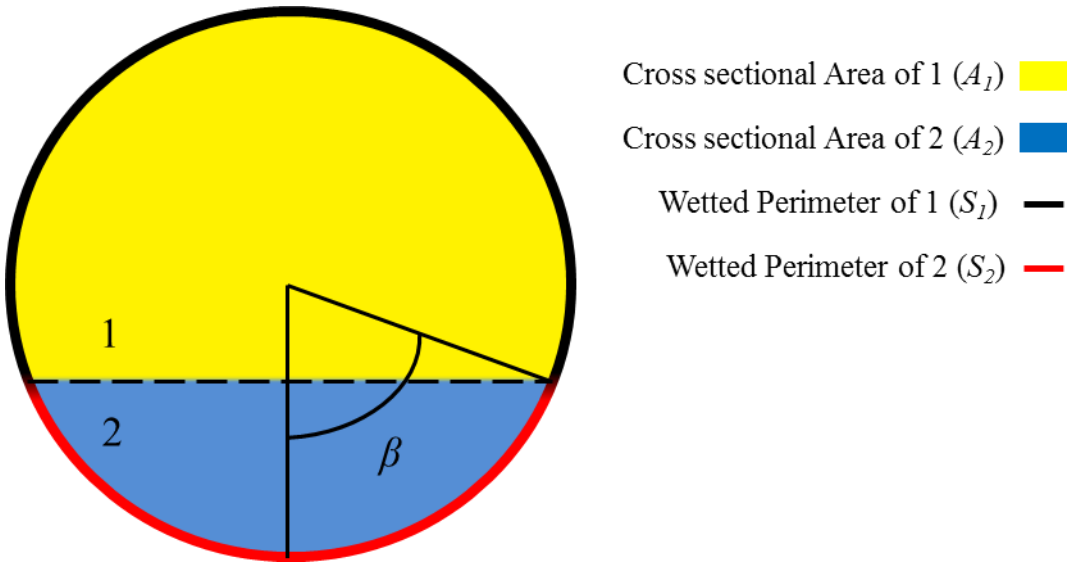

Figure 4: Two Layer model schematic of upper layer (denoted as 1) and lower layer (denoted as 2) in which β defines the height of both layers.

In each layer, there are different velocities and concentrations of the slurry. In reality, there is a continuous gradient of both parameters across the height of the cross section; however, the Two-Layer model simplifies this into two distinct values at each layer [27]. Figure 5 shows two different lines, one solid which represents the actual distribution of velocity and concentration. The profiles are shown against the height position of the pipe referred to as *y/D*. The dashed lines are an approximation; this creates two distinctly different concentration and velocities for the upper and lower layer.

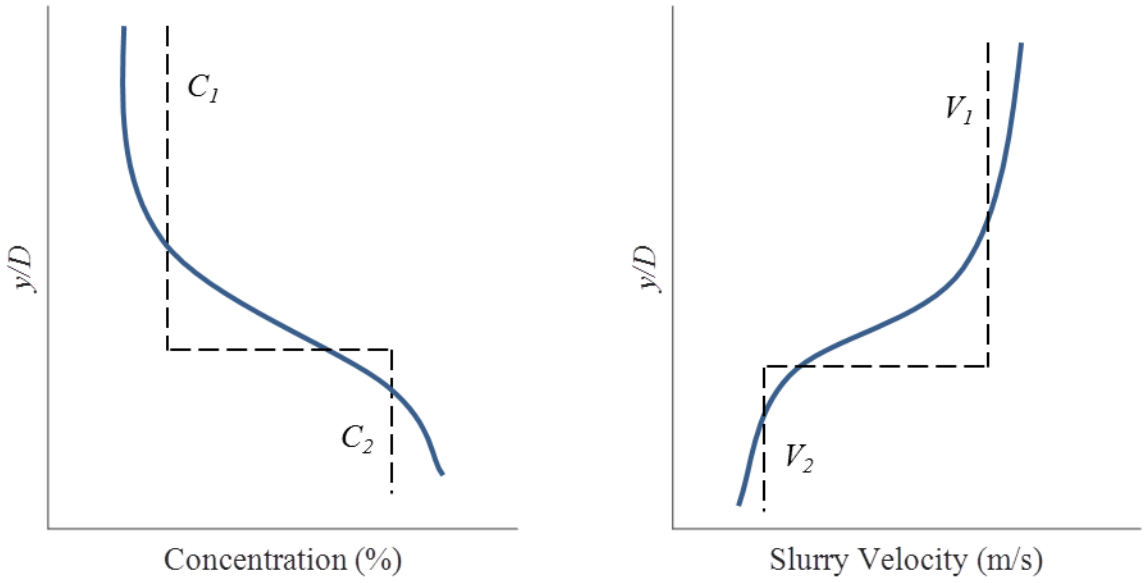

(a) (b)

Figure 5: (a) Concentration and (b) particle velocity profiles against the normalized pipe height (defined as *y/D*).

Using these two distinct layers, the total pressure drop of the mixture can be split between the two layers as

$$-\frac{dP}{dz}_{total} = -\left(\frac{dP}{dz}_{up} + \frac{dP}{dz}_{low}\right), \quad (2\text{-}13)$$

where *dz* is a differential element of the height about the cross sectional pipe. The pressure gradient at the upper layer,

$$-\frac{dP}{dz}_{up} = \frac{\tau_{1k}S_1 + \tau_{12}S_{12}}{A}, \quad (2\text{-}14)$$

is based on the shear stress acting on the upper wetted perimeter. S_1 is defined as the wetted perimeter for the slurry that consists in the upper layer, (refer to Figure 4). T_{lk} is upper layer kinematic stress from both the solid and liquid phase. T_{12} is defined as the shear stress between the upper and lower layer. The total cross sectional area of the pipe is defined as *A*.

Similarly, the pressure gradient of the lower layer,

$$-\frac{dP}{dz}_{low} = \frac{\tau_{2k}S_2 + \tau_c S_2 - \tau_{12}S_{12}}{A}, \quad (2\text{-}15)$$

is based on the sum of stress terms exerted by the moving slurry against the wetted perimeter. S_2 is defined as the wetted perimeter of the pipe in lower layer. In this case there are two components of shear stress: the kinematic friction denoted as τ_{2k}, and the coulombic friction denoted as τ_c. In the bottom layer, the stress between the two layers acts in the opposite direction when the lower layer is considered as the control volume.

When both these layers are represented in terms of their shear stress components, the total pressure gradient,

$$-\frac{dP}{dz}_{total} = \frac{\tau_{1k}S_1 + \tau_{2k}S_2 + \tau_c S_2}{A}, \quad (2\text{-}16)$$

is represented by the summation of kinematic friction at both layers and the coulombic friction at the bottom. However, at this current form, the stresses are not separated between the liquid and solid phase. The stresses on the pipe wall must be analyzed further in order to relate them to the fluid and solid phase parameters.

Shear Stresses for Upper Layer

Starting with the upper layer, only the kinematic shear stress,

$$\tau_{1k} = \tau_{1k,f} + \tau_{1k,s}, \quad (2\text{-}17)$$

is present; the kinematic friction caused by both the liquid and solid phases. The shear stress of the fluid phase,

$$\tau_{1k,f} = \frac{1}{2}(f_f \rho_f) v_1^2, \quad (2\text{-}18)$$

is found by using the fanning friction factor, f_f, and velocity. Similarly, the kinematic shear stress from the solid phase,

$$\tau_{1k,s} = \frac{1}{2}(f_s \rho_s) v_1^2, \quad (2\text{-}19)$$

can also be represented based on a solids frictional factor, f_s: The solids friction factor can be calculated based on a semi-empirical relationship to two parameters; one is the dimensionless particle size, d^+, and the linear concentration, λ. Based on the study conducted by Gillies et al. [27], the following relationship estimates the solids friction factor

$$f_s = \lambda^{1.25}\left[0.00005 + 0.00033\, e^{(-0.10d^+)}\right], \quad (2\text{-}20)$$

in which the dimensionless diameter [27],

$$d^+ = \frac{d\rho_f u^*}{\mu_f}, \quad (2\text{-}21)$$

is the ratio of particle diameter to the turbulent length scale of flow. The term ρ_f and μ_f, are defined as the liquid phase density and viscosity respectively. The term u^* is known as the frictional velocity,

$$u^* = \left(\frac{\tau_f}{\rho_f}\right)^{0.5}. \quad (2\text{-}22)$$

Applying equations 2-18 and 2-22 into 2-21, the dimensionless particle diameter can be rewritten as

$$d^+ = \frac{d\rho_f v_1 \left(0.5 f_f\right)^{0.5}}{\mu_f}. \quad (2\text{-}23)$$

The linear concentration,

$$\lambda = \left[\left(\frac{C_{max}}{C_r}\right)^{\frac{1}{3}} - 1\right]^{-1}, \quad (2\text{-}24)$$

is defined as the ratio between the particle diameter and the average distance between particles [11]. In order to calculate this accurately, the *in-situ* concentration is used. Here the C_{max} term is known as the packed bed concentration. This value is dependent on the size and shape of the particles. It can be determined experimentally, however, close estimates have been given to be about 0.62 for silica sand [10].

Shear Stresses for Lower Layer

The lower layer consists of both the kinematic and coulombic friction. The kinematic shear stress of the lower layer, τ_{2k}, is identically defined compared to the upper layer; however, the velocity of the lower layer must be used instead (refer to Figure 5). The main addition in the lower layer is the coulombic friction term, τ_c. The coulombic wall stress can be calculated based on the analysis of Gillies et al. [27] as

$$\tau_c = \frac{0.5gD^2(\rho_s - \rho_f)(C_2 - C_1)(\sin\beta - \beta\cos\beta)\eta_s}{S_2}. \quad (2\text{-}25)$$

The density difference between the particle and liquid phase is defined as the buoyancy force of the particle in the lower layer. This determines the amount of the sliding load the pipe is holding. The lower layer concentration, C_2, can be found based on the coulombic contact load. The beta angle is required to find the area the lower layer occupies within the cross section. Finally, the constant of coulombic friction,

$$\eta_s = \frac{\tau_w}{\sigma_s}, \quad (2\text{-}26)$$

is the ratio normal to shear stress at the pipe wall [27]. In which σ_s is the amount of immersed weight of solids unsuspended by the fluid lift forces. This is estimated based on a concentration profile; the immersed weight is all particles under 5% *y/D* of the pipe.

Using this model, the wear rate of a pipe can be compared to the solid phase friction to evaluate the occurrence of a trend. Based on previous data, the wear rate patterns change based on multiple variables and not all can be kept constant between studies such as diameter or velocity. However, this analysis may provide a normalized way to compare any given condition directly to the wear rate as all parameters will change the solids friction.

2.1.5 Types of Wear Testing Apparatus

One of the main driving forces of wear related research is due to the severe economic loss that industries face in their pipelines. In order to conduct such research, accurate measurement techniques are required to both quantitatively and qualitatively analyze the mechanisms that cause this wear. Multiple measurement types are available and are used in abundance in this field of study. Each wear measurement technique has both advantages and disadvantages. Understanding these

properties of the wear measurements gives a basis to determine which technique is the most appropriate to simulate the wear that occurs in slurry pipelines.

Slurry Pot Tester

One of the most common experimental methods used to measure wear is a slurry pot. The main benefit to the slurry pot test is the shorter test time compared to the time it takes a pipe section to wear [28]; this is due faster velocities and the ability to reach higher concentrations. The slurry pot can be described as a hollow cylinder in which the suspension is present. During testing; the suspension is rotated using an impeller located at the bottom of the slurry pot; this rotation allows the particles to stay suspended during the experiment. The system is normally sealed to ensure the effects of outside humidity are negated [28]. The wear is caused by the rotation of the slurry against test coupons of user chosen materials [10, 11]. The test coupons are normally placed on the rotating shaft in order to expose them to slurry while also simultaneously allowing the particles in the slurry to stay suspended [12, 14]. In some cases the samples are rotated independently using a 2^{nd} motor instead of being attached to the mixing impeller blades [31]. During cases in which erosion-corrosion mechanisms are analyzed, the slurry pot tester has built in cathodes and anodes in order to control the level of corrosion as a variable. The erosive mechanisms accelerate the corrosive decay of the material based on the transport of the slurry and can be modelled as an erosion-corrosion combination [32]. Another type of pot tester used by Clark et al. [33] incorporated a cylindrical aluminum specimen that was placed on the inside wall of the tester to investigate the effect of impact angle of particle-wall collisions to the erosion rate of the test specimen. In general, there have been many types of pot testers depending on the focus of the study, the main concern, however, has been to provide evidence in which the pot tester data is comparable with that of actual pipeline wear.

It is known that the hydrodynamics of the pot tester is much different than that of pipe flow, this leads to concern when using results from a slurry pot experiment to make a claim on pipe wear. Due to the different nature of pipe loop and slurry pot tests, exact comparisons are difficult. The high impeller speed velocities in these experiment lead to much faster wear of the steel specimens.

Ojala et al. [34] provided data on wear rate of 316L steel in a high speed slurry pot tester. Based on their experiments, after 20 minutes of run time there is a cumulative mass loss of almost 4 grams. This loss is occurring far more rapidly than in a pipe loop. In Wood et al. [35] pipe loop

experiment, a 4 g mass loss occurred after 200 hours on stainless steel. The reason behind this high wear in the slurry pot test is due rotation of 2000 rpm, which results in a 20 m/s velocity at the samples [34]. These velocities however do not occur within typical hydrotransport projects. These discrepancies between pipe loop and slurry pot tests indicate that using the slurry pot as a substitute to measure pipe wear may not be fully comparable.

The slurry pot also enables the analysis of the effects of combined erosion-corrosion mechanisms which is typically much more difficult measure in pipes [10, 11]. The level of dissolved oxygen is easier to control in a geometrically smaller testing setup, and therefore the effects of corrosion can be analyzed with controlled experiments. Another important benefit to slurry pot testing is the lower volume requirement of slurry compared to tests such as a recirculating pipe loop; typically slurry pot testers have internal volumes ranging from 3.8L [36] to 10L [29].

Jet Impingement

Another technique known as jet impingement has been used to study erosive wear; Okonkwo et al. [23] utilized this experimental setup to evaluate the erosive 22ehavior of Grade X42 pipeline steel. This method involves the use of compressed air to eject a suspension of abrasive particles through a nozzle towards a specimen holder of a target material [23]. Different researchers have had slight changes in the geometry of jet impingement, such as the angle of incident of the nozzle to the test specimen, however; the main concept is essentially similar. Xie et al. [37] has a reservoir of slurry that is transported via a slurry pump and sent through a nozzle against a specimen. Xie et al. [37] and Alam et al. [38] used water based slurry whereas Okonkwo et al. [23] ejected particles with air as the carrier fluid. This technique has the benefit of using a wide range of carrier fluids in terms of their viscosity and density, which is not possible in other types of setups such as a slurry pot due to issues such as particle suspension.

The benefit to this experimental setup is the range of velocities that can be tested; particle velocities as high as 80 m/s can be impacted against the coupon [23]. These velocities are significantly higher than that of impacting particles within pipe flow, and thus impact wear can be studied separately of abrasion while also having fast testing times. A second benefit to the control in the impact angle of the impingement and its correlation to impact wear. Typically the test coupon can be rotated to different angles to change the angle of impact from the nozzle [22, 23]. Most researchers that apply this experimental setup want to characterize the type of effects based on the impacts of the particles

on the test surface. Due to this, Scanning Electron Microscope (SEM) imaging is a significant part of the analysis process as it allows visual evidence of the erosive patterns. Typically, the test coupons used in jet impingement are small flat plates, which are easier for collecting SEM images compared to circular pipe test sections [22, 24].

The disadvantage with this testing system is that abrasive wear is almost non-existent unless the impact angle is very low. There is not a natural mix of both abrasion and impact together and rather is separated due to the nature of the setup. This may be good to characterize erosive mechanisms singularly [38]; it is not accurate at simulating the erosion which is caused by particle-laden flow within pipelines. Secondly, the velocity of the slurry in these experiments is higher than that in pipeline flow conditions in order to accelerate testing time [23], which may not accurately be comparable to pipe wear.

Coriolis Tester

The first Coriolis tester was used by Tuzson et al. [39] during 1984. The Coriolis creates flow parallel to the specimen wall, similar to pipe flow. The setup typically involves slurry that is sent downward to a rotating disc [25, 26]. At the rotating disc, there are exits towards the outside of the disc. Due to the rotation of the disc, centrifugal forces cause flow to head to these outer exits of the disc. Test section coupons are typically placed within these exit channels on the rotating discs [24, 25].. The velocity of the flow past specimen is comprised of the rotational speed and Coriolis acceleration of the device.

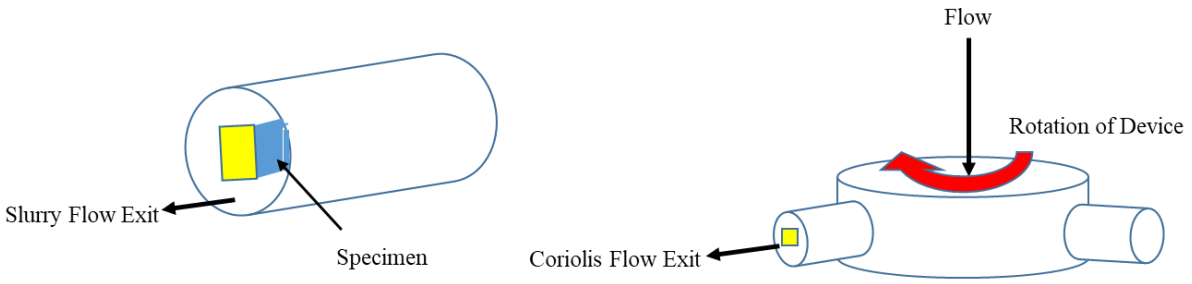

Figure 6: Diagram of a Coriolis Wear Tester [11], the specimen is the red cuboid attached to the yellow specimen sticker.

The test coupon is placed within the center of the pipe, and therefore erosion occurs on all sides of the coupon. The wear rate of each side of the specimen may vary due to a heterogeneous concentration profile of the slurry through the pipe [40]. There are multiple benefits to the Coriolis

tester such as the lower required amount of slurry to run tests compared to pipe loop tests. Also, due to significantly higher velocities that normally don't occur in pipelines, high amounts of wear can be measured; this in turn reduces testing times compared to pipe loop tests.

One of the negatives to using a Coriolis tester is the difference in the flow conditions between pipeline flow and the exit flow of the tester. Typically the velocity of the slurry in a pipe is closer to the deposition velocity of the particles, and a form of sliding bed is present, this phenomenon is not possible to create within a Coriolis tester [11]. Secondly, the nature of particle-wall effects in pipe flow is different compared to that in a Coriolis tester which may skew the results when trying to understand wear principles in pipelines [11].

Clark and Llewellyn [40] used a Coriolis tester to study the effect of radial position on the erosion of the test coupons. It was found that the impact angle of the particle-wall collisions greatly affected the wear rate. However, it was seen that Clark and Llewellyn [40] used a velocity of 20 m/s, and other researchers such as Xie et al. [37] used velocities between 14 to 24 m/s. At these high velocities, the effect of impact angles on the wear is different compared to pipelines which operate around 3 to 6 m/s. Therefore, it is difficult to predict pipeline behavior off this testing procedure.

Toroid Wheel

The Toroid wheel tester is another type of accelerated wear device used in testing. The device consists of rotating cylinders that have coupons on the outside of rotating disc. The geometry is different compared to the slurry pot or Coriolis tester, the main difference being the axis of rotation is horizontal rather than vertical.

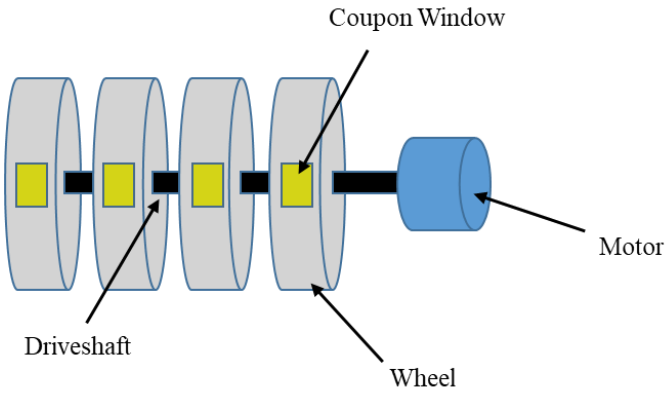

Figure 7: Example of a Toroid Wheel tester [8], the driving motor rotates the wheels, the inside of each wheel contains slurry.

Wear test plates are placed at the outer circumference of the wheels that rotate. Cooke et al. [8] summarizes the system description by stating that the rotation of the wheel causes the wear test plates to move against the slurry within the large encompassing cylinder.

The Toroid wheel shares a similar benefit to the slurry pot and the Coriolis tester; the minimal required volume of slurry to operate is much lower than that required in a recirculating pipe loop experiment. Where the Toroid wheel differs from a slurry pot is the amount of testing time required. The Toroid wheel can also be run for up to 1 week of continuous operation [42] at velocities that can be comparable to pipeline flow. Despite this, the hydrodynamics of the Toroid wheel coupons moving against stationary slurry is different compared to axial pipe flow. One of the reasons behind this is a non-uniform distribution of stress at the bottom of the wheel due to difficultly of suspending the particles. Secondly, the contact between the particles and testing coupons occur at different angles compared to pipe flow at similar velocities [42]. These effects can cause different erosion patterns despite similar flow conditions as pipelines. The testing may be an acceptable way to see the differences between materials as a screening process, but not enough evidence is provided by literature to confidently use it as a direct substitute to pipe flow tests.

Recirculating Pipe Loop

Despite the advantages of all the measurement techniques mentioned, the flow fields created within the above mentioned experiments are not identical to that of axial pipe flow. This causes major concern in the effectiveness of these techniques to understand the wear phenomenon within

a pipe. The best alternative to having field data on operating pipes is a recirculating pipe loop in which slurry is constantly pumped through a closed loop; this test is known to accurately simulating pipe flow conditions that occur in the slurry pipelines [8]. Within the pipe loop, a test section exists with test spools that can be replaceable. The wear rate is typically calculated based on the mass loss of these test spools after the circulation of slurry for a given time or the thickness that is decreased from the pipe wall [9, 12–14].

It has been seen through comparisons during experimentation in a pipe loop and service pipelines that the hydrodynamics are very similar. Schaan et al. [3] investigated the wear rate of a straight pipe section and a 90° bend and found a ratio of wear to be 0.38 between the two respectively. To compare this, Fotty et al. [6] conducted a pipe loop test at the equivalent flow conditions of Schaan et al. [3] at the Alberta Innovates and Technology Futures Facility. They reported to have found a wear ratio between the bend and straight section of 0.30, which is within 10% to the value reported by Schaan et al. [3]. This shows agreement between the hydrodynamics and mechanisms of wear between the recirculating pipe loop tests and operating pipelines. Another benefit to performing this experiment is the ability to change parameters of the flow that are also changing within operating pipelines: such as the velocity of the flow, the viscosity of the slurry, and non-dimensionalized coefficients such as the Reynolds Number. These parameters however, cannot easily be correlated to other setups such as a slurry pot or jet impingement and therefore have difficulties comparing them to operating pipelines.

A disadvantage that occurs within a pipe loop is the issue of particle degradation within the suspension [8]. Overtime, the particles that have properties such as its size and sharpness slowly round of and break into smaller pieces [9]. To account for this many researchers at the University of Alberta replace the slurry after a certain time within the test [9, 12]. This ensures the particle degradation does not affect the wear rates found within the pipe loop. The major challenges of pipe loop experiments are the large amounts of time due to slower wear rates, large volume requirements of slurry, and slurry replacement to avoid particle degradation. This increases the total cost and time of experiments and requires a large testing facility, but provides the most accurate understanding of wear mechanisms within pipe flow.

2.1.6 Characterization of Wear

There are three different ways methods that help characterize the wear rate of a material. These methods all present different forms of information that provide insight for understanding wear mechanisms. Not all of these methods quantify the wear; some are used as qualitative representation of the wear.

The most common is to measure the mass differential before and after the test; this measurement is the commonly used as a way to quantify the wear rate. This mass loss is analyzed by plotting it against several parameters such as the fluid flow velocity, suspension particle size, particle concentration, and testing time [44]. It is typically seen with metals such as aluminum that the mass loss exhibited is linear with respect to time within the duration of a test [10, 28]; therefore, just one mass loss measurement between the start and end of the experimentation should result in an accurate wear rate of the material. To check for measurement error, multiple mass measurements can be taken throughout the testing time. Based on the function of mass loss to time; the slope of the best fit can be used as an estimate of the wear rate of any given material after a wear test. The main drawback of mass loss measurements is that it does not show any indication of the type of wear mechanism that is dominant. Secondly, it does not give any quantitative properties about the flow. Due to these disadvantages, other measurements are required in parallel with the mass loss measurements in order to fully understand the wear occurring and to quantify it accordingly.

A qualitative method is the use of Scanning Electron Microscope (SEM) imaging to analyze the type of wear mechanisms that took place. Images contain features such as grooves, indentations and cuts showing the type of erosion that the material was most susceptible to. Okonkwo et al. [44] and Alam et al. [38] explored the use of SEM imaging to show the output of two erosive mechanisms within pipeline steel. This imaging technique allows access to determining which mechanism causes wear and thus narrows the focus of study into that specific element based on the type of failure on the material's surface. Many researchers have tried to implement different drag reduction strategies in order to improve the lifetime of operating pipelines. Using this measurement technique, not only can one identify if the drag reduction strategy is successful at decreasing the wear, but can also show which specific wear mechanism was decreased.

Another method that is used to qualitatively understand the mechanisms behind wear is based on the particle distribution at the cross section of a pipe. A densitometer works by sending gamma rays through the pipe perpendicular to the flow towards a receiver on the other side of the pipe. This imaging technique can capture the concentration of particles as a function of height. Depending on the distribution it can be easily determined which regime the slurry is in (i.e. a sliding bed or suspended turbulent regime). This was conducted in the current study during pipe flow erosion tests.

This technique can also be used as a way to control the regime within a pipe loop experiment. In some cases only a specific regime is desired and therefore the particle distribution must be constantly monitored (i.e. a sliding bed is not desired). In many erosion tests involving opaque pipes (such as carbon steel) majority of imaging techniques do not work. The densitometer utilizes gamma rays which can pass through metallic surfaces in order to provide a visualization of the flow distribution for all material types. This measurement can also be taken at two different locations in a pipe to see if there is a disturbance between the downstream and upstream locations. These disturbances such as a restriction in the flow may not be noticed otherwise and could lead to inaccurate data.

2.2 Polymer Additives

Polymer additives are commonly used as a method to reduce drag in liquid pipe flows. Polymers can be applied in different applications such as pipelines and naval watercrafts. One notable large scale example includes the Trans-Alaska Pipeline System, which runs for a distance of roughly 800 miles, utilizes polymer injection at pumping stations to reduce the input power required for crude-oil transportation [45]. The polymer additives have a concentration typically below 300 ppm; these solutions typically have a lower shear stress at a wall interface and therefore require less energy to pump.

2.2.1 Extensional Viscosity Theory

There are many different theories that are used to explain the phenomenon of polymer drag reduction in this field of research. One mechanism that was proposed by Lumley [46, 47] known as the extensional viscosity theory. This theory states that polymers have a tendency to stretch in buffer region of the turbulent flow. In these regions of the flow, typically in the buffer region of the boundary layer, the strain rate is the highest. As the polymers extend, the fluid's local viscosity in that region increases, this is known as the extensional viscosity. With the increase of this local viscosity, the small eddies are neutralized and the high fluctuations are significantly reduced; this causes the shear rate to drop. Choi et al. [48] stated that once this shear is reduced, the TBL is modified as the buffer layer expands, causing the overall friction to simultaneously decrease.

2.2.2 Reynolds Stresses

The drag reduction phenomenon is typically looked at as counter-intuitive due to initial observations. Typically the solvent for polymer additives is water, which has a lower viscosity than that of a polymeric solution. Typically, the drag associated to a fluid is related to the viscosity of the solution, however, in the case of the polymers, the drag is reduced in spite of the viscosity increase. The total shear stress of a fluid element in a turbulent regime can be shown as follows,

$$\tau_{ij} = \mu\left(\frac{du_i}{dx_j} + \frac{du_j}{dx_i}\right) + \rho\overline{u_i' u_j'} + \tau_p. \qquad (2\text{-}27)$$

The above equation has three components: the first term is the viscous stress term (also present during laminar flow), the second is the Reynolds Stress term, and the third is present only in a polymeric solution defined as the polymer stress. The dominant stress term in turbulent flow is the

Reynolds shear stress. The main reason behind this drag reduction is due to the monotonic reduction in the Reynolds shear stress term during turbulent flow [49]. The net reduction of both the Reynolds shear stress and velocity gradient reduction outweighs the viscosity increase of the solution and polymeric stress.

2.2.3 Elastic Theory

The second theory commonly used to explain the PDR phenomenon is known as the Elastic theory proposed by Tabor and de Gennes [50]. As mentioned before, the essence of PDR is resultant from the reduced strain rate from neutralizing small scale fluctuations within the flow. Tabor and de Gennes [50] argued that the elastic properties of the polymer molecules were crucial to this fluctuation reduction. Tabor and de Gennes [50] stated that the polymers behave similarly to springs that compress and extend as they are coiled molecules. This process of stretching absorbs some of the turbulent kinetic energy (TKE) and converts it into elastic potential energy. This section expands on this elastic theory in detail.

When the flow is highly turbulent (at a high Reynolds Number), the length scale of the turbulence, also defined as the smallest eddy size, decreases, and are more frequent, this causes an increase in the production of the TKE [51],

$$TKE = \frac{1}{2}\overline{u_i' u_j'} = \int_0^\infty E(k)dk, \qquad (2\text{-}28)$$

where *E(k)* is the energy spectrum of the turbulence, and *k* is the wavenumber. As mentioned before, the long coil polymer chains behave as springs dissolved within the flow. These molecules in the buffer layer go through a stretching process, which absorbs some of the TKE. Once this occurs, the cumulative elastic energy stored by stretched polymers becomes equivalent to the TKE within the buffer layer [50]. These stretched polymers then travel outside of the boundary layer and relax to return to a coiled state, and release their absorbed TKE, which translates into regular kinetic energy within the bulk flow. The process of this can be seen in Figure 8.

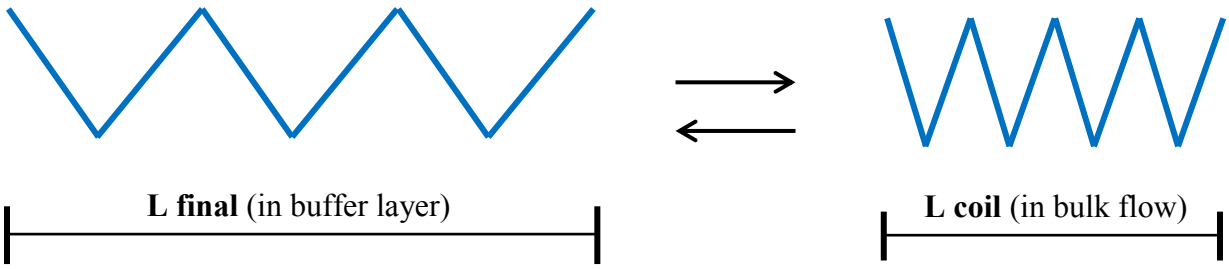

Figure 8: Visual Representation of polymer behavior using the Elastic Theory

It can also be stated that during this energy transfer process, the polymers terminate the small scale eddies within the boundary layer, which also leads to a reduction in the Reynolds stresses [49]. The elastic theory has been shown to be useful to predict DR based on experiments from Sreenivasan and White in 2000 [52] along with numerical works from Min et al. in 2003 [53]. Additionally, the Elastic theory states that the onset of drag reduction is greater during higher concentrations since there are more molecules stretching within the boundary layer to absorb TKE [52].

2.2.4 Polymer Degradation

The polymer molecules within turbulent flow exhibit a phenomenon known as mechanical degradation. These molecules are constantly exposed to elongation strain when they absorb TKE and strong shear stresses from wall friction, pumps and geometric changes such as bends [54]. The absorption of mechanical energy from these sources result in scission of the chains into shorter chains [54]. Due to these new entities having shorter lengths, the drag reduction capability decrease. Once the scission occurs, the lengths of the polymers are too short to cause any significant drag reduction. Researchers have seen a correlation between the amount of time a polymer solution is exposed to shear and its decline in drag reduction performance [55]. The DR performance of a polymer during turbulent flow is normally an exponential decay in respect to time [55]. This is because as the testing time increases, the amount of polymers that have underwent mechanical scission also increases, and the concentration of fully functioning polymers decreases. This is a major reason for higher concentration solutions to exhibit a much lower rates of decay compared to low concentrations. The shear within a system contributes greatly to the rate of the mechanical degradation of these polymers and will be further explored with both recirculating pipe flow and Taylor-Couette flow experiments in further sections.

2.2.5 Differences of Flexible and Rigid Polymers

There are many different types of polymers that are used in this field of research, typically categorized into two categories; rigid and flexible [56]. Flexible polymers are long linear chain-like structures that result in very high molecular weights compared to rigid polymers [56]. These flexible molecules undergo the elastic-spring mechanism which leads to a large portion of their drag reduction performance; in contrast, rigid polymers are not easily stretched and therefore provide DR based on the viscous theory. The main advantage to rigid polymers is their mechanical strength and stability, which results in a low susceptibility to mechanical scission [56]. In practical applications, this would result in less frequent replenishing of polymer solutions. However, since flexible polymers have much higher molecular weights, the total concentration to reach maximum drag reduction is significantly lower. In pipelines, these flexible polymers can be injected at pumping stations and therefore are a viable option. In this study, the focus will be on flexible polymers, primarily those known as polyacrylamides (PAM). These polymers have been widely tested for their drag reduction capabilities in the last 60 years due to their ease of manufacturability and practicality.

2.3 Taylor Couette Flow

Taylor Couette Flow is defined as the moving fluid between the gap of two concentric cylinders due to the rotation of one or both of the cylinders. It was first investigated by Taylor [57] in 1923 where experiments were conducted beyond the transitional Reynolds number and led to instabilities within the flow.

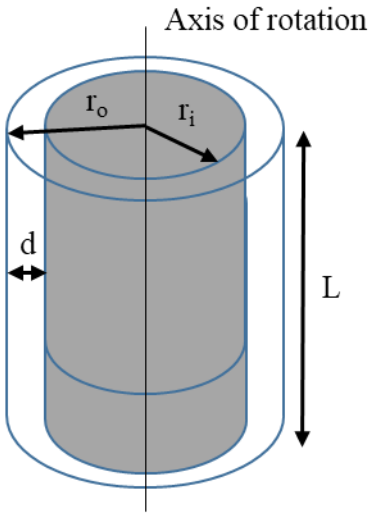

Figure 9: Basic schematic of single gap Taylor-Couette Flow [58]

Numerous flow regimes have been documented based on the rotational speeds of the inner and outer cylinders [59]. A typical Taylor Couette Device can have one of the four combinations:

- Outer Cylinder rotates with stationary inner cylinder
- Inner cylinder rotates with stationary outer cylinder (focus of this project)
- Both cylinders rotate in the same direction
- Each Cylinder rotates at opposing directions

The Reynolds number in Taylor Couette Flow,

$$Re = \frac{\omega r_i (r_o - r_i)}{\nu}, \qquad (2\text{-}29)$$

describes the degree of turbulence based on the ratio of inertial to viscous forces. Here, ω, is the rotational velocity in rad/s. The Reynolds number can be evaluated at either wall depending on the rotation speed of the corresponding wall. In this case, the inner cylinder *Re* is important as the outside wall will be stationary.

The properties of the flow gap can be expressed in terms of different geometric ratios. These ratios are important when using any non-dimensional analysis to estimate different flow parameters. A very common ratio used by many researchers in this field is known as the radius ratio,

$$\eta = \frac{r_i}{r_o}, \tag{2-30}$$

defined by Eckhardt et al. [60], where r_i is the inner cylinder radius and r_o is the outer cylinder radius. Depending on the rotation of the two cylinders, different turbulent regimes have been mapped out in a Taylor phase diagram by Monico et al. [61]. These phases describe the type of flow field that is present based on the Reynolds number of the inner cylinder and outer cylinders. The phases are subjected to change depending on the system's radius ratio; the phases stated by Monico et al. [61] are based on $\eta = 0.714$. At the instance in which outer Reynolds Number is zero, there are only two regimes that can take place, one known as Taylor Rolls, which consist of multiple eddies that form in the r-z plane, and the second known as featureless ultimate regime which has no distinct repetitive behavior.

Another important parameter is the aspect ratio of the system; this ratio shows the scale of the gap compared to the height of the chamber,

$$AR = \frac{L}{r_o - r_i}, \tag{2-31}$$

where *L* is the height of the TC fluid chamber. To compare different types of Taylor Couette flows, an important parameter that is generally analyzed is the non-dimensional torque,

$$G = \frac{T}{\rho \nu^2 L}, \tag{2-32}$$

defined by Wendt [62] Where ρ is the density of the fluid, ν is the kinematic viscosity of the fluid, and *T* is the torque required to rotate the fluid at the given angular velocity of the Taylor Couette (TC). The wall shear stress,

$$\tau_w = \frac{T}{8\pi R_o H^2}, \tag{2-33}$$

defined based on the amount of torque required to rotate the moving fluid at a given rotational speed. *T* is the torque resistance on the outer stationary wall, R_o is the radius of the outer wall from

the center of rotation, and *H* is the height of the cylinder. The drag reduction for a TC test is defined based on the torque differential of the two tests as

$$DR_{TC} = \frac{T_f - T_p}{T_f} \times 100\%. \qquad (2\text{-}34)$$

Another method used to evaluate the amount of turbulence in a flow is to find the instability of the flow based on the Rayleigh Number. Similar to Rayleigh-Bénard flow, Taylor Couette flow can have a specific analogy of the Rayleigh number, often referred to as the Taylor Number [60]. A similar property to the Prandtl number in Rayleigh-Bénard flow can be introduced here using the geometric properties as

$$\sigma = \left(\frac{0.5(1+\eta)}{\sqrt{\eta}}\right)^4, \qquad (2\text{-}35)$$

this is referred to as the geometric quasi-Prandtl number. It is useful in order to calculate the Taylor Number of the system. The Taylor number,

$$Ta = \frac{1}{4\nu^2}\,\sigma\,(r_o - r_i)^2\,(r_o + r_i)^2\,\omega^2, \qquad (2\text{-}36)$$

is a dimensionless parameter that is used to compare the centrifugal forces to the viscous forces of the flow. The *Ta* of the system is affected based on the gap and velocity in the same way as the Reynolds number. Monico et al. [61] have used this as a responding variable to the torque input of the system to verify the operating regime of the flow.

Different empirical models for the required torque to rotate the fluid at a given operating condition have been developed by different researchers. Wendt [62] found an empirical model to correlate the *G* to η, and *Re* of the flow given as

$$G = 1.45\frac{\eta^{\frac{3}{2}}}{1-\eta^{\frac{7}{4}}}Re^{1.5} \qquad for\ 400 < Re < 10^4, \qquad (2\text{-}37)$$

and,

$$G = 0.23\frac{\eta^{\frac{3}{2}}}{1-\eta^{\frac{7}{4}}}Re^{1.7} \qquad for\ 10^4 < Re < 10^5. \tag{2-38}$$

The empirical model was based on a best fit line from Wendt's original dataset [63]. The model from equation (2-38) will be one of the comparisons to the tested dataset from the TCD.

Lewis et al. [64] introduced an empirical model of predicting the amount of torque required to rotate the inner cylinder based on the *Re* and fluid properties based on a $\eta = 0.724$. The logarithmic relationship was found to be

$$logG = -0.00636(logRe)^3 + 0.1349(logRe)^2 + 0.885(logRe) + 1.61, \tag{2-39}$$

where all logarithmic operators are base 10 and apply for a range of $13{,}000 < Re < 10^6$.

Dubrulle and Hersant [64] continued the work to create a more robust model that predicts *G* from *Re*. They applied angular momentum transport and turbulent convection heat transport in order to generate a more advanced semi-empirical equation,

$$G = K_1\frac{\eta^2}{(1-\eta)^{\frac{3}{2}}}\frac{R^2}{\ln\left[\frac{(\eta^2)(1-\eta)R^2}{K_2}\right]^{\frac{3}{2}}}. \tag{2-40}$$

The main purpose of this equation was to incorporate different types of radius ratios, and those result in different *K* constants in order for the model to be more versatile at predicting the torque required at a certain Reynolds number. This equation is valid for *Re* of 10^3 and 10^6, and therefore should be used for flows higher than that. The data presented by Lewis and Swinney [65] was used to test this model and an accurate fit was found as well. At the radius ratio that Lewis and Swinney [63] worked at, $\eta = 0.724$, K_1 and K_2 were found to be 0.4 and 10^4 respectively. The main issue with this model is that the coefficients found for this radius ratio does not correlate well with testing data from larger radius ratios, and there isn't a strong method to find these coefficients. Once the flow is characterized with dimensionless fluid flow parameters, data between different experimental setups can be compared.

3 Experimental Facilities

3.1 Slurry Flow Loop at the Saskatchewan Research Council

The wear tests for this study were conducted at the Saskatchewan Research Council Pipe Technology Centre. The 75 mm nominal diameter black carbon steel pipe loop was used to conduct this study. The total length of the pipe loop is 80 m that consists of two u-bends, two straight sections and a pumping section.

The pipe loop consists of five components as shown in Figure 10. Based on the figure orientation, the flow occurs in the clockwise direction. The main piping of the loop consists of Schedule 160 carbon steel at a nominal diameter of 63 mm and 75 mm on each side of the u-bends. The large thickness ensures that the loop can be safely operated for wear tests for a long period of time. The tank has two main functions; to safely load the slurry into the loop, and to hold a volume during testing larger than the internal volume of the pipes.

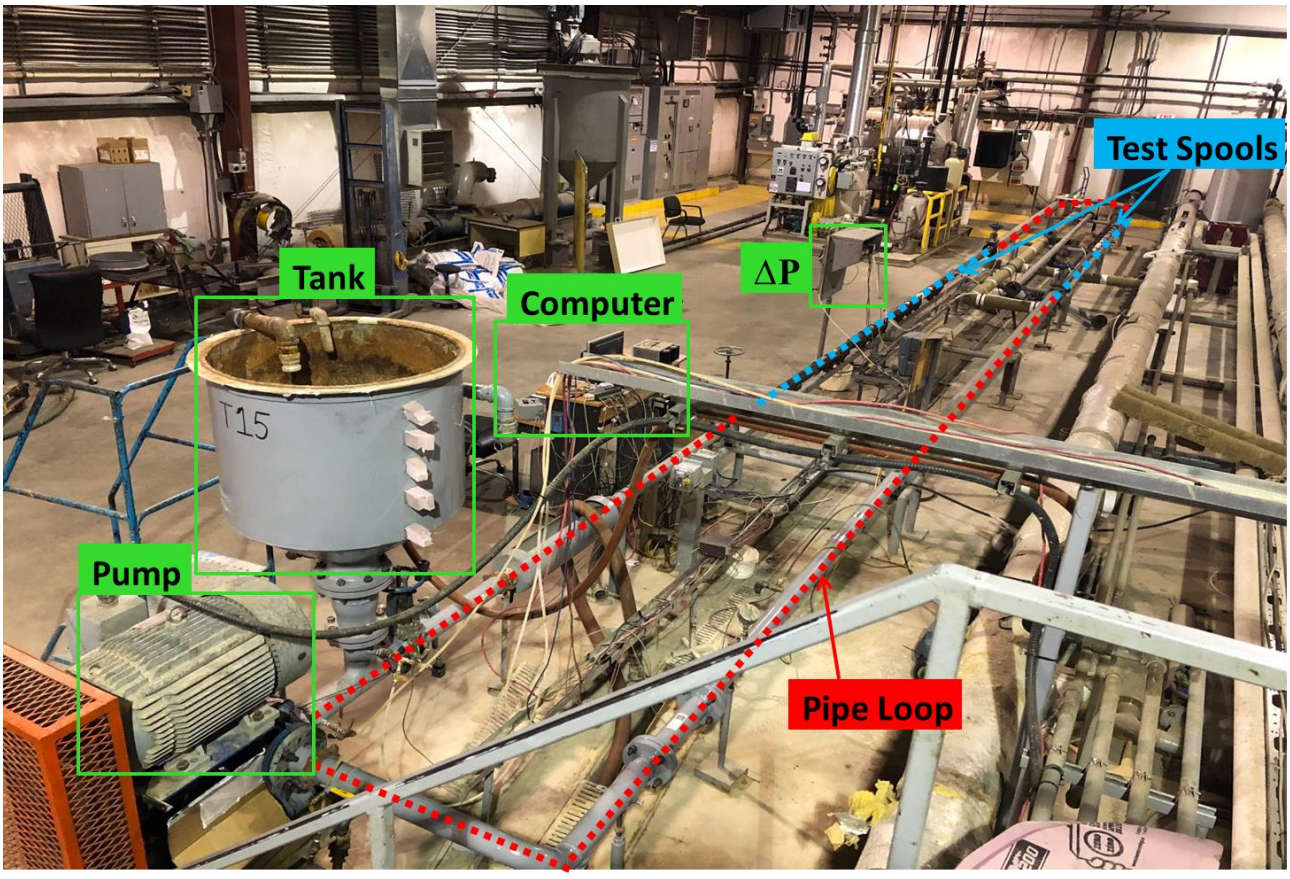

Figure 10: Schematic of SRC Pipe Loop used in current wear study.

A larger volume results in minimal particle degradation and therefore frequent slurry replacement is not required. Validyne pressure transducers are located across both test sections and send voltage data to the computer system. A Warman rubber-lined centrifugal pump (model # WPA 43A01AU) was paired to a 40 hp Hyundai motor (model # HIS 324SR234) to move the slurry through the loop. The pump speed is controlled using an interface on a 600 V Benshaw VFD (model # RS1040SX6B). Finally, there is a section of the loop upstream of the first u-bend that is jacketed; effectively acting as a parallel flow heat exchanger. This section connects to a separate tank that delivers a constant flow rate of R-134a (anti-freeze) in order to have stable temperature throughout the experiment.

3.1.1 Pipe Spool Sections

Two test sections exist during the flow tests in order to double the amount of data collected at the same allotted time. This is especially useful in wear tests since each test condition may take well over 250 hours to complete. One of the objectives of this study was to investigate the erosion rates between different materials. In order to achieve this successfully; the spool sections were aligned with a dummy spool of identical material on each side shown below in Figure 11.

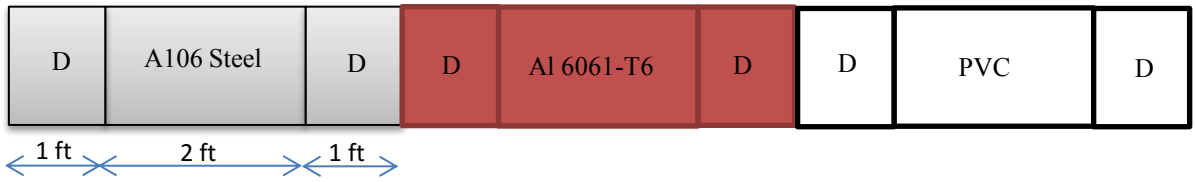

Figure 11: Layout of the pipe spools at both test sections, where D is denoted as dummy spools. Each material spool lengths are same as the carbon steel.

The test spools were 2 feet in length whereas the dummy spools were 1 foot. This accounted for the sudden change in both surface roughness and diameter change when different wear rates caused different diameters. It was shown in previous experiments, that the length of the spool (greater than 6 inches) did not contribute as a factor to the overall wear rate per length [11]; therefore 1 foot dummy spools provide enough transition length between the test sections. The spools all had internal diameters of 63 and 78 mm for each test section zone with schedule 40 thickness. The pipe flow loop was constructed out of schedule 160 thickness.

3.1.2 Experiment Techniques

Spool weights

The main experimental data consists of the weight losses from the spools. A high precision scale was used with an error of ±0.01g to make all measurements. The weight loss measurements were used to find the erosion rates for each material. The weight measurement consisted of three steps. Both test sections had two gate valves located up and downstream. The first step was to turn off the pump motor, and the gate valves were shut. With the gate valves shut, the spools were unclamped and removed at the locations shown in Figure 12.

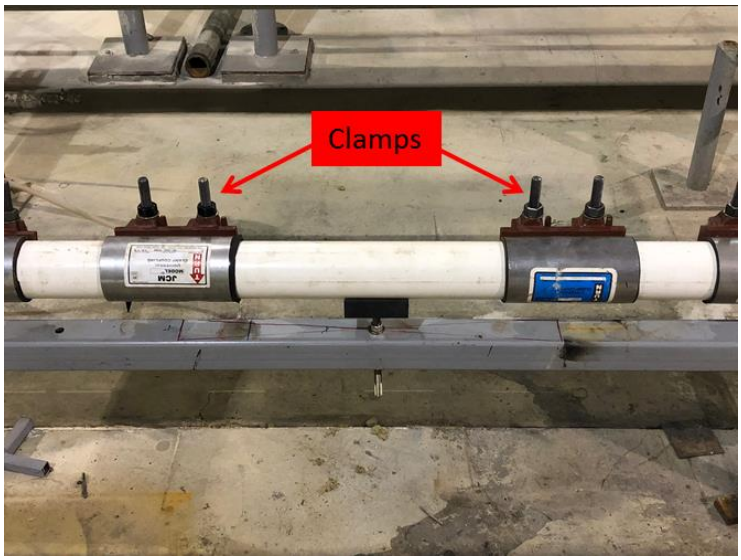

Figure 12: Spool clamps for SRC Pipe Loop during wear tests.

The clamps were designed to add a significant amount of compression on the spools to tightly connect two pieces together. The benefit of this clamping system allows the use of unthreaded spool pieces, as threading can contribute to a source of wear. Secondly, no adhesive is required to hold the spools together, which could also cause an error in weight loss measurements.

Once the experiments were completed, all the tests spools were placed in a vacuum oven for 48 hours to take a dry weight. This was especially important for PVC as plastics absorb a significant amount of water. Once all spools received heat treatment, they were measured on the high precision scale. This procedure took place every week, therefore if the test was not complete, the spools are placed back into the loop, or they are shipped to the University of Alberta for further analysis.

Concentration Gradient

In order to measure the concentration gradient throughout the height of the pipe, gamma ray densitometry was utilized. This was only used during an initial test with the slurry before the full test course was initiated. The densitometer consists of four components; the gamma source from Cesium 137, a shutter to control the gamma source, collimator to focus the beam, and a detector to generate an output.

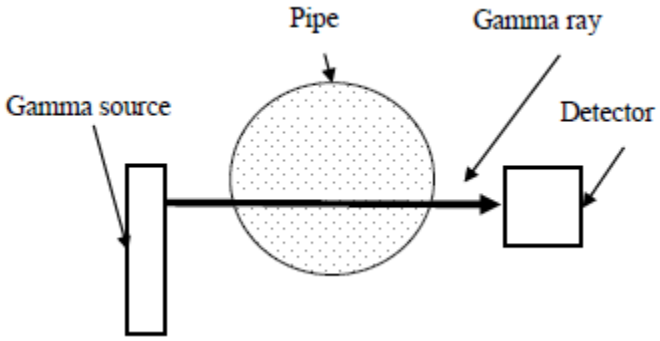

Figure 13: Major Components of a Gamma Ray Densitometry Setup [11]

The densitometer sends a signal of gamma rays perpendicular to the pipe flow in order to capture the concentration gradient as a function of vertical position as seen in Figure 13. The output of the detector is sent to the DAQ system (uses Ortec Maestro Multichannel Analyzer Software).

The gamma rays pass through the pipe, with a certain portion of it absorbed or deflected by the particles within the flow. Based on the difference of intensity between the source and the detector the solids concentration gradient can be found, an example of the result is shown was shown in Figure 5.

Pressure Gradient

During the time of the test, Validyne DP-15 pressure transducers with a 0.2 psi diaphragm recorded the pressure gradient across the test sections every five minutes. This data was important to calculate the solids frictional component. Secondly, it is a method to calculate the drag reduction when polymer additives are present within the slurry. The pressure gradient was also used with the addition of a flow meter during calibration tests before every test condition. During this calibration, a relationship between the flow rates, pump speed and pressure drop was tested. Using this relationship, the correct pump speed was used during the entirety of the test. The flow meter could not be placed during the test process due to damage concerns.

3.1.3 Controlling Slurry Properties

At the end of every test day a small sample of slurry was extracted from the pipe loop for further analysis. Three different lab scale tests were applied to this sample; viscosity measurements using a viscometer, dissolved oxygen levels using a DO probe, and a sieve analysis to determine the particle size distribution. All three parameters were controlled variables in this test, and therefore consistent readings needed to be verified. If any of these parameters changed dramatically before the slurry replacement, a shorter replacement time would be required. The dissolved oxygen levels were maintained by mixing Hydroguard I-15 into the system. This behaves as an oxygen scavenger and keeps DO levels under 0.5 ppm to ensure there is no corrosive effects in the weight loss measurements. In order to keep the slurry properties constant, the slurry was replaced after every week of testing (~100 hours). The temperature of the slurry was maintained at 25°C during tests using R-134a through the parallel flow heat exchanger.

3.1.4 Slurry Loading

The first step to prepare the slurry is to calculate the amount of solids required to reach the desired *in-situ* concentration. The desired volumetric concentration, solid density, and total volume of the loop are used to calculate the mass of solids that is required. The total volume of the loop is 205 L (which includes the volume of the tank). At 30% concentration, the particle mass would be calculated as

$$m_{solid} = V_{tot} \times C_r \times \rho_{solids} = 205\ L\ \times 0.3\ \times 2.65\ \frac{kg}{L} \cong 163\ kg. \qquad (3\text{-}1)$$

Once the solids mass calculation is complete, the loop is filled with water (carrier fluid) and the pump is started. The loop should be running at approximately 10 L/s (750 RPM) to ensure that plugging does not occur during the loading process. Once this condition is reached, the particles are gradually added into the tank, the process cannot be instantaneous to avoid high local concentrations of the solids. The carrier fluid is slowly heated to approximately 50°C in order to release trapped air bubbles that may have been stuck to the solid particles. Once the loading process is complete, the temperature of the slurry is reduced back to 20°C, and the experiment is initiated.

At the end of the 100 hours of testing, the slurry is replaced. At this time, a second line is connected to the loop while the pump is operating. This causes the slurry to be drained into a waste tank where it can be appropriately dealt with. Water is added to the loop during the draining process in

order to clean the loop of any residual particles left over, as they can affect the slurry conditions of the next test if not removed.

3.2 Toroid Wheel Testing Facility

One of the objectives of this study is to evaluate the wear characteristics of different materials in order to find a suitable substitute material to steel for pipe wear tests. Carbon steel pipes typically require over 250 hours of testing to detect any significant, and thus results in wear tests to be very expensive. One of the materials that have been chosen as a substitute is a polyurethane cast; however, before running pipe wear tests, a Toroid wheel tester (TWT) is used to compare the wear pattern to that of steel and aluminum. The TWT motion attempts to replicate the axial movement of slurry flow against the walls of a pipe [42]; however it is not entirely equivalent. Regardless, it is an appropriate screening test to evaluate a new material type for wear. The Toroid Wheel Tester is consists of four rotating disks that contain a slurry within it.

The experimental setup of the TWT consists of five components:

- Online computer control with LabVIEW software
- Variable frequency drive (VFD)
- 3 HP Motor (Shaft Diameter of 50 mm)
- Four rotating wheels with coupon slits to insert test materials (cross sectional area of 65 × 60 mm^2)
- An outer acrylic toroid wheel (AWT) used for visualization of the slurry flow

Figure 14 shows a sketch of the TWT setup used at the University of Alberta Chemical Engineering. Each wheel contains slurry that rotates against the outer wall to induce erosion of the coupons. The operation of the TWT starts with the command from LabVIEW, the user can set a desired RPM, which sends a signal to the VFD. Current is then sent to the motor which rotates the shaft to spin all five wheels. The motor is coupled to the main shaft using a pulley belt system with a 1:1 ratio. The entire TWT setup is 5.12 ft long, 2.88 ft wide and 3.52 feet wide.

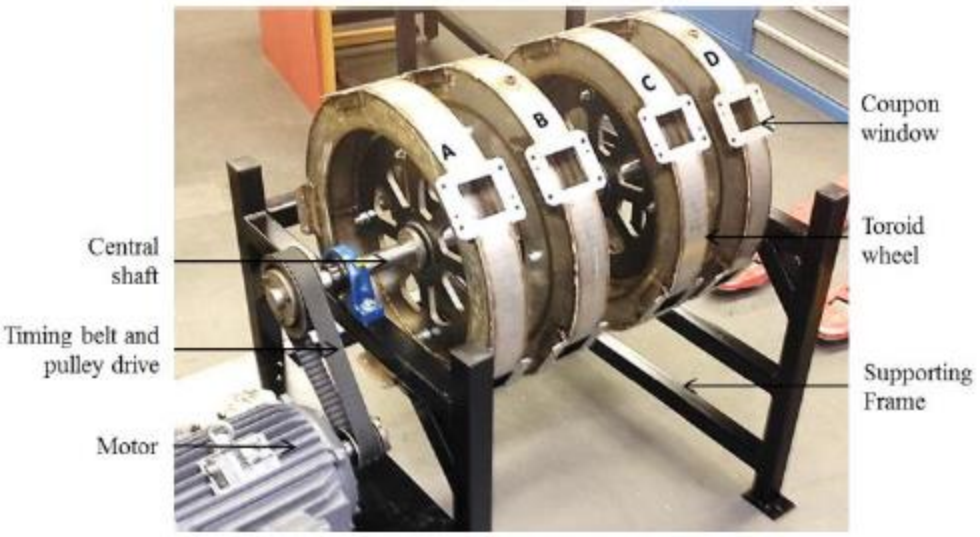

Figure 14: Toroid Wheel Setup designed by Sarker [42] used in the current study.

Each Toroid wheel has five coupon slits for material test coupons; these are referred to as the coupon windows. The coupon windows have an area of 65×65 mm^2 and are attached with screws to the test coupons. A gasket of 0.5 mm thickness is placed between interface of the metal rim of the coupon window and the test coupon to prevent any leakage during the testing. Additionally, a layer of lubricant from Rust Check is applied to the window facing side of the gasket. Each test coupon area is flat, and therefore the outer surface of the TWT is not a complete circular geometry. Due to this, an angle is created between the circular frame and the test coupon, a small gap is present (seen in Figure 15) which can cause leading edge effects in the erosive patterns in test sections.

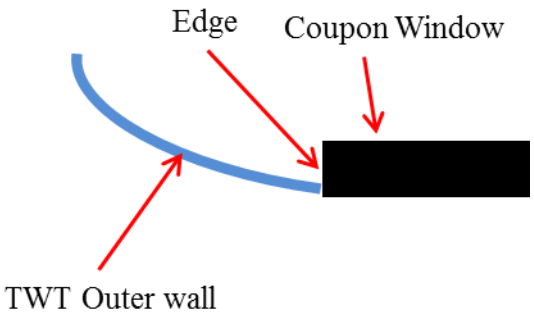

Figure 15: Schematic of a single wheel's coupon window and edge step change for the TWT experimental setup.

The process of loading the slurry is straightforward; four out of five coupons are attached while the TWT is unloaded, the slurry is loaded through the final open window and then closed. To ensure there is not a high DO level, two charging ports are located on either side of the wheels, this is to inject N_2 from one end and release any trapped air from the other. The slurry also has Hydroguard I-15 mixed at 1% by volume to prevent any corrosion.

3.3 Taylor Couette Flow Testing Facility

The benefit of exploring Taylor-Couette flow allows multiple polymer drag reduction tests to be measured quickly; this can be used as a screening process. One of the main objectives is to determine a polymer additive that increases the life of a pipe, however before direct pipe testing can be performed; the polymers that will be used must first be narrowed down from a larger selection. The Taylor Couette device is sometimes referred as a slurry pot in industry. As mentioned before, the benefits of the slurry pot include fast testing times and low working fluid volume requirements. It was also mentioned that this flow regime does not necessarily simulate the flow of pipelines, and therefore is only used as an initial screening process to refine the test matrix of polymers that will be used in a pipe loop test. Another benefit of using a pilot-scale device such as a TC is the ability to study the interactions of fine particles under the size of 44 μm with the polymer additives that will be used. In industrial applications, polymers have been used as a way of dewatering tailings that consist of tiny clay particles, and there is a concern that these particles may agglomerate with the polymers and render them ineffective at drag reduction. These tests should not be conducted in a recirculating pipe loop to avoid plugging.

The Taylor-Couette Device for this study has been designed and manufactured at the University for Alberta specifically for this study. The testing facility was designed that consisted of an inner cylinder enclosed within a stationary outer cylindrical shell. In order to generate Taylor Couette flow, the inner shaft has the ability to rotate and apply shear on the fluid entrapped within the gap, thus causing rotational motion. The Taylor-Couette Device (TCD) consists of three main components:

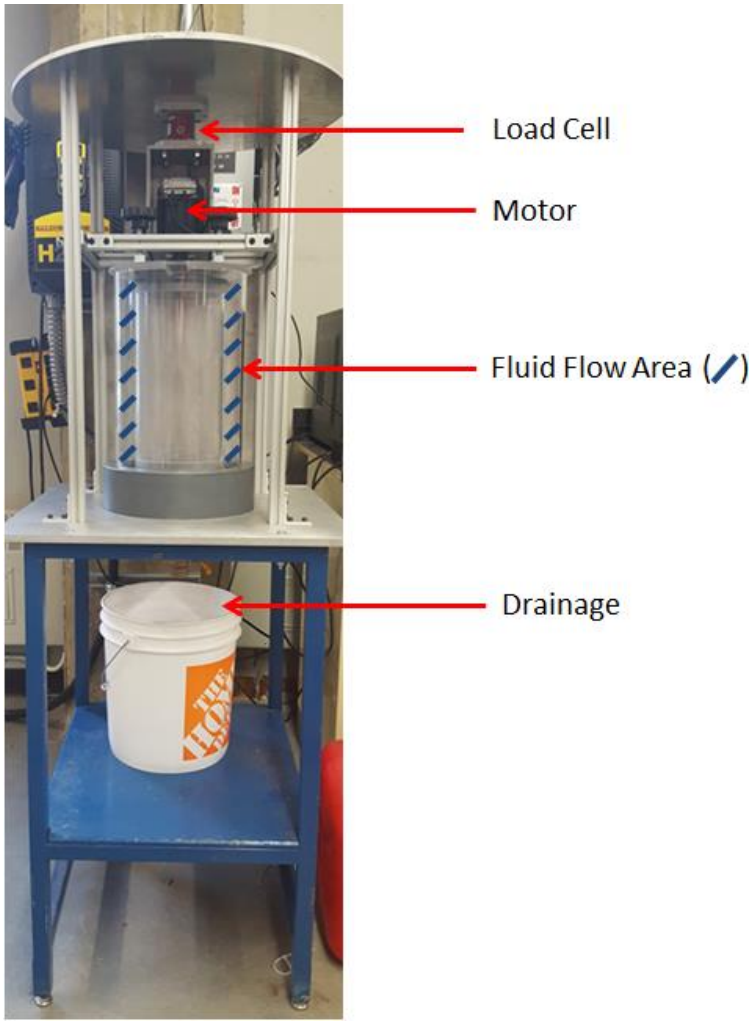

Figure 16: Taylor Couette device experimental setup at the University of Alberta, designed and manufactured for this study.

The motor applies torque to the inner cylinder through a coupling, while the outer cylinder remains stationary. A reaction load cell is attached between the motor casing and structural body; this results in the load cell applying a counter torque equal to the one exerted by the motor. This counter torque is logged as the output data of the system. Once the testing is complete, a drain valve is located at the bottom of the fluid flow chamber can be opened to expel the working fluid into a bucket. The TCD has been designed in order to span a large operating range within the featureless ultimate regime; the operating range has a Taylor Reynolds Number (Re_{TC}) of 100,000 to 210,000 which is achieved with a motor frequency of 30 to 55 Hz. This Reynolds number is based on the viscosity of water, and therefore may be lower for other fluids such as viscoelastic polymer solutions due to higher viscosities.

3.3.1 Fluid Flow Chamber

The dimensions of the fluid flow chamber can greatly affect the regime of the Taylor Couette flow. The chamber for this device consists of an outer and inner shell made out of acrylic. This was used in order to visually assess characteristics of the flow such as Taylor Rolls during any flow tests. The three main geometric properties that are of interest are the diameters of the inner and outer cylinders, along with the chambers height. These provide the aspect ratio, and radius ratio of the system, which as mentioned previously are important in the dimensionless analysis. Furthermore, in order to follow the TC phase diagram presented by Monico et al. [61], similar geometric ratios are required.

Based on the TCD dimensions presented in Table 1, the radius ratio, η, is 0.718, with a gap of 1.375 inches and an aspect ratio, AR, of 10.2. These values are within 5% of the ratios presented in the works of Ostilla and Monico [61]. The inner cylinder of the chamber is fixed to a double shielded bearing at the base using a coupling as indicated on Figure 17. This allows for smooth rotation, and minimizes residual torque within the system. It also provides the system to be fixed from both the top and bottom to avoid a cantilevered setup; this reduces the overall vibration and can significantly reduce the residual torque. The outer shell and inner cylinder have a wall thickness of 1/16 and 1/8 inches respectively. This provides enough hoop stress to contain the working fluid at the highest operating condition. The knobs at the top of the chamber are tightened to add compression on the outer shell to keep the fluid trapped inside. An o-ring is compressed at the interface between the outer shell and base to prevent leakage. The benefit of the compression system allows for the device to be completely disassembled for cleaning or repair.

Table 1: Dimensions of the Taylor Couette device fluid flow chamber.

Dimension	**Value**
Outer Shell Radius (r_o)	4.875 in
Inner Cylinder Radius (r_i)	3.5 in
Chamber Height (L)	14 in

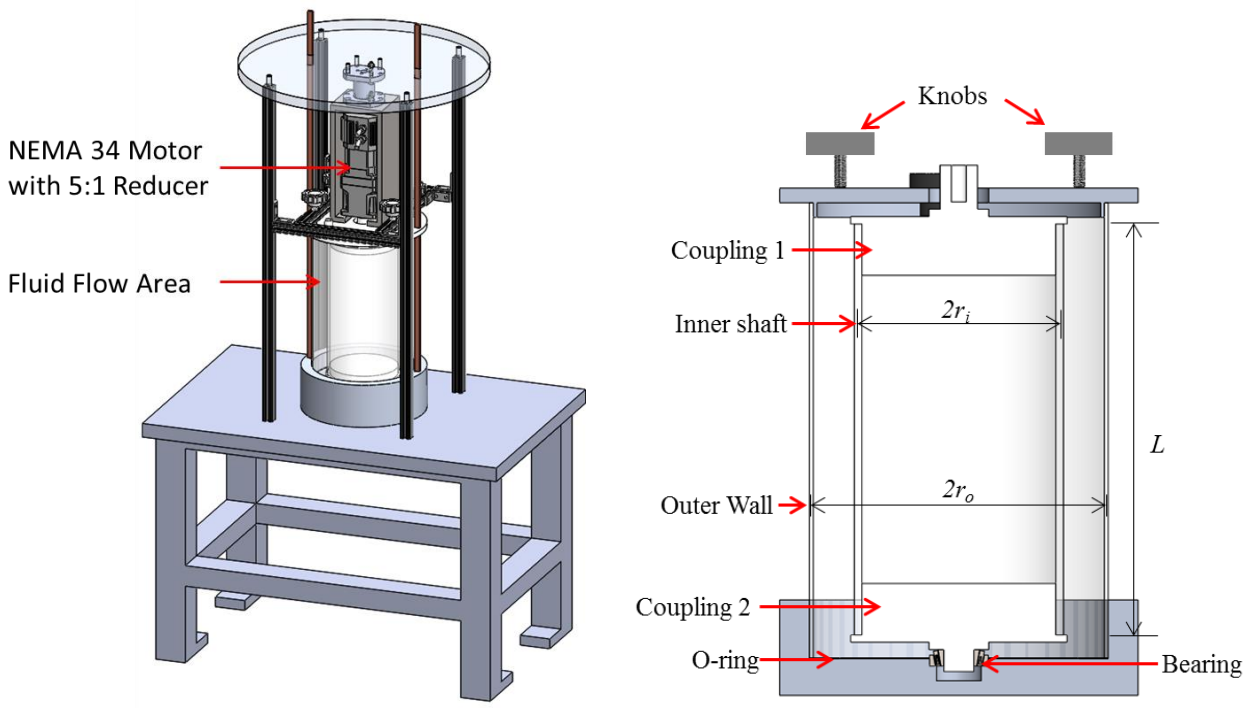

(a) (b)

Figure 17: (a) Diagram of the fluid flow chamber within TCD and (b) details of the fluid flow chamber.

3.3.2 Motor

A brushless servo DC motor manufactured by Teknic Inc. is located above the fluid flow chamber in the experimental setup. The motor has the capability of rotating bi-directionally and is controlled by a user interface known as MSP v1.7 developed by Teknic. The motor has a NEMA 34 frame size, and operates at 75V power input. The shaft diameter is 0.5 inches, which is connected to a coupling to rotate the inner cylinder of the fluid flow chamber. The motor is attached using 8 screws to a custom made motor mount that allows it to be supported only by the torque load cell. The motor is also dust and water resistant which provides protection during multiphase flow tests to guarantee the longevity of the motor. The maximum continuous torque provided by the 275 W (0.37 hp) motor is approximately 2.8 N·m at a maximum speed of 970 RPM. The startup torque is considerably higher during starts near 0 rpm, however under the current design conditions; experiments do not require more than 80% of the continuous torque at start up. A 500 Watt DC fan cooled power supply (IPC-5) converts 108 VAC into 75 VDC input for the motor. The system operates at 60 Hz to deliver this power. The IPC-5 is connected to a regular wall socket, and

connects to the motor using an 8-pin Molex to 2-pin sabre connection. The power supply has short-circuit, over-voltage, and over-current protection.

3.3.3 Data Acquisition

A reaction torque sensor manufactured by Futek Advanced Sensor Technology Inc. was installed in the experimental setup for load measurements to evaluate the performance of polymers. As mentioned previously, the load cell is independently connected to the motor mount, this results in the entire reaction torque of the motor to be exerted through the load cell. The reaction load cell has internal strain gauges that have electrical resistance to any geometric change. This means that applying any change in geometry, defined as the strain, will result in a voltage output proportional to the deformation. Four strain gauges are present in a Wheatstone configuration; this allows only the torsional deformation to exert a voltage rather than axial loading from the weight of motor. The Futek TFF425 FSH02811 has a maximum torque reading of roughly 7 N·m (1000 oz-in) which is far greater than the continuous torque operation range of the motor. In addition there is a 150% overload protection provided by the cell.

One of the main reasons to use the Futek load cell is the relatively low uncertainty (as shown in Table 2) at its rated output of 2 mV/V. However, due to such a low voltage output, a signal amplifier was installed in order to match the input of the National Instruments DAQ card. The signal amplifier chosen, Futek Model IAA100, increases the voltage to ±10 VDC which can be detected by the DAQ card in order to record the data in LabVIEW. The amplifier adds an additional step of uncertainty, with a non-repeatability of ±0.05%. Overall, the data acquisition system does not add a large uncertainty to guarantee accurate torque measurements.

Table 2: Uncertainty of FSH02811 Futek Reaction Torque Load Cell, where RO is rated output based on Futek specifications sheet.

Uncertainty	Value
Nonlinearity	±0.2% of RO
Hysteresis	±0.2% of RO
Non-repeatability	±0.2% of RO

3.3.4 Method and Calibration of TC Device

The testing procedure within the TCD follows a few steps; firstly, the TCD is cleaned of any residue from previous tests or build up. Once, the TCD is clean, it is filled up with the desired fluid to the height of the inside cylinder in order to keep a consistent aspect ratio during tests. The tests are run between 50 rpm to 800 rpm, and are considered all within the turbulent regime (which will be verified in later sections). Based on this velocity range, the expected Reynolds number range of the tests is within 1.6×10^4 and 2.6×10^5 for the water as the working fluid.

The servomotor from Teknic, model # CPM-MCVC-3432-RLN, is controlled by a program known as MSP V1.2. This program has two main modes, torque control and velocity control, both through maintaining a constant digital frequency input to the motor. The first mode, torque control, was only used to calibrate the load cell before any experiment was conducted run to guarantee all measurements are accurate.

A direct calibration approach in which a mass was hung from a supporting bolt on the motor casing which was attached to the reaction torque sensor; this setup is illustrated by Figure 18. Weights varying from 100g to 2000g were suspended, for each mass the load cell voltage reading was captured and compared to the actual torque. The conversion factor is based on a plot of the load cell output against the torque caused by the mass, shown in Figure 19. This resulted in a linear relationship between the voltage output and torque within reasonable agreement. A sensitivity value of 0.63 Nm/V was determined between the load cell output and torque to a precision of 0.01.

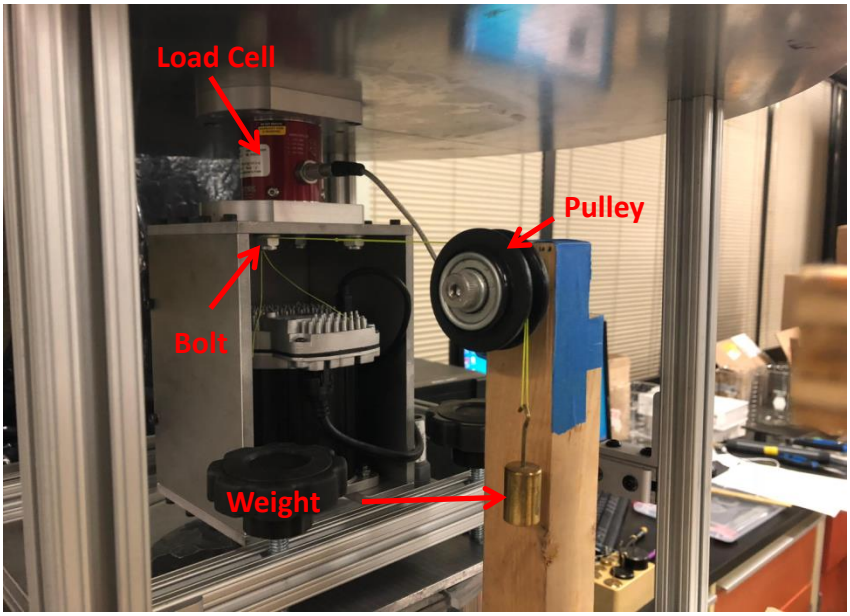

Figure 18: Calibration procedure of motor for TCD using a pulley-weight system.

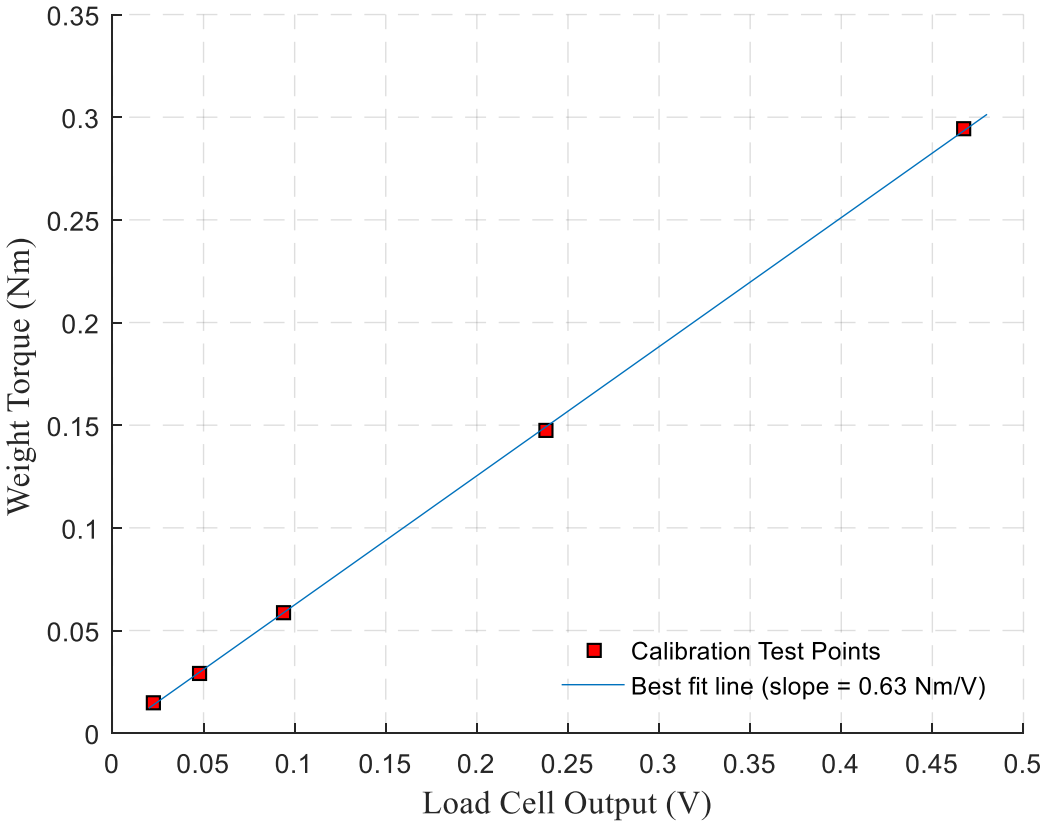

Figure 19: Calibration procedure of motor for TCD using a pulley-weight system

After system calibration, the data from the load cell is gathered through a DAQ card from National Instruments. The program used to operate this data collection is LabVIEW. A simple block diagram has been created in order to save data at a certain sampling rate for a user defined time period. In the case of tests involving only water, the sampling frequency was set to 100 Hz, and the sampling time was set to 1 minute. Tests were conducted at the desired starting rpm, and increased (or decreased) by increments of 50 rpm. The motor is controlled by the MSP V1.2 program provided by the manufacturer Teknic. The mean of the torque was taken from each 1 minute dataset in order to calculate the overall torque value at a corresponding rotational velocity. No filtering or noise cancellation was applied to the datasets. The standard deviation of the torque datasets were higher during the lower velocities but still at an acceptable range of less than 20%. The TCD can operate bi-directionally, however, to keep the tests consistent, only CCW tests have been conducted which result in 'positive' voltage outputs from the torque load cell. It was documented that tests around 540 to 550 rpm should be avoided as there are large vibrations at this range, possibly due to the system approaching its natural frequency.

3.3.5 Evaluating TCD Performance

Before polymer solutions can be tested for their drag reduction characteristics, the credibility of the TCD must be evaluated. This will be accomplished by checking the repeatability of measurements at equivalent conditions, comparing torque outputs to previous experiments by other researchers as well as theoretical outputs.

Repeatability

Two tests were conducted between 200 rpm to 700 rpm using water as the working fluid. The first test involved increasing the speed at intervals of 50 rpm, whereas the second test started at 700 rpm and incrementally decreased the rpm. A lower velocity than 200 rpm was not used due to lack of load cell resolution at very low torque values. This however will not be case in the future for lower velocities when a suspension which higher bulk viscosity is used. In between the two tests, the system was refilled with water and partly reassembled.

Based on the data of the average torque values shown in Figure 20, it can be seen that the data sets look identical regardless of the order in which tests were conducted. This demonstrates that the system has very low hysteresis; which agrees with the Futek load cell uncertainty rating of ±0.2% for hysteresis. It should also be noted that the device was drained and refilled between the two

tests along with reassembly of the top lid. The data shown in Figure 20 has a maximum discrepancy is 0.01 Nm (less than 2%); this suggests that the repeatability is not affected based on reassembly of the device, or refilling of the working fluid. It can also be concluded from this test, that there is a negligible amount of residual torque in the system. Overall, the average is around 0.05 Nm, taking into account the resolution of the device is 0.04 N-m, this amount may largely consist of noise.

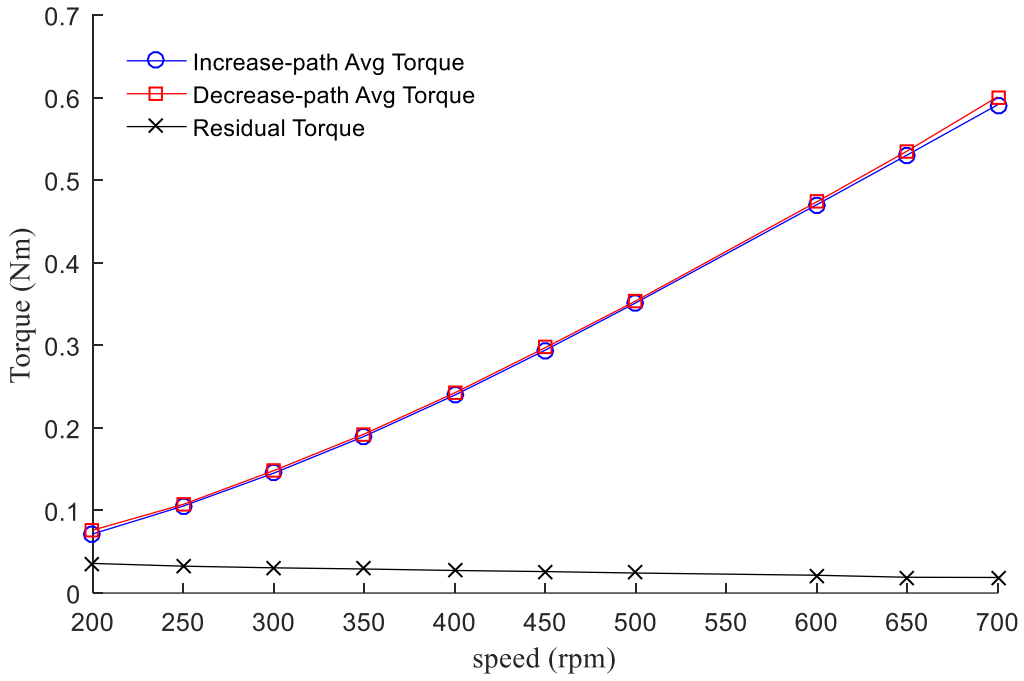

Figure 20: Torque measurements of water at increasing and decreasing velocities using the TCD.

Comparison to Previous Experiments

The average data from the experiments completed with water in the TCD has been compared with the models described in the previous section in Figure 21. In addition, the raw data of experiments performed by Lathrop et al. [65] is also compared as they extensively investigated the relationship between torque and Reynolds number for Taylor Couette flows The data from Bhambri's study [58] was also included for comparison.

Based on Figure 21, it can be seen that the data collected from the TCD follows a similar trend as the models from all other researchers' models. The main discrepancy is a larger increase in the dimensionless torque as the *Re* increases. This discrepancy is also seen in greater effect with Bhambri's [58] data. There are a few reasons to provide justification for this discrepancy from the

models; firstly, there may higher torque due to a free surface at the top level of the water when the TCD is operating. Another important factor is that these previous models have been based on a certain aspect (AR) and radius ratio (η), for example Lewis and Swinney [63] used a η of 0.724 and AR of 11.4, whereas the current TCD has a η of 0.74 and AR of 10.2. These ratios are is closer to Bhambri's setup [58] in which η was 0.76 and AR was 10.57.

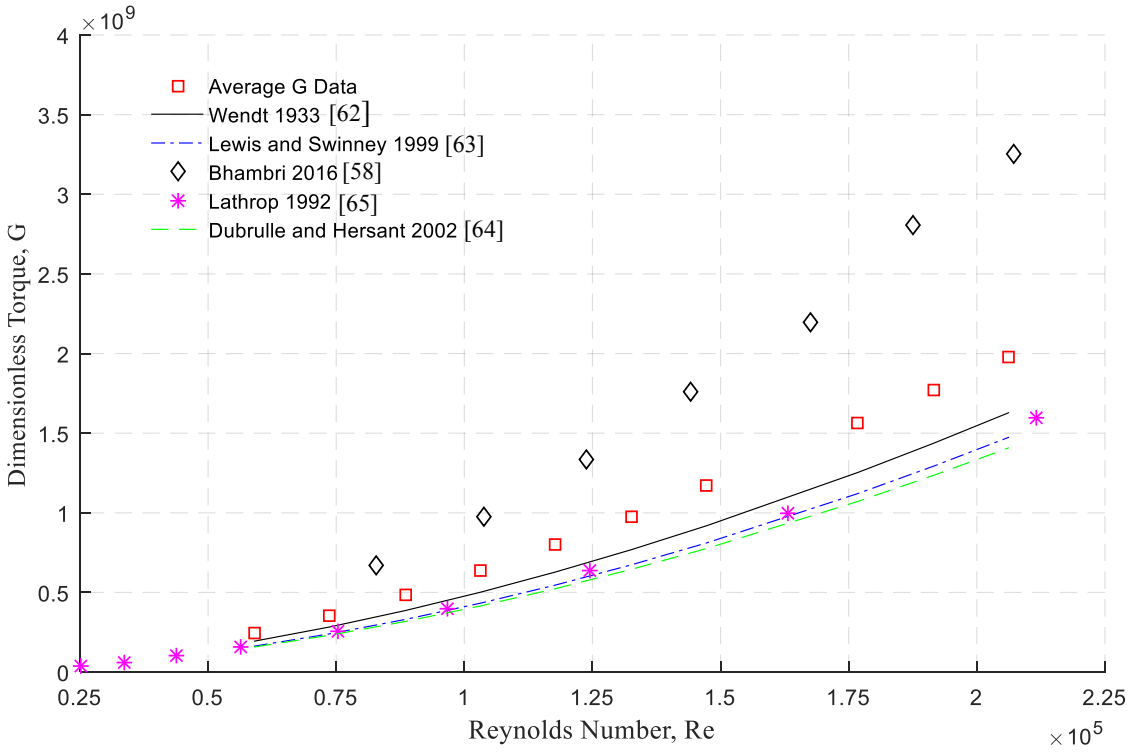

Figure 21: Relationship between dimensionless torque and Reynolds number.

The increasing torque as at higher Re is a result of a greater surface area contact within the current TCD and Bhambri's experiment. To show this, three of the experimental setups have are shown in Figure 22.

From Figure 22, it can be seen that the working fluid was only located in the gap portion of Lathrop's [65] design, where as in Bhambri [58] and the current TCD, there was fluid both above and underneath the rotating cylinder. The increased surface area against rotating fluid can cause this increase in the torque compared to previous models which was seen in Figure 21.

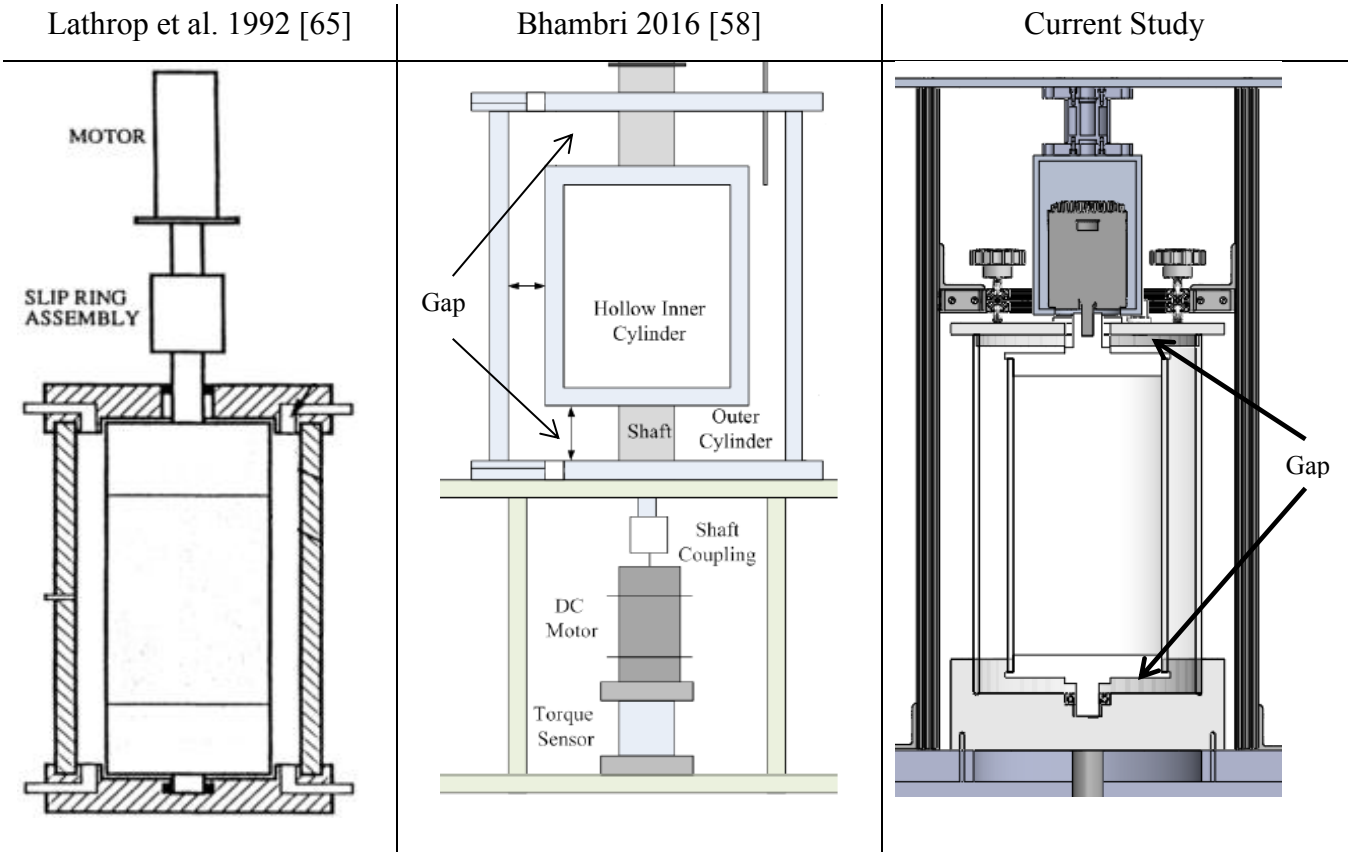

Figure 22: Comparison of Taylor Couette Devices between the current study, Bhambri [58] and Lathrop et al. [65].

Lathrop et al. [65] modified the general relationship between the Reynolds number and friction coefficient and presented the following equation

$$\frac{Re}{\sqrt{G}} = N log_{10}\sqrt{G} + M. \qquad (3\text{-}2)$$

The ratio of *Re* and *G* can be related based on the coefficient of friction,

$$C_f = \frac{\tau_w}{\frac{1}{2}\rho U_\infty^2} = \frac{G}{Re^2}, \qquad (3\text{-}3)$$

which can be applied to equation (3-2) to relate the friction of the system to the *Re* as

$$\frac{1}{\sqrt{C_f}} = Nlog_{10}Re\sqrt{C_f} + M. \quad (3\text{-}4)$$

N and *M* are constants that can be calculated based on the torque measurements at specific Reynolds numbers. Lewis et al. found their torque data to fit was very closely to this relationship at an *N* of 1.56 and *M* of -1.83, which occurred at a von-Karman value (κ) of 0.44. This is perhaps the only analytical equation that is typically used to fit data sets at different aspect ratios in order to create empirical models due to the lack of any other relationship. The universal accepted von-Karman value for turbulent flow near a wall is κ of approximately 0.40; thus, the *M* and *N* constants that were empirically driven for equation (3-4) show that it is quite accurate. It should be mentioned that Lathrop [63] and Lewis [65] treated the bulk core region of the flow as an extension to the boundary layer in order to create these models.

A linear plot between $\frac{1}{\sqrt{C_f}}$ and $log_{10}Re\sqrt{C_f}$ can be used in order to find the *N* and *M* values which correspond to the slope and y-intercept respectively. Using parameter denoted as *N*, the von-Karman is expressed as

$$\kappa = \frac{[(1-\eta^2)ln10]}{\sqrt{2\pi}N\eta}. \quad (3\text{-}5)$$

Based on equation (3-4), Figure 23 was created to compare current TCD data in order to evaluate the accuracy of the experiments in terms of theory. The best fit line returned an N of 1.83 and an *M* of -3.93. Using the *N* value (slope of the best fit line) that was found, equation (3-5) was applied in order to find the von-Karman value. In this current study, a Von-Karman value of 0.36 was concluded, which is has a deviation of 10% with the theoretical value of 0.40.

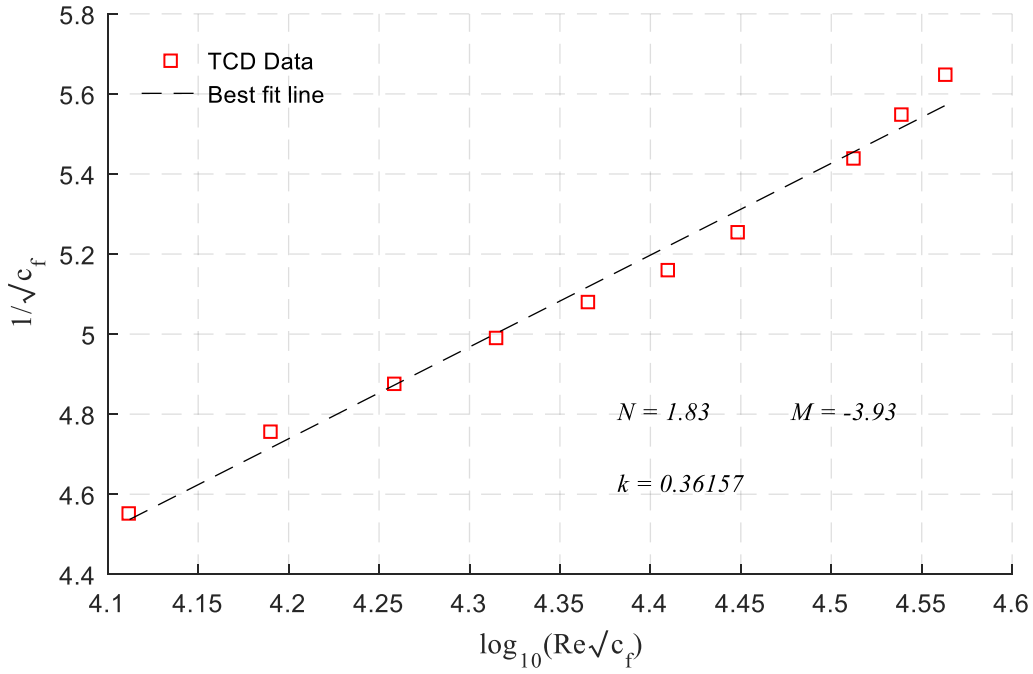

Figure 23: Comparison of current TCD water results to the Prandtl-Karman Law.

A summary of past research studies have been compared to the current TCD. Table 3 shows that the deviation from theory in this current study is within an acceptable amount relative to other studies that have been conducted.

Table 3: von-Karman value comparison between current study and previous works.

Research Study	**Von-Karman Value**	**% Deviation from Theory**
Lathrop et al. 1992	0.41	2.5
Lewis and Swinney 1999	0.44	10
Bhambri 2016	0.46	15
Current Study	0.36	10

The water data from the TCD has been compared to previous researchers and theoretical models, and there has been an acceptable level of agreement. The next area of investigation is to show that the flow is in the correct regime as the desired regime is turbulent.

Lathrop et al. [65] applied a Power-Law scaling of the non-dimensional torque to the Re,

$$G \sim Re^{\alpha}, \qquad (3\text{-}6)$$

where alpha,

$$\alpha = log_{10}\frac{d(G)}{d(Re)}, \qquad (3\text{-}7)$$

is denoted as the Torque scaling exponent. Lathrop et al. [65] predicted a transitional Reynolds number based on this power law scaling and assumed there was a logarithmic relationship between u^+ and y^+ at the boundary of each cylinder. Due to this, the system would behave as a wall-bounded shear flow; therefore a turbulent regime is present. Lewis et al. [63] verified this using a sharp change in slope for the torque scaling exponent at a *Re* of 13,000. Secondly, it was also observed that the azimuthal velocity component of travelling waves in the flow peaked at the stated R_T and leveled off with increasing *Re*, which provided further verification to this transitional point.

Using the *N* and *M* constants found in equation (3-4), α can be rewritten as

$$\alpha = \left(\frac{1}{2} + \frac{log_{10}e}{log_{10}G + \frac{2M}{N}}\right)^{-1}. \qquad (3\text{-}8)$$

The torque scaling exponent was calculated for the TCD data and compared to the Lewis and Swinney's data to show an agreement. Illustrates the transitional point in Taylor Couette flow from Lewis and Swinney's study from comparing the torque scaling exponent to the Reynolds Number. Overlapping the TCD data from this study shows that system is operating higher than the transitional Reynolds number while following the turbulent regime slope. There is a slight deviation within the magnitude of α, but this is mainly due to higher torque values in the TCD compared to Lewis and Swinney study, the reasons for which was presented previously. Due to a consistent slope with the turbulent regime line, and a magnitude within 10% of α from Lewis and Swinney study at any given point, it can be concluded that the TCD data is correctly within the turbulent regime.

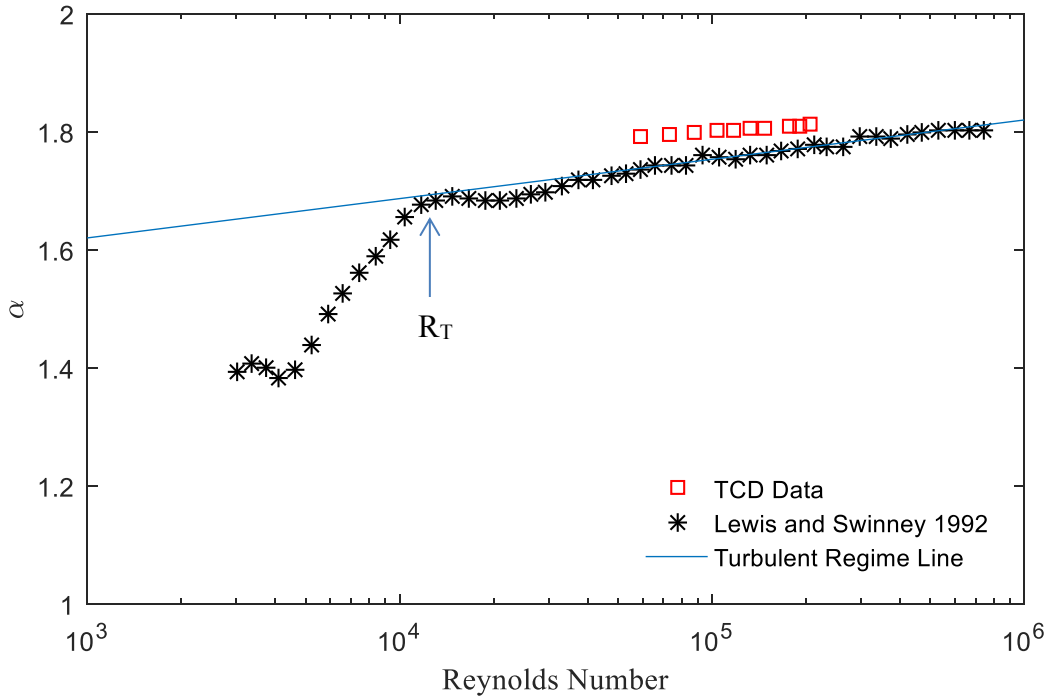

Figure 24: Transitional Point into turbulence for Taylor Couette Flow using current setup [63].

3.3.6 DR in Taylor Couette Flow

In order to calculate the drag reduction performance of a polymer solution, a baseline test at the identical velocity condition must be conducted with only the carrier fluid. The comparison of drag force between the carrier fluid and polymeric solution tests gives the drag reduction. The drag force can be defined as the shear stress the fluid exhibits against the wall. The drag reduction,

$$DR = \frac{\tau_f - \tau_p}{\tau_f} \times 100\%, \qquad (3\text{-}9)$$

is a function of the difference in shear stress where τ_f is the wall shear stress of carrier fluid and τ_p = wall shear stress of polymeric solution.

In an apparatus such as Taylor-Couette device, the wall shear stress at any given rotational speed is directly proportional to the input torque, and thus can also be substituted into equation (2-29) as shown [55]:

$$DR = \frac{T_f - T_p}{T_f} \times 100\% \qquad (3\text{-}10)$$

This procedure to calculate the DR of a polymer solution is used for all analysis sections of this study. In order to keep the pipe flow rate and rotational speeds constant, proportional–integral–derivative (PID) controllers were used to control the pump and motor power to guarantee accurate values.

3.4 Water Flow loop at the University of Alberta

The single-phase polymer drag reduction tests were conducted in a recirculating pipe loop located in University of Alberta's Mechanical Engineering building. The pipe loop consists of a constant diameter of 50 mm largely made of schedule 40 clear PVC, with two u-bends and leading schedule 40 stainless steel (SS-304L) pipe sections. The loop is power by a 40 hp centrifugal pump (LCC-M 50-230, GIW Industries Inc.), and a 10 hp progressive cavity pump (Moyno 2F090G1CDB3SAC,) to transfer mixed polymers from an external tank into the testing region. A schematic of the test facility is shown in Figure 25.

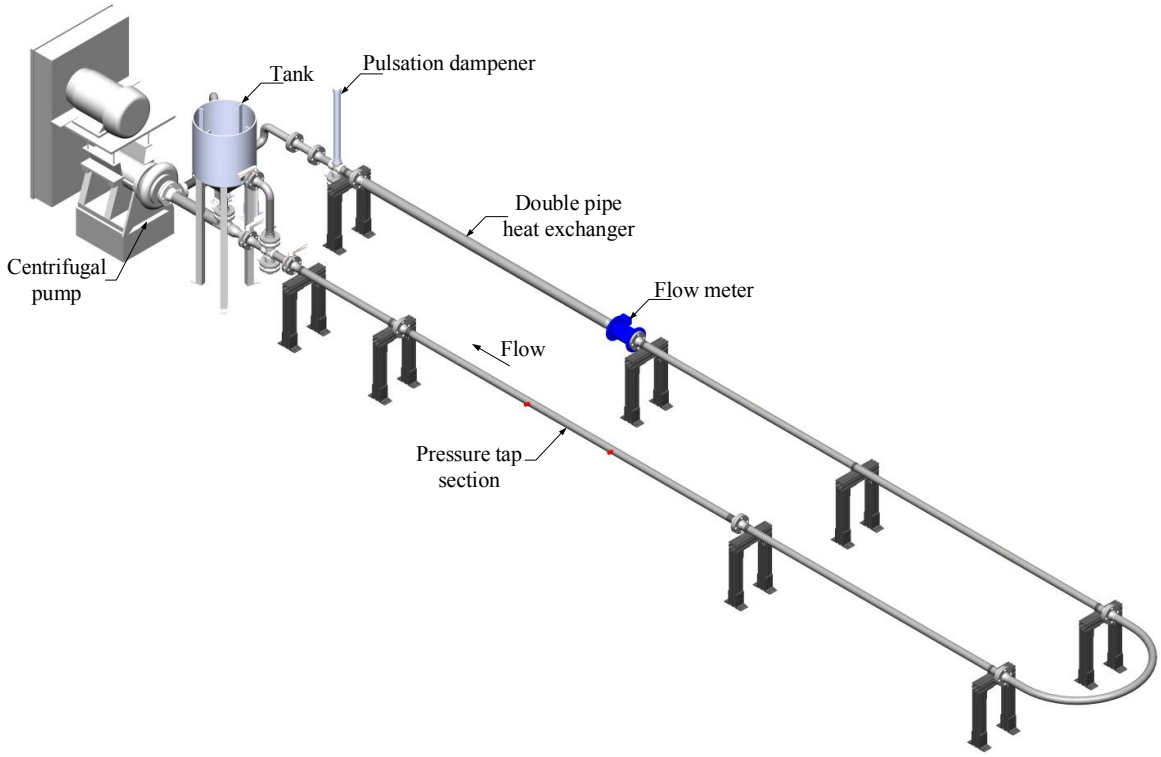

Figure 25: In-house recirculating pipe loop at the University of Alberta.

A parallel flow heat exchanger is used to control the temperature of the tests using 5°C cold water. The temperature of the polymeric solution is measured by a K-type thermocouple, and all tests are maintained at 25±2°C. Pressure drop measurements are taken between two pressure tap locations using a Validyne DP-15 pressure transducer with an internal 0.2 psi diaphragm. The pressure transducer was calibrated using pressurized air from a Druck DPI 60 pressure calibrator.

The loop is controlled using LabVIEW software (by National Instruments DAQ) which is connected to a PID controller. The volume flow rate is received from a coriolis flow meter which is collected by the PID controller, this allows for closed loop control to maintain a constant pump rpm. This flow rate was held constant for all polymer tests. The LabVIEW program also collected all pressure drop measurements at a frequency of 100 Hz.

3.4.1 Polymer Preparation

In order to find the charge density effect, SNF Floerger provided fifteen polyacrylimide polymers with ranging anionic charges of 10% to 50% across three molecular weights. Each polymer was was mixed using a marine impeller inside a large overhead tank. The tank is made of polyethylene has a total capacity of 240 L. The marine impeller (Lightnin Labmaster L5U10F) sits 2/3 the way down of the tank height, as this results in the optimal condition of mixing [66] . The diameter of the impeller and tank is 12 inches and 2 feet respectively, this ensures an optimal diameter ratio of 0.5 reported by Abu Rowin et al. [66]. The impeller is attached to a 10 mm diameter shaft which is connected to a motor system at the top. The impeller blades are unbaffled and the mixing tank has a concical bottom with a slope of 25° to easily discharge the fluid into the Moyno Pump.

To prepare a solution of polymers, the tank is filled with a desired amount of water from a storage tank with 30°C water. The storage tank has water placed in it 48 hours prior to the test to reduce the dissolved oxygen content. The dry polymer powder is added gradually on a mass basis depending on the desired concentration of the solution. They are weighed using a scale (Mettler Toledo, AB104-S) with an accuracy of 0.1 mg.

Table 4 includes the parameters used for mixing that delivers the most optimal mixing condition. Optimal condition is defined as both the lowest overall shear rate to minimize degredation and mixing time to run experiments in an efficient schedule [66]. Once the polymers have been mixed at 75 rpm for 2 hours, the solution is discharged into the Moyno pump, to which they are pumped into the flow loop to begin testing.

Table 4: Mixing conditions prior to tests using the recirculating pipe loop at the University of Alberta.

Parameter	Quantity
Mixing Time	120 mins
Solution Volume	210 L
Mixing Speed	75 rpm

Once the polymer solution is fully transferred to the loop from the mixing tank, the centrifugal pump is slowly ramped up to the desired speed to begin the experiment. A standard 5-minute ramp-up procedure is used for all tests in order to keep the initial shear rate exhibited by the pump constant between all tests.

3.4.2 DR in Pipe Flow

Depending on the type of flow system this wall shear stress can be represented differently. In a pipe flow setup, the wall shear stress is directly related to the pressure drop along the axial direction of the pipe. Therefore, the equation can be written in similar fashion using the pressure drop at both conditions as [53]:

$$DR = \frac{\Delta P_f - \Delta P_p}{\Delta P_f} \times 100\%. \qquad (3\text{-}11)$$

4 Analogous Material Testing

Majority of pipelines consists of carbon steel in industrial applications of hydro-transport; therefore it is the most common material that is tested. However, due to its strong mechanical properties, the testing time required to reach an observable amount of wear is greater than 100 hours (under typical slurry flow conditions). Large testing times are one of the most prominent challenges for pipeline erosion studies. To mitigate this problem, it was hypothesized that using a substitute material with higher susceptibility to erosion could reduce testing times for future erosion studies. In order to use a substitute material, it must exhibit similar forms of wear behavior in respect to the flow conditions. In this section, multiple materials have been tested in two experimental setups to determine their validity as a substitute material for carbon steel. The first experimental setup, the Toroid wheel tester (explanation of device presented in Chapter 2.1.5), was used as a screening test. This experiment required a smaller volume of slurry compared to the SRC pipe loop, and therefore allowed for multiple tests in the shorter time frame. After refining the selection of materials, the second phase of analogous material testing was conducted in the SRC pipe loop. This experiment simulated the effect of a pipe flow regime across all materials. The resultant wear rates were evaluated against carbon steel in order to determine a substitute.

4.1 Wear Tests using Toroid Wheel Tester

4.1.1 Objective and Test Matrix

The Toroid wheel tester (TWT) was used as a screening test to evaluate the wear profile of two materials against A53 carbon steel (a common mild steel used in pipelines). One of the materials chosen was an aluminum alloy, Al6061-T6. It is a common metal that was predicted to undergo similar type of erosion compared to steel because they both have primarily ductile properties as shown in Table 5. The second material used for the study was a polyurethane (PU) coating, PMC-790. This is a casting compound, and was used as a coating over a PVC specimen. The initial use of the PU coating as a measurement tool for wear rates was utilized by Loewen [9] at the University of Alberta prior to this study. The results of that study showed PU to have a significantly larger wear rate than carbon steel, therefore, as a substitute it would significantly cut down testing times. The mechanical material properties of PU is also shown in Table 5. PU coating has a significantly lower mechanical strength and hardness, a higher wear rate can be anticipated compared to the metals, however it is unknown which wear mechanism is dominant.

Table 5: Material Properties of TWT Experiment Samples.

Material	Elastic Modulus	Hardness	Density (g/cm^3)	Yield Strength (Mpa)
A106 CS	210 Gpa	123 (Vickers)	7.8	330
Al6061	68.9 Gpa	107 (Vickers)	2.7	276
PU	4.41 Mpa*	90 (Shore A)	1.4	16.5

*Stress at 100% elongation

The hydrodynamics of the TWT is not equivalent to that of slurry pipe flow. Heterogeneous pipe flow consists of a mix between impact and abrasive wear mechanisms, whereas the TWT can show mainly one or the other depending on the flow regime. With the TWT, the goal is to separate these wear mechanisms and determine which one predominantly affects the erosion of the target material. In doing so, a material can be eliminated based on if its susceptibility to each mechanism is different to that of carbon steel. To achieve this, two different test conditions were created, shown in Table 6. The first test uses 150 µm lane mountain sand particles, at a velocity value of 2 m/s. In this condition, the vast majority of particles will be dispersed within the flow due to strong near wall lift. It can be expected that most particle-wall collisions will occur at high angles causing impact wear. In contrast, test 2 utilizes 1 mm gravel particles, these larger particles will cause a sliding bed has coulombic frictional dominance. This creates a test condition that will cause high amounts of abrasive wear on the target materials.

Table 6: Toroid wheel tester analogous material test matrix.

Test #	Materials	d_{50} (µm)	Velocity (m/s)	Conc. (%)	Wear Mechanism
1	St, PU, Al	150	2	20	Impact Predominantly
2	St, PU, Al	1000	2	20	Abrasion Predominantly

4.1.2 Wear Rates

Table 6 shows the initial and final mass for each of the target materials based on particle size. In order to remove the effect of water retained within the test specimen, each sample was heat treated for three days after each experiment. Each test had a run time of 96 hours, this was used to calculate a simple averaged wear rate (the density of the material was divided in order to compare the volume loss of the material). The steel and aluminum coupons were industrially manufactured and therefore have consistent initial weights between coupons. The PU coupons were created in-house

using a two-part casting method. This resulted in a variation of the thickness of the PU coating; this can be seen as a large change in initial weight between two test coupons shown in Table 7. Each specimen required a cross sectional area of 80 × 100mm, and a minimum thickness of 20 mm. The initial weight was taken after cleaning each sample in acetone solution and drying at room temperature.

Table 7: TWT mass loss measurements after 96 hours of continuous operation.

Test	Initial (g)	after testing (g)	3 day heat (g)	Wear (cm/yr)
Steel – 1 mm	490.29	489.95	489.95	**0.05**
Al 6061 – 1 mm	168.18	165.32	165.32	**1.21**
PU – 1 mm	74.31	74.36*	74.07	**0.20**
Steel – 150 µm	491.99	491.99	491.99	**0**
Al 6061 – 150 µm	168.44	168.16	168.16	**0.12**
PU – 150 µm	54.43	54.47*	54.19	**0.20**

*Water absorption caused mass increase

It can be determined that steel has the lowest overall wear compared to the aluminum and polyurethane; this is understandable as steel pipes are mainly used in industry over other materials due to its superior yield stress (as seen in Table 5) resulting in a higher pipe pressure rating. It was also observed that there is no measurable amount of material loss in the steel coupon at 150 µm; this may be due a large difference of hardness between the steel and the particle. The aluminum showed the most amount of wear from sliding friction as seen from the 1 mm gravel tests. The wear rates of the polyurethane during both 1 mm gravel and 150 µm sand are equal. Based on these patterns, both steel and aluminum have shown higher wear during sliding compared to the impact of smaller particles. However, the polyurethane seems to be unaffected by the particle size or the type of wear mechanism. This leads to the possibility that PU coating may not be a suitable substitute material for carbon steel. However, based on mass measurements alone it is not possible to compare the erosion of the different materials. Analyzing surface profiles of the coupons provides more insight on the type of wear mechanisms that are involved for each respective material. Using 1 mm particle size at 1.9 m/s; it is expected that there will be significant sliding motion.

4.1.3 Wear Profiles

The wear rates do not provide any details on the type of wear mechanisms that affected the target material. In order to visualize the wear profile of the materials, a surface profile was taken. This was conducted after the coupons were retrieved from the TWT and the dry weights were recorded. A needle surface contracer (Mitutoyo; Model: CV-3100H4) was used to collect the surface roughness of the coupons. The surface contracer was controlled using the FORMPAK software, and was programmed by Sarker [42].

Analyzing the wear profile of the carbon steel specimen under the flow of 1 mm gravel slurry, a relatively flat erosion profile was observed, this is shown in Figure 26. A flat erosion profile is a indicator of abrasive wear from high coulombic friction, this was expected. However, it seems that a large portion of the mass loss was a result of the leading edge loss. This effect is common in this TWT apparatus and is denoted as the edge effect. The edge effect is caused by a step change in the leading edge in the Toroid Wheel. This sudden step change increases particle-particle interactions downstream, this causes in more localized wear as mentioned by Sarker [42]. The localized wear is caused based on higher frequency of particle collisions against the target material at angles of 20° and lower. This edge effect skews the mass loss measurements that were attained, and therefore these erosion profiles should be used as the main source of judgement to compare the different material types.

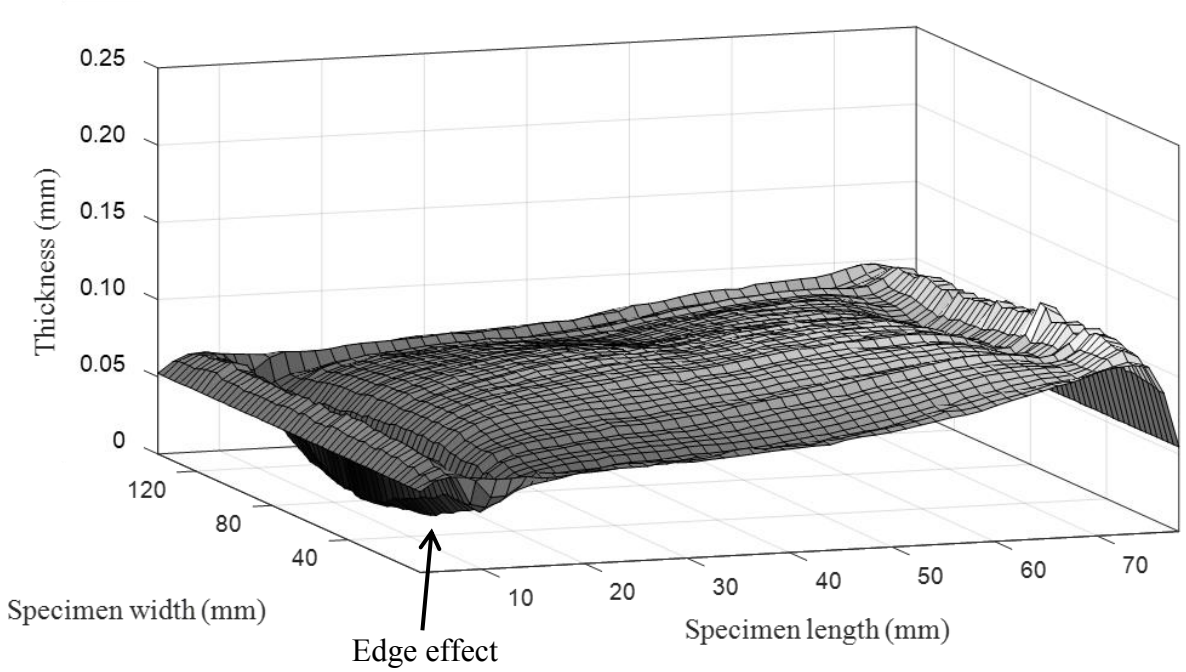

Figure 26: Erosion profile of A106 Carbon Steel coupon using 1 mm gravel.

The erosion profile of the aluminum alloy is provided in Figure 27. The erosion can be described as a canyon; the wear is flat in similitude to the carbon steel coupon. The aluminum alloy has a larger thickness loss, and a larger edge effect, this is due to a lower mechanical strength compared to carbon steel. The 1 mm gravel test results for the aluminum showed higher susceptibility to the coulombic friction compared to the steel.

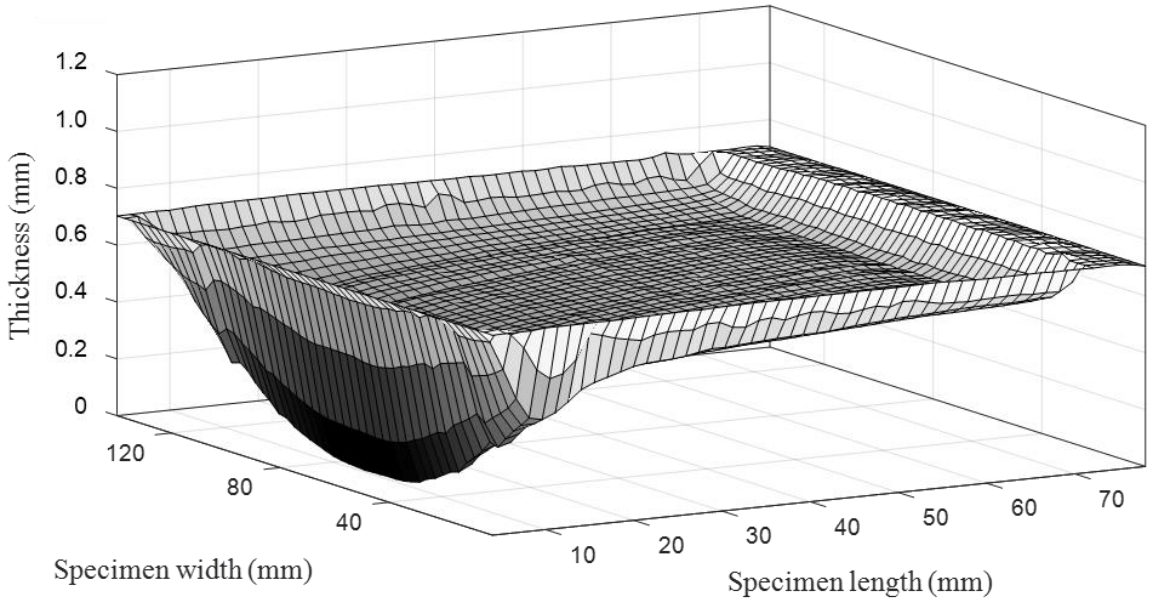

Figure 27: Erosion profile of Al 6061-T6 coupon using 1 mm gravel.

The polyurethane coupon has shown an entirely different erosion profile to the other two ductile metals as seen in Figure 28. The localized erosion at the central part of the coupon can be seen. The erosion about the flow direction (length wise) is not uniform during coulombic friction dominance. The polyurethane did not show any sign of wear from these edge effects either. The localized wear at the center shows lack of abrasive wear from coulombic friction. This is acceptable since the material is generally advertised for its abrasive resistant characteristics. Localized wear at the center of the coupon is most likely resultant of impact wear rather than abrasion.

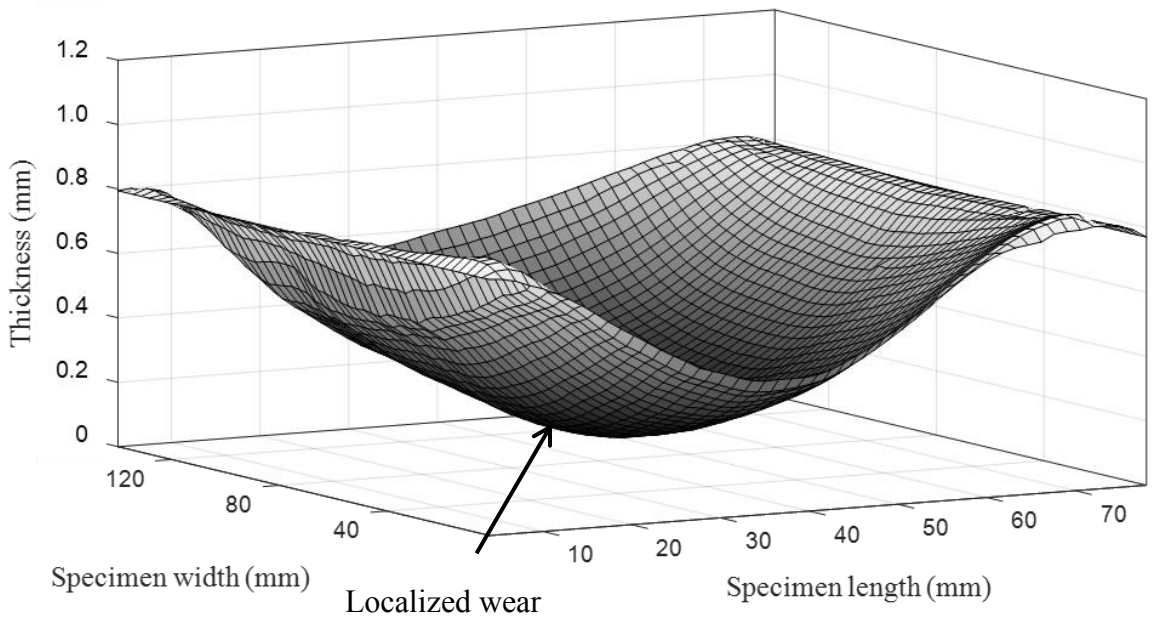

Figure 28: Erosion profile of polyurethane coupon using 1 mm gravel.

Based on the mass measurements, the steel did not undergo any wear by the 150 μm sand. This is evident based on Figure 29 as well since there is no edge effect wear or any other localized wear on the surface. There does however seem to be a gradual increase in thickness; however, when looking at the magnitude, this increase is less than 0.02 mm, which can be deemed as just flat with imperfections from manufacturing rather than any sign of wear.

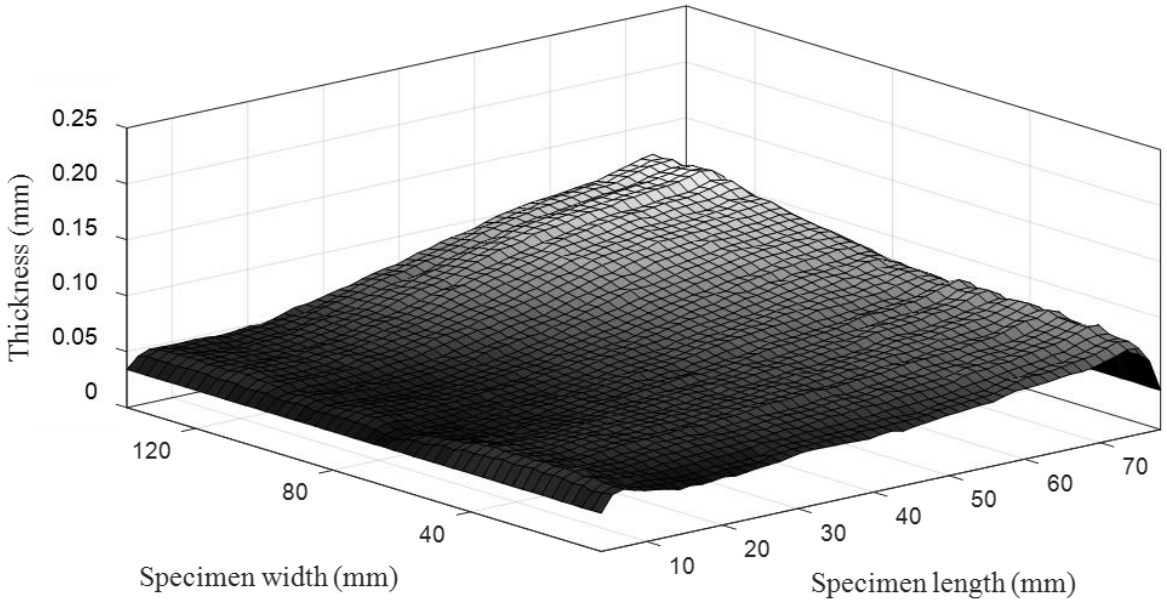

Figure 29: Erosion Profile of ASTM X42 Carbon Steel Coupon using 150 μm sand.

The erosion profile of the aluminum at the 150 μm sand test condition fits well with the initial prediction. There is a significant localized wear at the central portion of the coupon as seen in Figure 30. This is because the 150 micron sand is mainly suspended due to near wall lift and only strikes the target material at angles greater than 20°. The locations of these impacts occur at the central portion of the coupon due to the geometry of the TWT flow. Since there are a very low percentage of particles that are sliding, the leading edge effect is non-existent. Due to the lack of wear in the steel, it cannot be compared, however is worth to be investigated in a larger wear setup.

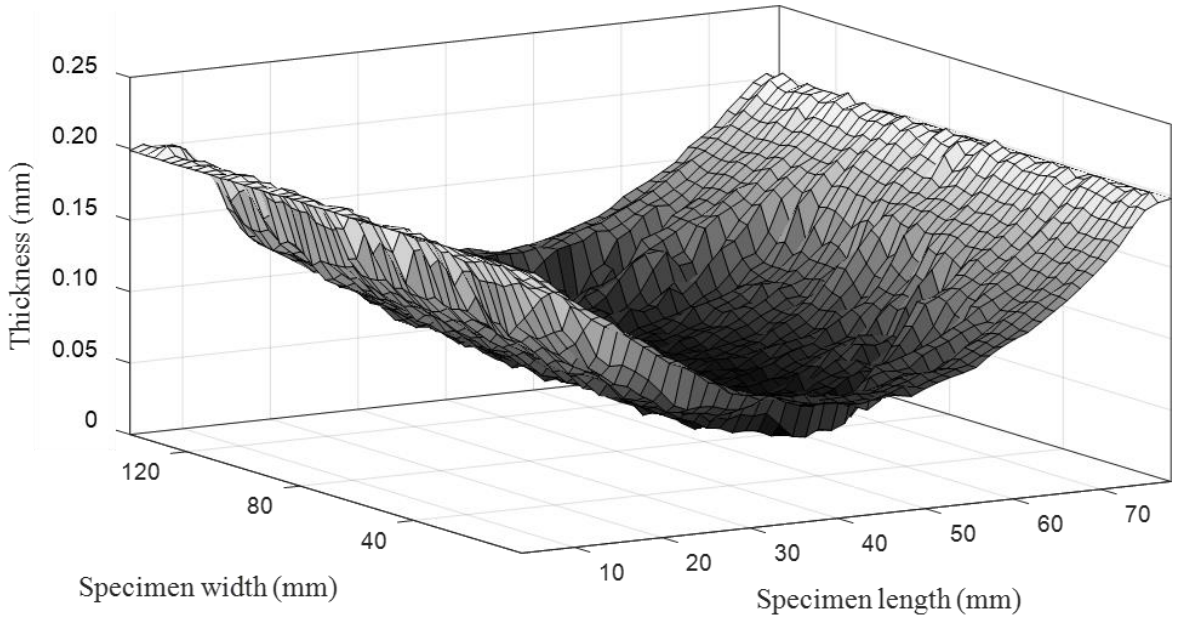

Figure 30: Erosion profile of Al 6061-T6 coupon using 150 μm sand.

The erosion profile of the PU is identical for the 150 μm sand and 1 mm gravel test. Regardless of the particle type, it seems only the impacting particles at the middle of the plate caused localized wear. The 150 μm had a larger frequency of particles impacting the specimen compared to the 1 mm test, however based on mass measurements the wear rate of the two tests were identical. Since it is known that the PU is abrasive resistant, the suspended flow test should have resulted in higher wear rates (with the same erosion profile) due to a higher frequency of particle impacts. However, one thing to note is that noted that the lane mountain sand had a Moh hardness of 7, whereas the gravel has around an 8. The harder particles create a larger mass loss per collision. Due to these two reasons, the smaller sand particles do not have as much of an effect per impact, but causes an equivalent amount of wear with the higher frequency of impacts.

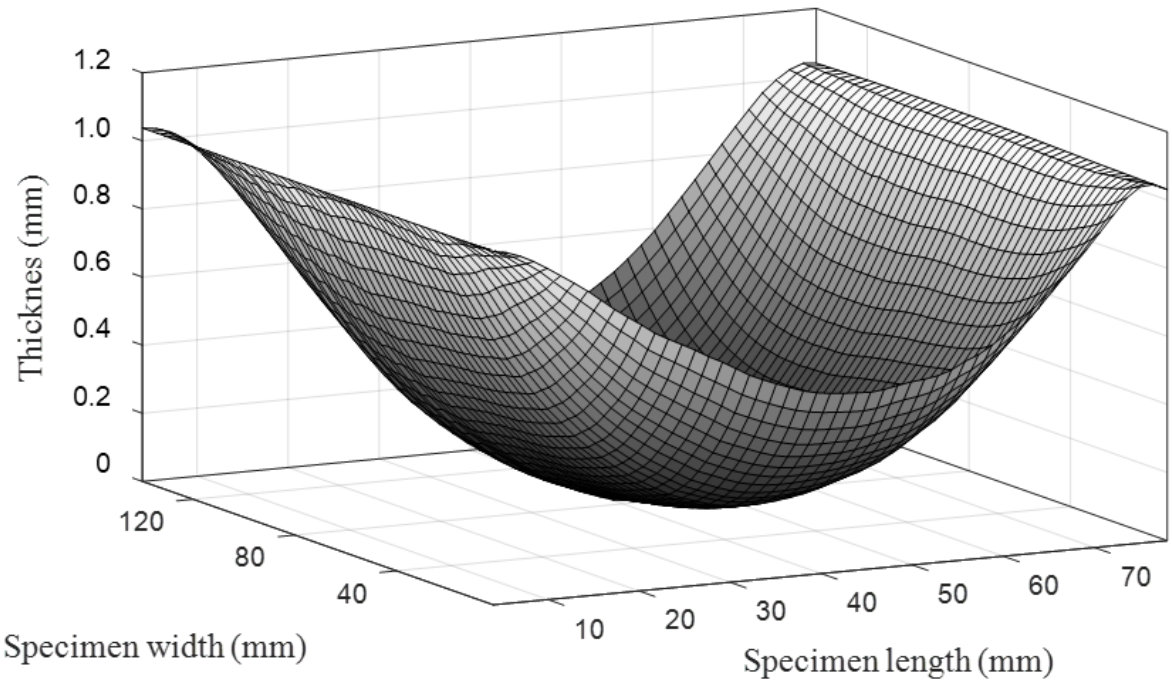

Figure 31: Erosion profile of polyurethane coupon using 150 μm sand.

Overall, the main conclusion to this test is that the erosive characteristics of the PU are not similar to that of pipe metals. The higher abrasive resistance may cause different wear patterns during pipe loop tests and was not a feasible option due to the high costs of the pipe coating process.

4.2 Wear Tests using Slurry Pipe Loop Facility

According to the results of the TWT tests, the steel and aluminium coupons have similar wear patterns and have been further tested in the large SRC pipe flow loop (see Chapter 2.2 for details). In addition to these ductile metals, PVC pipes were also used in the experiment. Based on the previous wear tests, the polyurethane coating did not provide similar wear trends and did not meet certain feasibility criteria, instead PVC was used due to its relatively high pressure rating for pipe flow and cheap cost. In addition, PVC is used in many applications in industry. The potential cost savings from running PVC instead of steel for wear tests is a strong motivation for this study. The objective of this wear test was to compare the wear rates of the materials and evaluate whether any can be a replacement to steel during wear testing. In order to achieve this, two parameters were manipulated that commonly are controlled during industrial slurry flows; the bulk velocity (based on volume flow rate) and in-situ solids concentration.

Based on Table 8, it can be seen that each material is subject to two different velocities per test. This is achieved based on the diameter difference of two tests sections in the SRC flow loop. The purpose of this test matrix is to see the trend of the wear rate as the slurry conditions become more rigorous. The concentration was bracketed between 20% and 30% as this is the most common condition in industrial flows, additionally, concentrations lower 20% may require too large of a testing time to measure significant wear, while higher than 30% may result in deposition at low velocities. The type of flow that is of interest in this study is suspended flow, this means that velocities relatively higher than the deposition velocity must be used to avoid plugging, and create a large portion of kinematic friction (rather than having coulombic dominance). The deposition velocity of the system was averaged to be about 1.8 m/s, and therefore the lowest velocity tested was 2.3 m/s. As for the upper boundary, the limiting case was the maximum input of the pump. At peak performance, the pump can provide a volumetric flow rate of about 27 L/s, based on this value, the maximum bulk velocities were chosen.

Table 8: Analogous material wear experiment test matrix for recirculating pipe flow loop at SRC.

Test #	**Particle Type**	**d_{50} (µm)**	**Conc.**	**Volumetric Flow (L/s)**	**Bulk Velocity (m/s)** **Section 1** **Section 2**	**Materials**
1-1	Sand	250	20%	11.04	3.54 2.31	St, Al, PVC
1-2	Sand	250	30%	19.88	6.38 4.16	St, Al, PVC
1-3	Sand	250	30%	25.38	8.22 5.30	St, Al, PVC

The first test conducted involved the use of gamma ray densitometry. This was required in order to verify that the flow was fully suspended; this was done by capturing the concentration profile about the height of the pipe.

It can be seen using Figure 32, that at 3.5 m/s at 30% in-situ solids concentration, there is approximately 50% of the total solids within *y/D* of 0.05. At this condition based on the SRC Two-Layer model (see Chapter 2.1.4), the particles contribute largely to coulombic friction. This means, that at the slowest velocity setting (within the *D*=3″ test section), over 50% of the solids are fully

suspended. The heterogeneous flow conditions are therefore acceptable for the current study because it exposes each material to a wide range of impact and sliding wear. This is very important to see the behaviour of the erosion in the materials, as well as the use of polymer additives and their contribution to wear reduction.

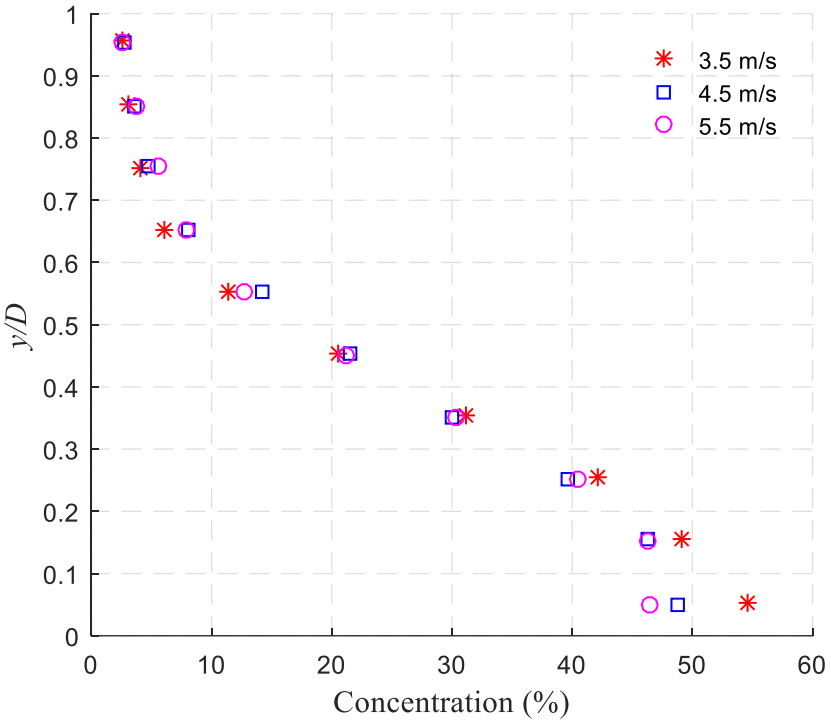

Figure 32: Concentration profile of *in-situ* 30% silica sand slurry based from densitometry measurements.

To start off, the velocity was chosen as it was directly controlled variable during all pipe flow tests. The wear rates are calculated based on the mass measurements of the spools before and after the tests. The mass loss measurements of all coupons were converted to an average thickness loss of the cross sectional pipe area by normalizing the data by the material density, length of spool, and internal diameter of pipe. This results in value that can be compared between the different pipe diameters and materials. The results of the average thickness loss rate have been plotted against the bulk velocity in the experiments and can be seen below.

The wear rate trend against the bulk slurry velocity is shown in Figure 33 to Figure 35 for all three materials. The carbon steel and PVC materials follow an exponential relationship with an increase in velocity. For the purpose of this study, the similarity of the trend (seen in Figure 34 and Figure

35) between the PVC and carbon steel data provides initial evidence that they may be used as a substitute for one another during erosion tests. According to Figure 33, the aluminium data also showed an overall exponential trend; however there is inconsistency between the 2.5″ and 3″ test section results. This phenomenon may have been caused by leading edge wear to accelerate the wear rates of the 2.5″ spool sections, which has been analyzed further later in this chapter. Regardless, from these plots, it is shown that aluminum is sensitive to the diameter change within the tests and may hinder future attempts at using it as a substitute material to carbon steel. It should also be taken into account that velocity does not give a completely universal trend that can be compared to in different experimental or industrial setups. This is due to other parameters such as concentration and particle size that may affect the behaviour of the flow. Instead, the wear rate should be compared to a universal parameter that describes the physical nature of the flow. Initially, the Reynolds Number is considered as a parameter that can take into the account of diameter change within the setup, the density and viscosity of the suspension as well as the velocity. The updated averaged thickness loss based wear rate has been plotted against the Reynolds Number based on carrier fluid rheology measurements conducted.

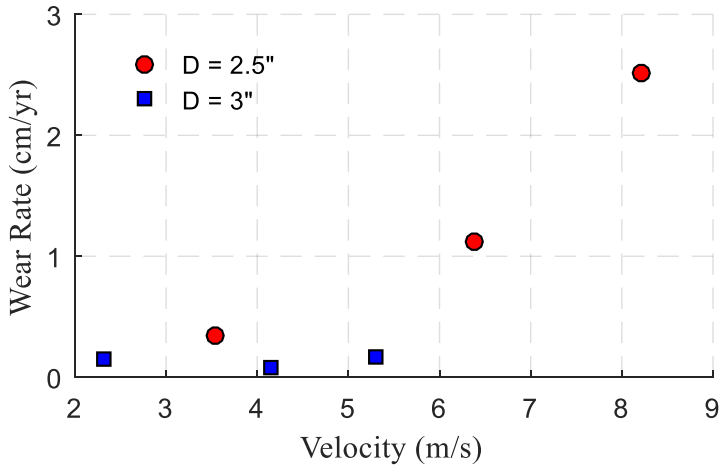

Figure 33: Al6061-T6 wear rate against bulk velocity from SRC Pipe Tests.

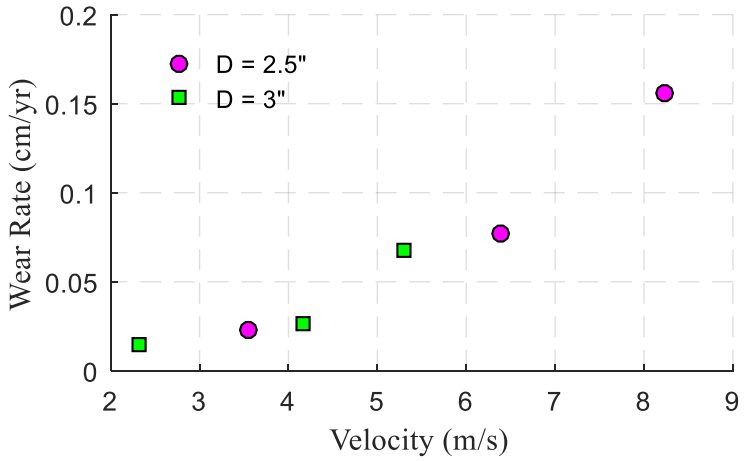

Figure 34: A106 Carbon Steel wear rate against bulk velocity from SRC Pipe Tests.

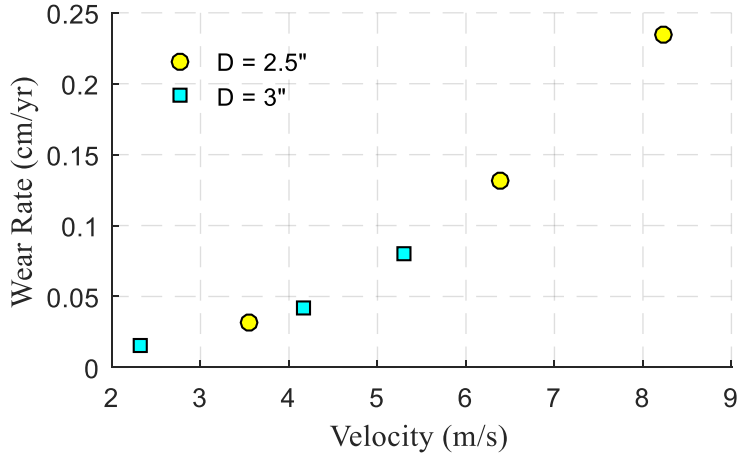

Figure 35: PVC wear rate against bulk velocity from SRC Pipe Tests.

Analyzing the wear rates against Reynolds number from Figure 36 to Figure 38, a discrepancy between the 2.5″ and 3″ diameter sections can be seen across all three material types. The deviation between the two distinct trends is the greatest with the aluminum, and lowest with the steel. In Sadighian's study, the steel also demonstrated two different linear trends of wear based on the two different spool section diameters when plotted against parameters as a function of the flow characteristics [11].

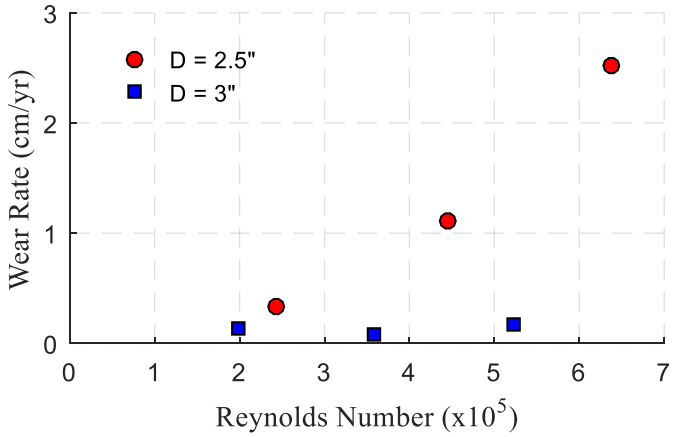

Figure 36: Al6061-T6 wear rate against Reynolds Number from SRC Pipe Tests.

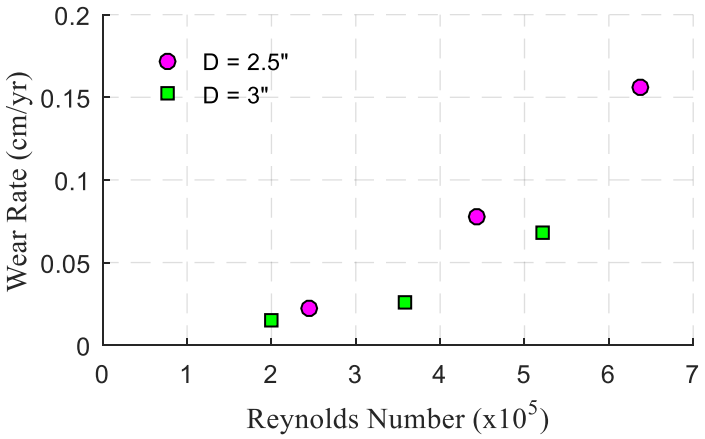

Figure 37: A106 Carbon Steel wear rate against Reynolds Number from SRC Pipe Tests.

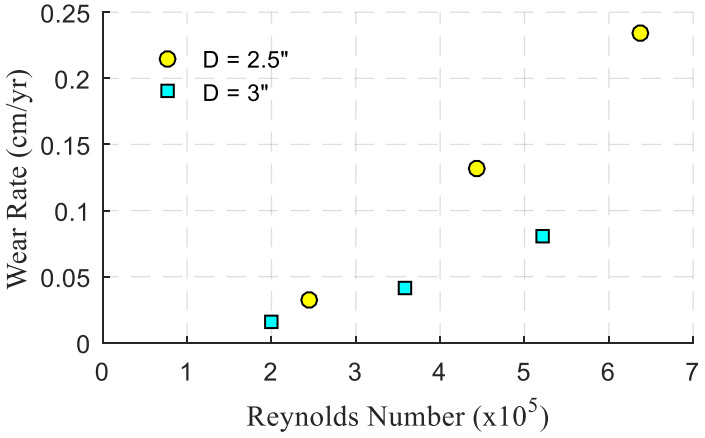

Figure 38: PVC wear rate against Reynolds Number from SRC Pipe Tests.

It be concluded that the Reynolds Number of the flow is not a good indication to find erosive trends as it does not directly correlate with wear. Instead, the SRC Two Layer model can be used to find a direct correlation between the solids friction and the wear of a material. Sadighian's [11] previous works showed a logarithmic relationship between the wear rates of a pipe against the solids pressure gradient of the slurry flow. A similar approach was used for the mass loss data collected in this current study.

4.2.1 Comparison of Wear Rate to Solids Friction

The solids pressure drop was calculated applying the SRC Two-Layer model based on the flow conditions of the experiments. To guarantee that these solid friction values are accurate, a few test conditions were run with and without particles; the pressure drop difference between these two calibration tests agreed with the SRC Two Layer Model results.

As discussed before, a slurry flow is comprised of a solid phase (of moving particles) and a liquid medium that the solids are suspended within. As the suspension moves against the walls of the pipe, each phase creates an amount of friction. The fluid phase and wall has a shear stress at the boundary layer. The solid phase has two types of friction, one is the kinematic friction of the particles moving that are suspended, and the second is the portion of the particles within the sliding bed section of the heterogeneous flow. The sum total of both these components can be defined as the solid phase friction. Within the respective time of the SRC experiments, it can be assumed that the wear of the pipe walls is caused by the solid phase of the flow [11]. The sum total of the solid and liquid phase is the total pressure drop in a slurry flow that can be directly measured experimentally. Since the solid phase is the main component of friction to cause wear, it will be analyzed directly against the wear rates of each material.

The carbon steel thickness loss rate against the solids pressure drop of the slurry is presented above in Figure 39. Unlike Sadighian's work, the wear rate seems to be linearly proportional the solids friction. However, this may be the case due to a shorter variation of friction between all tests compared to the operational condition of Sadighian's study. As the solids pressure drop increases, the portion of kinematic friction is largely dominant compared to the coulombic friction. As a result, when kinematic friction increases, the thickness loss in the carbon steel does so as well. This is to be expected since ductile materials are vulnerable to erosion from low angle impacts which occur at conditions where kinematic friction dominates. The use of solids friction number

yields a linear trend in which both testing spool diameters fit. However, the Reynolds number plots did not show a cohesive trend that fit both sets of data; this shows that the solids friction is a more robust method to evaluate the erosive trends of a material.

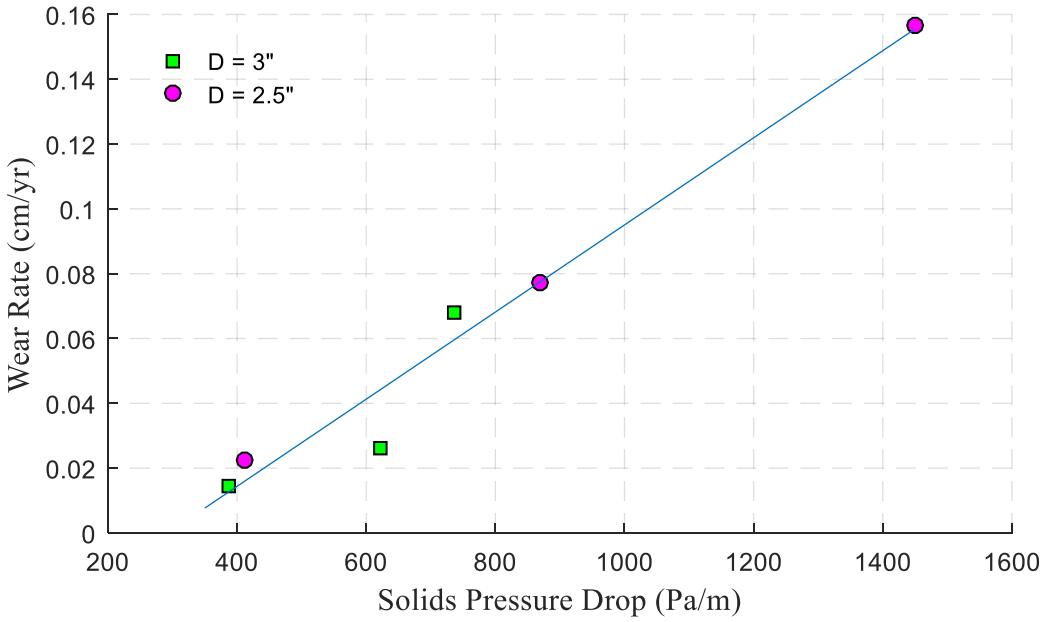

Figure 39: A106 Carbon Steel wear rate as a function of calculated solids friction.

This method was also applied on the data for the PVC, which previously showed two distinctly different wear rate trends based on the spool diameter. However, based on Figure 40, it can be seen that the PVC wear rate yielded a linear trend against the solids friction. Similar to the steel wear, the PVC data shows consistency between the two different diameter spool sections. Compared to the steel, the PVC test spools also exhibited a linear trend between the increase in solids friction and the wear rate. As expected the magnitude of the wear rates at any given condition was higher for the PVC than the carbon steel. This shows that the PVC is more sensitive to the effect of the solid friction than the steel. At around 500 Pa/m, the difference between the two wear rates yielded 15%. However, the maximum wear rate of the PVC is 0.234 cm/year whereas the carbon steel yields 0.156 cm/year; which results in a 33% higher wear rate in PVC. Therefore, at high flow rates (bulk velocities higher than 6 m/s); a significant amount of time can be saved running PVC spools. Due to the linear nature of the erosion rates at this solid friction range, erosion tests using PVC could potentially be used a substitute. However, more data would be required to accurately model a relationship to predict the corresponding steel wear rates from PVC tests.

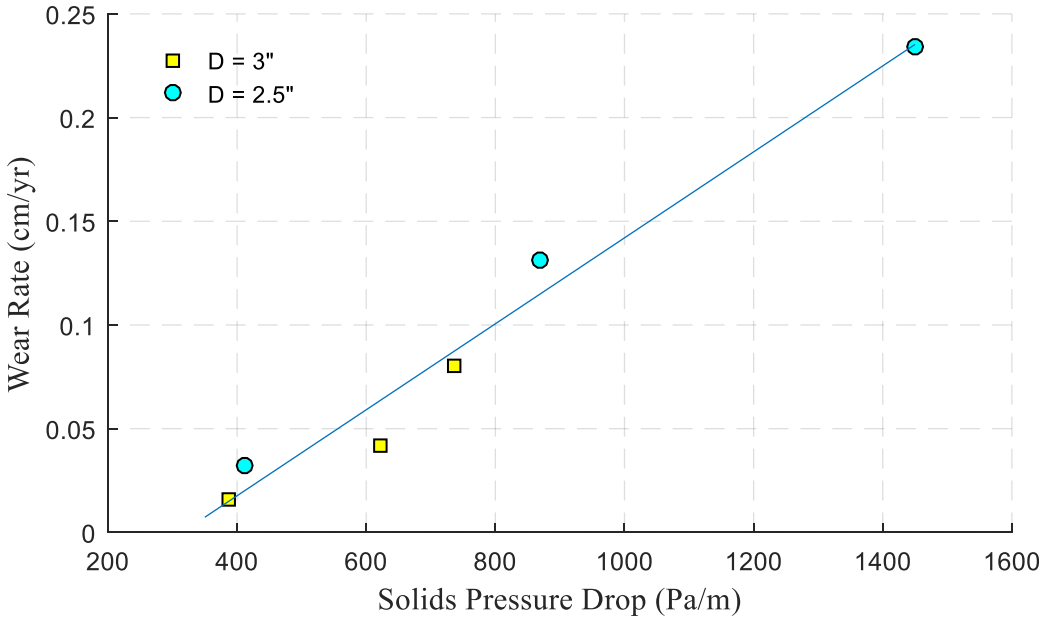

Figure 40: PVC wear rate as a function of calculated solids friction.

The magnitude of the wear rates within the aluminum samples were an order of magnitude higher than both the PVC and carbon steel specimens at very high velocity tests in which the solids friction was large. This disproportion was seen between the aluminum and steel samples from the TWT tests in the initial screen study. However, based on the trend from Figure 41, there is not a linear trend between the wear rate and solids friction. During low velocity tests, the increase in solids based shear stress on the material did not cause an increase in erosive tendency.

The high wear rates found in the 2.5″ sections for tests 1-2 and 1-3 were still in doubt and further analysis was taken place to explain this trend. One of the initial predictions for the discrepancy between the 3″ and 2.5″ spool mass loss measurements was due to significant leading edge wear. Leading edge wear can be caused due to misalignment of pipe spools. In order to check this phenomenon, the aluminum spools were cut into two one foot sections and weighed again, in order to see if there was a substantial difference between the wear. The leading and trailing edge spool wear rates are also shown in Figure 41, and a slight amount of leading edge wear is seen. The amount of difference in erosion in each half is less than 5% of the total erosion, and therefore it can be concluded that leading edge wear is not the cause of the sudden spike in wear rates for the 2.5″ diameter spool sections.

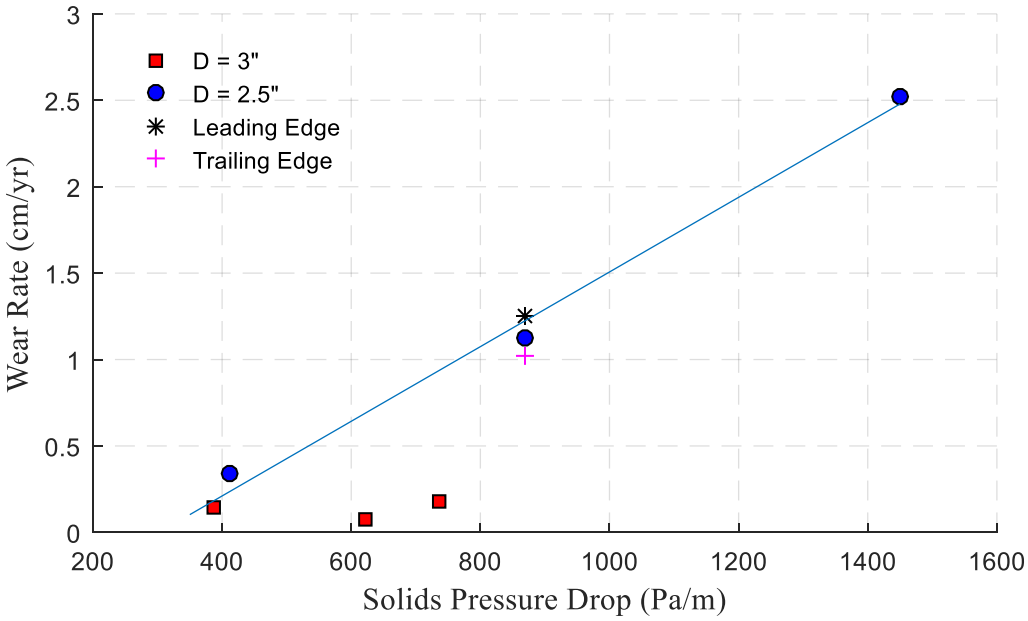

Figure 41: Al6061-T6 wear rate as a function of calculated solids friction.

Apart from the calculated solids friction, the SRC loop also had pressure transducers that recorded the pressure loss of the fluid flow across each test section. These pressure measurements were recorded throughout the entirety of all wear experiments. In addition, the pressure drop of the liquid phase, in this case water, was also measured at all corresponding flow rates. The solids friction was calculated directly using the pressure data of the slurry flow and water flow data by applying the following relationship:

$$-\frac{dP}{dz}_{solid} = -\left(\frac{dP}{dz}_{slurry} - \frac{dP}{dz}_{water}\right), \qquad (4\text{-}1)$$

in which the pressure values are all taken at equivalent velocities. The first apparent difference between Figure 39 and Figure 42 is the range of the pressure loss values, in this case the maximum occurs at roughly 3200 Pa/m whereas when calculated using the SRC Two-Layer model software it resulted in about 1500 Pa/m. The main reason for this discrepancy comes from the water based pressure measurements rather than the slurry flow.

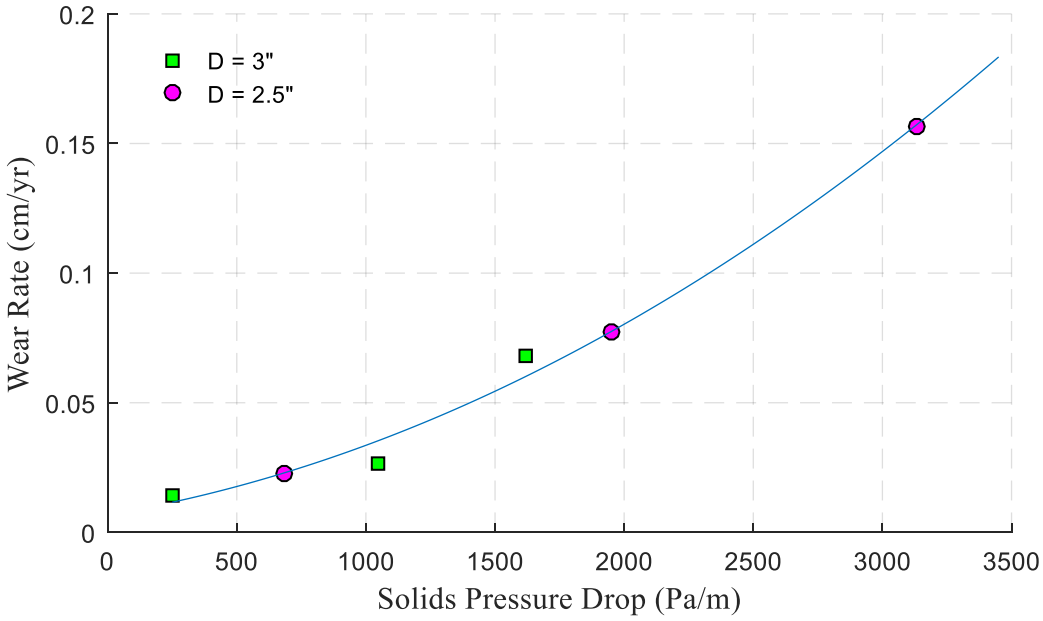

Figure 42: A106 Carbon Steel wear rate fitted as a 2nd order curve in respect to the measured solids friction.

Compared to the anticipated pressure loss due to water, the measurements were far lower. This can be seen in the table below.

Table 9: Comparison of Solids Friction between SRC Two-Layer Model and direct measurements (all values in Pa/m).

Calculated Slurry ΔP	**Calculated Water ΔP**	**Calculated Solids ΔP**	**Measured Slurry ΔP**	**Measured Water ΔP**	**Measured Solids ΔP**
1058	670	**388**	803	553	**250**
2401	1989	**412**	2171	1485	**686**
2712	2091	**621**	2635	1586	**1049**
4089	3354	**735**	4259	2638	**1621**
7147	6277	**870**	6429	4477	**1952**
11776	10327	**1449**	10318	7183	**3135**

It can be seen that the slurry pressure measurements are within 10% of the calculated values, however there is a large difference between the water based tests. The trend of the wear rate for the carbon steel does slightly change to a 2nd degree curve in Figure 39 rather than a linear trend seen before in Figure 42. This does agree with the trends presented by Sadighian, however it cannot

be determined if this trend illustrates the nature of the wear rate better than the calculated solids friction values.

Using the directly measured solids friction values, the PVC once again shows a similar trend with the carbon steel when compared with the same set of data as seen in Figure 43. Previously both materials showed a linear trend against the calculated solids pressure drop, and in this case both materials show a 2nd degree relationship. The consistency between the material wear trends strongly shows that they can be used as substitutes as their wear rate susceptibility to changes in flow conditions are similar.

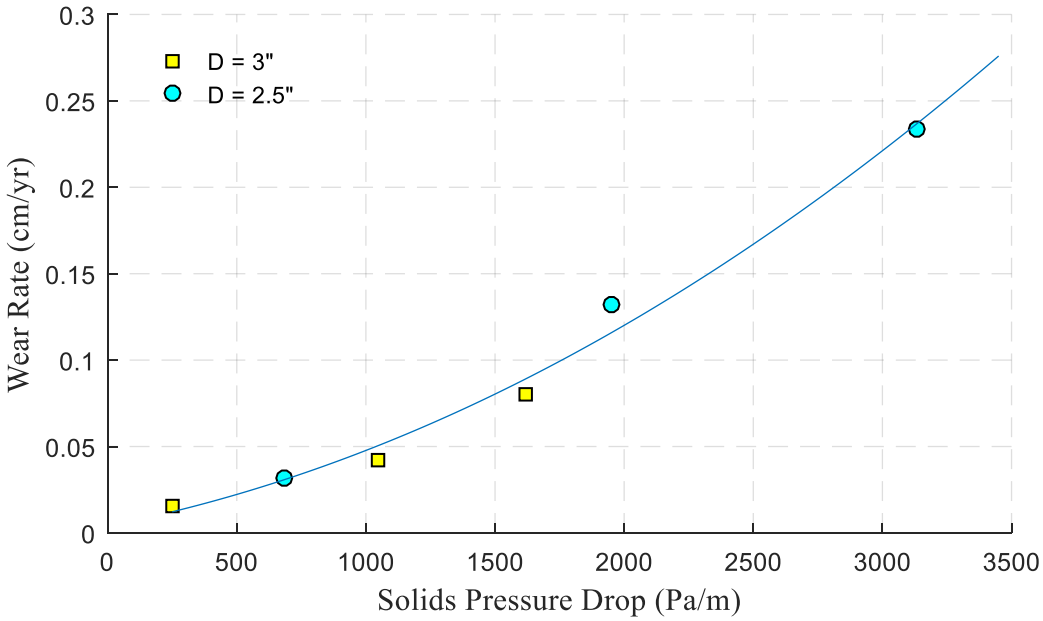

Figure 43: PVC wear rate fitted as a 2nd order curve in respect to the measured solids friction.

According to Figure 44, the Al-6061 wear rate is still scattered between two distinct trends regardless of the new y-axis values of direct solid pressure drop data. The leading edge and trailing edge do not show a significant difference in wear rate and therefore this discrepancy was not due to misalignment or testing errors. The reasons for this behaviour are not clear, but, it can be suggested to avoid the use of Al-6061 as a wear substitute towards carbon steel.

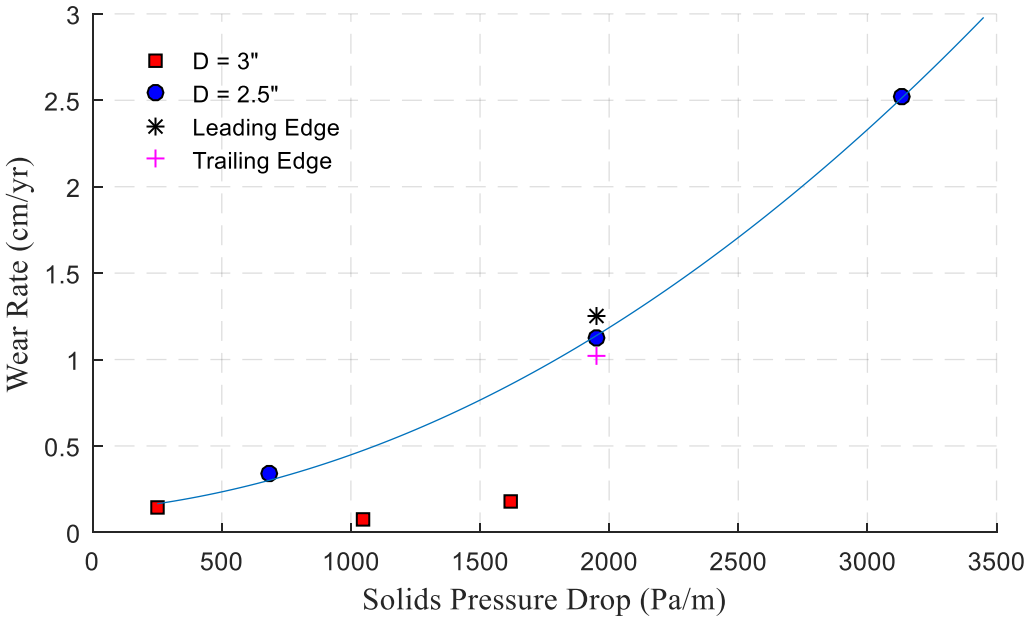

Figure 44: Al6061-T6 wear rate fitted as a 2nd order curve in respect to the measured solids friction.

4.3 Summary

In conclusion, the carbon steel and PVC showed a linear response between the wear rate and solids friction calculated using the SRC Two-layer model. Using directly measured solids friction, both materials still showed equivalent trends of a second order fit between the wear rate and solids friction. The similarity between the PVC and carbon steel allows the PVC to be a feasible substitute for erosion testing for velocities in a range of 2 to 9 m/s. The aluminum alloy showed an inconsistent trend between the two different diameter test section wear rates. This was seen throughout each comparison: using velocity, and both versions of solids friction. Due to this irregular trend for the wear rate of aluminum, it is not known what trend will occur in a different experimental setup, and therefore is not a recommended.

5 Performance of Polymer Additives in Single Phase Flow

In this section the effect of polymers on the drag reduction characteristics of polyacrylimide (PAM) polymers will be investigated. There are two main objectives for this study:

1. To investigate the effect of charge density property on drag reduction performance.
2. To use the data from pipe flow and compare to a small-scale Taylor-Couette device in order to check the validity ofusing such a device for scale-up experiments involving polymer additives.

Many researchers have investigated the mechanisms that trigger the effect of polymer drag reduction; recently the main parameter that is believed to influence drag reduction is the molecular weight of the polymer. Based on the elastic theory (details in Chapter 0), polymers that are partially stretched in nature, stretch within the boundary layer absorbing energy, then travel to the mean flow regime outside of the and relax to their coiled state in the main flow regime. The process of relaxing releases the energy originally absorbed from the boudary layer. In many cases polymers are represented by small springs within flow to explain the phenomenon. A high MW polymer means it has a longer stretched length than a polymer of lower MW; just like in the case of a spring analogy, the greater the ΔL between the coiled and stretched states, the larger the energy transfer by the polymers, and the larger effect of relaminerization on the flow seen as higher drag reduction. However, in the case of PAM polymers, another important characteristic that is often prsented by manufacturers is the charge density.

5.1 Drag Reduction tests using Water Pipe Loop Facility

5.1.1 Effect of Molecular Weight and Concentration

To investigate the effect of charge density on the drag reduction performance, all polymers were tested for 2 hours in the flow loop. The following table shows a summary of each polymer.

Table 10: All SNF Polymers used for testing in Taylor Couette and in-house pipe flow loop experimental setups.

Product #	MW (Mg/mol)	CD (%)
MT2232-1	8 – 10	10
MT2232-2	10 – 12	10
MT2232-3	12 – 15	10
MT2232-4	8 – 10	30
MT2232-5	10 – 12	30
MT2232-6	12 – 15	30
MT2232-7	8 – 10	50
MT2232-8	10 – 12	50
MT2232-9	12 – 15	50
LN3475-1	8 – 10	20
LN3475-2	10 – 12	20
LN3475-3	12 – 15	20
LN3475-4	8 – 10	40
LN3475-5	10 – 12	40
LN3475-6	12 – 15	40
MT2239-1	2-4	30
MT2239-2	4-6	30
MT2239-3	6-8	30

All polymers were tested at both a concentration of 50 ppm and 100 ppm. The first immediate problem detected was the range overlap of molecular weight between the polymers due to the large distribution band of the manufacturing process. For example, a sample of polymer MT2232-1 may have MW of 10 Mg/mol as well as a MT2232-2; this results in a situation where the effect of charge density and molecular weight on drag reduction performance cannot be distinguished. Therefore the first test was conducted while holding the charge density constant at 30%.

Based on the batch of polymers from Table 10, it was seen that there was a very insignificant change in the drag reduction due to molecular weight as seen in Figure 45. This is contrary to the typical theory that higher molecular weight results in higher drag reduction. In order to

troubleshoot the problem, three additional SNF PAM polymers were used that consisted of molecular weights from 2 to 8 Mg/mol that were not present in the original test matrix batch. Based on Figure 45, it can be seen that up until 8 Mg/mol the drag reduction significantly increases based on the increase of molecular weight, however once this threshold is reached, the drag reduction performance is limited. An important theory was introduced as an initial explanation to this phenomenon.

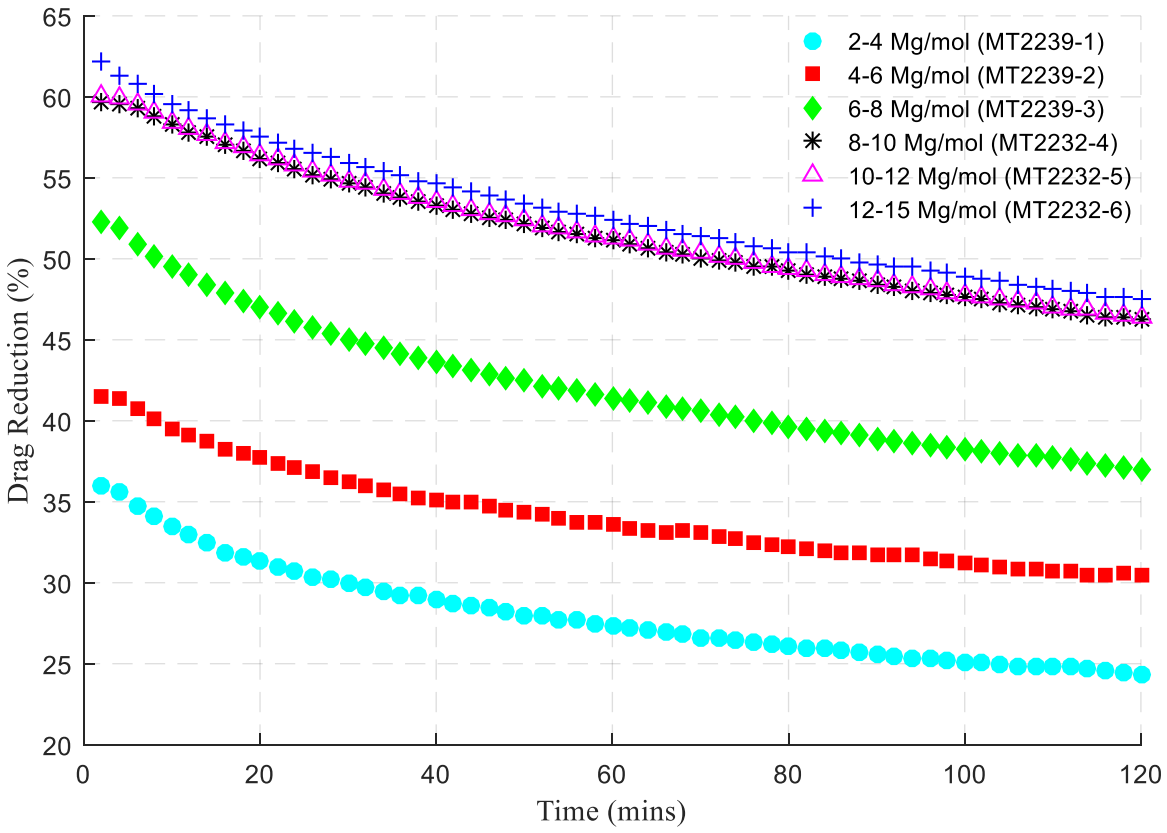

Figure 45: Drag reduction performance of multiple PAM polymers with varying molecular weight at 30% anionic charge density, at *Re* = 100,000 (50 ppm) in pipe flow loop.

Initially, as the MW increases, and the stretched length of polymers are higher, a larger sum of energy can be absorbed by the polymers at the viscous sub-layer of the flow. However, there is a maximum threshold amount of turbulent kinetic energy can be absorbed from the flow using this mechanism at a specific Reynolds Number. This means that a polymer with a larger ΔL spring effect would not absorb more energy than the maximum absorbable amount at the boundary layer.

Furthermore, if the flow rate was increased for the experiment, thus increasing the Reynolds Number, a higher amount of turbulent kinetic energy would be available for absorption by the polymers, and thus a threshold of 8-10 Mg/mol of the molecular weight would not be expected and rather it would be higher. Additionally at a higher Reynolds number, the magnitude of the maximum drag reduction would also increase.

This can be compared to the phenomenon of maximum concentration within the flow. Once a certain threshold of concentration is achieved, most of the Reynolds stress in the turbulence is reduced; at after such a point only the viscous stress increases thus hindering the drag reduction performance. In the case of molecular weight, the ΔL of polymer stretching exceeding the amount of energy that is absorbable, whereas for the concentration there is an abundance of polymers to the point where a percentage of them have no energy to absorb and therefore are only increasing viscosity of the solution.

A few differences do exist between high molecular weight and high concentration. From Figure 45 it can be see that increasing the length of polymers past the threshold at a certain Reynolds number does not add any benefit to the drag reduction or the degredation of the polymers. For high conecentration, seen in Figure 46, the initial drag reduction (the maximum) does not increase significantly after 50 ppm, but the degredation of polymers over time is lower at 100 ppm. This can be explained with a simple analogy; at both concentrations (50 and 100 ppm) some percentage of polymers are stretching and coiling to dissapate the turbulent kinetic energy, but over time are degrading at which point polymers that were inactive begin to take the place of the degraded polymers and begin the elastic spring absorption process.

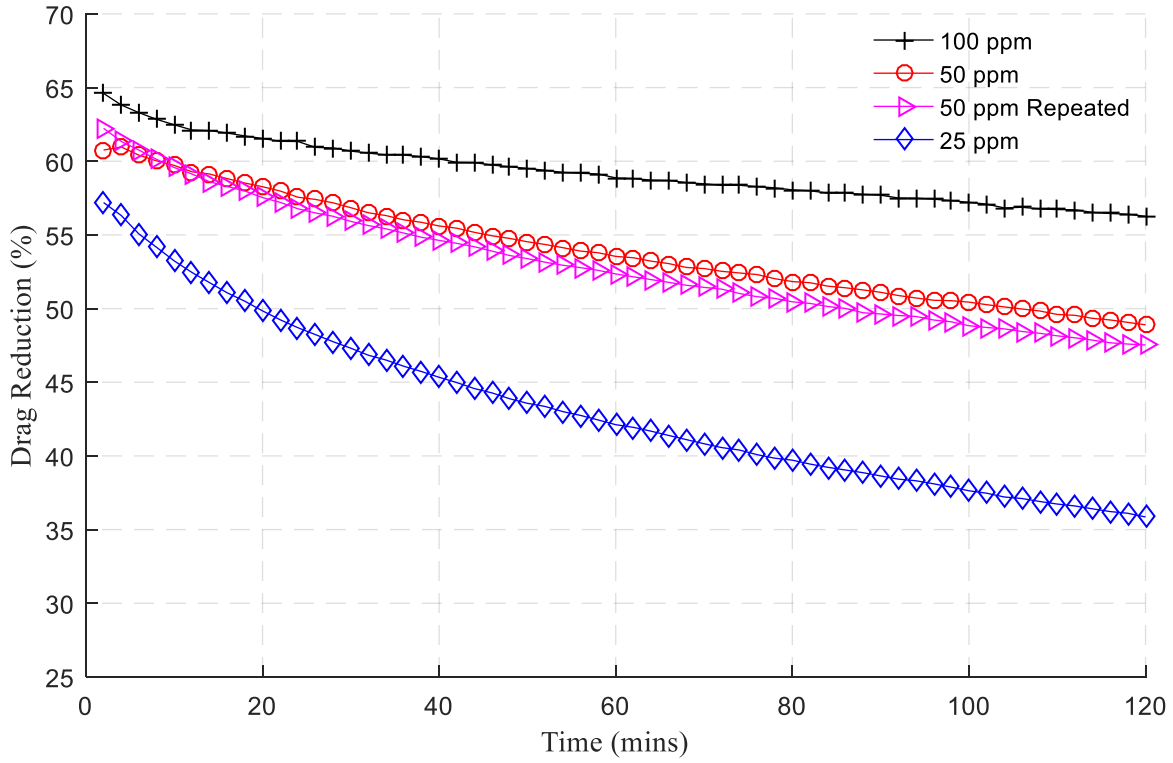

Figure 46: Concentration sweep for product # MT2232-6 at 30% anionic charge density.

The key difference between the two concentrations lies in the fact that at 100 ppm, there are a higher percentage of inactive polymers that can replace ones that degrade; this inevitably results in maintaining higher drag reduction over a large span of time.

5.1.2 Effect of Charge Density on Drag Reduction

Based on a molecular weight and concentration sweep, it can be concluded that after a certain range, both do not affect the maximum drag reduction performance. While operating in this range, polymers from Table 1 can be used to see if charge density (as an isolated variable) plays a part in the drag reduction performance.

Before the effect of charge density on polymers can be analzyed the effect of charge density should be discussed. The best way to describe it is to refer back to the elastic spring absorption mechanism explained for molecular weight. When a polymer has a highly negative charge, around 50% charge density, a tendency occurs known as polymer repellance reported by Green et al. [67], when this phenomenon occurs it hinders the maximum coiling ability of a polymer, in other words, the length of the polymer at its coiled state is increased.

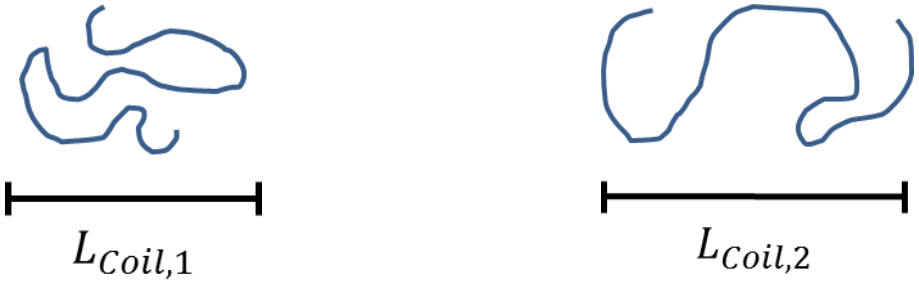

Figure 47: Diagram of coiling length difference of polymers with different charge densities.

The lower the charge density of a PAM polymer, the more compact it can become when releasing energy into the mean flow regime. The difference of the coiled length is depicted in Figure 47. $L_{Coil,1}$ is the legnth from a low charge density polymer and therefore is shorter than $L_{Coil,2}$. As discussed before the amount of energy a polymer absorbs comres from the ΔL of the stretched and coiled states. The purpose of increasing molecular weight was to increase the stretched length; in comparison, the purpose of charge density is to shorten the coiled length in an attempt to increase ΔL. This results in the expectation that at higher charge density will cause longer coiled length, and therefore a lower ΔL, and thus a lower drag reduction performance.

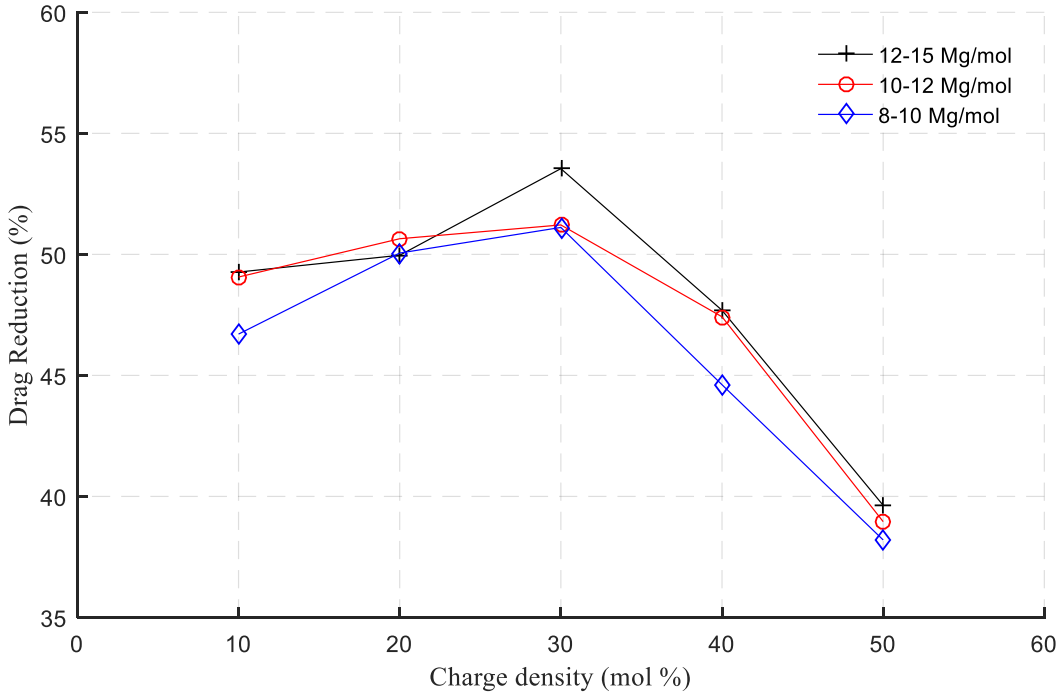

Figure 48: Drag reduction for 15 different polymers with varying charge densities and molecular weights at 50 ppm after 60 mins of recirculation.

As expected from the previous section, the overall trend for charge density does not change based on the molecular weight since all polymers used are higher than the threshold length. However, it can be seen from Figure 48 that the expected results for charge density does not completely agree with the experimental results. Beyond a charge density of 30% the drag reduction is considerably reduced. Between 30% to 50% charge, the polymer repellence effect is prominent and causing a sharply linear decay in drag reduction performance. The peak performance lies between a range of 20 to 30% in which the polymers can still be tightly coiled.

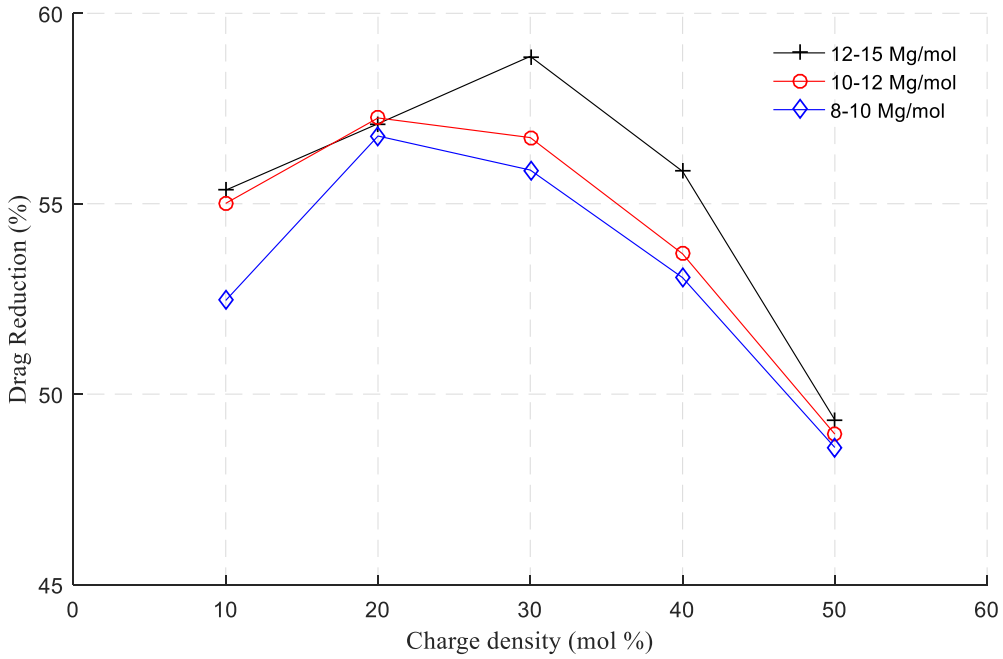

Figure 49: Drag reduction for 15 different polymers with varying charge densities and molecular weights at 100 ppm after 60 mins of recirculation.

A similiar trend is witnessed when the concentration is increased from 50 to 100 ppm. There is a sharp linear decline in the drag reduction after 30% due polymer repellance and longer coiled length. From both Figure 48 and Figure 49 is that the highest MW polymer seems to have a peak closer to 30% charge density, whereas the other 2 polymers are closer to 20%. One explanation is that the ΔL for the highest MW may be higher because the increased stretching length of the polymer is larger than the length at the coiled state at 30% charge density, whereas this peak ΔL occurs at a coil length at 20% for MWs that have a slightly shorter stretched length. Another aspect that needs to be considered is the effect of degradation, in theory, only molecular weight and concentration of polymers dictate the degradation, and therefore regardless of the recirculation time of the loop, this equivalent pattern of drag reduction should be seen based on the charge density.

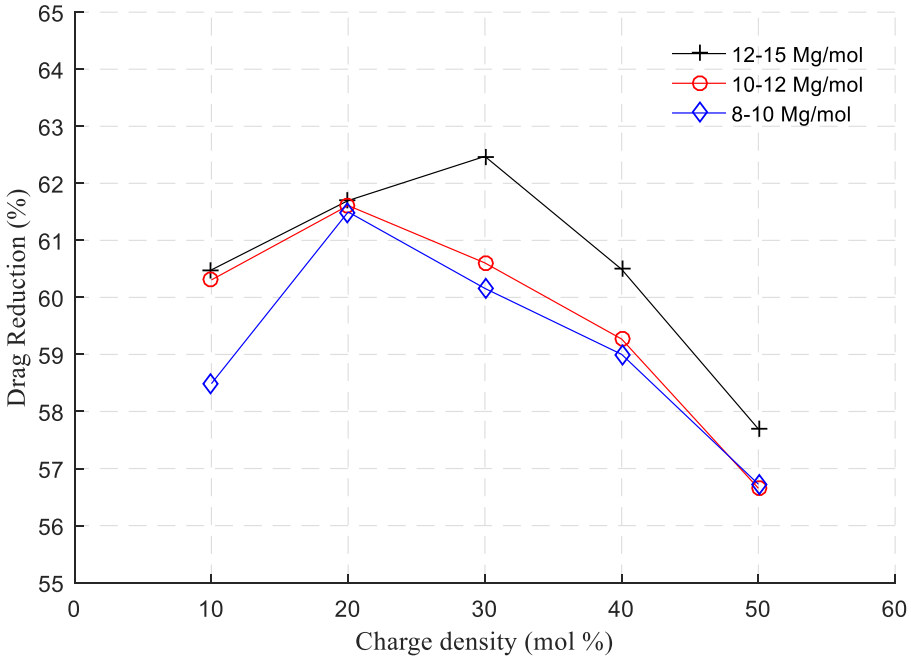

Figure 50: Drag reduction for 15 different polymers with varying charge densities and molecular weights at 100 ppm after 10 mins of recirculation.

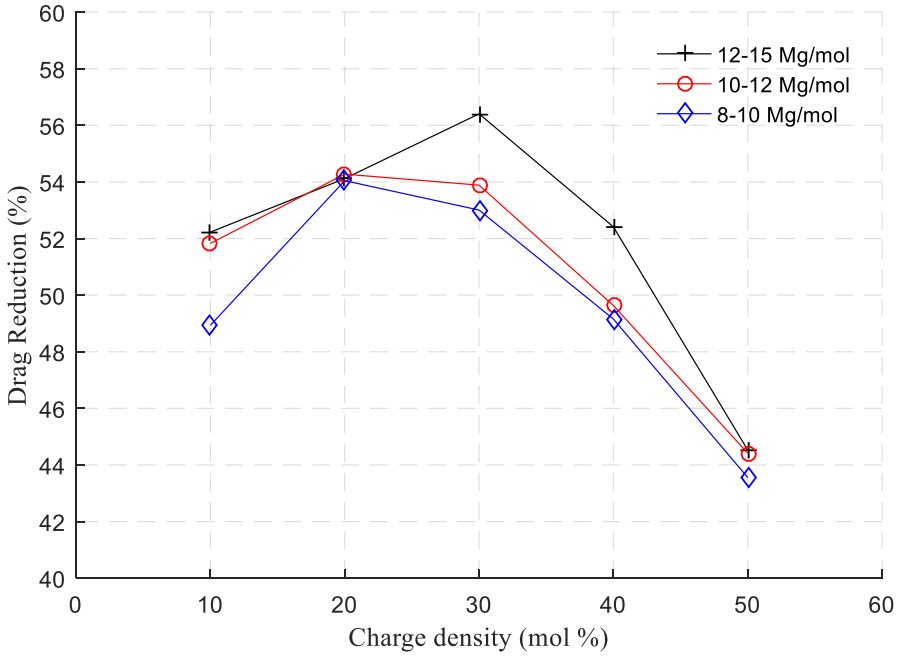

Figure 51: Drag reduction for 15 different polymers with varying charge densities and molecular weights at 100 ppm after 120 mins of recirculation.

Throughout the entire 125 minutes of recirculation, the overall trend of a peak charge density of 20% to 30% is always evident. This agrees with the initial hypothesis that charge density is not a contributor to the degradation since it only affects the coiled length. An important factor that has needs to be investigated is the 10% charge density. For all three polymers it is not the optimal case for DR performance, which does not agree with initial expectations as the coiled length should be the lowest at 10%. This may be explained due to the homogeneity of the polymer solution.

It is known from past experiments by Green et al. 2000 [67] that when multiple polymers are tangled closely together and heterogeneously dispersed within a solution, the overall performance of drag reduction is decreased. It is known that when the charge density of polymers are very low and close to neutral, they have a higher probability of coming in contact with one another, compared to being electrically repelled. This means that as the charge density increases, the different polymer chains are more likely to stay apart, thus improving the homogeneity of the solution. However, when the polymer charge density is highly negative, the polymers repel parts of their own chain which was discussed as the polymer repellence effect causing a longer coiled length. Due to conflicting parameters, it is normal to see a certain peak at which the polymers maintain a homogenous solution while having a short coiled length.

5.2 TCD Polymer Tests

As discussed before, the TCD serves two purposes, the ability to compare a large number of polymers for their drag reduction effectiveness, and the ability to have a screening process to test a polymer's performance between single phase and particle laden flows. Inheritably, objective two will be successful because the geometry of the flow will not affect the polymer's ability to flocculate and form aggregates with fine clay. However, there may be a difference in drag reduction performance within the TCD compared to channel flow, if this is true, comparison between polymers in single phase cannot be carried over and applied to pipe/channel flow. SNF has produced 15 different PAM polymers with varying molecular weights and charge densities to see if these two important properties show the same trends in a TCD compared to pipe flow.

In the previous section, it was experimentally shown that within pipe flow there is an optimal charge density between 20 to 30 mol% for anionic PAM polymers. The reasoning used to explain this phenomenon was due to two effects; firstly at very low charge density, the polymers do not repel each other and therefore have a greater possibility of being entangled and causing the solution

to become heterogeneous thus reducing DR performance. On the other hand, at a very high charge density the polymer chains begin to repel against themselves causing them to have a longer coiled state, and thus reducing the amount of energy they can absorb based on the elastic spring mechanism of polymer drag reduction. Due to conflicting performance loss on each end of the charge density spectrum, an optimal peak was concluded and was reflected in the data. In this section the objective will be to see if this process is also occurring in Taylor-Couette flow in an environment which the polymers are stretched in a circular component rather than axially.

5.2.1 Mixing Time for TCD Tests

The first step to ensure that all polymer tests are run correctly is to understand the drag reduction curve of the test setup. In the pipe loop for example, the entirety of the solution is premixed in a large tank, and it is expected that the maximum drag reduction, MDR, occurs right at the beginning of the test, and slowly the polymers break down from the high shear rate of the pump. It is known that such a source of shear is not present within a recirculating Taylor Couette device which means a different degradation curve may be expected. Additionally, a different mixing technique was used for these experiments since a large mixing tank would produce a larger quantity of solution that required. The TCD required a solution volume of 8.4L; therefore, a magnetic stirrer was used to make 1L master solutions of polymers at 840 ppm. This master solution was added to the tap water within the TCD when the experiments began. This results in an inhomogeneous solution when the experiments started and therefore would take a certain amount of time to reach the MDR

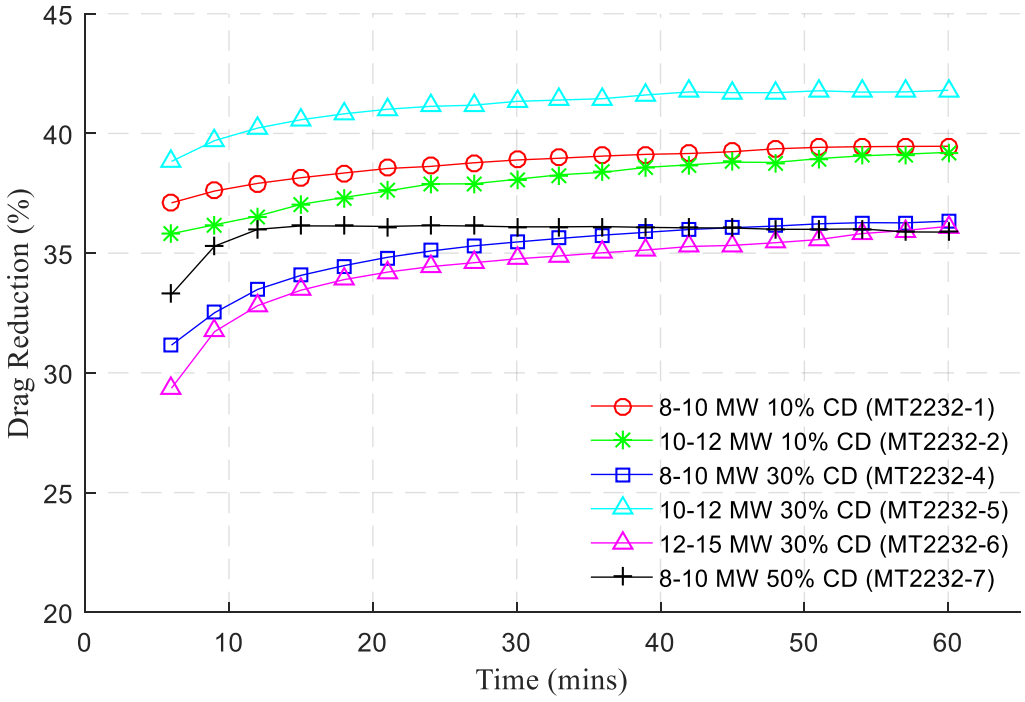

Figure 52: Drag reduction as a function of time for a sample size of SNF PAM polymers at 100 ppm using the Taylor Couette device.

A sample of the 15 polymers was taken in order to see their drag reduction curve over time for an entire hour of testing. The data collection process started after a 5 minute mixing time. Six out of the fifteen polymers were chosen for this test; three polymers swept the entire charge density range while having a constant molecular weight, and three polymers with different molecular weights at one specific CD. By observing the drag reduction curves from Figure 52, this technique resulted in an initial mixing time of 30 minutes to reach the MDR. Due to the overall low shear rate within the TCD (compared to that of a 20 HP centrifugal pump at 1000 rpm) there is no degradation of polymers during the 60 minute testing time when at a concentration of 100 ppm.

The mixing time to reach MDR for any given charge density is approximately identical, however, as the charge density increases, the mixing time is reduced. The sharper initial increase in DR is seen in 50% CD; the mixing time is for this condition is approximately 12 minutes, whereas the 10% CD polymers have a 30 minute mixing time period. Highly charged polymer chains have a stronger repulsion force between them which improves the homogeneity of the solution; this can cause the reduction in mixing time for polymers with 30%+ CD. Molecular weight does not play a factor on the mixing time when applying the master solution method; this is to be expected

because the max stretched length of the polymers is not a contributor to its ability to be mixed. Overall, this figure indicates that using a mixing time of 30 minutes after adding a master solution is sufficient at reaching MDR for the entirety of the test matrix. The test also reiterates the phenomenon that highly charged particles have a greater ability to become homogenous based on the initial mixing time. Finally, at 100 ppm, the effects of degradation are not present at 60 minutes of testing.

5.2.2 Effect of Degradation in TCD

All tests in the TCD were run at a concentration at 100 ppm in order to compare to the pipe loop study. However, a concentration sweep was conducted to evaluate the degradation of the polymers under TC flow.

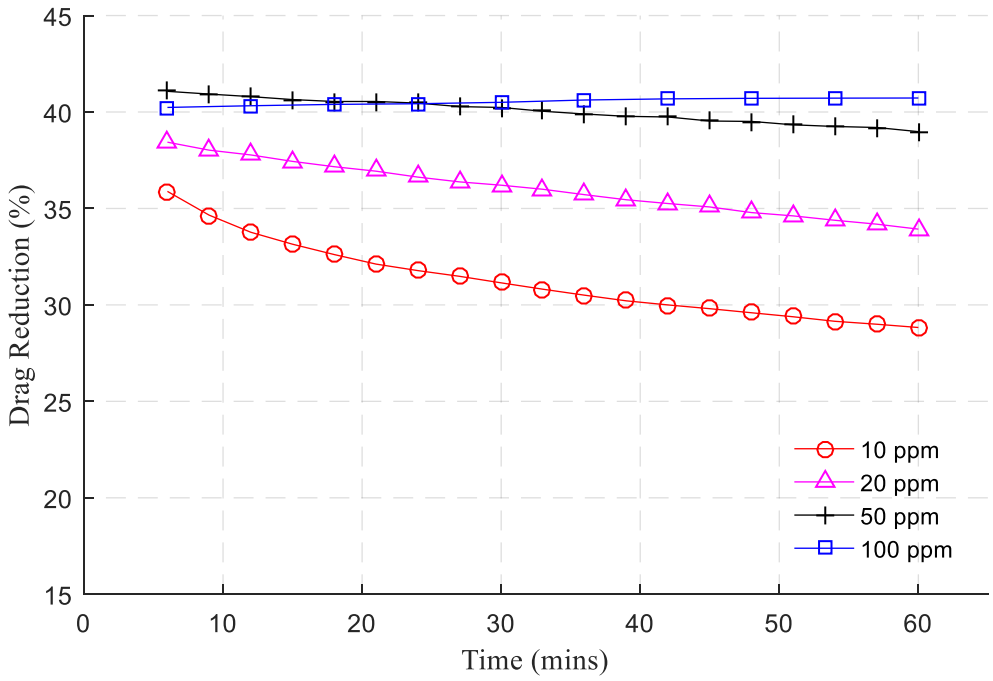

Figure 53: Concentration Sweep for PAM product % MT2232-1 with 10 mol% anionic charge using the Taylor Couette device.

At very low concentrations, a similar drag reduction profile to that of pipe flow is seen within the TCD. This is due the shear rate causing degradation; however this phenomenon happens at 10 times less of a concentration due to the severe difference between maximum shear rates of the centrifugal pump and walls of the TCD. In order to remove extra effects such as degradation, 100 ppm was used in all TCD tests to easily assess the MDR of all polymers.

5.2.3 Effect of Charge Density in TCD

A similar parametric study of polymer charge density was conducted in the Taylor-Couette device. The concentration for these tests was held at 100 ppm for equivalent viscosity of the solution compared to the pipe loop tests. However, the effects of degradation were not of interest, and therefore based on the concentration sweep, no 50 ppm runs were done as they have a gradually slow DR over time. Each test was run for a total time of 60 minutes, however the drag reduction around 40 minutes were used in the plots; this guaranteed that the MDR is considered based on the mixing time experiments.

Based on Figure 54, the overall trend of each molecular weight is oscillatory within the range of 35% to 40% drag reduction. This is not expected, as the range of drag reduction for these polymers were between 45 to 60% within the pipe flow tests. It's also noticeable that at a constant charge density, the largest MW polymer does not always produce the highest drag reduction despite this been shown as a generally accepted trend in pipe and channel flow. These results indicate that both the charge density and molecular weight do not have an effect on the drag reduction. To verify that the tests were accurate, 4 repeats of 3 different test conditions were run; however, no major difference within the data was seen between trials. This step does provide insight that an uncertainty of ±2% in drag reduction exists for the TCD experiments. This correlates to a relative uncertainty of 5% of the data points which is deemed acceptable. The highest MDR that is noticeable within this data occurs at 10% CD for the lowest MW and at 30% CD for the medium MW. However, this does not agree with the pipe flow data, and the DR performance is less than 5% of an increase from the average DR.

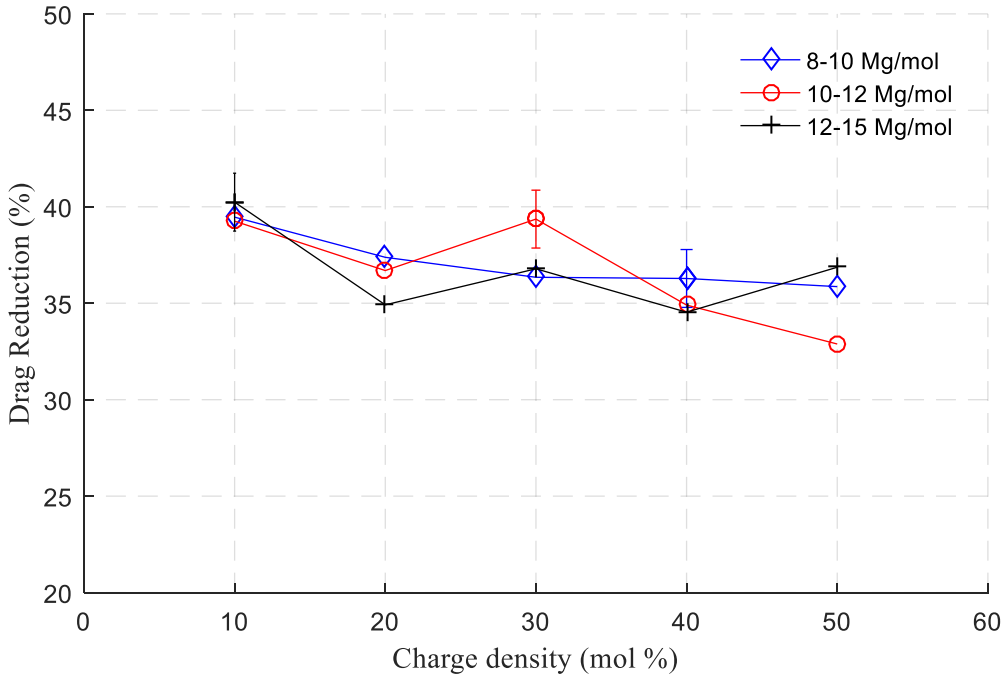

Figure 54: Drag reduction vs charge density for 15 polymers with varying molecular weights using TCD.

The theory that was presented during the pipe flow study suggested that the molecular weight and charge density both effectively change the stretching length, ΔL. This affects the total turbulent kinetic energy the polymer chains can transfer from the boundary layer to the mean flow regime. In this case, the lowest performing polymer, the 8 Mg/mol at 50% CD (based on pipe flow study), has a threshold ΔL that absorbs the maximum amount TKE, thus all higher performance polymers do not have significantly improve drag reduction. The effect of this can be seen in Figure 55.

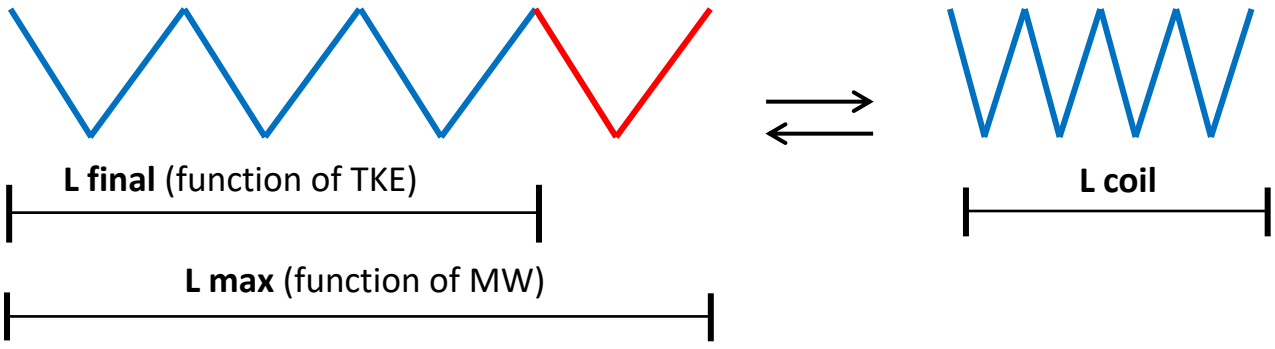

Figure 55: Diagram of the effect of threshold length for drag reduction performance of a long chained polymer molecule.

There is also another possibility that may cause a change in drag reduction performance between polymers within TCD and pipe flow. The amount of shear stress within the fluid elements at the boundary layer may be different. At lower levels of shear stress, it results in the Reynolds stress to also be decreased, which is known to be the primary stress reduction caused by the polymer chains. Lower Reynolds stress can hinder its ability to reach the L_{max} causing a limit on their drag reduction performance. In addition to this, a lower Reynolds stress results a lower amount of TKE production and thus the better performing polymers cannot be detected within the conditions of these experiments. Both the TKE and stretching will be further analyzed to explain the DR performance within the TC flow.

5.2.4 Comparison of TCD to Pipe Loop

The difference in the scale of turbulence may result in the disagreement between the results from the pipe flow and TC flow experiments. The scales of the flow are known to greatly affect the fluctuation behavior of a flow which is directly related to the energy absorption mechanism initiated by the polymers for drag reduction. The higher the Reynolds number of a flow, the shorter the length scale, and the shear rate in the turbulent boundary layer (TBL) is great. However the Reynolds Number is defined differently between pipe flow and TC flow.

The drag reduction of product # MT2232-1 was compared at different operating conditions between both the pipe loop and TC device. The trend was related with the Reynolds number of the flow however an inconsistent trend is observed from Figure 56. There data from the two experimental setups do not collapse; this is because the Reynolds number is defined differently for each setup (equations shown in Chapter 2). Therefore, the Reynolds number is not an equivalent parameter to measure the degree of turbulence between the two different experimental setups. The data set presented in this section were repeated three times, and all data points were within 1% accuracy.

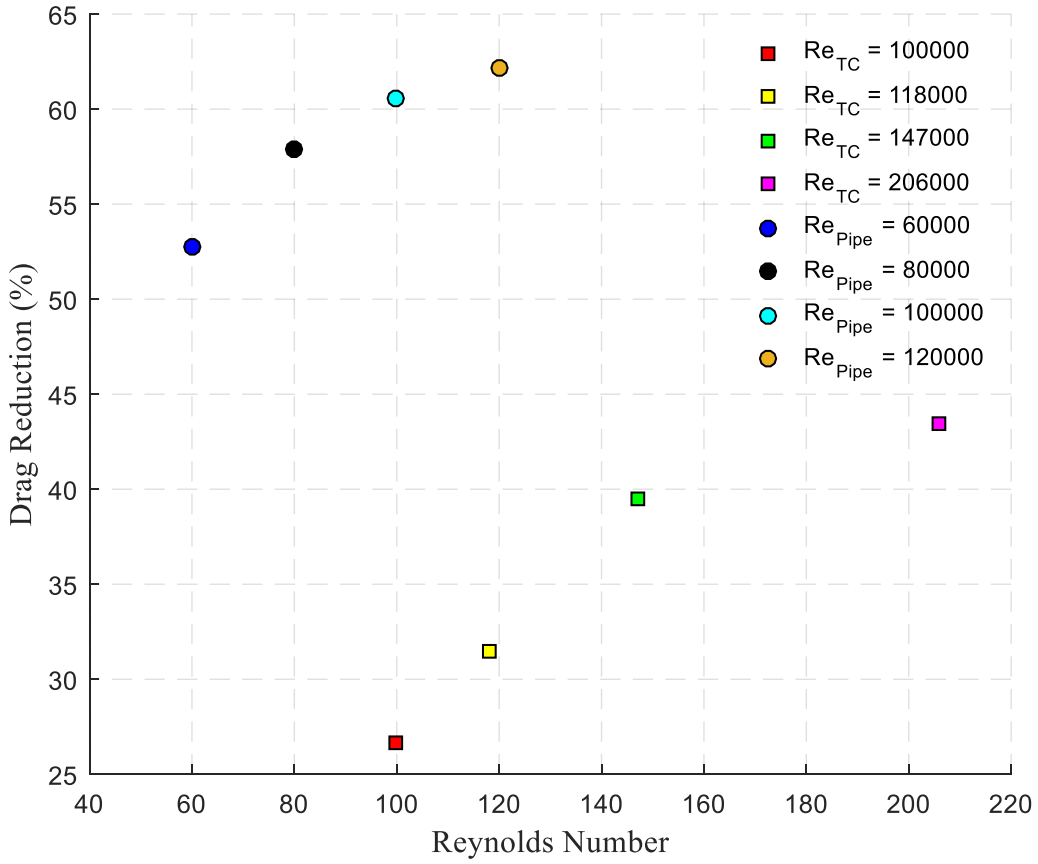

Figure 56: Effect of Drag Reduction at different Reynolds Numbers between two experimental setups.

Rather than the Reynold number, the length scale was calculated for both TC flow experiments at different rotational speeds and the pipe flow experiments and used as a comparison for the level of turbulence in the respective flows. The shear velocity and length scale was found using an empirical relationships from Burger et al. [45] and Grossmann et al. 2016 [59].

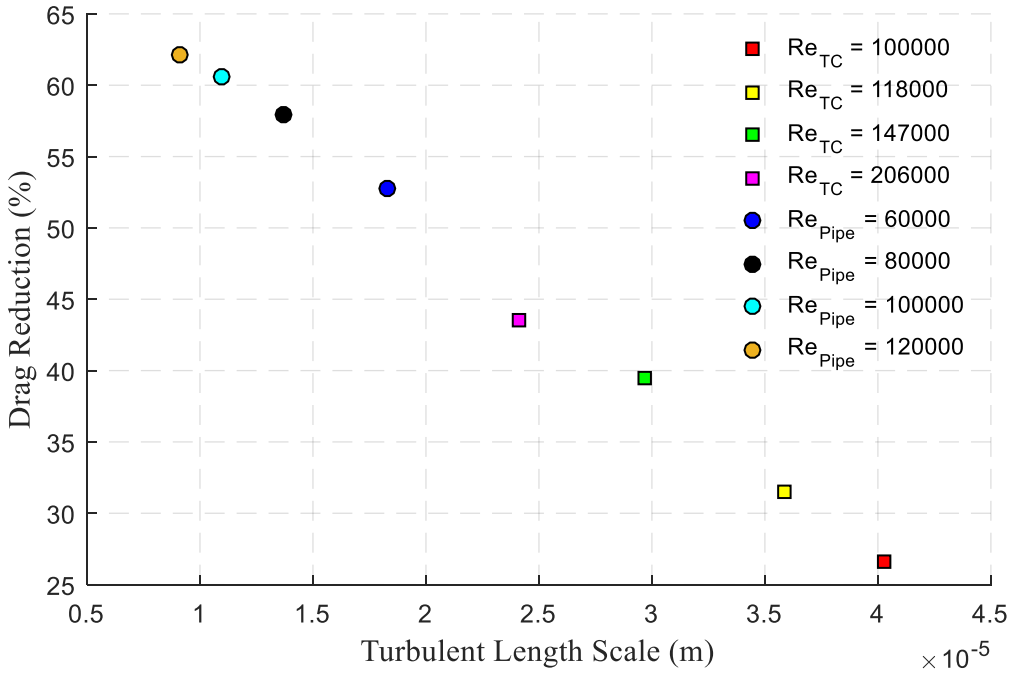

Figure 57: Effect of Drag Reduction at different Turbulent Length scales between two experimental setups.

The pipe flow experiments were conducted between a range of *Re* from 60k to 120k whereas the TC device experiments were tested between 100k and 206k. As mentioned before *Re* is defined differently for TC and pipe flow, therefore it is not a comparable measure for the amount of turbulence present within the flow regime. Using the relationship exemplified in Figure 57, it can be concluded that the pipe flow experiments had the shortest length scale compared to all TC flow experiments. In addition, it can also be observed that there is a linear trend between the effect of drag reduction and the turbulent length scale of the flow, both the TC data and pipe data fit within this single linear trend. It can be seen that the during the lowest length scale, occurring at *Re* of 120k during the pipe test, the highest DR is witnessed of about 62%. In contrast, at a maximum speed of 650 rpm (Re TC of 206k) only a DR of 44% is found. The difference between these depends on the amount of stretching the polymers undergo. The further the polymer is allowed to stretch, the greater the amount of energy it can absorb from the flow. In the case of lower length scales, the shear rate in the TBL is greater. In these conditions the polymer stretches to its maximum length due to the force applied on the chain and thus provides peak drag reduction performance.

Another technique to compare the turbulence between the TC and pipe flow can be achieved with the use of frictional Reynolds Number,

$$Re_\tau = \frac{u_\tau D}{\nu}, \qquad (5\text{-}1)$$

is defined as the ratio of the physical dimension of the setup to the length scale (defined previously). As Re_τ increases, it is another way to show that the shear rate near the wall increases. Therefore, the polymers will reach longer stretching lengths and result in higher DR performance. Initially, the frictional velocity of each experimental condition was plotted against the DR performance; this can be seen in Figure 58. The friction velocity suggests that the increased amount of wall shear in the pipe flow experiments leads to a larger magnitude of DR.

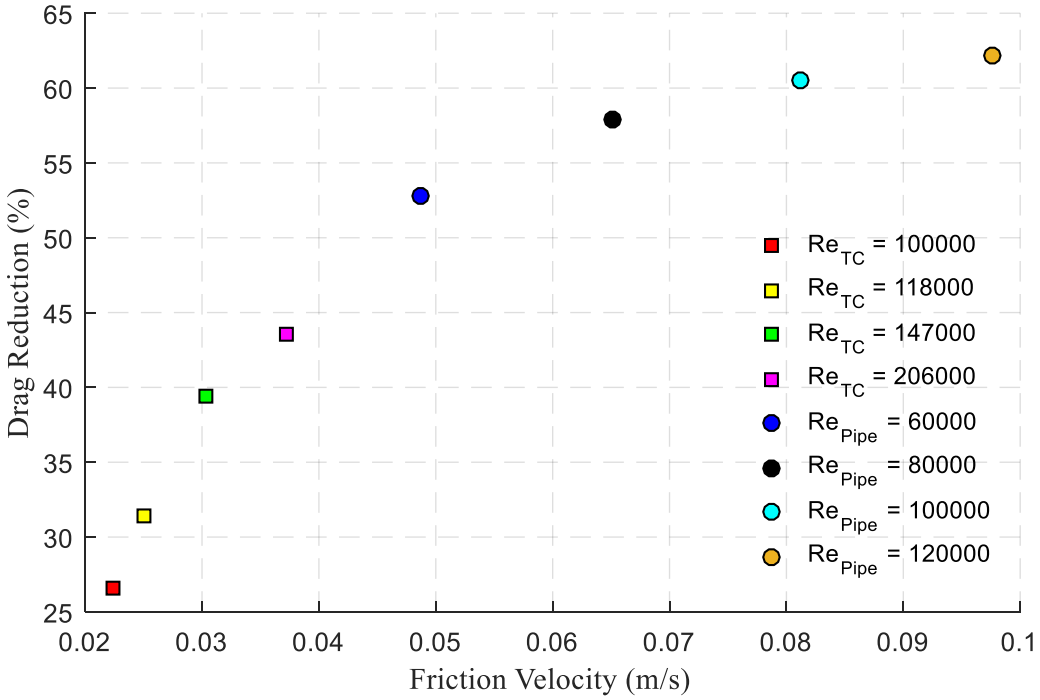

Figure 58: Drag reduction comparison of PAM between Taylor Couette and Pipe flow using friction velocity (u_τ).

A strong fractional power relationship between the drag reduction and frictional Reynolds Number can be seen based on Figure 59. Two important conclusions can be made; firstly, the polymers perform significantly better at higher Re_τ. Secondly, at a certain threshold the polymers reach their

stretching limit, and the drag reduction increase after this point does not increase significantly. Any additional shear causes the polymer chains to rupture.

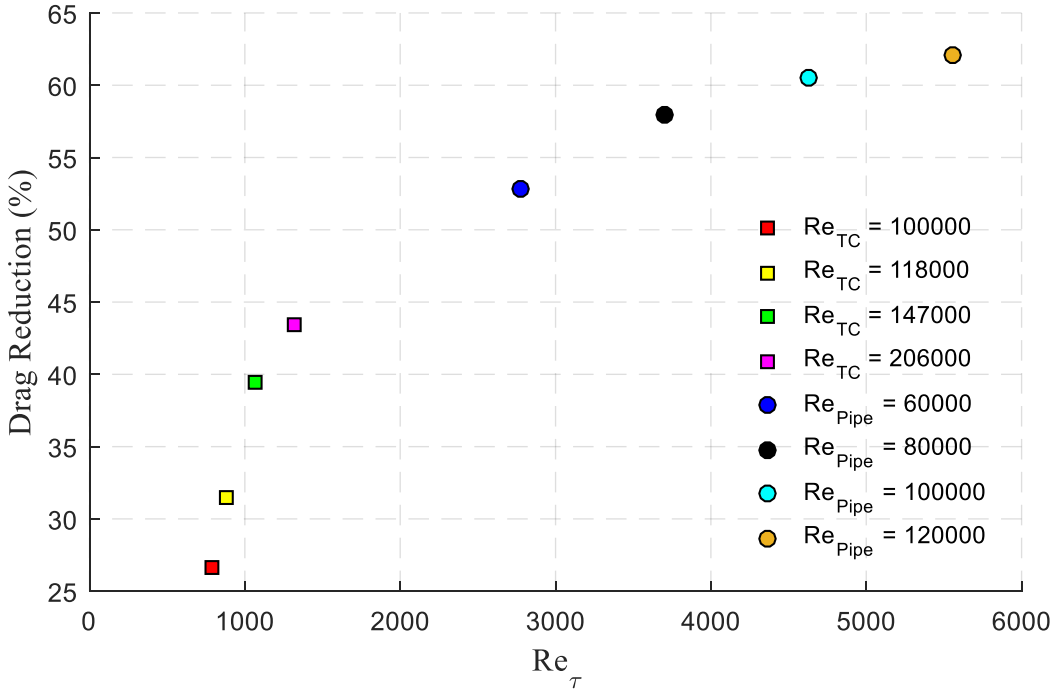

Figure 59: Drag reduction comparison of PAM between Taylor Couette and Pipe flow using Re_τ.

The time scale of the turbulence can also be used as a method to compare the pipe flow and TC flow experiments. The turbulent time scale is defined as the amount of time that the shortest eddies are present during the flow, if this time is larger than the polymers' stretching time, the polymer will not fully expand to capture all the energy, this phenomenon is known as the Time Criterion for drag reduction stated by Hershey and Zakin 1967 [68] as

$$T_z > \frac{\mu_s}{\rho u_\tau^2} \qquad (5\text{-}2)$$

where T_z is the average time it takes for a stretched polymer to return to a coiled configuration which was initially stated by Zimm 1956 [69]. The ratio between the stretching time of the polymer and the time scale is defined by the Deborah Number,

$$De = \frac{T_z}{T_s}. \qquad (5\text{-}3)$$

A shorter time scale results in a faster rate of eddy formation and dissipation which disrupts the nature of the flow abruptly and is described by a higher Deborah number. At shorter time scales higher velocity fluctuations are present and therefore an environment where polymers have more TKE to absorb. The TC and pipe flow data against their corresponding time scales was analyzed and represented in Figure 60.

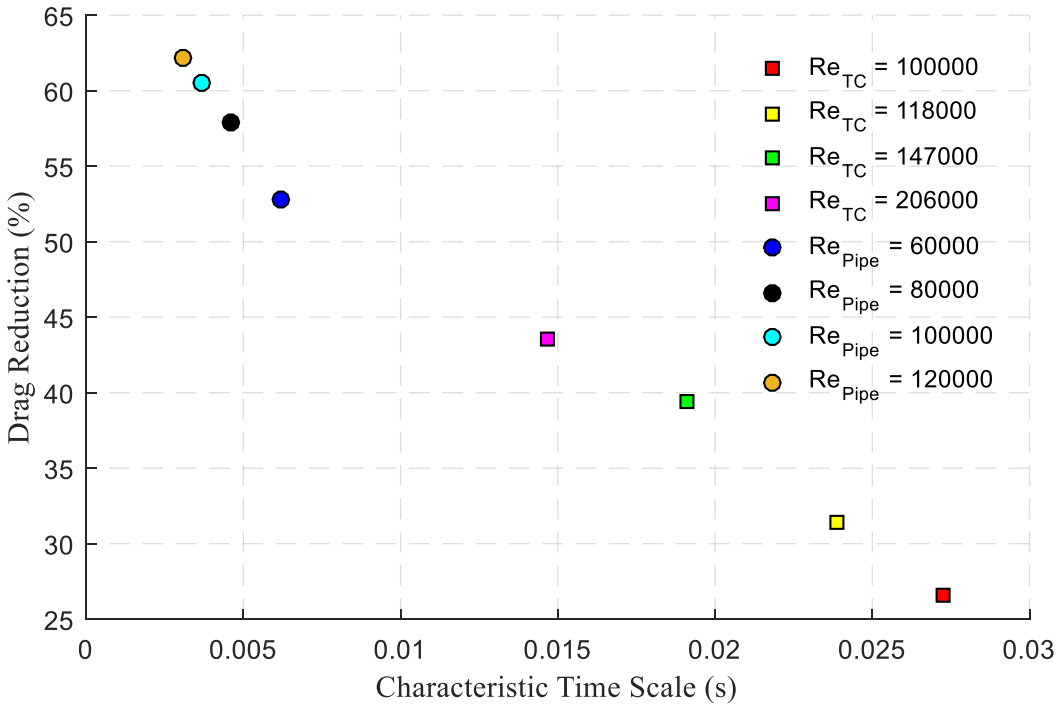

Figure 60: Drag reduction performance of PAM at different Characteristic time scales.

As expected, the pipe flow experiments have a significantly shorter time scale; and thus greater velocity fluctuations. With the shorter time scales corresponding to a test with larger amount of TKE, this allows polymers to fully stretch and thus distinguishes the performance difference of each polymer. The fit between the trend of the pipe flow and TC flow do not fully converge to one single linear trend. Each experimental data set does show linearity however both have slightly different slopes.

5.2.5 Polymer Stretching

The TKE levels in the boundary layer may not be the only cause of the disagreement between the pipe flow and TCD experiments. It is known that within pipe flow, polymers typically stretch based on the direction of the dominant component of the shear velocity. For any given fluid

element within the boundary layer, the viscous stress tensor determines the orientation and direction of the stresses that act upon it. Based on the directions, it allows a polymer chain to stretch or deform to absorb TKE.

The viscous stress tensor is defined as (in which the 3 spatial axes are denoted as 1, 2 and 3

$$\varepsilon = \begin{bmatrix} \varepsilon_{11} & \varepsilon_{12} & \varepsilon_{13} \\ \varepsilon_{21} & \varepsilon_{22} & \varepsilon_{23} \\ \varepsilon_{31} & \varepsilon_{32} & \varepsilon_{33} \end{bmatrix}. \quad (5\text{-}4)$$

The strain rate tensor indicates the amount of deformation of the fluid element. This deformation affects the stretching phenomenon of the polymers within the flow. However, one of the key differences is the definition of this matrix between TC flow and pipe flow. Within pipe flow, the 3 axes are typically used as x, y and z spatially, whereas the r, θ and z components are used in TC flow.

Within the boundary layer of the of Taylor Couette flow, Grossman et al. (2016) [59] states the dominant component of stress tensor is the r-θ component is defined as

$$\tau_{r\theta}(r_i) = \frac{\rho v^2 G}{r_i}. \quad (5\text{-}5)$$

As mentioned before, when polymers are added to the flow, the Reynolds Stresses decreases, however, if the overall shear stress of the system decreases, the polymers may have hindered performance since they won't fully stretch to their L_{max}. A lower stretched length would result in a reduced ΔL and with it a lower amount of energy absorption.

The wall shear stress of the pipe flow,

$$\tau_{w,pipe} = \frac{D\left(\frac{\Delta P}{L}\right)}{4}, \quad (5\text{-}6)$$

is a function of the pipe length, diameter and pressure drop. Each experimental condition between the two flows will be analyzed based on their wall shear stress and its effect on the drag reduction performance.

Figure 61 demonstrates that a higher wall shear stress allows the polymer molecules to stretch to their maximum length; therefore, when testing very high MW chains, the TC flow does not have even shear to fully stretch the polymers. Because of this, the full drag reduction capabilities of the

polymers are limited and the different between them cannot be assessed. Similarly to the graph of frictional Reynolds number, the trend against the wall shear stress is fractional power law relationship; this suggests that as the wall shear stress reaches a certain threshold, the stretching of polymers do not continually extend and therefore a significant improvement does not occur. The agreement between the DR relationship for Figure 59 and Figure 61 is logical; both the frictional *Re* and wall shear stress are related to the total frictional resistance of the wall-bounded flow.

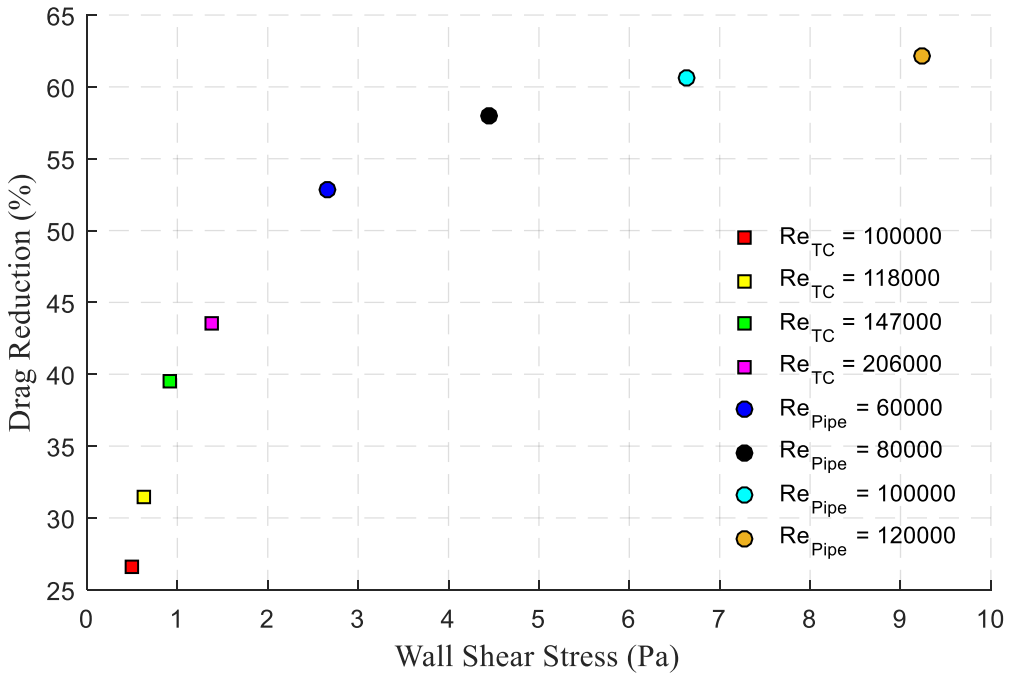

Figure 61: Drag Reduction Performance against wall shear stress for different experimental setups.

5.2.6 Effect of Molecular Weight in TCD

So far it has been determined that the scale of turbulence and shear stress affect the polymer stretching phenomenon during drag reduction. Due to a lower shear and lower fluctuations, the polymers that were tested did not show any difference in characteristics within the TC flow. If however, polymers with a lower MW than the threshold MW in the TC were tested, they could be used as a direct replacement to pipe flow studies. The threshold MW would need to be found for the low shear testing facility since it can result in a saturation point for large polymer chains to be indistinguishable from each other.

Two polymers at 30% anionic charge density with low molecular weights were tested against the high MW in order to see how large of an impact this MW range has on DR. At 4-6 Mg/mol a similar drag reduction performance to the high MW PAMs was observed as seen in Figure 62. This means that the threshold MW at which polymers cannot be tested is still lower than this level. In order to check to see if the mixing technique of the master solution caused any effect on the disagreement between the pipe flow and TC experiments, the marine impeller tank setup was used to create a fully homogenous 100 ppm solution to use in the TCD. Based on the drag reduction profiles, the initial mixing period is not present compared to the master solution method, however the MDR of the polymers remain the same; validating that the master solution method did not change the MDR performance once the initial mixing time was passed.

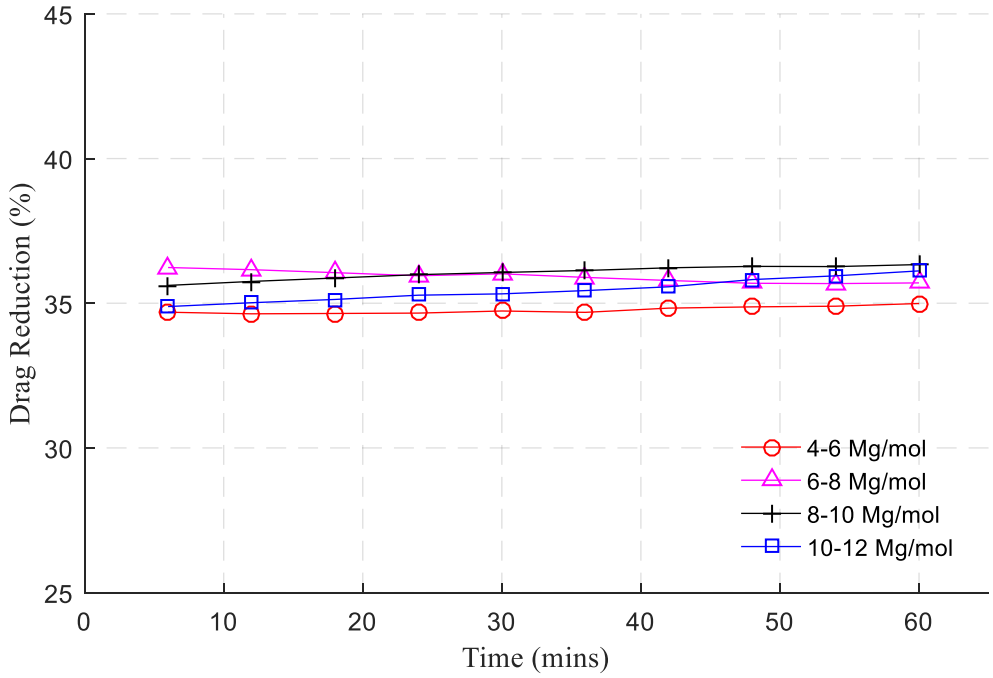

Figure 62: Effect of PAM molecular weight on the drag reduction within Taylor Couette flow at 100 ppm.

Tests will need to be continued in the future to measure the drag reduction against lower MWs at these conditions to find the threshold. At this case, a relationship between the threshold molecular weight and turbulent scales of an experimental setup can be derived. Using such a relationship one can easily determine if a given set of polymers can be used as a comparison between two different systems.

5.3 Summary

The PAM polymers tested showed different drag reduction performance between the TC device and pipe flow experiments. The degree of turbulence of the two experimental setups was compared using the length and time scales of the flows. It was found that the scales of the flow are smaller in the pipe loop compared to TCD; this shows that the shear rate near the wall is greater for the pipe. This is simultaneously shown with the increased wall shear stress for the pipe flow experiments as well. A higher wall shear stress allows the high molecular weight polymers to be stretched further, and therefore result in a higher drag reduction performance, however, after a certain threshold, the polymers reach their max stretching length and further DR is not seen with increased shear.

Analyzing the length scales further, the magnitude of drag reduction between the two experiments collapsed linearly for multiple operating conditions. This linear relationship can be used to predict the DR magnitude of a desired pipe flow condition by extrapolating the results from a TC device. This trend was only found using only one PAM polymer, and further tests are required to check if this effect is universal.

6 Performance of Polymer Additives in Slurry Flow

The final objective of this study was to assess the wear rate reduction capabilities of drag reducing agents such as polymer additives. In this section the wear results between slurry flow with and without polymers are compared to evaluate if they can be used for such a purpose in industrial applications.

6.1 Slurry Test in TCD

The next series of tests involved the use of fine kaolin clay particles to evaluate the polymer drag reduction effectiveness during two phase flow. Typically, in a pipe loop course particles are used within the working fluid, however, course particles cannot be fully suspended within the Taylor Couette Device at the current rotational speed. The use of these fine clay particles simulate a tailings flow from an oil sands extraction process. The experimental procedure for these tests was similar to the single phase experiments. A high concentration master solution was created with PAM powder in a 2L beaker using a magnetic stirrer. This master solution was added into the TC device before operation. An added step for the two phase experiments required the TC device to be rotated to the desired speed for the test, and premeasured kaolin clay was slowly added to the flow.

The kaolin clay was typically positively charged when entering the flow. The anionic PAMs are negatively charged and therefore caused flocculation immediately and an inhomogeneous mixture. In order to rectify this problem, premixing using a marine impeller inside of a tank was used; however, even in this case there was immediate flocculation of the clay in the polymer solution. To avoid this problem, larger particles were used to inhibit the effect of charge. This lead to another issue within the TCD, at the maximum operating speed of 650 rpm, there was still settling of particles. This was seen with lane mountain sand at 125 μm and silica sand at 32.5 microns. Another issue with the setup was the leakage of particles into the shield housing of the bearing unit. This lead to a buildup of small particles within the bearing; larger magnitude of residual torque in the system was witnessed, which reduced the overall accuracy of tests. It was concluded that the use of two-phase flow would not be sufficient in this testing apparatus, and that the TCD would only be utilized for evaluating polymer drag reduction in single phase flow.

6.2 Effect of Polymers on Pipe Wear

To recreate the adverse conditions of industrial pipelines, the SRC Pipe loop was used to evaluate the performance of polymer additives during 30% silica loaded slurry. The polymer chosen for this experiment is ALKAPAM A-1103D. The flow rate of the experiment was held constant in respect to test 1-3 (shown in Table 8) from the analogous material testing phase (refer to Chapter 4.2). The purpose of keeping the flow rate constant between baseline tests and tests with polymer additives is to ensure that the rate of delivery of the particles is constant. During an industrial process, regardless of the power input change due to drag reduction, the particle transportation rate is pre-determined due to other factors and for most cases would be held constant. The wear tests typically take 2 to 3 weeks of continuous operation with slurry replacements occurring every 100 hours. This leads to an issue with polymer additives, specifically PAMs, as they are quite susceptible to degradation (refer to Chapter 5.2.2). Typically, polymer additive tests only required an original solution of concentrated polymers that slowly degrade throughout the testing time. In the case of these wear tests, mechanical degradation of the polymers must be avoided. To rectify this situation, the use of polymer injection was introduced. A 2000 ppm PAM solution is injected at 2.5L/hr into the pipe downstream of the pump inlet; this would result in immediate mixing of the concentrated polymers into the bulk flow. The constant addition of PAM throughout the test would allow a constant drag reduction rate and would negate the effect of degradation.

Prior to the wear test involving polymers, initial experiments were required to find an appropriate injection rate into the system to guarantee that the overall drag reduction was constant; this ensures that at a constant pump speed the flow rate did not fluctuate. In other words, the amount of polymers degraded from the shear of the system must be equally added to the system to maintain a constant drag reduction rate.

6.2.1 Polymer Injection System

The injection system utilized a peristaltic pump that injected a master solution of PAM into the flow of moving slurry within the loop. This master solution was prepared within a beaker using a magnetic stirrer at 400 rpm for 2 hours (identical procedure to the TC flow tests). During this initial test, the pressure drop of the system was measured between both spool test sections. The injection rate that was used for this study was calculated based on degradation tests done in the pipe flow loop setup located at the University of Alberta. Based on the shear of that system (with the pump

operating at roughly 800 rpm), the amount of polymer degradation was calculated using the degradation curve shown in Figure 63.

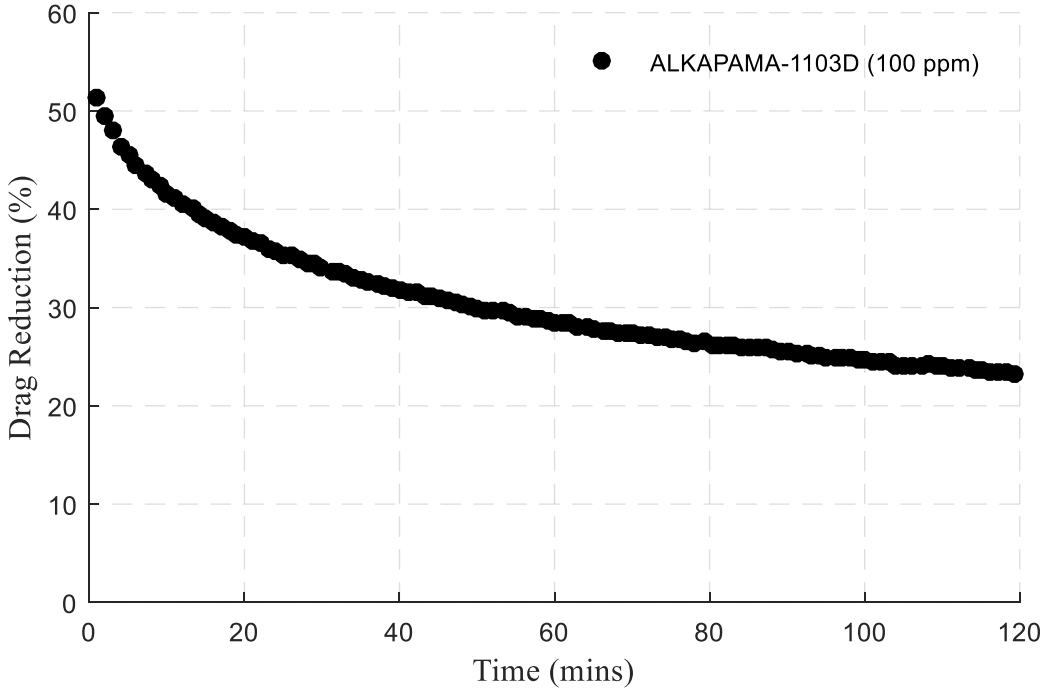

Figure 63: Variation of drag reduction performance of ALKAPAM A-1103D 100 ppm solution using the University of Alberta pipe flow loop.

The degradation rate of ALKAPAM after 2 hours is about 15%/hour, based on the mass of polymer; this results in a mass loss of 5 g/ hr. This is the polymer mass that must be replenished in the SRC loop to achieve constant drag reduction. The injection concentration was chosen to be 2000 ppm limited by the mixing factor based on the magnetic stirrer technique. This corresponds to a solution injection rate of 2.5L/hr. The pressure drop using this injection rate was compared to the baseline condition at both the 2.5 and 3 inch spool sections. Both of these comparisons can be seen in Figure 64 and Figure 65.

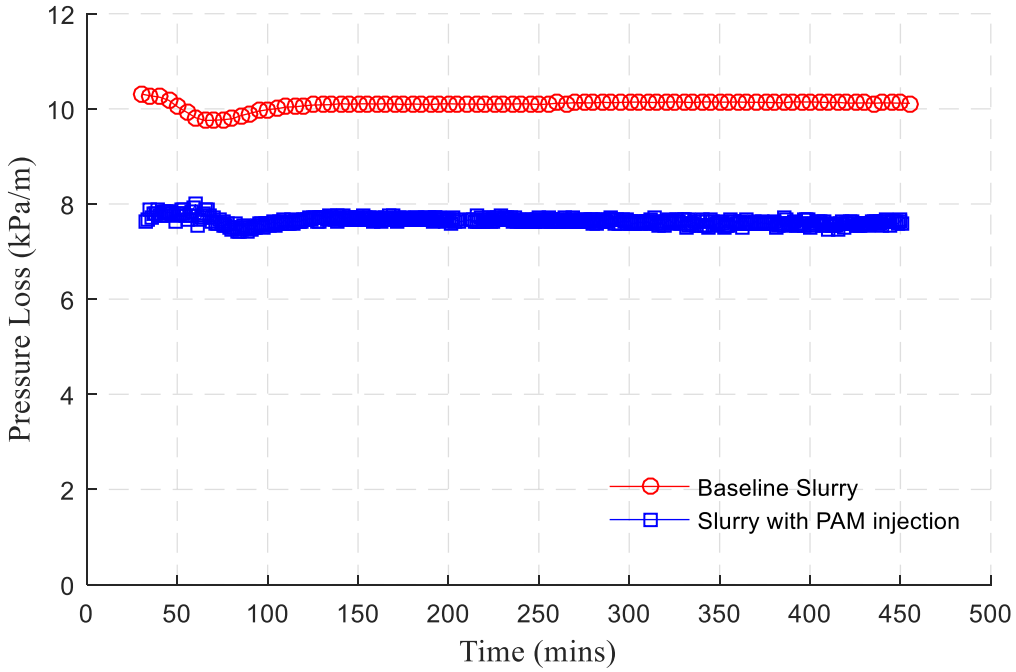

Figure 64: Slurry Pressure drop versus time for a velocity of 8.2 m/s at D = 2.5″ at the SRC pipe loop experimental setup.

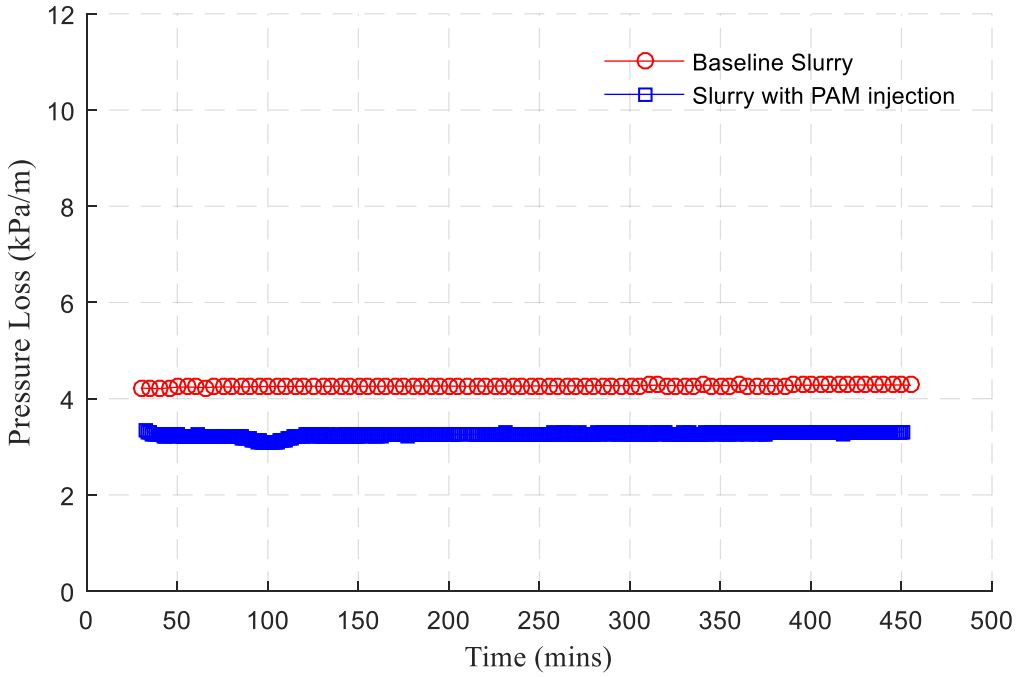

:

Figure 65: Slurry Pressure drop versus time for a velocity of 5.3 m/s at D = 3″ at the SRC pipe loop experimental setup.

The total pressure drop of the slurry has decreased in both sections and therefore drag reduction is present. Secondly, the pressure loss does not change in respect to time; this shows that the flow will operate at a constant volumetric flow rate. It was also important to check that the drag reduction in both test sections were consistent, this is important to show that there is no discrepancy between the 2.5″ and 3″ data. Based on Figure 66, it's shown that the total pressure drop has a 25% continuous drag reduction using the current injection system. This also verifies that the drag reduction is approximately the same across both test sections.

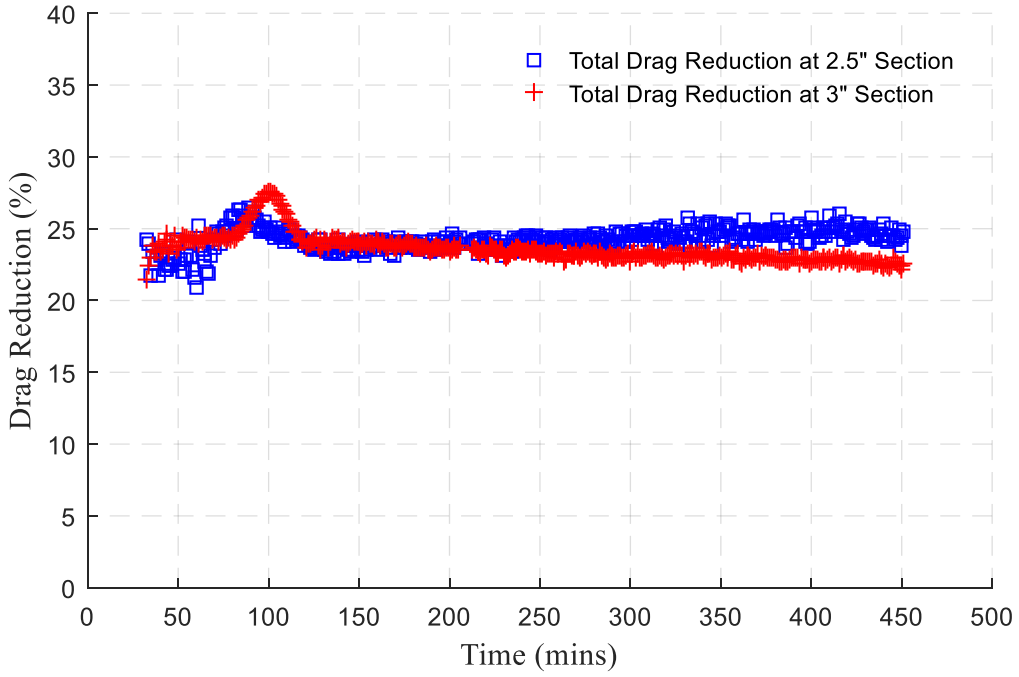

Figure 66: Drag reduction plot of the PAM at both test sections based on pressure drop measurements.

It is important that at this injection rate at the same volumetric flow of water, the drag reduction was seen to be 52%; this can be seen in the table below.

Table 11: Drag reduction difference of PAM injection into water and slurry.

Working Fluid	**Drag Reduction with PAM injection**
30% Silica sand Slurry	25%
Water	52%

There is additional tests conducted to fully explain the reason behind this change in DR, however, it is hypothesized that the polymer molecules ability to stretch is hindered with the presence of

particles. One of the reasons for this may be the entanglement of the long chained molecules around certain particles, or smaller pieces of degraded particles.

6.2.2 Wear Rate Reduction

Using the verified injection rate from the initial experiments, wear tests were conducted for 100 hours for all materials to see the effect of the polymers on the wear rate. The volumetric flow rate was equivalent to the conditions of test 1-3 (shown in Table 8) during the analogous material testing phase. This test had the most rigorous slurry flow conditions to guarantee the fastest wear, thus cutting down on the total testing time. Secondly, it also results in the highest mass loss values which reduce the overall uncertainty of the experiments. A decrease in the wear rate is observed in both test sections for the Al-6061 as seen in Figure 67. However, the magnitude of difference in the 3″ section is minimal compared to the overall wear rate reduction seen in the 2.5″ section. As seen before, the Al6061 exhibits different behavior based on the test section. It can still be concluded that at an equal velocity the polymer additives have reduced the overall wear of the material.

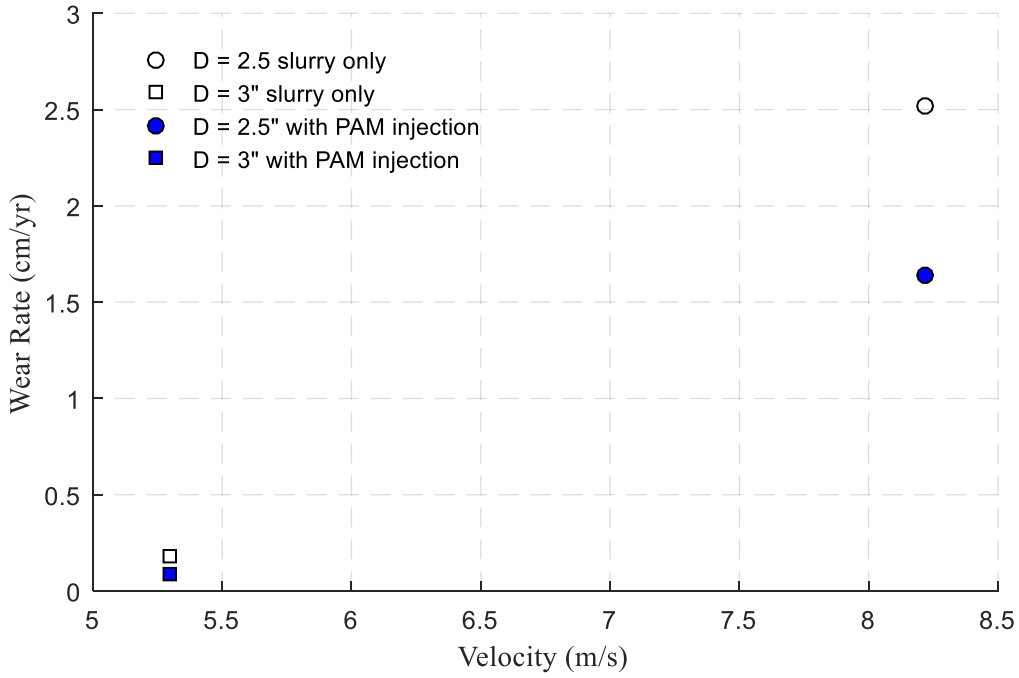

Figure 67: Wear Rate reduction of Al-6061 using 100 ppm polymers with a constant 2000 ppm solution injection at 2.5L/hr.

The PVC and carbon steel both show significant reduction in wear with the presence of polymers at both pipe diameters, and correspondingly, at two disntinct velocities. The wear rate continues to increase with the velocity as expected but the magnitude of both conditions are lower than the non-polymer counterparts. It is also observed that the amount of wear rate reduction between the two conditions are not equal despite an identical drag reduction at both test sections. These observations are displayed in Figure 68 and Figure 69.

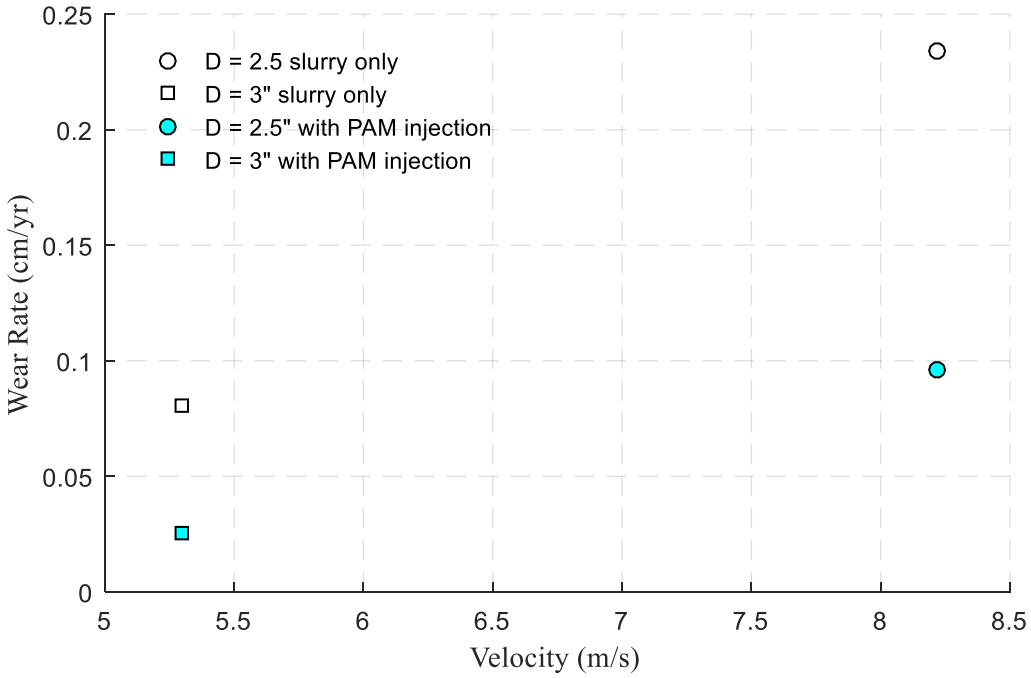

Figure 68: Wear Rate reduction of PVC using 100 ppm polymers with a constant 2000 ppm solution injection at 2.5 L/hr.

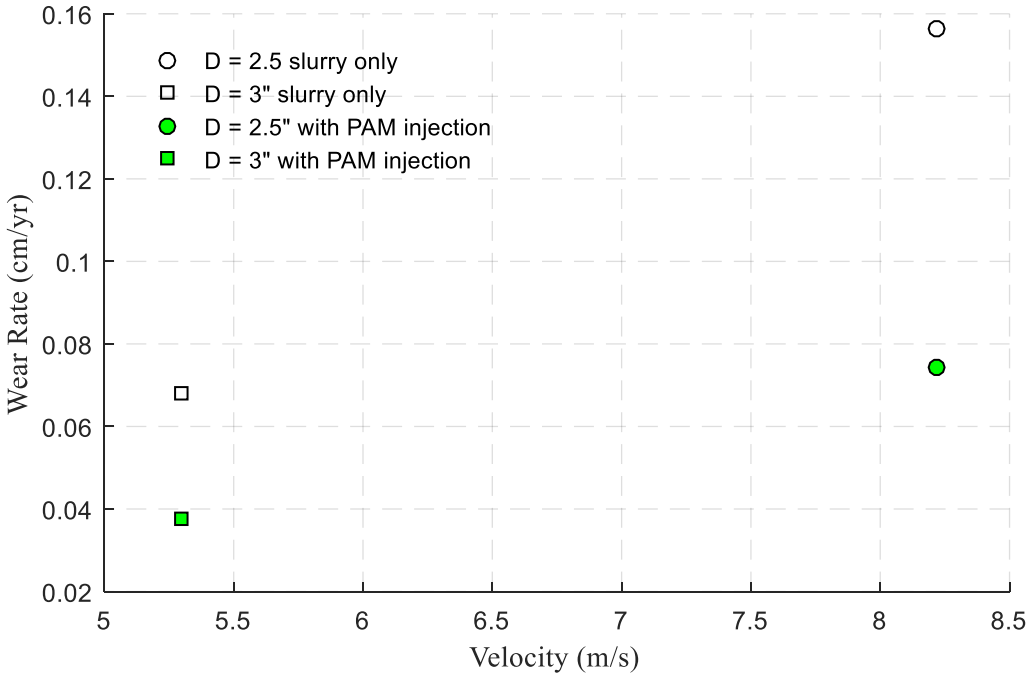

Figure 69: Wear Rate reduction of A106 Carbon Steel using 100 ppm polymers with a constant 2000 ppm solution injection at 2.5 L/hr.

The wear rate reduction was calculated for both the PVC and carbon steel and plotted against the corresponding velocity. Previously, it was determined that the PVC was a good fit as a substitute material to carbon steel for wear tests. Figure 70 is used to evaluate their effects during flow condition changes with the polymer additives. Based on the trends, each material has a different trend as the velocity of the test section increased; the wear rate of the PVC was reduced by 10% as the velocity increased from 5.3 to 8.2 m/s.

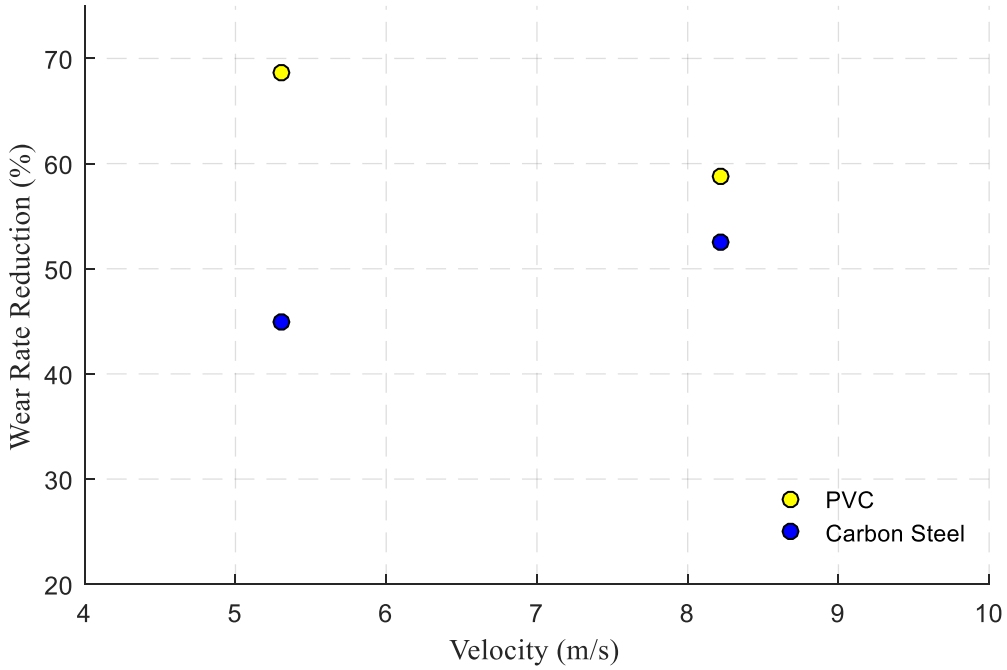

Figure 70: Comparison of Wear Rate Reduction between PVC and CS at different velocity conditions.

It is significant that the magnitude of wear rate reduction at this testing range is always larger for the PVC than the carbon steel. One of the reasons for this could be the component of friction reduction in the solid phase from the polymers. For example, the carbon steel may be more susceptible to high angle impacts compared to the PVC, and the PAM may reduce the vorticities in the flow thus reducing the probability of particle impacts directly at the wall. At higher velocities, the particles are more dispersed and may have a higher collision rate will the wall, this could be one of the reasons the carbon steel witnesses higher wear reduction at higher velocities. In contrast, the PVC may be more susceptible to the low impact angles, which tends to be prominent at the velocity ranges that have been tested, this is far more frequent than large angle impacts and therefore could cause higher wear rate reductions. Regardless of the mechanistic behavior of the flow after the polymer additives, the PAM is notably reducing the wear and thus the impacts of the particles are also reduced.

6.3 Summary

PAM polymer additives have been added to slurry in both the TCD and the SRC pipe flow loop. The TCD tests required the use of fine particles to avoid any particle settling, however, the negatively charged polymers caused flocculation and resulted in drag increase. The pipe flow wear tests were run with a PAM injection rate of 6 g/hr to avoid any mechanical degradation; this held the total polymer concentration in the slurry at approximately 100 ppm. The results showed that A106 carbon steel, PVC and Al6061-T6 all showed significant reduction in wear rates with the presence of polymers. Pipe wear reduction is therefore possible with the use of polymer additives.

7 Conclusions and Future Works

The purpose of this study was broken down into three sections. The first component was an in depth study of PAM polymers and their effectiveness in single phase flow; this was carried out both in Taylor Couette flow and pipe flow. The second stage of the study investigated the commonality and differences of different materials' wear characteristics at different flow conditions. This analogous material testing was conducted to find a suitable replacement material to carbon steel for erosion experiments in an attempt to reduce costs and testing times. An initial screen test was implemented in a Toroid Wheel tester, and 300 hour tests at a large bracket of flow conditions were conducted at the SRC Pipe Centre pilot scale flow loop. The final component of the tests utilized the PAM polymers in stage one at the equivalent testing conditions in stage two, in an attempt to observe whether DRAs such as the PAM polymer reduced the overall wear rate of pipe materials.

7.1 Wear Rate Patterns for Analogous Material Testing

In order to reduce the testing time of lengthy erosion experiments, one of the objectives of the study was to find a substitute material to carbon steel. Using a Toroid Wheel Tester, three materials were compared at two distinctly different flow conditions, one highly dominated by coulombic friction, and the other dominated by impact. The three materials were polyurethane coating, Al6061-T6 alloy, and A53 carbon steel. From the wear rate trends found from the TWT tests, it was clear that polyurethane coating was not a usable substitute to steel for wear tests, but Al 6061 alloy shared similar erosive patterns to its carbon steel counterpart. Once the PU coating was eliminated from the testing matrix, it was replaced with PVC in the next phase of testing that utilized a pilot scale pipe loop to recreate industrial slurry flow conditions.

The SRC Two-Layer model was implemented to calculate the solids friction (both kinematic and coulombic) of the slurry at the operating condition in order to find a trend for the wear rates measured from the pipe loop tests. The aluminum spools showed an initial plateau at which the wear rates did not change despite the increase in solids friction. Once the velocity surpassed a threshold of 5 m/s, there was a dramatic increase in wear rate, with a magnitude of 10 times that of the carbon steel. Due to these discrepancies, the aluminum is not recommended as a direct replacement for carbon steel during wear tests. The carbon steel and PVC pipes showed a linear wear rate increase in respect to the solids friction, however, the difference in sensitivity to the

solids friction was separable between the materials at solids frictions greater than 500 Pa/m (based on the SRC Two-Layer values). As a result the PVC would only yield a substantial reduction in testing times at rigorous testing conditions (velocities higher than 6 m/s). The final verdict was to recommend the PVC as a suitable replacement to carbon steel for pilot scale pipe flow loop tests.

7.2 Design of a Taylor Couette Device Setup

The TCD has been built for the purpose of running screening tests on a wide range of polymer additives to evaluate their drag reduction effectiveness. It also gives the ability to run suspensions and see their effects when polymers are introduced. The first step before these complex experiments can be attempted is to assess whether the TCD follows patterns and trends from past research studies and agrees with Taylor Couette Flow theory. Most baseline studies have used water as the working fluid and thus were done during this step for the current study. The TCD data consisted of the torque output based on the rotational speed. This data was normalized based on geometric and fluid parameters, and compared to previous works from Lewis and Swinney [63], Lathrop et al [65], Dubrulle and Hersant [64] and Bhambri [58]. It was found that the relationship between the torque and Reynolds number was similar; however there was higher magnitude in torque for both Bhambri and this current study. It was suggested that a large contributing factor to this is fluid that is present underneath the rotating cylinder which increases contact area and thus increases torque. It was also shown that a Von-Karman value of 0.38 fit the TCD data and could be deemed acceptable since it was 5% off the theoretical value. Finally, it was shown that the flow was always higher than the transitional Reynolds number for turbulence and followed the general trend of the turbulent best fit line between the torque scaling constant and Reynolds number, and therefore is in the correct turbulent regime.

7.3 Effect of Charge Density on Drag Reduction

A critical point for the anionic charge density was observed that resulted in the maximum drag reduction for PAM polymers of different molecular weights. This critical point occurred at a 30% anionic charge based on pilot scale flow loop tests conducted at the University of Alberta. This critical point occurs when the CD is high enough to keep the individual polymer chains from flocculating to retain homogeneity within the solution. At the same time the polymer is not excessive charged to avoid internal resistance that hinders the polymers' compressive length during its stretching process. This phenomenon of the CD was not seen once the tests were

conducted in the TC device; the magnitude of drag reduction was significantly lower compared to the pipe loop tests.

7.4 PAM Drag Reduction between TC Flow and Pipe Flow

One of the most apparent differences between pipe flow and TC flow was a significantly lower magnitude of drag reduction in the latter experiments. The PAM polymers did not have distinguishable performance differences in respect to the charge density in the TC device. In order to investigate this issue, sweeps at multiple operating speeds in both experimental setups were conducted. Analyzing turbulent flow characteristics such as the length scale and frictional Reynolds number of the two flows, it was discovered that TC flow had larger length and time scales. Due to this, the velocity fluctuations were lower than pipe flow resulting in an overall lower amount of TKE within the flow. Under these conditions, the polymers did not have enough absorbable energy at the boundary to reach their full stretching length. It was also found that a linear relationship between the turbulent length scale and drag reduction was present for the PAM polymers regardless of the experimental setup; this shows that operating the TC device at higher speeds may correspond to experiments directly comparable to the pipe flow performance.

7.5 Effect of Polymer Additives in Clay Suspension

PAM polymers have been added into a kaolin clay suspension within the in-house designed Taylor Couette Device. The use of clays were possible due to the 1 micron diameter, this allowed full suspension of the particles. However, due to a strong dominance of surface forces at a small diameter, specifically, it created positively charged particles. Due to the negative charge density of the polymer tails, this caused an electrical attraction, and thus lead to flocculation. The flocculated particles had a larger diameter and could not be suspended by the TC flow. At this condition, there was no drag reduction seen by the polymers. This is a potential risk with the use of negative charge density PAMs in flows with fine particles.

7.6 Effect of Polymer Additives on Wear Rate

Flexible polymers, PAMs, have been injected into a pilot scale wear test experiment that to evaluate whether wear rate reduction is present. Three different types of materials were used, the Al6061 alloy, A106 carbon steel and PVC, identical to the analogous material testing tests. Based on the mass measurements of the polymer additive tests, it was observed that significant wear

reduction was seen for all three materials. The magnitude of the wear reduction was between 50% towards 70% depending on the velocity and material type. Due to this significant amount of wear reduction, the use of polymer additives, specifically PAMs, are very useful for industrial applications in which the transport of slurries is required. Secondly, it was also verified that injection systems of a concentrated polymer is a feasible option to maintain a consistent drag reduction during pipeline conditions. The injection rate must be matched with the amount of polymers that degrade from the system, however in industrial applications pipelines are not closed loop and therefore injection will be required after some amount of pipe distance.

7.7 Future Works

Many of the objectives that were set at the start of this study have been completed with positive results; however, further investigations are necessary to fully understand the phenomenon observed. Firstly, more data is required to relate the wear rate of PVC and carbon steel before it can be used as a direct substitute for flow loop tests. These tests must include a multitude of flow conditions in which the velocity, slurry concentration, and particle sizes are manipulated. With a larger matrix of data, the response in the wear rate for each material can be modelled as a function of the manipulated variables; this allows for an empirical based equation that can correlate the PVC wear rate found in a test to an estimated CS wear rate within a reasonable amount of accuracy.

Future works are also required before a concrete method can be created that links the drag reduction effectiveness of a TC device to flow loop conditions. In these future experiments, different families of polymers need to be tested (such as alkaline PAMs, CMCs, XG, etc.) to evaluate their response as the turbulent scales change. In the case that some or all of these polymers show a linear change within their drag reduction as a function of the turbulent scales of the flow, methods of linearization and extrapolation can be used off faster TC flow experiments to predict the drag reduction performance at a given pipe flow condition with lower length scales.

Lastly, it was concluded that wear reduction with the presence of PAM polymers, however, the amount of data collected is limited. Further investigation is required to evaluate each material's specific response to the polymer. Trends such as the wear reduction against the slurry concentration, particle size, polymer concentration and flow conditions are all important in order to fully understand the effects of the polymers. In the current study, only PAM polymers were utilized, but it is still unknown if rigid polymers also show significant wear rate reduction.

Furthermore, the mechanism of the polymers that reduce the wear rate is also not fully understood yet. It is hypothesized that the polymers reduce the amount low angle impacts of particles against the pipes and the overall coulombic friction near the bottom wall of the pipe, however densitometry and PIV experiments during two-phase flow with polymer additives can be useful to drawing concrete conclusions.

8 References

[1] H. Bhabra, "Slurry pipeline now goes the distance," *World Pumps*, vol. 2013, no. 6, pp. 38–40, 2013.

[2] L. L. Parent and D. Y. Li, "Wear of hydrotransport lines in Athabasca oil sands," *Wear*, vol. 301, no. 1–2, pp. 477–482, 2013.

[3] R. S. Sanders, J. Schaan, R. Hughes, C. Shook, W. Crescent, and S. Albert, "Performance of sand slurry pipelines in the oil sands industry," *Can. J. Chem. Eng.*, vol. 82, no. August, pp. 850–857, 2004.

[4] G. I. Parslow and D. J. Stephenson, "Paint layer erosion resistance behaviour for use in a multilayer paint," vol. 212, pp. 103–109, 1997.

[5] C. Huang, P. Minev, J. Luo, and K. Nandakumar, "A phenomenological model for erosion of material in a horizontal slurry pipeline flow," *Wear*, vol. 269, no. 3–4, pp. 190–196, 2010.

[6] A. Fuhr, M. Krantz, and B. Fotty, "An investigation into developing slurry flow conditions and their effect on wear profiles using a pilot scale flow loop," in *BHR Group - 19th International Conference on Hydrotransport 2014*, 2014.

[7] S. El-sayed, "Measuring wall forces in a slurry pipeline," MSc Thesis, Department of Mechanical Engineering, University of Alberta, 2010.

[8] R. Cooke, G. Johnson, and P. Goosen, "Laboratory Apparatus for Evaluating Slurry Pipeline Wear," *Econ. Wear Mater.*, no. March, pp. 1–17, 2000.

[9] D. J. Loewen, "Characterization of Wear in a Laboratory-Scale Slurry Pipeline," MSc Thesis, Deparment of Mechanical Engineering, University of Alberta, Edmonton, 2013.

[10] R. G. Gillies and C. A. Shook, “Modelling high concentration settling slurry flows,” *Can. J. Chem. Eng.*, vol. 78, pp. 709–716, 2000.

[11] A. Sadighian, “Investigating Key Parameters Affecting Slurry Pipeline Erosion,” PhD Thesis, Chemical and Materials Engineering, University of Alberta, 2016.

[12] I. M. Hutchings, “A model for the erosion of metals by spherical particles at normal incidence,” *Elsevier Wear*, vol. 70, no. 3, pp. 269–281, 1981.

[13] A. Elkholy, “Prediction of abrasion wear for slurry pump materials,” *Elsevier Wear*, vol. 84, no. 1, pp. 39–49, 1983.

[14] A. V. Levy and G. Hickey, “Liquid-solid particle slurry erosion of steels,” *Elsevier Wear*, vol. 117, no. 2, pp. 129–146, 1987.

[15] G. R. Desale, B. K. Gandhi, and S. C. Jain, “Development of Correlations for Predicting the Slurry Erosion of Ductile Materials,” *J. Tribol.*, vol. 133, no. 3, p. 31603, 2011.

[16] Y. I. Oka, H. Ohnogi, T. Hosokawa, and M. Matsumura, “The impact angle dependence of erosion damage caused by solid particle impact,” *Wear*, vol. 203–204, pp. 573–579, 1997.

[17] S. L. Sinha, S. K. Dewangan, and A. Sharma, “A review on particulate slurry erosive wear of industrial materials: In context with pipeline transportation of mineral−slurry,” *Part. Sci. Technol.*, vol. 6351, no. April 2016, pp. 1–16, 2015.

[18] R. Gupta, S. N. Singh, and V. Seshadri, “Study on the uneven wear rate in a slurry pipeline,” *Bulk Solids Handl.*, vol. 15, no. 4, pp. 603–607, 1995.

[19] A. V. Levy and P. Chik, “The effects of erodent composition and shape on the erosion of steel,” *Elsevier Wear*, vol. 89, no. 2, pp. 151–162, 1983.

[20] G. R. Desale, B. K. Gandhi, and S. C. Jain, “Effect of erodent properties on erosion wear of ductile type materials,” *Elsevier Wear*, vol. 261, no. 7–8, pp. 914–921, 2006.

[21] G. R. Desale, B. K. Gandhi, and S. C. Jain, “Slurry erosion of ductile materials under normal impact condition,” *Elsevier Wear*, vol. 264, no. 3–4, pp. 322–330, 2008.

[22] Y. I. Oka, K. Okamura, and T. Yoshida, “Practical estimation of erosion damage caused by solid particle impact: Part 1: Effects of impact parameters on a predictive equation,” *Wear*, vol. 259, no. 1–6, pp. 95–101, 2005.

[23] P. C. Okonkwo, R. A. Shakoor, E. Ahmed, and A. M. A. Mohamed, “Erosive wear performance of API X42 pipeline steel,” *Eng. Fail. Anal.*, vol. 60, pp. 86–95, 2016.

[24] M. Antonov, J. Pirso, A. Vallikivi, D. Goljandin, and I. Hussainova, “The effect of fine erodent retained on the surface during erosion of metals, ceramics, plastic, rubber and hardmetal,” *Wear*, vol. 354–355, pp. 53–68, 2016.

[25] J. H. Neilson and A. Gilchrist, “Erosion by a stream of solid particles,” *Wear*, 1968.

[26] R. W. Lyczkowski and J. X. Bouillard, “State-of-the-art review of erosion modeling in fluid/solids systems,” *Prog. Energy Combust. Sci.*, vol. 28, no. 6, pp. 543–602, 2002.

[27] R. G. Gillies, C. A. Shook, and J. Xu, “Modelling Heterogeneous Slurry Flows at High Velocities,” *Can. J. Chem. Eng.*, vol. 82, no. 5, pp. 1060–1065, 2004.

[28] W. Tsai, J. A. C. Humphrey, I. Cornet, and A. V. Levy, “Experimental measurement of accelerated erosion in a slurry pot tester,” *Wear*, vol. 68, no. 3, pp. 289–303, 1981.

[29] B. Yu, D. Y. Li, and A. Grondin, “Effects of the dissolved oxygen and slurry velocity on erosion-corrosion of carbon steel in aqueous slurries with carbon dioxide and silica sand,” *Wear*, vol. 302, no. 1–2, pp. 1609–1614, 2013.

[30] H. M. Clark, “Specimen diameter, impact velocity, erosion rate and particle density in a slurry pot erosion tester,” *Wear*, vol. 162–164, no. Part B, pp. 669–678, 1993.

[31] A. A. Gadhikar, A. Sharma, D. B. Goel, and C. P. Sharma, “Fabrication and testing of slurry pot erosion tester,” *Trans. Indian Inst. Met.*, vol. 64, no. 4–5, pp. 493–500, 2011.

[32] S. S. Rajahram, T. J. Harvey, and R. J. K. Wood, “Electrochemical investigation of erosion-corrosion using a slurry pot erosion tester,” *Tribol. Int.*, vol. 44, no. 3, pp. 232–240, 2011.

[33] H. M. Clark, “Particle velocity and size effects in laboratory slurry erosion measurements OR do you know what your particles are doing?,” *Tribol. Int.*, vol. 35, no. 10, pp. 617–624, 2002.

[34] N. Ojala, K. Valtonen, P. Kivikytö-Reponen, P. Vuorinen, P. Siitonen, and V.-T. Kuokkala, “Effect of test parameters on large particle high speed slurry erosion testing,” *Tribol. - Mater. Surfaces Interfaces*, vol. 8, no. 2, pp. 98–104, 2014.

[35] R. J. K. Wood and T. F. Jones, “Investigations of sand-water induced erosive wear of AISI 304L stainless steel pipes by pilot-scale and laboratory-scale testing,” *Wear*, vol. 255, no. 1–6, pp. 206–218, 2003.

[36] B. K. Gandhi, S. N. Singh, and V. Seshadri, “A study on the effect of surface orientation on erosion wear of flat specimens moving in a solid-liquid suspension,” *Wear*, vol. 254, no. 12, pp. 1233–1238, 2003.

[37] Y. Xie, J. (Jimmy) Jiang, K. Y. Tufa, and S. Yick, “Wear resistance of materials used for slurry transport,” *Wear*, vol. 332–333, pp. 1104–1110, 2015.

[38] T. Alam and Z. N. Farhat, “Slurry Erosion of Pipeline Steel : Effect of Velocity and Microstructure,” *J. Tribol.*, vol. 138, no. 2, pp. 1–10, 2015.

[39] J. J. Tuzson, “Laboratory slurry erosion tests and pump wear rate calculations,” *J. Fluids Eng.*, vol. 106, no. 2, p. 135, 1984.

[40] H. M. Clark and R. J. Llewellyn, “Assessment of the erosion resistance of steels used for slurry handling and transport in mineral processing applications,” *Wear*, vol. 250–251, no. PART 1, pp. 32–44, 2001.

[41] Y. Xie, H. M. Clark, and H. . M. Hawthorne, “Modelling slurry particle dynamics in the Coriolis erosion tester,” *Wear*, vol. 225–229, pp. 405–416, 1999.

[42] N. R. Sarker, “A Preliminary Study of Slurry Pipeline Erosion Using a Toroid Wear Tester,” MSc Thesis, Department of Mechanical Engineering, University of Alberta, 2016.

[43] C. Y. Wong, C. Solnordal, L. Graham, G. Short, and J. Wu, “Slurry erosion of surface imperfections in pipeline systems,” *Wear*, vol. 336–337, pp. 72–85, 2015.

[44] C. S. Ramesh, R. Keshavamurthy, B. H. Channabasappa, and S. Pramod, “Influence of heat treatment on slurry erosive wear resistance of Al6061 alloy,” *Mater. Des.*, vol. 30, no. 9, pp. 3713–3722, 2009.

[45] E. D. Burger, “Studies of Drag Reduction Conducted over a Broad Range of Pipeline Conditions when Flowing Prudhoe Bay Crude Oil,” *J. Rheol. (N. Y. N. Y).*, vol. 24, no. 5, p. 603, 1980.

[46] J. L. Lumley, “Drag Reduction by Additives,” *Annu. Rev. Fluid Mech.*, vol. 1, no. 1, pp. 367–384, 1969.

[47] J. L. Lumley, “Drag reduction in turbulent flow by polymer additives,” *J. Polym. Sci. Macromol. Rev.*, vol. 7, no. 1, pp. 263–290, 1973.

[48] H. Choi, P. Moin, and J. Kim, “Active turbulence control for drag reduction in wall-bounded

flows," *J. Fluid Mech.*, vol. 262, no. A, pp. 75–110, 1994.

[49] C. M. White and M. G. Mungal, "Mechanics and Prediction of Turbulent Drag Reduction with Polymer Additives," *Annu. Rev. Fluid Mech.*, vol. 40, no. 1, pp. 235–256, 2008.

[50] P. G. Degennes and M. Tabor, "A cascade theory of drag reduction," *EPL*, vol. 2, no. 7, pp. 519–522, 1986.

[51] A. S. Monin, "Statistical Fluid Mechanics: The Mechanics of Turbulence," *Am. J. Phys.*, vol. 45, no. 10, p. 1010, 1977.

[52] K. R. Sreenivasan and C. M. White, "The onset of drag reduction by dilute polymer additives, and the maximum drag reduction asymptote," *J. Fluid Mech.*, vol. 409, pp. 149–164, 2000.

[53] T. Min, J. Yul Yoo, H. Choi, and D. D. Joseph, "Drag reduction by polymer additives in a turbulent channel flow," *J. Fluid Mech.*, vol. 486, pp. 213–238, 2003.

[54] D. L. Hunston and J. L. Zakin, "Flow-assisted degradation in dilute polystyrene solutions," *Polym. Eng. Sci.*, vol. 20, no. 7, pp. 517–523, 1980.

[55] H. J. Choi, C. A. Kim, J. I. Sohn, and M. S. Jhon, "Exponential decay function for polymer degradation in turbulent drag reduction," *Polym. Degrad. Stab.*, 2000.

[56] A. S. Pereira, R. M. Andrade, and E. J. Soares, "Drag reduction induced by flexible and rigid molecules in a turbulent flow into a rotating cylindrical double gap device: Comparison between Poly (ethylene oxide), Polyacrylamide, and Xanthan Gum," *J. Nonnewton. Fluid Mech.*, vol. 202, pp. 72–87, 2013.

[57] G. I. Taylor, "Stability of a Viscous Liquid Contained between Two Rotating Cylinders," *Philos. Trans. R. Soc. A Math. Phys. Eng. Sci.*, vol. 223, pp. 289–343, 1923.

[58] P. Bhambri, “Drag reduction using additives in a Taylor-Couette Flow,” MSc Thesis, Department of Mechanical Engineering, University of Alberta, 2016.

[59] S. Grossmann, D. Lohse, and C. Sun, “High–Reynolds Number Taylor-Couette Turbulence,” *Annu. Rev. Fluid Mech*, vol. 48, pp. 53–80, 2016.

[60] B. Eckhardt, S. Grossmann, and D. Lohse, “Torque scaling in turbulent Taylor–Couette flow between independently rotating cylinders,” *J. Fluid Mech.*, vol. 581, pp. 221–250, 2007.

[61] R. O. Monico, E. Van Der Poel, R. Verzicco, S. Grossmann, and D. Lohse, “Exploring the phase diagram of fully turbulent Taylor-Couette flow,” *J. Fluid Mech*, vol. 761, pp. 1–26, 2014.

[62] F. Wendt, “Turbulente Strömungen zwischen zwei rotierenden konaxialen Zylindern,” *Ingenieur-Archiv*, vol. 4(6), pp. 577–595, 1933.

[63] G. S. Lewis and H. L. Swinney, “Velocity structure functions, scaling, and transitions in high-Reynolds-number Couette-Taylor flow.,” *Phys. Rev. E*, vol. 59, no. 5B, pp. 5457–5467, 1999.

[64] B. Dubrulle and F. Hersant, “Momentum transport and torque scaling in Taylor-Couette flow from an analogy with turbulent convection,” *Eur. Phys. J. B*, vol. 26, no. 3, pp. 379–386, 2002.

[65] D. P. Lathrop, J. Fineberg, and H. L. Swinney, “Transition to shear-driven turbulence in Couette-Taylor flow,” *Phys. Rev. A*, vol. 46, no. 10, pp. 6390–6405, 1992.

[66] W. Abu Rowin, R. S. Sanders, and S. Ghaemi, “A Recipe for Optimum Mixing of Polymer Drag Reducers,” *J. Fluids Eng.*, vol. 140, no. November, pp. 1–10, 2018.

[67] V. S. Green, D. E. Stott, L. D. Norton, and J. G. Graveel, “Polyacrylamide molecular weight and charge effects on infiltration undersimulated rainfall,” *Soil Sci. Soc. Am. J.*, vol. 64, pp. 1786–1791, 2000.

[68] H. C. Hershey and J. L. Zakin, “Existence of two types of drag reduction in pipe flow of dilute polymer solutions,” *Ind. Eng. Chem. Fundam.*, vol. 6, no. 3, pp. 381–387, 1967.

[69] B. H. Zimm, “Dynamics of polymer molecules in dilute solution: Viscoelasticity, flow birefringence and dielectric loss,” *J. Chem. Phys.*, vol. 24, no. 2, pp. 269–278, 1956.

Appendix

A. Mass Loss Data

Table AP1: Mass loss data of test 1-1 at SRC

Sample#	Initial wt (g)	Interval #	Start (or Restart) Date & Time	Stop Date & Time	Semi-dry wt (g)	Final wt (g)
1-PVC-2.5	1010.06	1	29 Jan, 10:48	30 Jan, 10:38	1010.12	
		2	30 Jan, 11:31	2 Feb, 10:40	1009.61	1008.63
		3	5 Feb, 9:30	9 Feb, 13:30	1008.66	1007.94
		4	12 Feb, 9:00	16 Feb, 13:00	1007.97	1007.36
1-PVC-3	1308.83	1				
		2			1309.17	1308
		3			1308.44	1307.6
		4			1308	1307.24
1-Al-2.5	1841.22	1				
		2			1822.17	1821.87
		3			1811.79	1811.47
		4			1803.85	1803.52
1-Al-3	2374.1	1				
		2			2355.89	2355.45
		3			2347.69	2347.28
		4			2342.54	2342.07
1-CS-2.5	5.286 kg	1				
		2			5.282	5.281
		3			5.279	5.279
		4			5.277	5.276
1-CS-3	6.737 kg	1				
		2			6.731	6.729
		3			6.727	6.727
		4			6.726	6.725

Table AP2: Mass loss data of test 1-2 at SRC

Sample#	Initial wt (g)	Interval #	Start (or Restart) Date & Time	Stop Date & Time	Semi-dry wt (g)	Final wt (g)
1-PVC-2.5	1010.69	1	20-Feb-18	23-Feb-18	1009.02	1008.5
		2	26-Feb-18	2-Mar-18	1006.73	1006.21
		3	5-Mar-18	9-Mar-18	1004.6	1004.02
		4				
1-PVC-3	1300.01	1			1300.15	1299.73
		2			1299.16	1298.54
		3			1298.44	1297.72
		4				
1-Al-2.5	1837.62	1			1802.75	1802.56
		2			1764.94	1764.89
		3			1728.46	1728.17
		4				
1-Al-3	2368.6	1			2365.76	2365.45
		2			2362.4	2362.01
		3			2359.67	2358.68
		4				
1-CS-2.5	5.086 kg	1			5.078	5.078
		2			5.071	5.071
		3			5.065	5.064
		4				
1-CS-3	6.967 kg	1			6.958	6.958
		2			6.954	6.954
		3			6.952	6.951
		4				

Table AP3: Mass loss data of test 1-3 at SRC

Sample#	Initial wt (g)	Interval #	Start (or Restart) Date & Time	Stop Date & Time	Semi-dry wt (g)	Final wt (g)
1-PVC-2.5	1022.83	1	12-Mar-18	16-Mar-18	1019	1018.28
		2	19-Mar-18	23-Mar-18	1014.77	1014.02
		3				
1-PVC-3	1307.38	1			1306.52	1305.43
		2			1304.44	1303.63
		3				
1-Al-2.5	1841.18	1			1745.18	1744.91
		2			1658.43	1658.18
		3				
1-Al-3	2378.43	1			2371.01	2370.66
		2			2363.11	2362.56
		3				
1-CS-2.5	5.035 kg	1			5.02	5.019
		2			5.003	5.002
		3				
1-CS-3	6.701 kg	1			6.686	6.685
		2			6.676	6.676
		3				

Table AP4: Mass loss data of test 2-1 at SRC

Material	Initial Weight (g)	Final Weight wet (g)	Final Weight Dry (g)
PVC 2.5	1015.15	1013.87	1013.30
PVC 3	1301.7	1301.68	1301.1
Al 2.5	1803.27	1742.89	1742.75
Al 3	2368.2	2364.29	2364.1
CS 2.5	5018	5010	5010
CS 3	6754	6750	6749
CS 2.5 Rep	5030	5021	5021
CS 3 Rep	6611	6607	6607

B. Viscosity and Dissolved Oxygen Data

Table AP5: Viscosity and DO data of test 1-1 at SRC

Time (hours)	Viscosity (mPa·s)	DO (ppm)
0.5	1.04	1.07
4.25	1.14	0.66
21.33361	1.2	0.23
26.91694	1.22	0.19
43.83361	1.33	0.19
50.75028	1.29	0.19
67.91944	1.36	0.19
74.83611	1.34	0.23
91.83611	1.3	0.14
96.51889	1.1	2.57
120.5192	1.2	0.14
144.3844	1.19	0.14
168.3847	1.09	0.16
192.3414	1.15	0.24
195.5097	1.08	3.11
220.7597	1.13	0.11
243.5097	1.18	0.09
267.9264	1.17	0.1
291.5097	1.23	0.15

Table AP6: Viscosity and DO data of test 1-2 at SRC

Time (hours)	Viscosity (mPa·s)	DO (ppm)
0.838889	1.21	0.27
24.92222	1.6	0.12
53.75583	1.22	0.12
72.83917	1.24	0.12
77.50917	1.22	0.13
101.7592	1.52	0.11
125.9264	1.25	0.1
149.7597	1.25	0.1
177.1775	1.16	0.16
201.1778	1.33	0.12
225.2297	1.17	0.12
249.3964	1.19	0.12
273.2828	1.21	0.1

Table AP7: Viscosity and DO data of test 1-3 at SRC

Time (hours)	Viscosity (mPa·s)	DO (ppm)
0.835833	1.26	0.02
5.7525	1.72	0.11
24.7525	1.68	0.12
29.83583	1.82	0.11
48.83583	2.85	0.11
53.75278	1.39	0.1
74.33611	1.24	0.17
98.09083	1.25	0.12
120.1742	1.12	0.18
144.5911	1.18	0.52
168.2578	1.18	0.66
192.0078	1.24	0.43

C. Pressure Loss U of A Pipe Loop

Table AP8: Pressure Drop Data of Product # LN3475-1 (at 50 ppm)

Time (mins)	Average ΔP (psi)	Std (psi)
0-10	0.034538103	0.001426
11-20	0.036394344	0.001188
21-30	0.038807324	0.001127
31-40	0.040247592	0.00105
41-50	0.041469058	0.00098
51-60	0.04240084	0.000869
61-70	0.043333621	0.000918
71-80	0.04427106	0.000871
81-90	0.045004672	0.000858
91-100	0.045581879	0.000823
101-110	0.046385042	0.001433
111-120	0.047201849	0.000836

Table AP9: Pressure Drop Data of Product # LN3475-1 (at 100 ppm)

Time (mins)	Average ΔP (psi)	Std (psi)
0-10	0.031743	0.001542
11-20	0.03367	0.001361
21-30	0.03475	0.001262
31-40	0.035626	0.001262
41-50	0.036493	0.001159
51-60	0.036973	0.001066
61-70	0.037424	0.001115
71-80	0.037906	0.001098
81-90	0.038351	0.001107
91-100	0.038731	0.001119
101-110	0.039104	0.001041
111-120	0.039476	0.001043

Table AP10: Pressure Drop Data of Product # LN3475-2 (at 50 ppm)

Time (mins)	Average ΔP (psi)	Std (psi)
0-10	0.0352391	0.0012476
11-20	0.03719251	0.0011234
21-30	0.03871498	0.0011106
31-40	0.0399594	0.0009742
41-50	0.04091897	0.0009281
51-60	0.04188686	0.0009448
61-70	0.0427594	0.0009323
71-80	0.04351498	0.0008933
81-90	0.04416839	0.0008323
91-100	0.04487354	0.0008362
101-110	0.04552812	0.0008232
111-120	0.04613328	0.0007917

Table AP11: Pressure Drop Data of Product # LN3475-2 (at 100 ppm)

Time (mins)	Average ΔP (psi)	Std (psi)
0-10	0.0322913	0.0014209
11-20	0.0334498	0.0012556
21-30	0.0343619	0.0012425
31-40	0.035186	0.0011415
41-50	0.0358587	0.0011557
51-60	0.0364123	0.0011604
61-70	0.0369775	0.001024
71-80	0.0374982	0.0010301
81-90	0.0379353	0.0010503
91-100	0.0383205	0.0010685
101-110	0.0386814	0.0010066
111-120	0.0391058	0.0010126

Table AP12: Pressure Drop Data of Product # LN3475-3 (at 50 ppm)

Time (mins)	Average ΔP (psi)	Std (psi)
0-10	0.0354577	0.0013846
11-20	0.0376802	0.0011221
21-30	0.0392414	0.0010481
31-40	0.0405123	0.0009634
41-50	0.0416032	0.0009179
51-60	0.0425111	0.0009319
61-70	0.0432854	0.0008891
71-80	0.0440854	0.0008299
81-90	0.0447862	0.0008923
91-100	0.0454223	0.0008396
101-110	0.046016	0.0007706
111-120	0.0465887	0.0007981

Table AP13: Pressure Drop Data of Product # LN3475-3 (at 100 ppm)

Time (mins)	Average ΔP (psi)	Std (psi)
0-10	0.0321328	0.0015313
11-20	0.0334927	0.0013899
21-30	0.0344288	0.0012927
31-40	0.0352509	0.0011896
41-50	0.0359624	0.0011757
51-60	0.0365265	0.0011531
61-70	0.0370832	0.0012128
71-80	0.0376143	0.001142
81-90	0.0380556	0.0010393
91-100	0.0384621	0.0010815
101-110	0.0388965	0.0011205
111-120	0.0393093	0.001048

Table AP14: Pressure Drop Data of Product # LN3475-4 (at 50 ppm)

Time (mins)	Average ΔP (psi)	Std (psi)
0-10	0.0375369	0.001463
11-20	0.040525	0.0011835
21-30	0.042691	0.001045
31-40	0.0444007	0.0010047
41-50	0.0457471	0.0009247
51-60	0.0469616	0.000857
61-70	0.0480218	0.0008631
71-80	0.0489083	0.0008138
81-90	0.0498223	0.0008037
91-100	0.0506429	0.0007023
101-110	0.0513446	0.0007609
111-120	0.0520123	0.0007241

Table AP15: Pressure Drop Data of Product # LN3475-4 (at 100 ppm)

Time (mins)	Average ΔP (psi)	Std (psi)
0-10	0.0340636	0.001264
11-20	0.0358319	0.0011251
21-30	0.0371469	0.0010431
31-40	0.038222	0.0009407
41-50	0.0390671	0.0009453
51-60	0.0399646	0.0009481
61-70	0.0406569	0.0009348
71-80	0.0413072	0.0009328
81-90	0.0419123	0.0008498
91-100	0.0424789	0.0008182
101-110	0.0429854	0.000791
111-120	0.0434953	0.0008207

Table AP16: Pressure Drop Data of Product # LN3475-5 (at 50 ppm)

Time (mins)	Average ΔP (psi)	Std (psi)
0-10	0.0363772	0.0012495
11-20	0.0388649	0.0010482
21-30	0.0407158	0.0009534
31-40	0.0422223	0.0008608
41-50	0.0435106	0.000831
51-60	0.0446002	0.0007561
61-70	0.0455574	0.0007912
71-80	0.0464799	0.0007389
81-90	0.0472933	0.0007678
91-100	0.0480246	0.0007233
101-110	0.0487075	0.0007259
111-120	0.0494027	0.0007036

Table AP17: Pressure Drop Data of Product # LN3475-5 (at 100 ppm)

Time (mins)	Average ΔP (psi)	Std (psi)
0-10	0.0341922	0.0011931
11-20	0.0355656	0.0010485
21-30	0.0367601	0.0009607
31-40	0.0378131	0.0010007
41-50	0.0386622	0.0008745
51-60	0.0394512	0.0008209
61-70	0.0401882	0.0008657
71-80	0.0408502	0.0008133
81-90	0.0414527	0.000815
91-100	0.0420649	0.0008
101-110	0.042575	0.000791
111-120	0.0431213	0.000786

Table AP18: Pressure Drop Data of Product # LN3475-6 (at 50 ppm)

Time (mins)	Average ΔP (psi)	Std (psi)
0-10	0.0352606	0.0015635
11-20	0.0381599	0.0012232
21-30	0.0401807	0.001118
31-40	0.041782	0.0009874
41-50	0.0431517	0.0009569
51-60	0.0443359	0.0009525
61-70	0.0454126	0.0009534
71-80	0.046385	0.0008288
81-90	0.0472324	0.0008652
91-100	0.0480589	0.0007908
101-110	0.0487709	0.0008085
111-120	0.0495077	0.0007777

Table AP19: Pressure Drop Data of Product # LN3475-6 (at 100 ppm)

Time (mins)	Average ΔP (psi)	Std (psi)
0-10	0.0333256	0.0010911
11-20	0.0343629	0.0009327
21-30	0.0352146	0.0009141
31-40	0.0360128	0.0010301
41-50	0.0369566	0.0009552
51-60	0.0376261	0.0008968
61-70	0.0382318	0.0009347
71-80	0.0387609	0.0009238
81-90	0.039318	0.0008808
91-100	0.039789	0.0008776
101-110	0.0402812	0.0008627
111-120	0.0407226	0.0008781

Table AP20: Pressure Drop Data of Product # MT2239-1 (at 50 ppm)

Time (mins)	Average ΔP (psi)	Std (psi)
0-10	0.0493812	0.0008316
11-20	0.0514418	0.0006582
21-30	0.0526659	0.0005403
31-40	0.0535156	0.0005132
41-50	0.054214	0.000534
51-60	0.0547943	0.0004858
61-70	0.0553156	0.0005135
71-80	0.0557832	0.0004854
81-90	0.0561552	0.0005077
91-100	0.0565644	0.0005031
101-110	0.0568494	0.0004587
111-120	0.0570952	0.0004733

Table AP21: Pressure Drop Data of Product # MT2239-2 (at 50 ppm)

Time (mins)	Average ΔP (psi)	Std (psi)
0-10	0.0449393	0.0007498
11-20	0.0466666	0.0005731
21-30	0.0478308	0.0005141
31-40	0.0488043	0.0004731
41-50	0.0494333	0.0004356
51-60	0.0500912	0.0004146
61-70	0.0505702	0.0004053
71-80	0.0510819	0.0004368
81-90	0.0515705	0.0004028
91-100	0.0518852	0.000443
101-110	0.0523042	0.0003839
111-120	0.05258	0.0003873

Table AP22: Pressure Drop Data of Product # MT2239-3 (at 50 ppm)

Time (mins)	Average ΔP (psi)	Std (psi)
0-10	0.0371361	0.0010565
11-20	0.0394271	0.0008557
21-30	0.041023	0.0007109
31-40	0.0422604	0.0006368
41-50	0.0432314	0.0006183
51-60	0.0440567	0.0005944
61-70	0.0447255	0.0005376
71-80	0.0454106	0.00057
81-90	0.0460401	0.0005835
91-100	0.046594	0.0005462
101-110	0.0470358	0.0005318
111-120	0.0474913	0.0005347

Table AP23: Pressure Drop Data of Product # MT2232-1 (at 50 ppm)

Time (mins)	Average ΔP (psi)	Std (psi)
0-10	0.0321414	0.0010458
11-20	0.0342338	0.0008402
21-30	0.0356679	0.0008079
31-40	0.0368982	0.0007319
41-50	0.0379617	0.000712
51-60	0.038797	0.0006743
61-70	0.0395156	0.0006314
71-80	0.0401514	0.0006068
81-90	0.0407531	0.0006317
91-100	0.0412975	0.0006179
101-110	0.0418338	0.0006303
111-120	0.0423067	0.0005731

Table AP24: Pressure Drop Data of Product # MT2232-1 (at 100 ppm)

Time (mins)	Average ΔP (psi)	Std (psi)
0-10	0.0295925	0.0012088
11-20	0.0313015	0.0009836
21-30	0.032383	0.0008758
31-40	0.0332301	0.0008844
41-50	0.0339311	0.0008601
51-60	0.0346	0.0008656
61-70	0.035205	0.0008167
71-80	0.0356762	0.0007795
81-90	0.0361163	0.0007525
91-100	0.0365707	0.000779
101-110	0.0369408	0.0007544
111-120	0.0373579	0.000756

Table AP25: Pressure Drop Data of Product # MT2232-2 (at 50 ppm)

Time (mins)	Average ΔP (psi)	Std (psi)
0-10	0.0312972	0.0011439
11-20	0.0333639	0.0009255
21-30	0.0347689	0.0008196
31-40	0.0357561	0.0007547
41-50	0.0362968	0.0007329
51-60	0.037071	0.0006867
61-70	0.0378286	0.0006611
71-80	0.0384892	0.0006299
81-90	0.039084	0.0006299
91-100	0.0396917	0.0006149
101-110	0.0402173	0.000673
111-120	0.0407384	0.000596

Table AP26: Pressure Drop Data of Product # MT2232-2 (at 100 ppm)

Time (mins)	Average ΔP (psi)	Std (psi)
0-10	0.0283569	0.0012296
11-20	0.0298449	0.0010005
21-30	0.030904	0.0009155
31-40	0.0316141	0.0008864
41-50	0.0322722	0.0009056
51-60	0.032774	0.0008783
61-70	0.0332879	0.0008488
71-80	0.0337684	0.0008412
81-90	0.0341962	0.0007946
91-100	0.0345466	0.0008104
101-110	0.034918	0.0007623
111-120	0.0352938	0.0008339

Table AP27: Pressure Drop Data of Product # MT2232-3 (at 50 ppm)

Time (mins)	Average ΔP (psi)	Std (psi)
0-10	0.0300343	0.0013037
11-20	0.0323304	0.0009925
21-30	0.0338903	0.0008472
31-40	0.0350875	0.0007916
41-50	0.0360113	0.0008094
51-60	0.0369018	0.0007285
61-70	0.0375913	0.0007564
71-80	0.0382611	0.000675
81-90	0.0388752	0.0006772
91-100	0.0394062	0.0007021
101-110	0.0399646	0.0006672
111-120	0.0404521	0.0006135

Table AP28: Pressure Drop Data of Product # MT2232-3 (at 100 ppm)

Time (mins)	Average ΔP (psi)	Std (psi)
0-10	0.0282118	0.0013898
11-20	0.0296654	0.0010962
21-30	0.0306403	0.0009532
31-40	0.0313611	0.0009116
41-50	0.0319626	0.0009224
51-60	0.0324877	0.0008441
61-70	0.0329714	0.0008108
71-80	0.03338	0.0008175
81-90	0.0337795	0.0007582
91-100	0.0342413	0.0007913
101-110	0.0345874	0.000791
111-120	0.0349368	0.0007557

Table AP29: Pressure Drop Data of Product # MT2232-4 (at 50 ppm)

Time (mins)	Average ΔP (psi)	Std (psi)
0-10	0.0299857	0.0010063
11-20	0.0315165	0.0009241
21-30	0.0328146	0.0008349
31-40	0.0338642	0.0008403
41-50	0.0347682	0.0007583
51-60	0.0355634	0.0007501
61-70	0.0363414	0.0007484
71-80	0.0369539	0.0006541
81-90	0.0375957	0.0006683
91-100	0.0382101	0.0007072
101-110	0.0387559	0.0006463
111-120	0.0392691	0.0006639

Table AP30: Pressure Drop Data of Product # MT2232-4 (at 100 ppm)

Time (mins)	Average ΔP (psi)	Std (psi)
0-10	0.028926	0.001014
11-20	0.0296629	0.0009445
21-30	0.0303759	0.0009136
31-40	0.0310073	0.0008748
41-50	0.0315403	0.0008658
51-60	0.032075	0.0009032
61-70	0.0325566	0.0008162
71-80	0.0329606	0.0007948
81-90	0.0333211	0.0008088
91-100	0.0337411	0.0007863
101-110	0.0340817	0.0007891
111-120	0.0344133	0.000735

Table AP31: Pressure Drop Data of Product # MT2232-5 (at 50 ppm)

Time (mins)	Average ΔP (psi)	Std (psi)
0-10	0.0297867	0.0009768
11-20	0.0313735	0.0008831
21-30	0.0326657	0.0008081
31-40	0.0337121	0.0007815
41-50	0.0346156	0.0007392
51-60	0.0354549	0.0007508
61-70	0.0361705	0.000666
71-80	0.0368424	0.0006735
81-90	0.0374755	0.0006556
91-100	0.0380629	0.0006424
101-110	0.0385804	0.00064
111-120	0.0391223	0.000622

Table AP32: Pressure Drop Data of Product # MT2232-5 (at 100 ppm)

Time (mins)	Average ΔP (psi)	Std (psi)
0-10	0.0286188	0.0011081
11-20	0.0293291	0.0009496
21-30	0.0300215	0.0009168
31-40	0.0305922	0.0008748
41-50	0.0310937	0.0008864
51-60	0.0315789	0.0008068
61-70	0.0319995	0.0008112
71-80	0.0323522	0.0007975
81-90	0.032777	0.0008444
91-100	0.0330869	0.0008218
101-110	0.0334444	0.0008084
111-120	0.0337496	0.0008067

Table AP33: Pressure Drop Data of Product # MT2232-6 (at 50 ppm)

Time (mins)	Average ΔP (psi)	Std (psi)
0-10	0.0290599	0.0010842
11-20	0.0302077	0.0008913
21-30	0.0312501	0.0008955
31-40	0.0322276	0.000857
41-50	0.0330238	0.0008075
51-60	0.0337809	0.0007827
61-70	0.0344406	0.0007743
71-80	0.0350381	0.0007102
81-90	0.0356426	0.0007231
91-100	0.0362095	0.0006644
101-110	0.0367053	0.0006609
111-120	0.0372502	0.0006817

Table AP34: Pressure Drop Data of Product # MT2232-6 (at 100 ppm)

Time (mins)	Average ΔP (psi)	Std (psi)
0-10	0.0268353	0.0014174
11-20	0.0279581	0.0011232
21-30	0.0285719	0.0010795
31-40	0.0290594	0.001021
41-50	0.0295221	0.0009323
51-60	0.0299546	0.0009392
61-70	0.0303265	0.0008932
71-80	0.0306145	0.0009643
81-90	0.0309285	0.0008676
91-100	0.0312496	0.0008913
101-110	0.0316396	0.0008569
111-120	0.0319256	0.0008684

Table AP35: Pressure Drop Data of Product # MT2232-7 (at 50 ppm)

Time (mins)	Average ΔP (psi)	Std (psi)
0-10	0.0349737	0.0013514
11-20	0.0383286	0.0009922
21-30	0.0406331	0.0007999
31-40	0.0423661	0.0007412
41-50	0.043722	0.0006636
51-60	0.0448973	0.0006237
61-70	0.045913	0.0005786
71-80	0.0468378	0.0005595
81-90	0.0476842	0.0005233
91-100	0.0484564	0.0005238
101-110	0.0491517	0.0005283
111-120	0.0498364	0.0005317

Table AP36: Pressure Drop Data of Product # MT2232-7 (at 100 ppm)

Time (mins)	Average ΔP (psi)	Std (psi)
0-10	0.0308666	0.0010888
11-20	0.0327719	0.0009567
21-30	0.0342541	0.0007996
31-40	0.0355007	0.0007449
41-50	0.0364705	0.0007326
51-60	0.0373654	0.0006956
61-70	0.0381933	0.0006694
71-80	0.0389203	0.0006383
81-90	0.0395862	0.0006244
91-100	0.0401652	0.0006108
101-110	0.040728	0.0006202
111-120	0.0412835	0.0006195

Table AP37: Pressure Drop Data of Product # MT2232-8 (at 50 ppm)

Time (mins)	Average ΔP (psi)	Std (psi)
0-10	0.0339451	0.0015132
11-20	0.0375679	0.0009857
21-30	0.0398512	0.000833
31-40	0.0416814	0.0007139
41-50	0.0430418	0.0006186
51-60	0.0442849	0.0006542
61-70	0.045377	0.0006151
71-80	0.046202	0.0005481
81-90	0.0468514	0.000623
91-100	0.0478634	0.000565
101-110	0.0486176	0.0005646
111-120	0.0493933	0.0005402

Table AP38: Pressure Drop Data of Product # MT2232-8 (at 100 ppm)

Time (mins)	Average ΔP (psi)	Std (psi)
0-10	0.0309033	0.001099
11-20	0.0328912	0.0009469
21-30	0.0343048	0.0008401
31-40	0.0354329	0.0007641
41-50	0.0363676	0.0007451
51-60	0.0371388	0.0006998
61-70	0.0378671	0.0006745
71-80	0.0385419	0.0006947
81-90	0.0391409	0.0006248
91-100	0.0396765	0.0006556
101-110	0.0401639	0.0006631
111-120	0.0406765	0.0006343

Table AP39: Pressure Drop Data of Product # MT2232-9 (at 50 ppm)

Time (mins)	Average ΔP (psi)	Std (psi)
0-10	0.0335532	0.001574
11-20	0.0371413	0.0010152
21-30	0.0394604	0.0008102
31-40	0.0412253	0.0007485
41-50	0.0426253	0.0006625
51-60	0.0438203	0.0006299
61-70	0.0448318	0.0005897
71-80	0.0457547	0.000587
81-90	0.0465825	0.0005956
91-100	0.0473927	0.0005717
101-110	0.048075	0.000551
111-120	0.0487306	0.0005693

Table AP39: Pressure Drop Data of Product # MT2232-9 (at 100 ppm)

Time (mins)	Average ΔP (psi)	Std (psi)
0-10	0.0301078	0.0010791
11-20	0.0322429	0.000971
21-30	0.0338461	0.0008074
31-40	0.0349859	0.0007672
41-50	0.0359865	0.0007765
51-60	0.0368438	0.0007297
61-70	0.0376266	0.0006949
71-80	0.0383045	0.0006627
81-90	0.0389368	0.0006651
91-100	0.0395133	0.0006407
101-110	0.0400411	0.0006754
111-120	0.0405639	0.0006535

Table AP40: Pressure Drop Data of Product MT2232-1 at different flow rates (at 100 ppm)

Q (L/s)	Average ΔP (psi)	Std (psi)
2.084	0.014403268	0.0009231
2.78	0.021393678	0.0009806
4.865	0.039940385	0.0013951

D. Pressure Loss from SRC Pipe Loop

Table AP41: Pressure Drop of Slurry flow (Test 1-1)

Average Pressure Loss at D=2.5" (kPa/m)	Std (kPa/m)	Average Pressure Loss at D=3" (kPa/m)	Std (kPa/m)
2.0527	0.1267	0.7446	0.0855

Table AP42: Pressure Drop of Slurry flow (Test 1-2)

Average Pressure Loss at D=2.5" (kPa/m)	Std (kPa/m)	Average Pressure Loss at D=3" (kPa/m)	Std (kPa/m)
6.3798	0.2137	2.5352	0.1790

Table AP43: Pressure Drop of Slurry flow (Test 1-3)

Average Pressure Loss at D=2.5" (kPa/m)	Std (kPa/m)	Average Pressure Loss at D=3" (kPa/m)	Std (kPa/m)
10.2256	0.1607	4.2367	0.0273

Table AP44: Pressure Drop of ALKAPAM in water only using SRC Loop (with injection)

Mag Flowrate (L/s)	3" TS dP/L (kPa/m)	2.5" TS dP/L (kPa/m)
30.91	3.6755	10.0008
28.98	3.2489	8.8438
26.34	2.7188	7.3563
24.01	2.3059	6.2241
21.68	1.9177	5.2344
19.29	1.5435	4.1572
16.87	1.2065	3.2006
14.38	0.8995	2.391
12.17	0.6604	1.7203
9.71	0.4337	1.1215
7.12	0.2443	0.6093
4.77	0.1132	0.2626
2.36	0.0231	0.0283

Table AP45: Pressure Drop of Slurry flow with ALKAPAM Injection (Test 2-1)

Average Pressure Loss at D=2.5" (kPa/m)	Std (kPa/m)	Average Pressure Loss at D=3" (kPa/m)	Std (kPa/m)
7.6405	0.0778	3.2562	0.0416

Table AP46: Pressure Drop of Slurry flow with ALKAPAM Injection stopped after 56 mins

Time (mins)	3" TS dP/L (kPa/m)	2.5" TS dP/L (kPa/m)	
0-14	3.291	7.925	
15-28	3.279	7.864	
29-42	3.277	7.830	
43-56	3.279	7.825	Injection stopped
57-70	3.280	7.777	
71-84	3.282	7.776	
85-98	3.287	7.766	
99-112	3.288	7.756	
113-126	3.291	7.752	
127-140	3.286	7.712	

E. Inputs for SRC Two Layer Model

Table AP46: SRC Two Layer Model inputs (all concentrations used are *in-situ*)

Mixture Volumetric Flowrate (m^3/s)	Pipe Internal Diameter (m)	Pipe Wall Roughness (mm)	Pipeline Slope (degrees)	**Coarse Solids Volume Fraction in:**		Coarse Particle Properties:		Carrier Properties:	
				Settled Bed	Mixture	Density (kg/m^3)	d_{50} (mm)	Density (kg/m^3)	Viscosity ($mPa \cdot s$)
0.01104	0.063	0.05	0.00	0.63	0.200	2650	0.25	998	0.89
0.01104	0.078	0.05	0.00	0.63	0.200	2650	0.25	998	0.89
0.01988	0.063	0.05	0.00	0.63	0.300	2650	0.25	998	0.89
0.01988	0.078	0.05	0.00	0.63	0.300	2650	0.25	998	0.89
0.02538	0.063	0.05	0.00	0.63	0.300	2650	0.25	998	0.89
0.02538	0.078	0.05	0.00	0.63	0.300	2650	0.25	998	0.89

F. Taylor Couette Tests Raw Data

Table AP47: Torque data from TC device at 500 rpm with polymer solutions

Product #	Torque Average (Nm)	Std (Nm)
MT2232-1	0.2174	0.0109
MT2232-2	0.2209	0.0177
MT2232-3	0.2163	0.0151
MT2232-4	0.2310	0.0162
MT2232-5	0.2140	0.0171
MT2232-6	0.2319	0.0209
MT2232-7	0.2251	0.0203
MT2232-8	0.2371	0.0166
MT2232-9	0.2228	0.0223
LN3475-1	0.2215	0.0133
LN3475-2	0.2244	0.0224
LN3475-3	0.2297	0.0207
LN3475-4	0.2333	0.0233
LN3475-5	0.2303	0.0161
LN3475-6	0.2317	0.0139
MT2239-2	0.2285	0.0183
MT2239-3	0.2248	0.0135

Table AP48: Torque data of polymer # MT2232-1 at multiple speeds using TC device

Speed (rpm)	Torque Average (Nm)	Std (Nm)
350	0.1458	0.0131
400	0.1682	0.0084
500	0.2174	0.0174
650	0.3237	0.0227

G. Taylor Couette Device Drawing Package

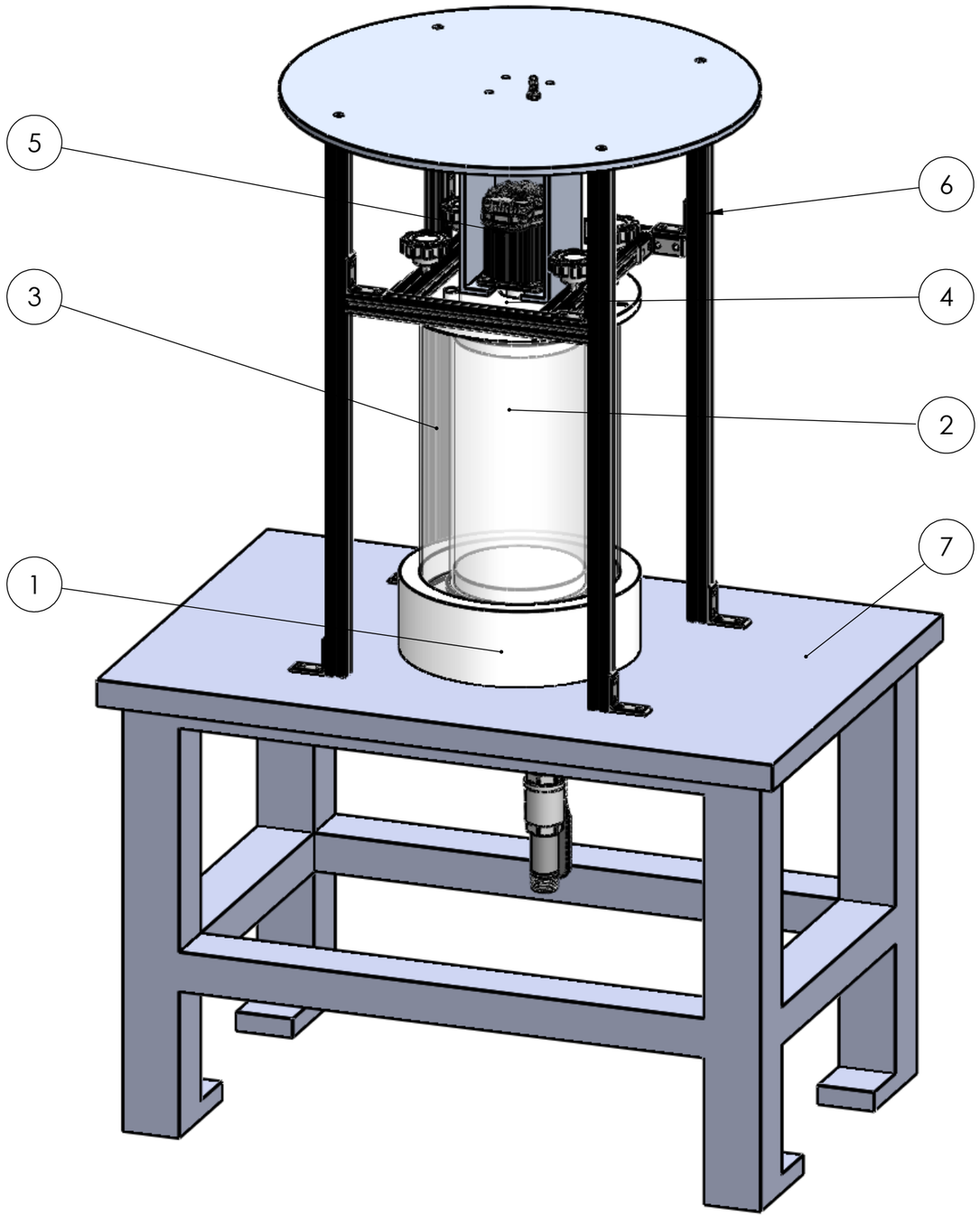

ITEM NO.	Name	QTY.
1	TC Bottom Subassembly	1
2	Inside Cylinder Subassembly	1
3	Outside Cylinder	1
4	Lid Subassembly	1
5	Motor Subassembly	1
6	Support Assembly	1
7	Table	1

For any unspecified holes, refer to individual piece, it will have the thread specfications to know which screw to use.

Ghaemi Group	DO NOT SCALE DRAWINGS
Drawn By: Rafat Jami	MATERIAL: Multiple
Name of Part: Total Assembly	UNLESS OTHERWISE SPECIFIED: DIMENSIONS ARE: INCHES [mm] TOLERANCES: 0.002 in
	SCALE:1:7 | SHEET 1 OF 30

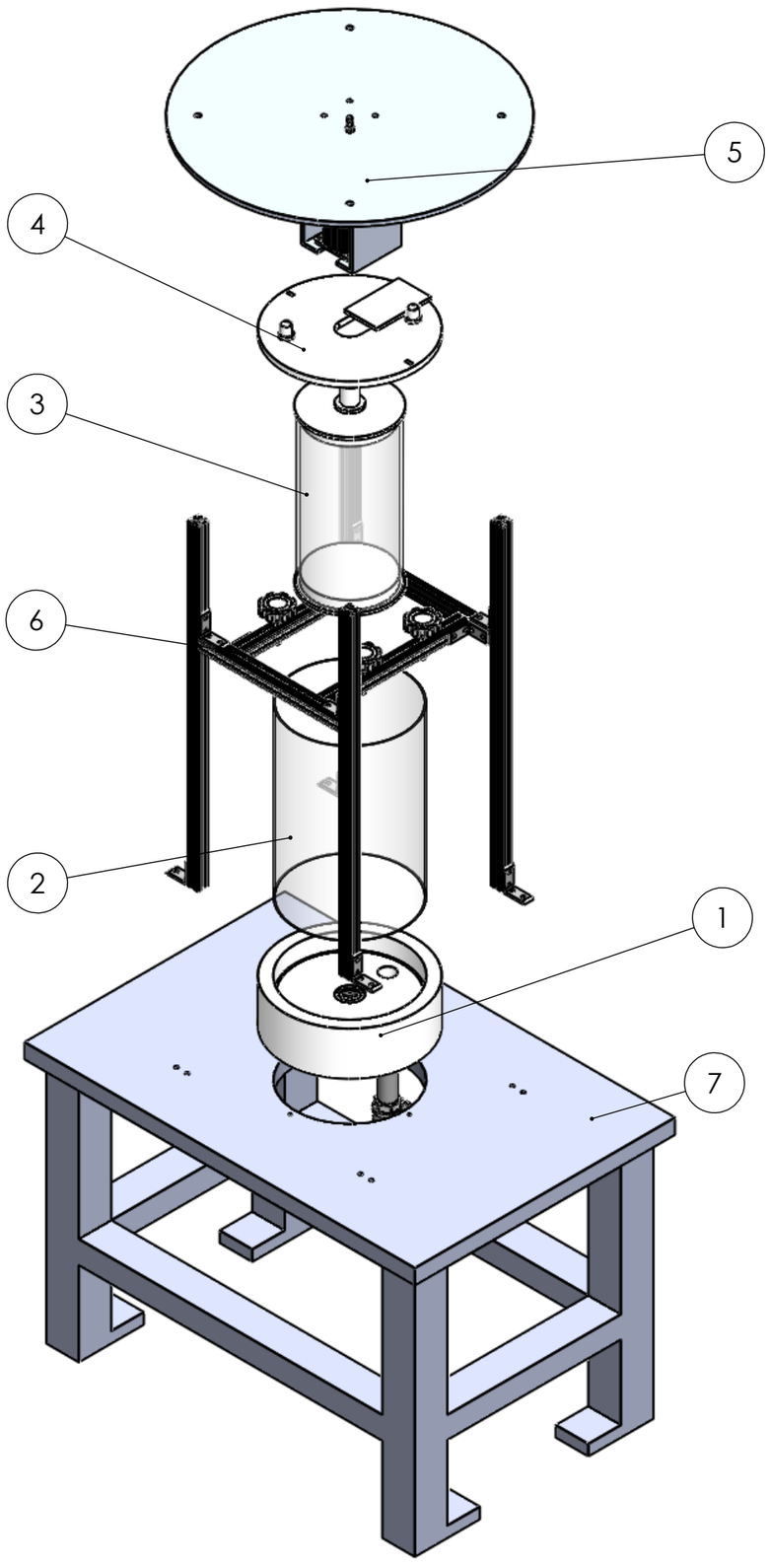

ITEM NO.	DESCRIPTION	QTY.
1	TC Bottom Subassembly	1
2	Outside Cylinder	1
3	Inside Cylinder Subassembly	1
4	Lid Subassembly	1
5	Motor Subassembly	1
6	Support Assembly	1
7	Table	1

NOTE: Item #5 includes the top circular plate

Ghaemi Group	DO NOT SCALE DRAWING
Drawn By: Rafat Jami	MATERIAL: Multiple
Name of Part: Total Assembly Exploded View	UNLESS OTHERWISE SPECIFIED: DIMENSIONS ARE: INCHES [mm] TOLERANCES: 0.002 in
	SCALE:1:10 SHEET 2 OF 30

Machining Required

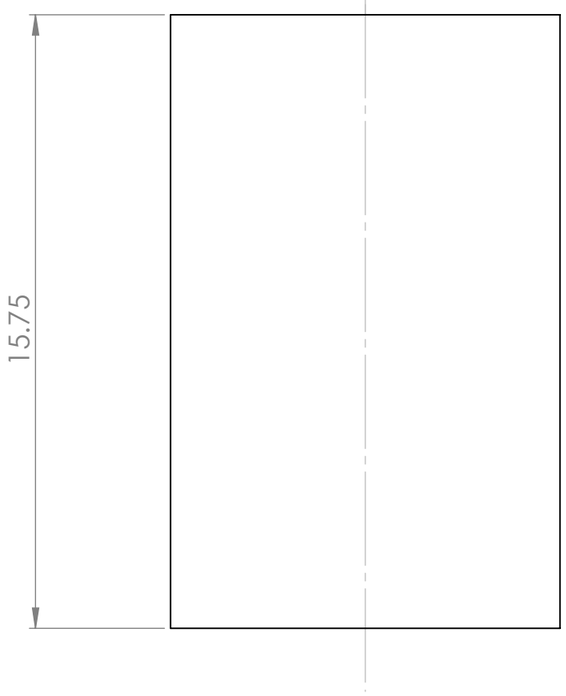

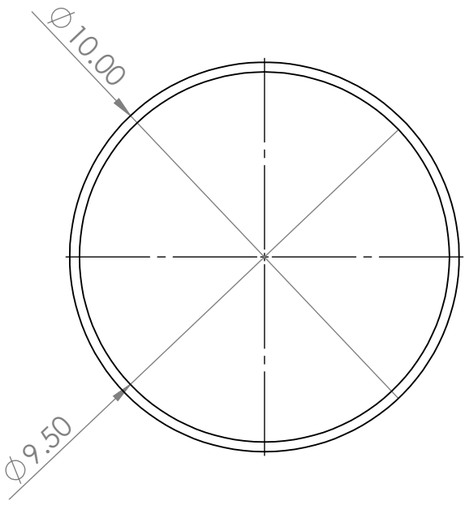

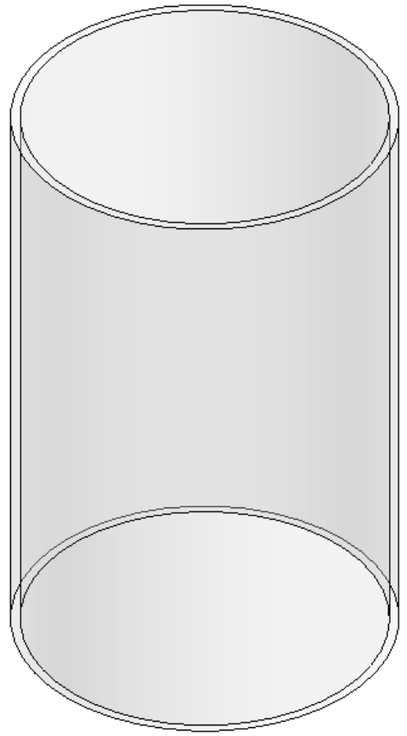

Needs to be turned on a lathe
for consistent inner diameter alignment.

This part must be purchased from McMaster Carr.
The part # is 84865K212, however, the piece needs
to be cut to this custom length.

Ghaemi Group	DO NOT SCALE DRAWING
Drawn By: Rafat Jami	MATERIAL: Clear Cast Acrylic
Name of Part: Outer Cylinder	UNLESS OTHERWISE SPECIFIED: DIMENSIONS ARE: INCHES [mm] TOLERANCES: 0.002 in
SCALE:1:4	SHEET 3 OF 30

ITEM NO.	PART NUMBER	DESCRIPTION	QTY.
1	tff425 FSH02811	Torque Sensor	1
2	Custom	Motor Mount	1
3	Custom	Support Top	1
4	Any	M8 nut	8
5	Any	M8 Bolt 50 mm long	8
6	CPM-_ _ _ _ - 3432_-LS	Motor	1

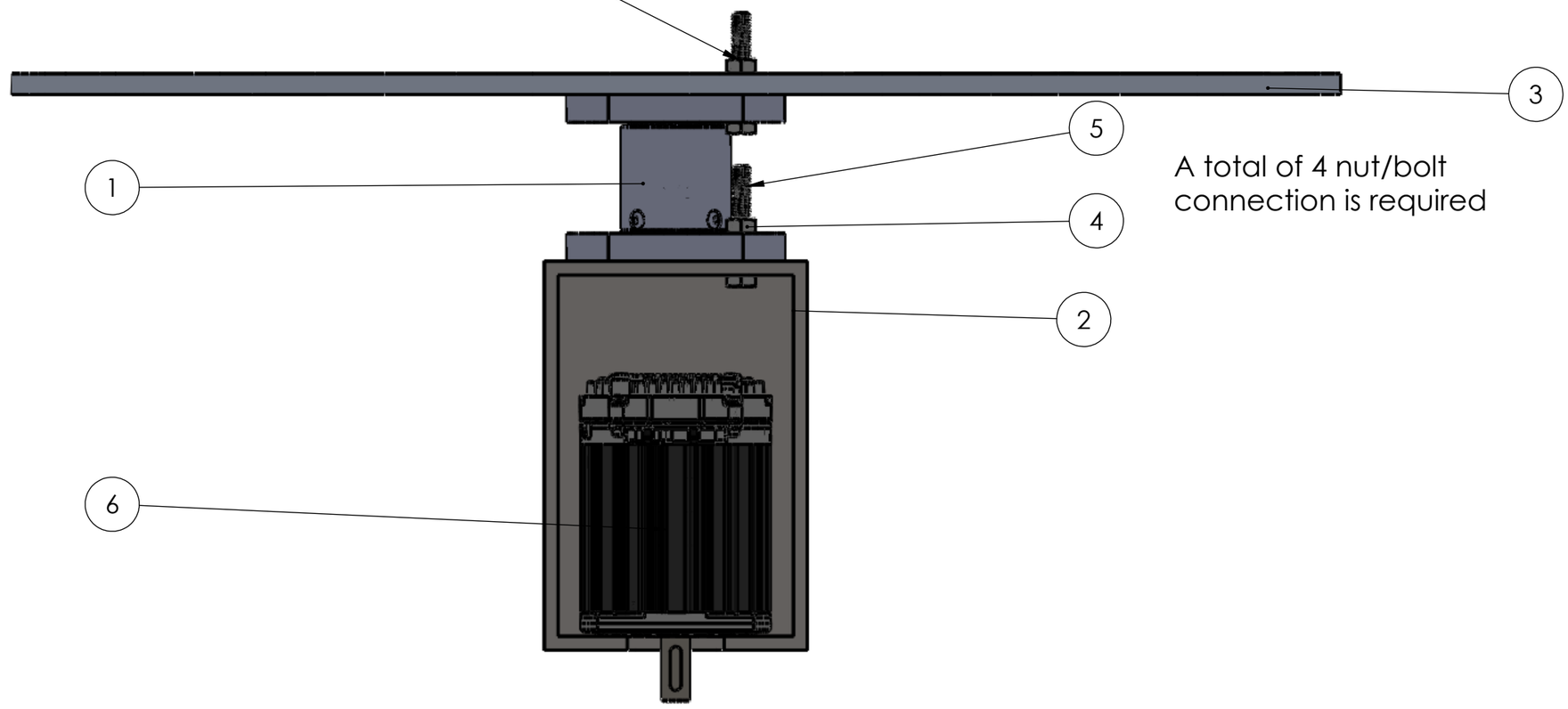

Ghaemi Group	DO NOT SCALE DRAWING
Drawn By: Rafat Jami	MATERIAL: Multiple
Name of Part: Motor Subassembly	UNLESS OTHERWISE SPECIFIED: DIMENSIONS ARE: INCHES [mm] TOLERANCES: 0.002 in
SCALE:2:5	SHEET 4 OF 30

ITEM NO.	DESCRIPTION	QTY.
1	Torque Sensor	1
2	Motor Mount	1
3	Support Top	1
4	Motor	1

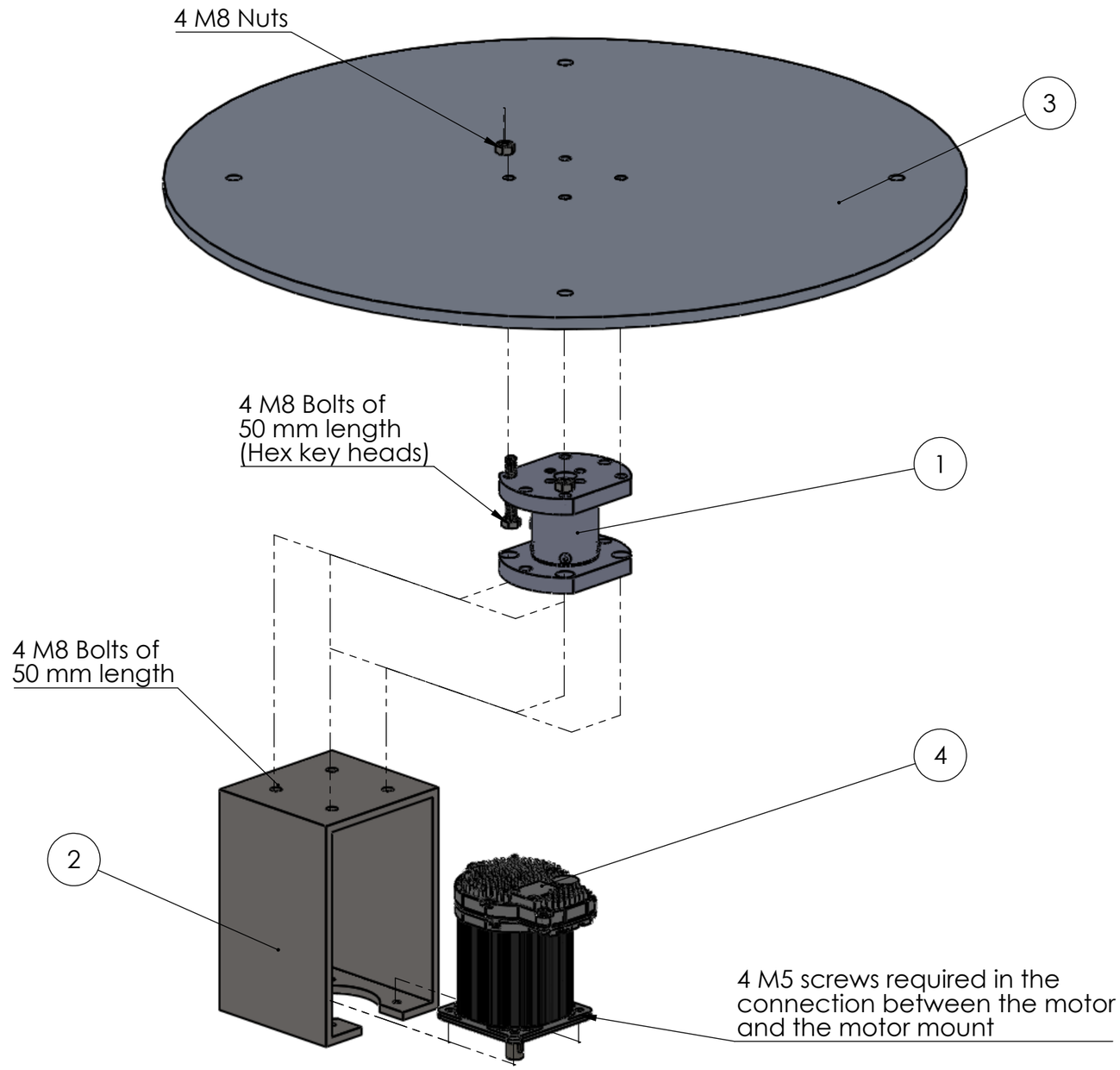

Ghaemi Group	DO NOT SCALE DRAWING
Drawn By: Rafat Jami	MATERIAL: Multiple
Name of Part: Motor Subassembly	UNLESS OTHERWISE SPECIFIED: DIMENSIONS ARE: INCHES [mm] TOLERANCES: 0.002 in
	SCALE:1:4 SHEET 5 OF 30

ITEM NO.	DESCRIPTION	QTY.
1	Torque Sensor	1
2	Motor Mount	1
3	Support Top	1
4	Motor	1

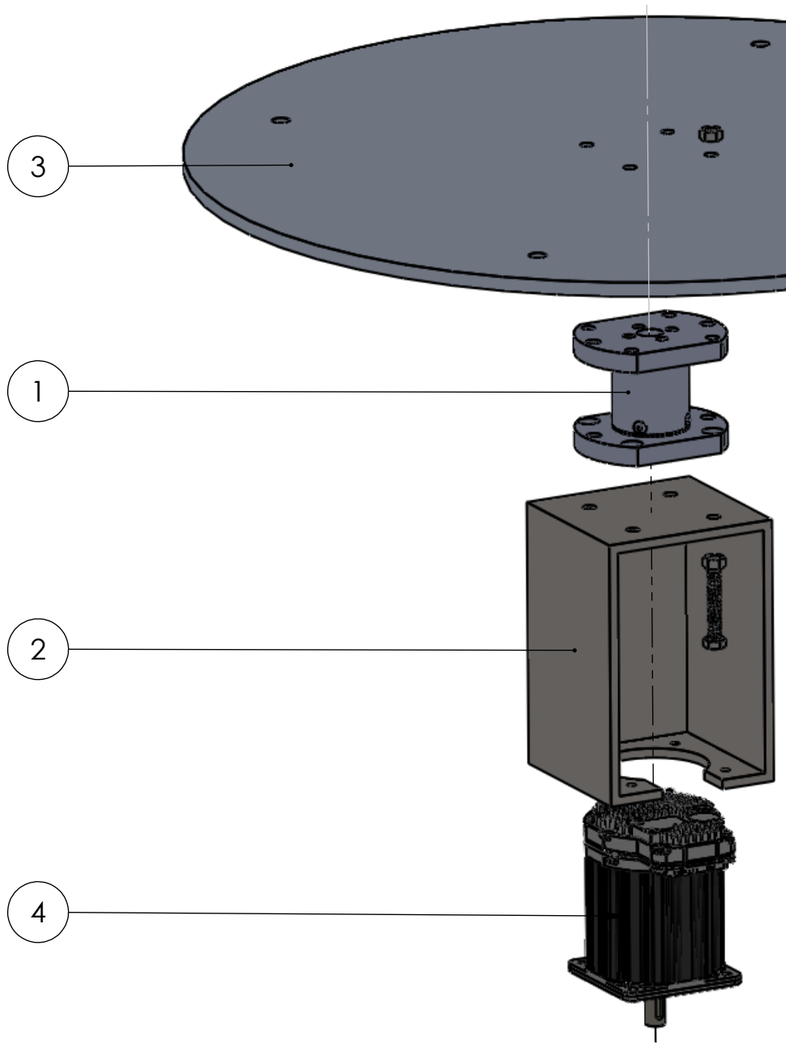

This figure displays that the motor and torque sensor must be coincentric in this assembly.

DO NOT SCALE DRAWING	REVISION
Drawn By: Rafat Jami	MATERIAL: Multiple
Name of Part: Motor Subassembly	UNLESS OTHERWISE SPECIFIED: DIMENSIONS ARE: INCHES [mm] TOLERANCES:
SCALE:1:4	SHEET 6 OF 30

MODEL TFF425

Reaction Torque Sensor with Thru Hole Center

FEATURES

- Easily integrates into OEM applications
- Designed for Torque auditing
- Aluminum construction
- Built-in overload protection
- Strain gauge based

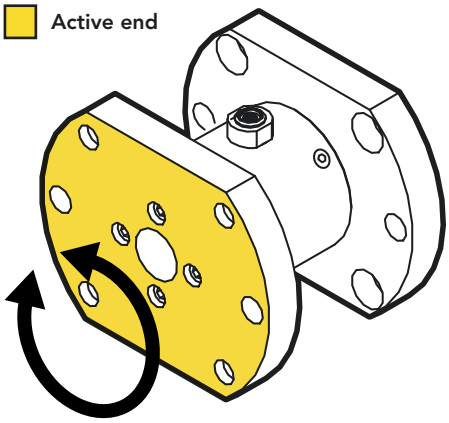

– Output (CCW)
+ Output (CW)

SPECIFICATIONS	
PERFORMANCE	
Nonlinearity	±0.2% of RO
Hysteresis	±0.2% of RO
Nonrepeatability	±0.05% of RO
ELECTRICAL	
Rated Output (RO)	1 mV/V nom (5 in-oz) 2 mV/V nom (10 in-oz to 500 in-lb)
Excitation (VDC or VAC)	18 max
Bridge Resistance	350 Ohm nom (5 to 1000 in-oz) 700 Ohm nom (100 to 500 in-lb)
Connection	4 Pin LEMO® Receptacle (EGG. OB. 304 CLL)
Wiring/Connector Code	CC4
MECHANICAL	
Weight (approximate)	14 oz [397 g]
Safe Overload	150% of RO
Material	Aluminum
IP Rating	IP40
TEMPERATURE	
Operating Temperature	–60 to 200°F (–50 to 93°C)
Compensated Temperature	60 to 160°F (15 to 72°C)
Temperature Shift Zero	±0.002% of RO/°F (0.0036% of RO/°C)
Temperature Shift Span	±0.002% of Load/°F (0.0036% of Load/°C)
CALIBRATION	
Calibration Test Excitation	10 VDC
Calibration (standard)	5-pt CW
Calibration (available)	5-pt CW & CCW
Shunt Calibration Value	60.4 kOhm (10 to 1000 in-oz) 100 kOhm (5 in-oz, 100 to 500 in-lb)

DIMENSIONS inches [mm]

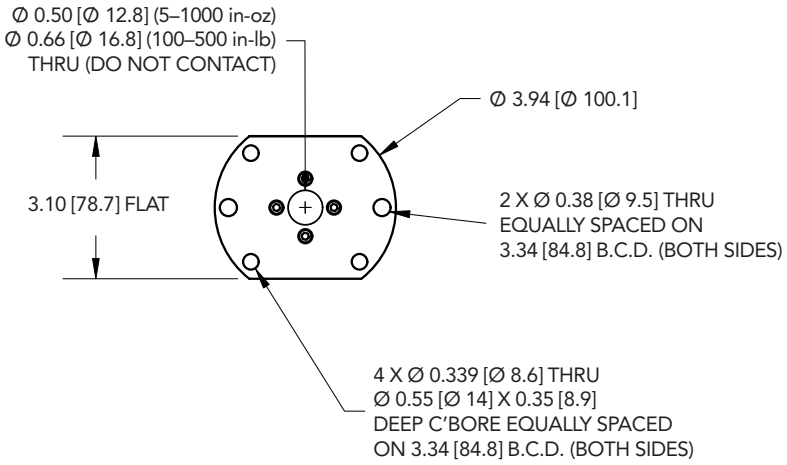

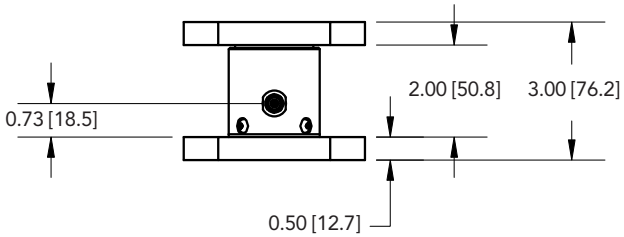

CAPACITIES

ITEM #	in-oz	Nm	Torsional Stiffness in-oz/rad
FSH02801	5*	0.04	325
FSH02802	10*	0.07	650
FSH02804	50*	0.35	3500
FSH02806	160*	1.1	11000
FSH02807	400*	2.8	30000
FSH02811	1000	7.1	71000
FSH02808	100 in-lb	11	77000 in-lb/rad
FSH02809	200 in-lb	22	95000 in-lb/rad
FSH02810	500 in-lb	56	199000 in-lb/rad

*** WITH OVERLOAD PROTECTION**
FOR HIGHER CAPACITIES REFER TO MODELS TFF600–750 AND TDF600–675

CONNECTOR CODE (CC4)

PIN	WIRING CODE
1	+ EXCITATION/RED
4	– EXCITATION/BLACK
2	+ SIGNAL/GREEN
3	– SIGNAL/WHITE

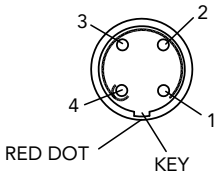

Drawing Number: FI1137-G

10 Thomas, Irvine, CA 92618 USA
Tel: (949) 465-0900
Fax: (949) 465-0905

www.futek.com

ANSI Z540-1 ISO 17025 ISO 9001 ISO 13485 U.S. Manufacturer

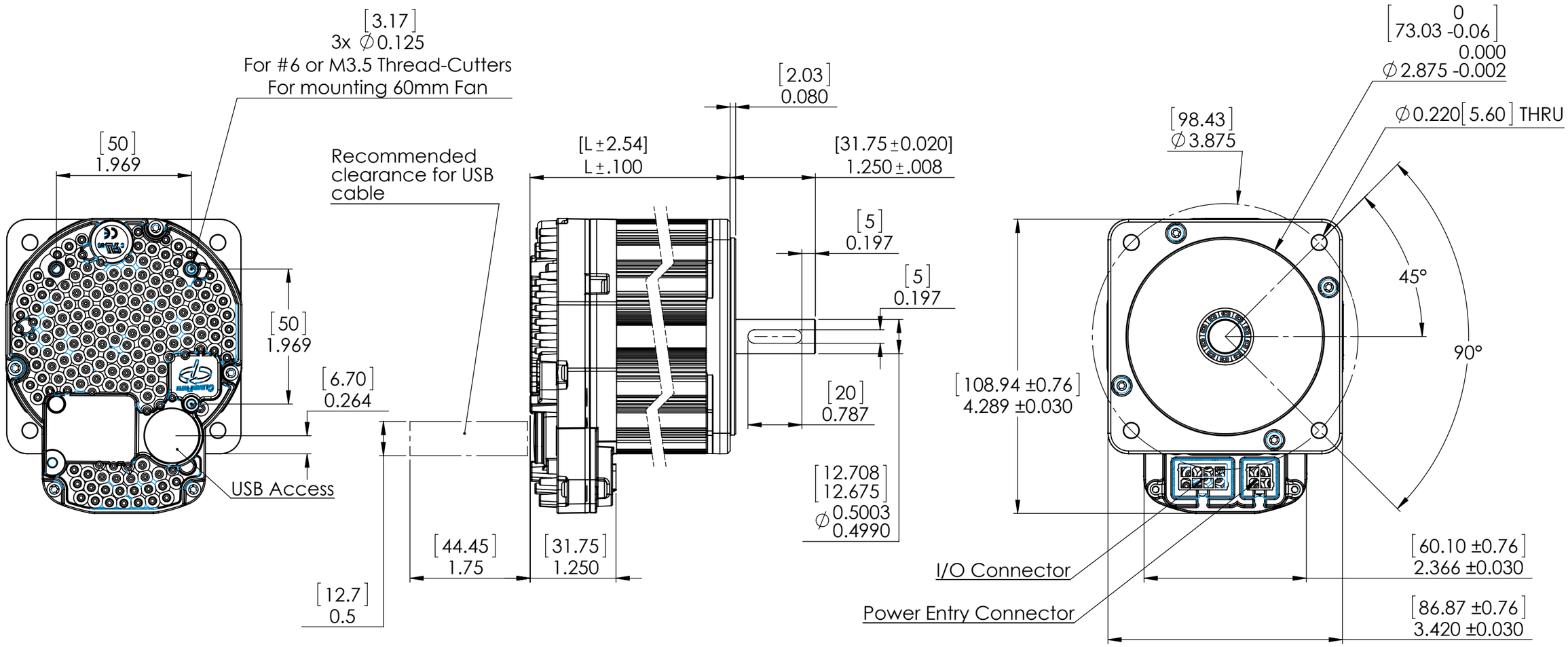

Model Number	L
CPM-_ _ _ _ -3411_ - _ _	79.70 [3.138]
CPM-_ _ _ _ -3421_ - _ _	98.52 [3.879]
CPM-_ _ _ _ -3432_ - _ _	117.52 [4.627]
CPM-_ _ _ _ -3441_ - _ _	136.70 [5.382]

Teknic, Incorporated
Rochester, NY 14534 USA

Third-Angle Projection

34xx ClearPath Motor Family

DWG. NO./REV D1170/001

1 of 1 Pages

Machining Required

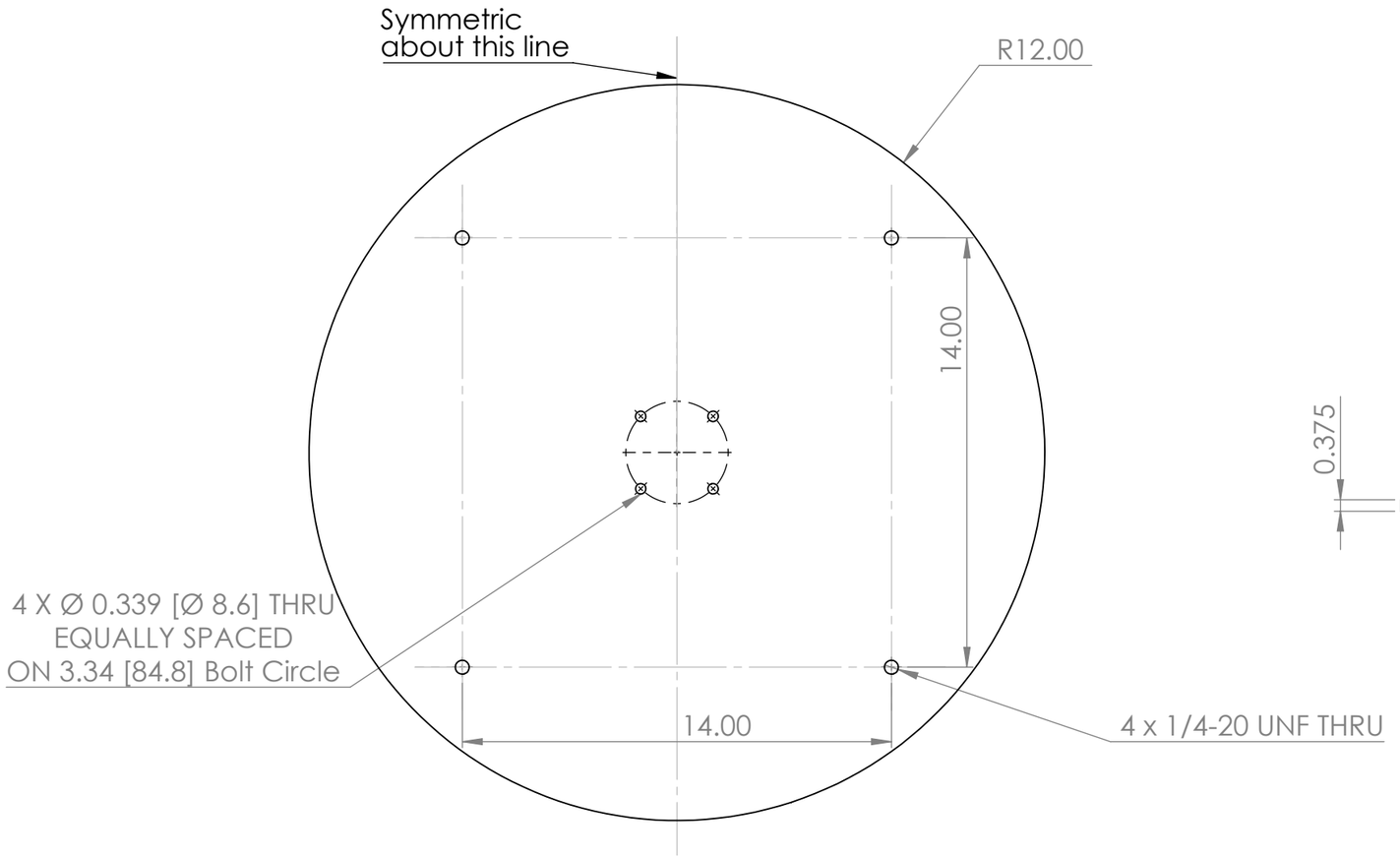

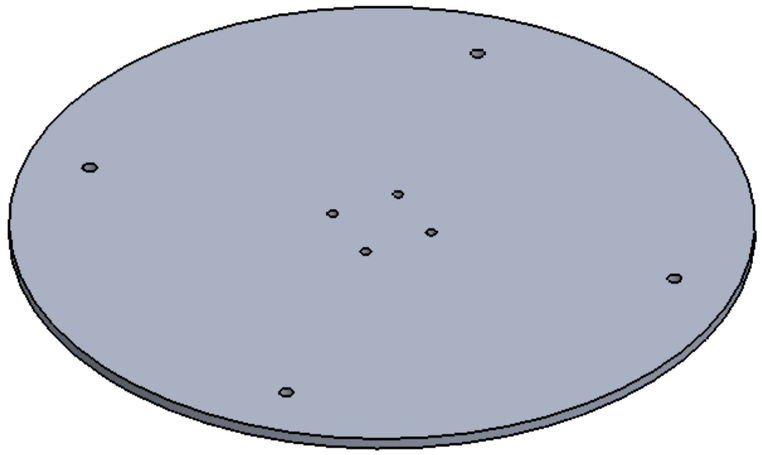

The alignment of the centre 4 holes are the most important as they will hold the inner rotating cylinder vertical.

Ghaemi Group	DO NOT SCALE DRAWING
Drawn By: Rafat Jami	MATERIAL: 6061 Aluminum Alloy
Name of Part: Support Top	UNLESS OTHERWISE SPECIFIED: DIMENSIONS ARE: INCHES [mm] TOLERANCES: 0.002 in
SCALE:1:5	SHEET 10 OF 30

Machining Required

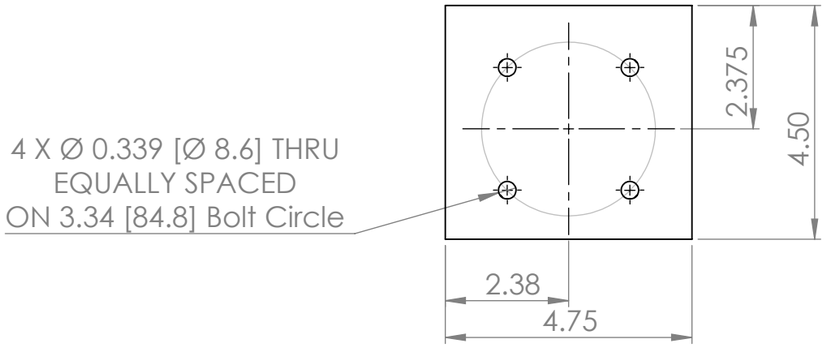

A tiny hole can be placed at the centre for alignment.

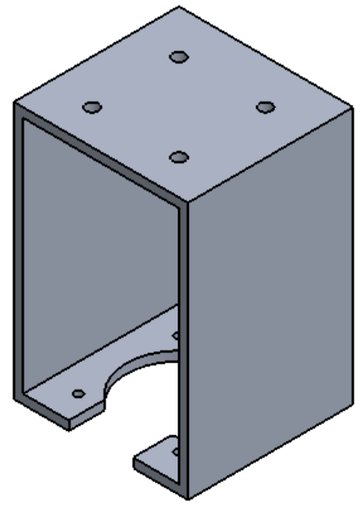

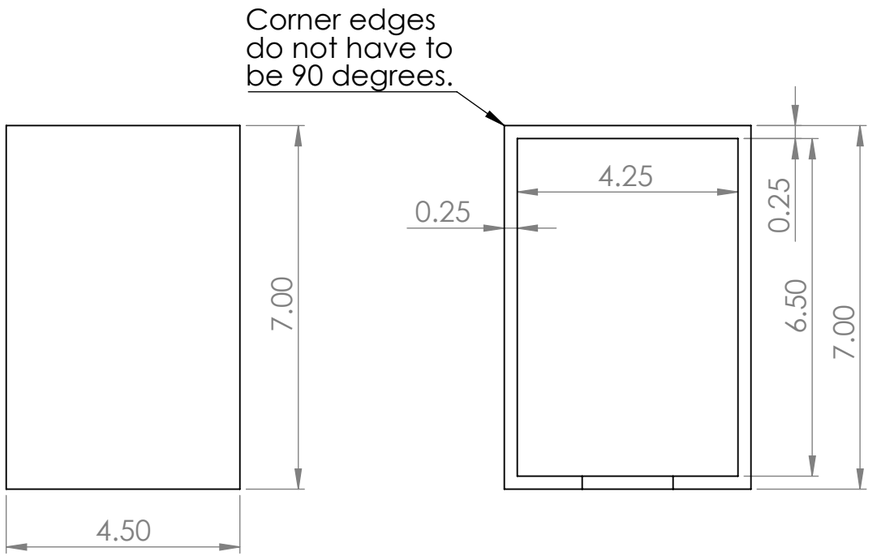

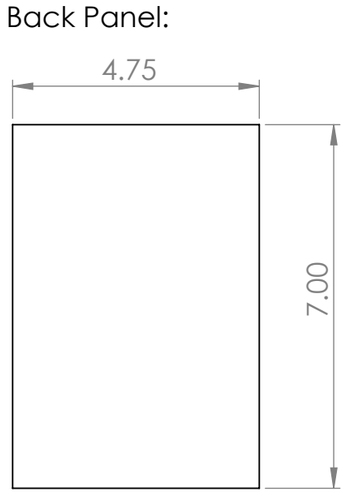

Each piece can be machined individually and welded together.

Both Side Pieces have same dimensions

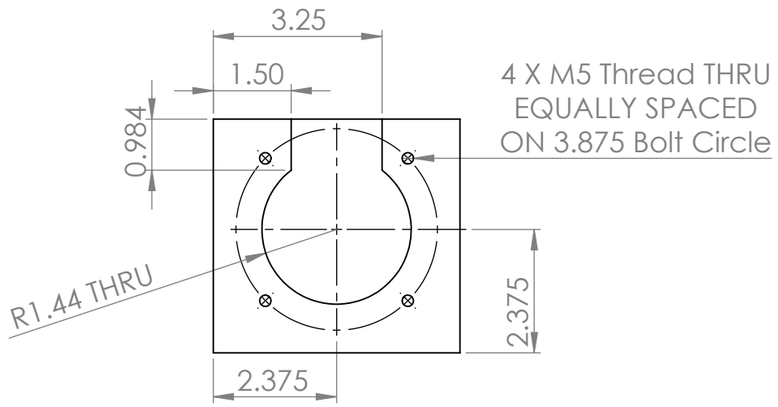

Ghaemi Group	DO NOT SCALE DRAWING
Drawn By: Rafat Jami	MATERIAL: 6061 Aluminum
Name of Part: Motor Mount	UNLESS OTHERWISE SPECIFIED: DIMENSIONS ARE: INCHES [mm] TOLERANCES: 0.002 in
	SCALE:1:3 SHEET 11 OF 30

ITEM NO.	PART NUMBER	DESCRIPTION	QTY.
1	Custom	TC Bottom	1
2	9557K217	O-ring	1
3	4882K95	Drainage Pipe 1	1
4	2342K191	Double Sealed Bearing	1
5	47865K250	Brass Ball Valve	1
6	4882K55	Drainage Pipe 2	1

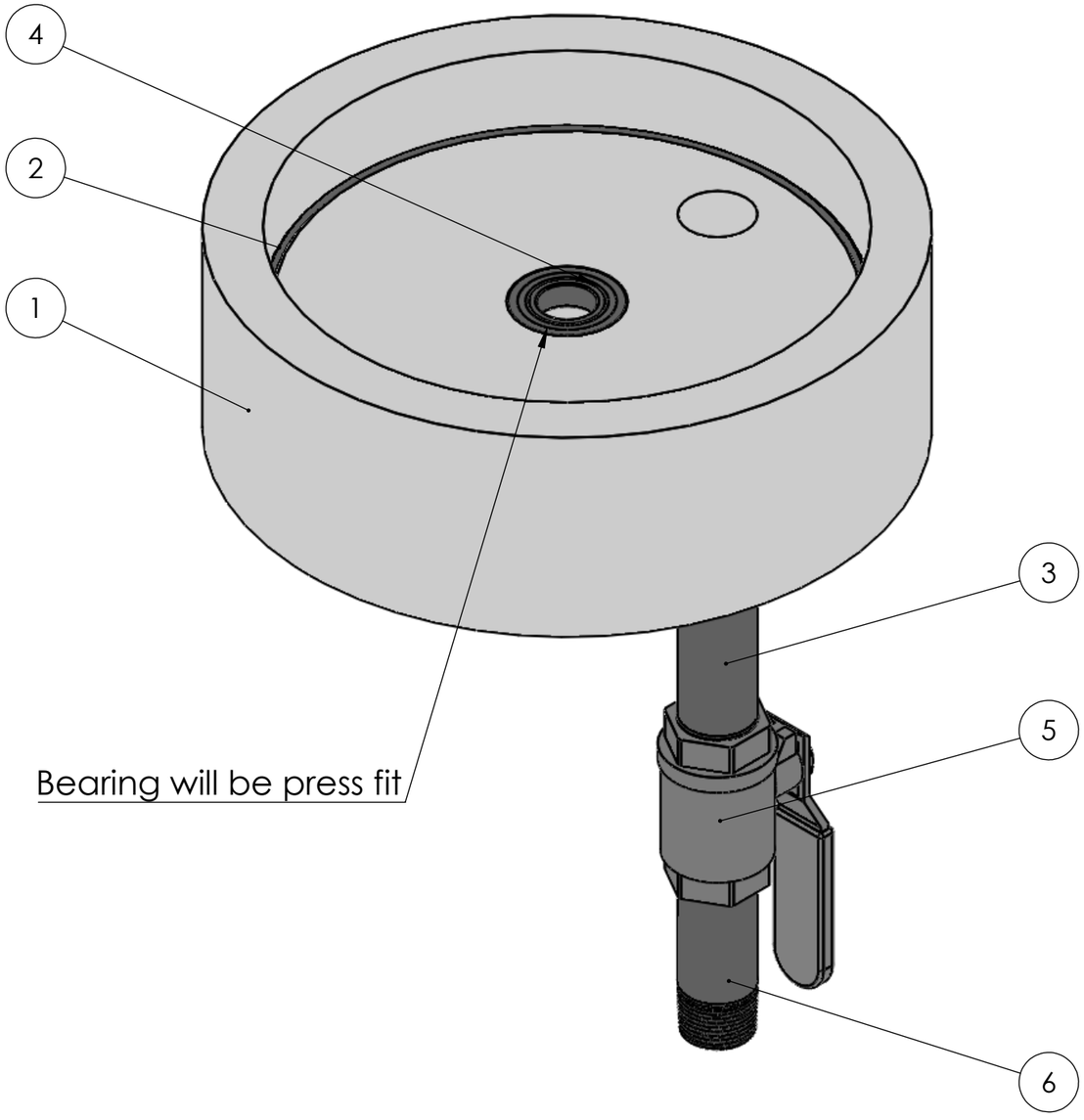

Side View:

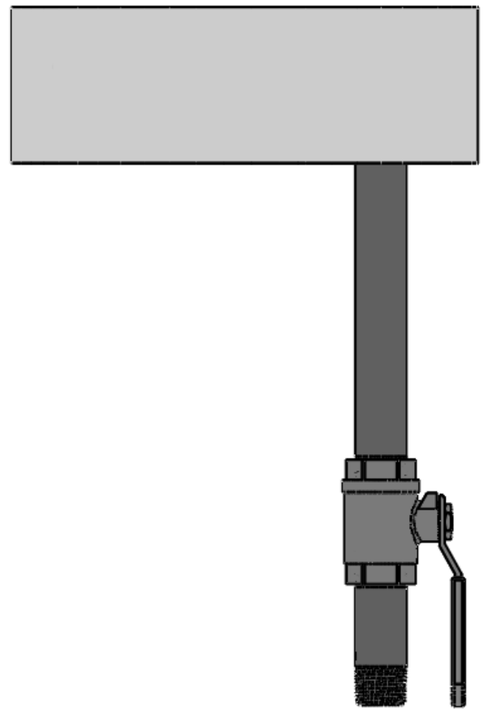

Ghaemi Group	DO NOT SCALE DRAWING
Drawn By: Rafat Jami	MATERIAL: Multiple
Name of Part: TC Bottom Subassembly	UNLESS OTHERWISE SPECIFIED: DIMENSIONS ARE: INCHES [mm] TOLERANCES: 0.002 in
	SCALE:2:5 SHEET 12 OF 30

ITEM NO.	DESCRIPTION	QTY.
1	TC Bottom	1
2	O-Ring	1
3	Drainage Pipe 1	1
4	Double Sealed Bearing	1
5	On/off Valve	1
6	Drainage Pipe 2	1

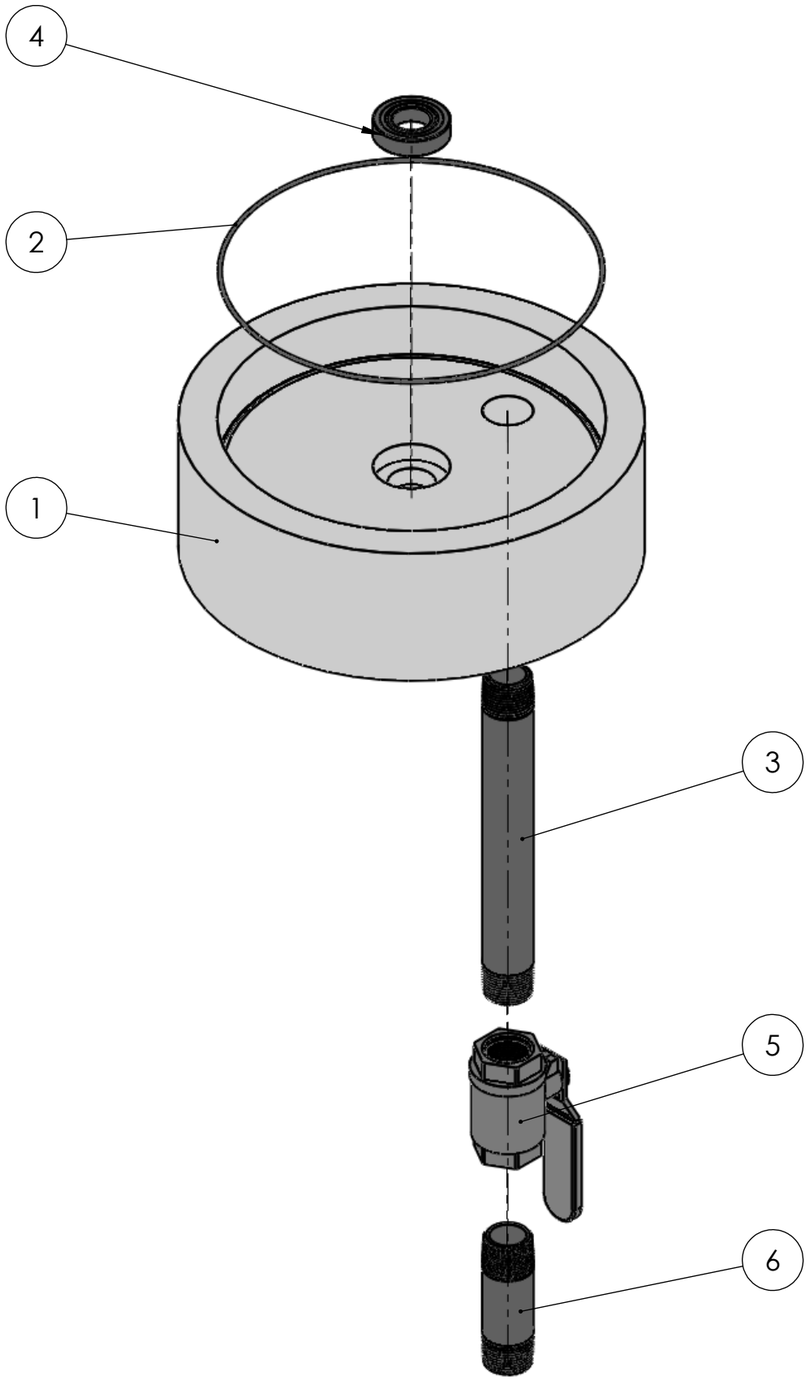

Ghaemi Group	DO NOT SCALE DRAWING
Drawn By: Rafat Jami	MATERIAL: Multiple
Name of Part: TC Bottom Subassembly	UNLESS OTHERWISE SPECIFIED: DIMENSIONS ARE: INCHES [mm] TOLERANCES: 0.002 in
	SCALE:1:4 SHEET 13 OF 30

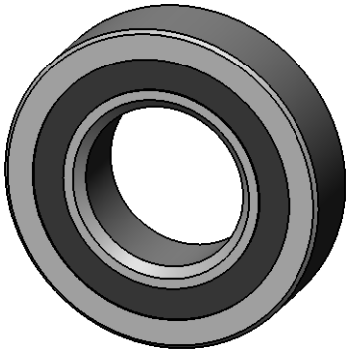

Trade Number: R16-2RS

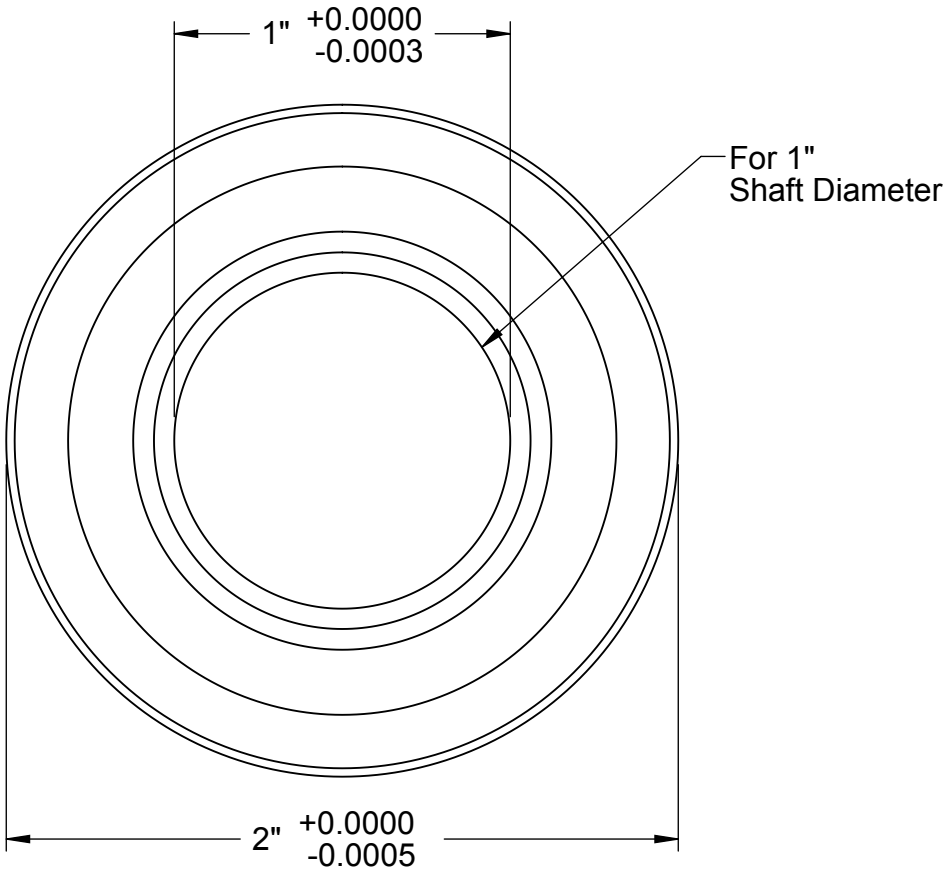

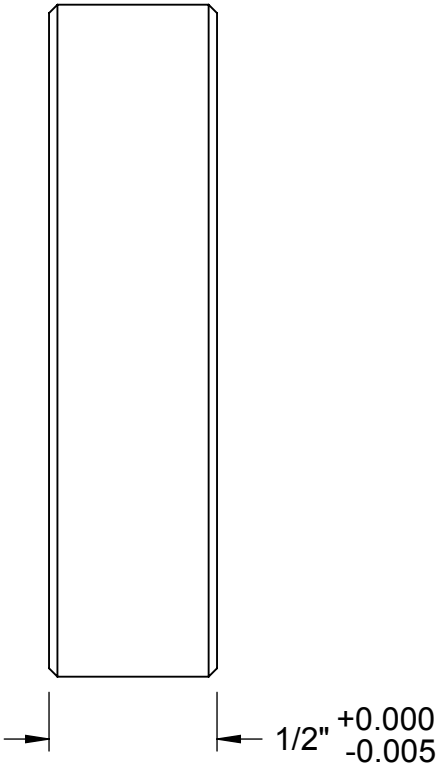

McMASTER-CARR® CAD

http://www.mcmaster.com

PART NUMBER **2342K191**

Permanently Lubricated
Ball Bearing

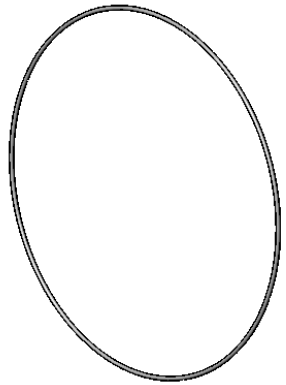

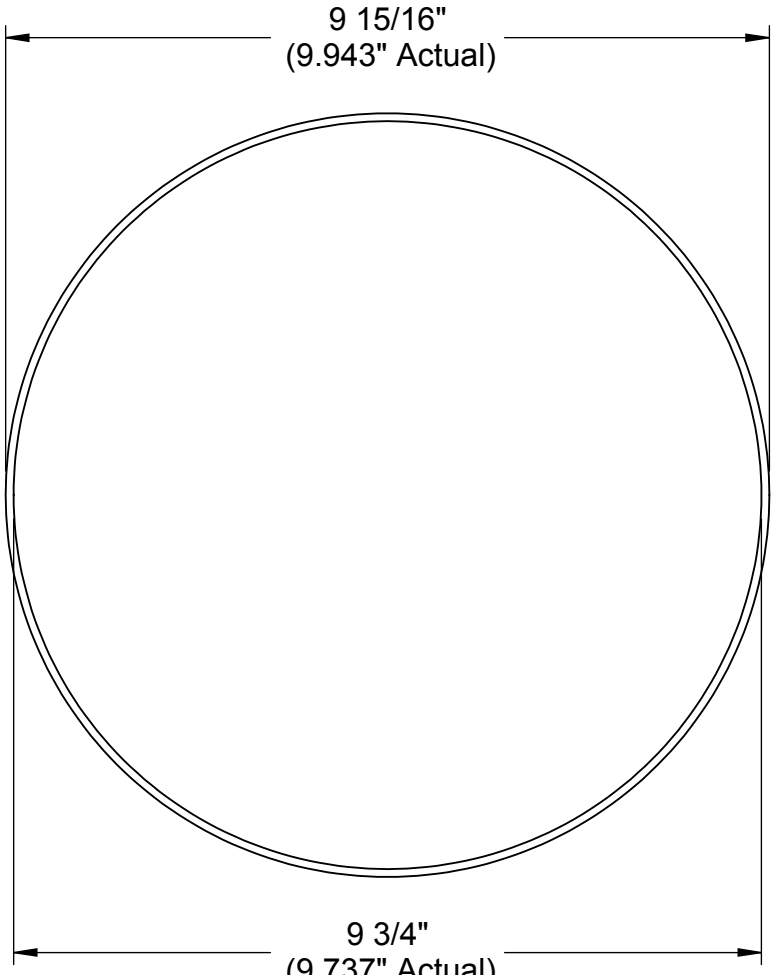

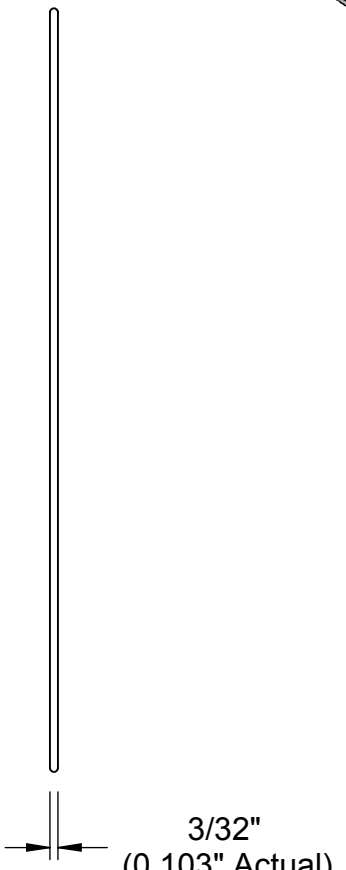

McMASTER-CARR® CAD

http://www.mcmaster.com

PART NUMBER **9557K217**

Multipurpose
O-Ring

Machining Required

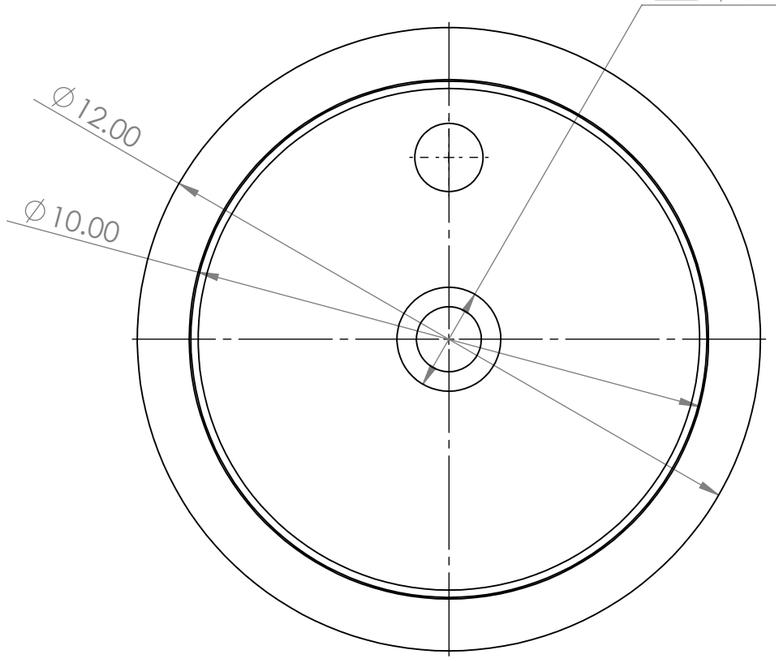

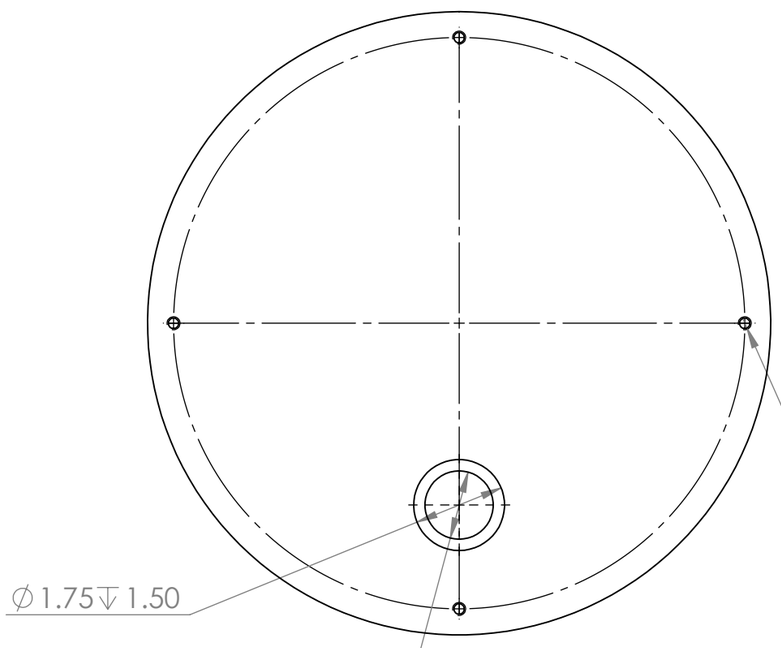

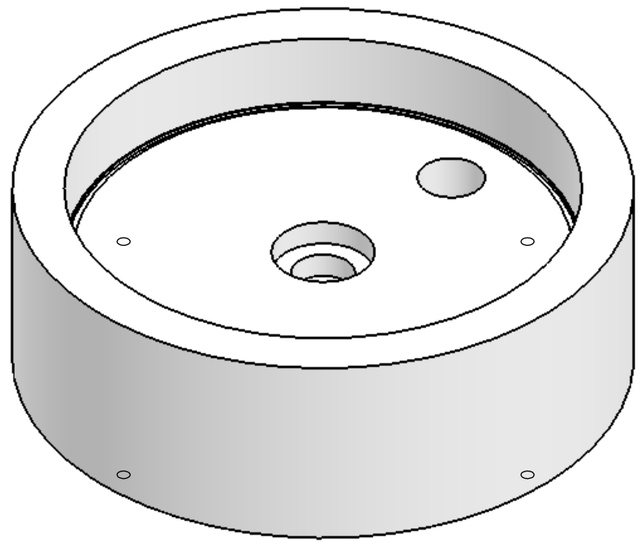

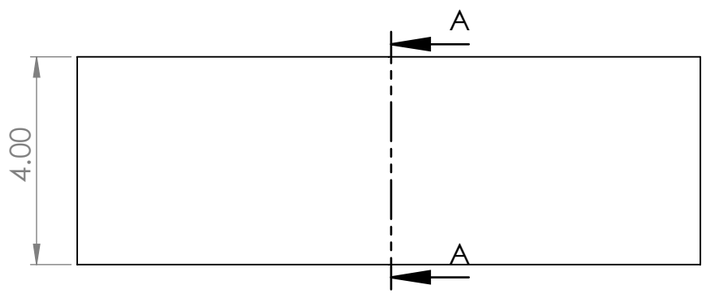

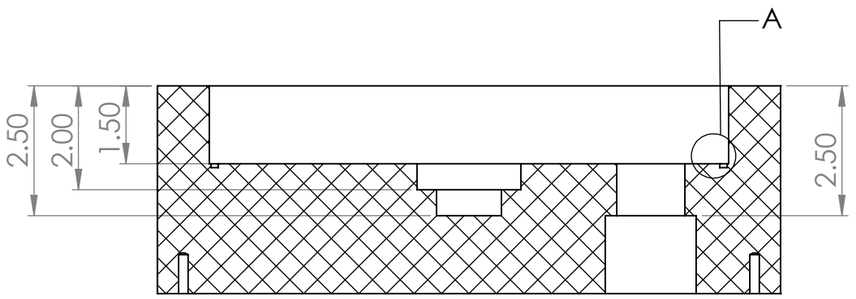

SECTION A-A

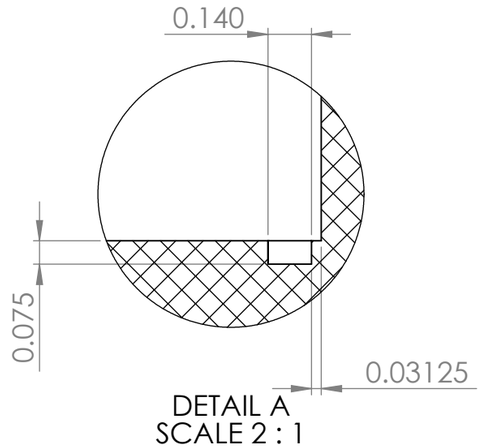

DETAIL A
SCALE 2 : 1

The large 10" inside diameter has clearance fit tolerance to the Outside Cylinder Part that is ordered by McMaster Carr.

DO NOT SCALE DRAWING	REVISION
Drawn By: Rafat Jami	MATERIAL: PVC
Name of Part: TC Bottom	UNLESS OTHERWISE SPECIFIED: DIMENSIONS ARE: INCHES [mm] TOLERANCES:
SCALE:1:3	SHEET 16 OF 30

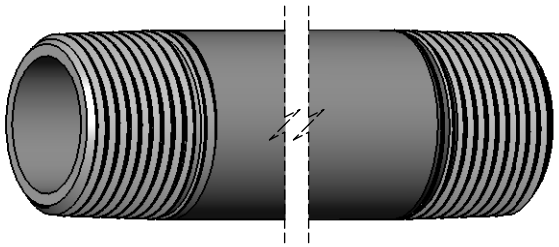

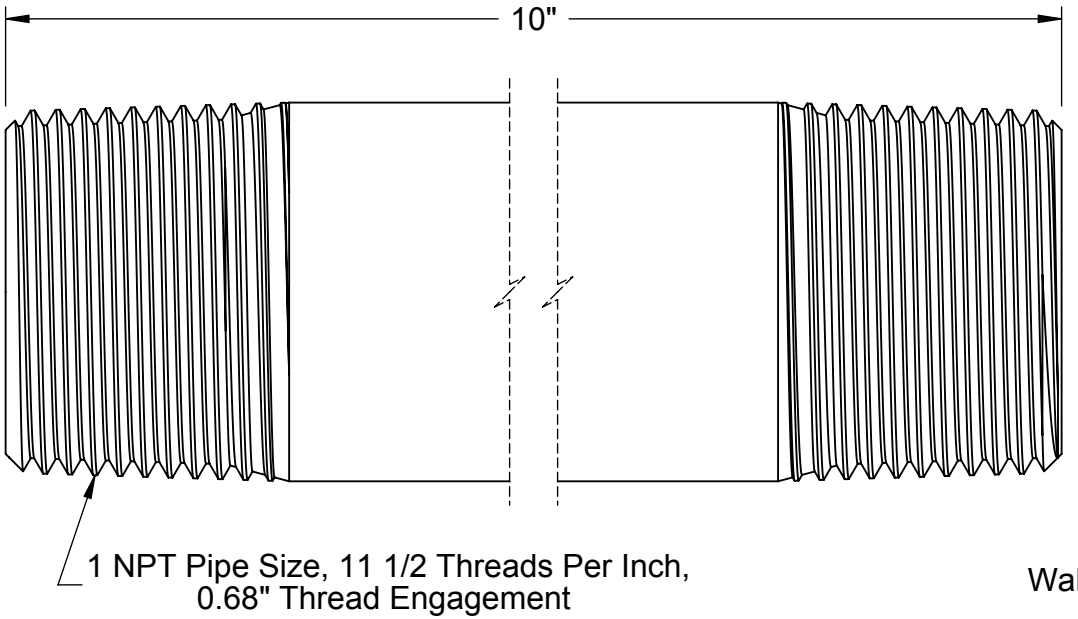

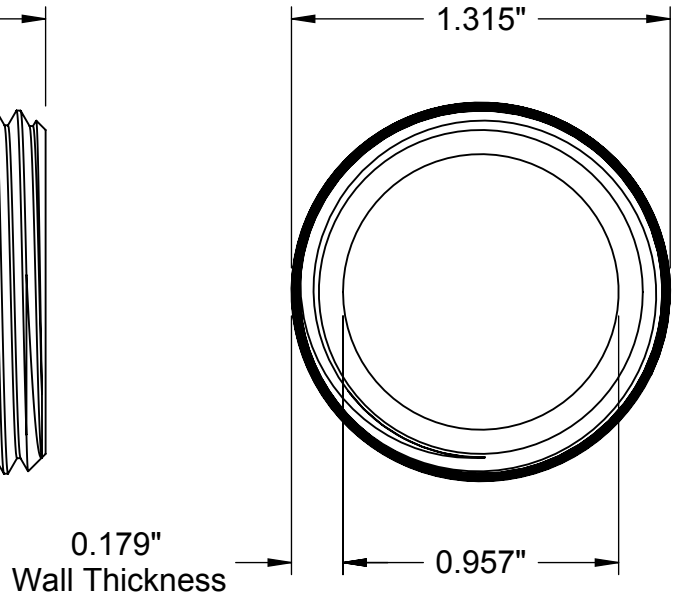

McMASTER-CARR® CAD	PART NUMBER 4882K95
http://www.mcmaster.com	Thick-Wall Dark Gray PVC Threaded Pipe Nipple

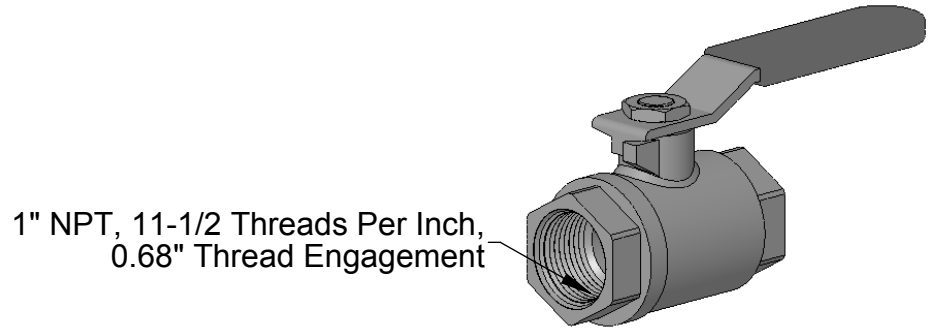

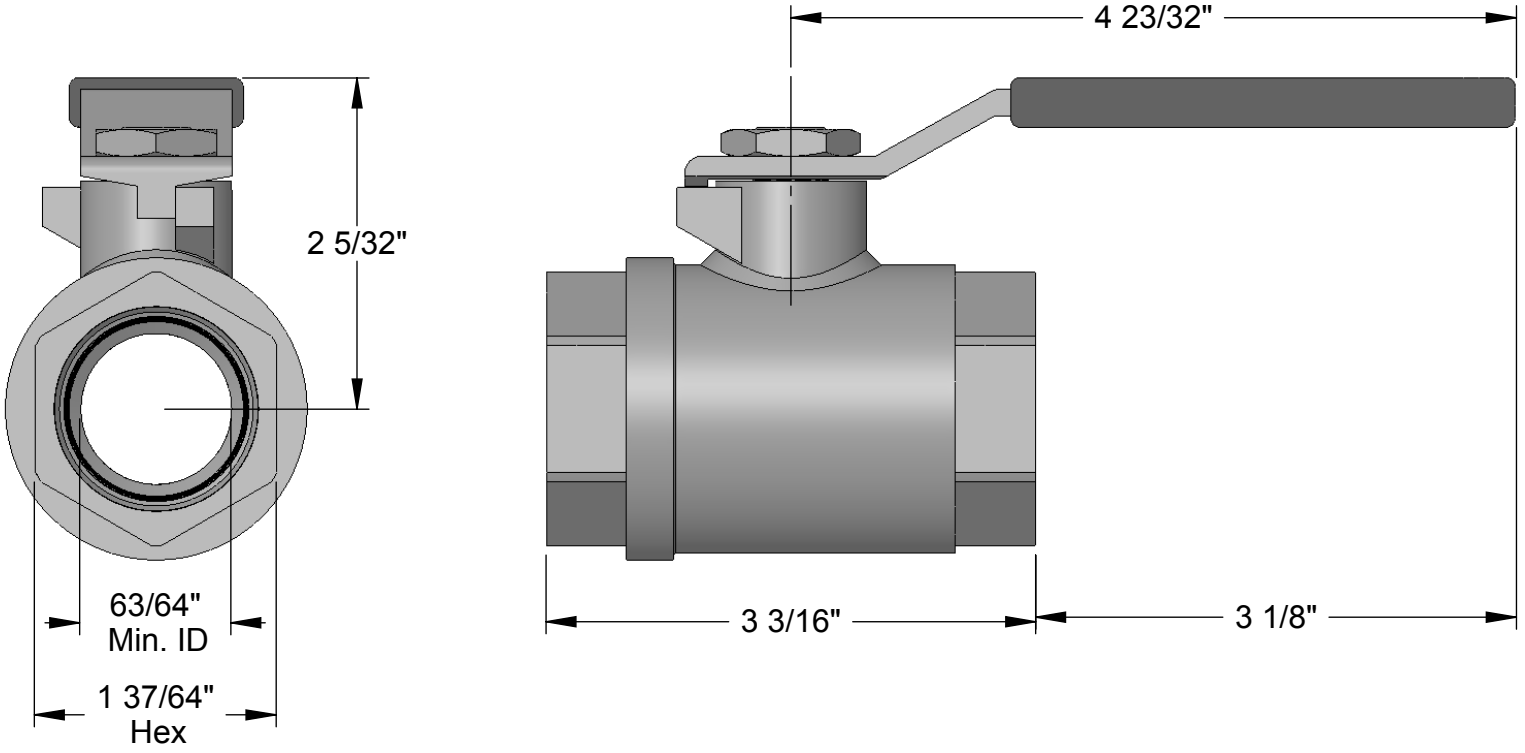

McMASTER-CARR® CAD

http://www.mcmaster.com

PART NUMBER **47865K25**

Brass Ball Valve
with Lever Handle

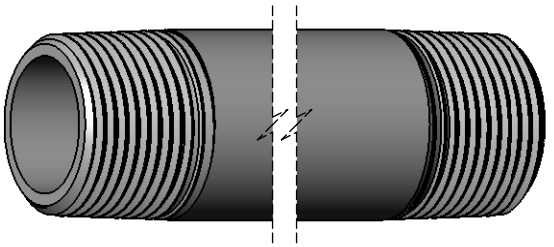

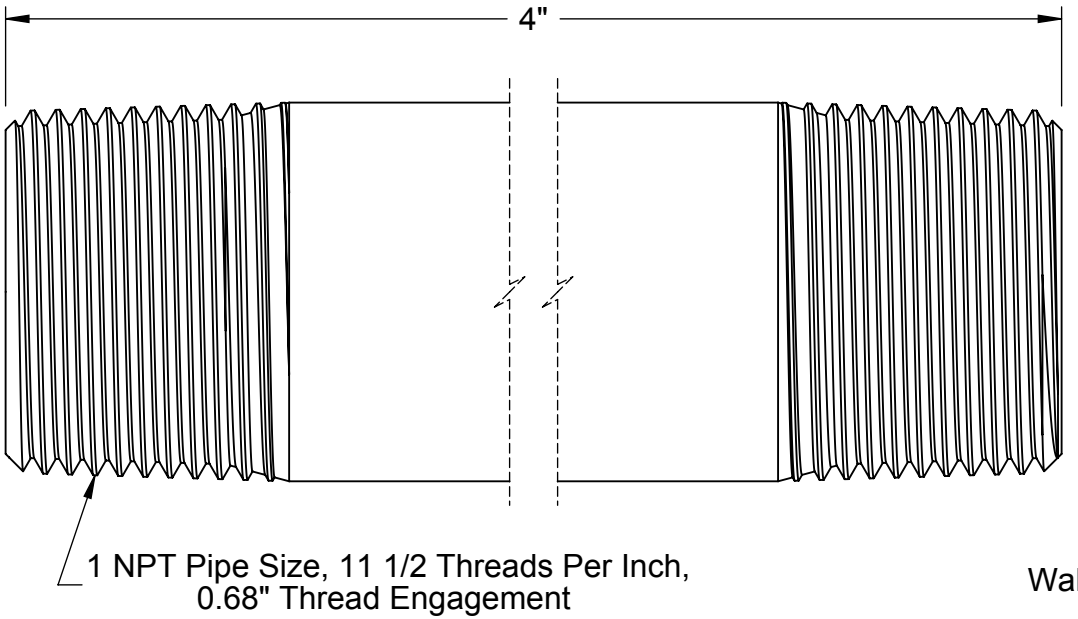

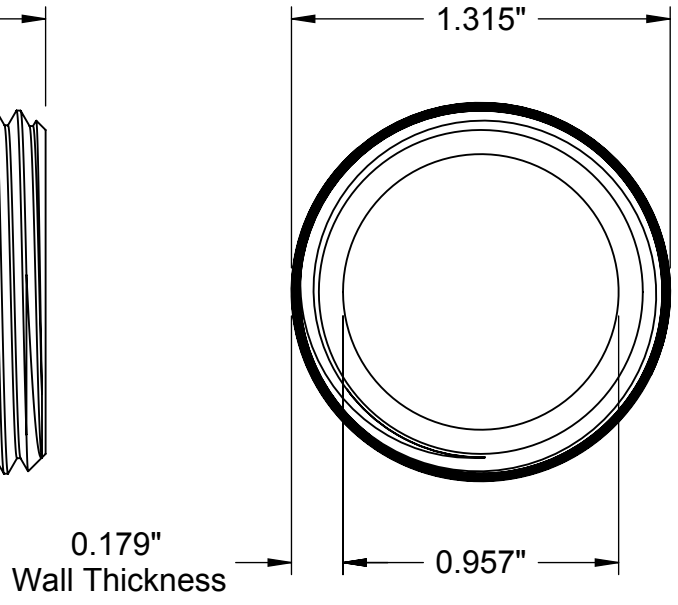

McMASTER-CARR® CAD

http://www.mcmaster.com

PART NUMBER **4882K55**

Thick-Wall Dark Gray
PVC Threaded Pipe Nipple

ITEM NO.	PART NUMBER	DESCRIPTION	QTY.
1	47065T412	Support Leg	4
2	47065T239	Bracket	12
3	47065T209	Truss	4
4	5532T57	Threaded Knob	4

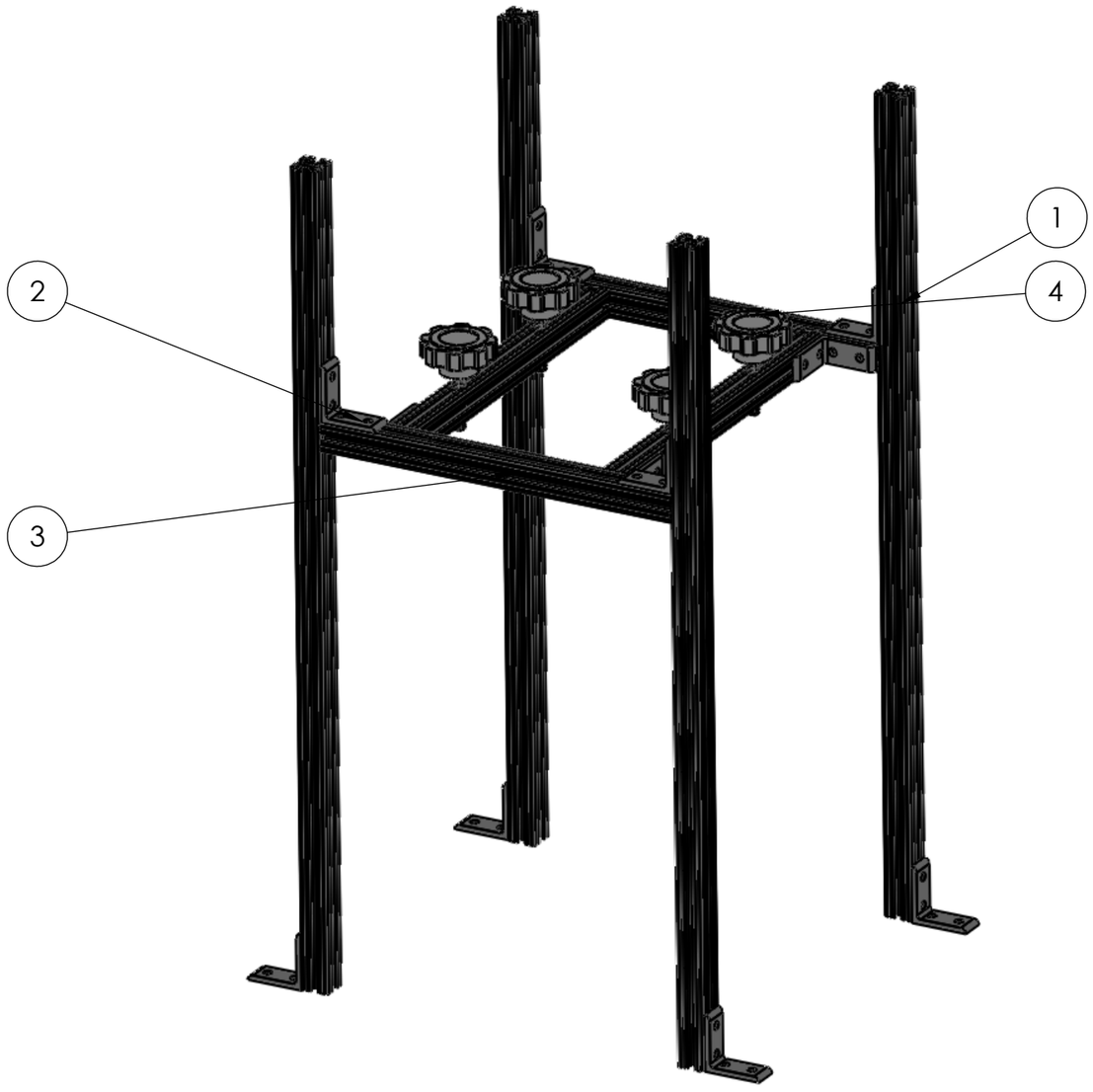

All parts can be purchased from McMaster Carr. Fasteners for the brackets and extrusions are all supplied by McMasterr Carr for these pieces.

Ghaemi Group	DO NOT SCALE DRAWING
Drawn By: Rafat Jami	MATERIAL: Multiple
Name of Part: Support Assembly	UNLESS OTHERWISE SPECIFIED: DIMENSIONS ARE: INCHES [mm] TOLERANCES: 0.002 in
	SCALE:1:5 SHEET 20 OF 30

ITEM NO.	DESCRIPTION	QTY.
1	Support Legs	4
2	Bracket	12
3	Truss	4
4	Knobs	4

The purpose of the knobs is to add compression on the lid and outer cylinder, which in turn compresses the O-ring inside the base.

Ghaemi Group	DO NOT SCALE DRAWING
Drawn By: Rafat Jami	MATERIAL: Multiple
Name of Part: Support Assembly Exploded View	UNLESS OTHERWISE SPECIFIED: DIMENSIONS ARE: INCHES [mm] TOLERANCES: 0.002 in
	SCALE:1:4 SHEET 21 OF 30

Machining Required

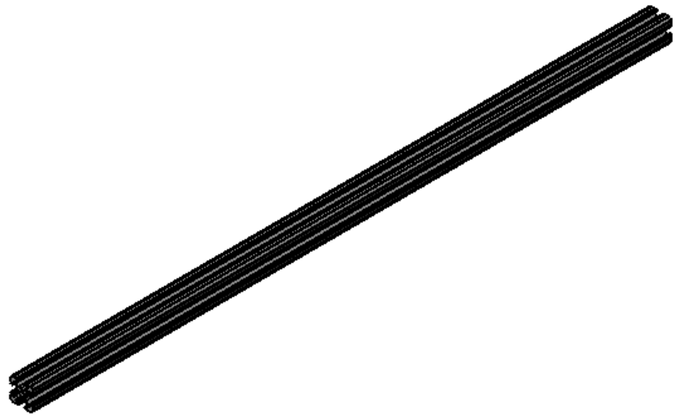

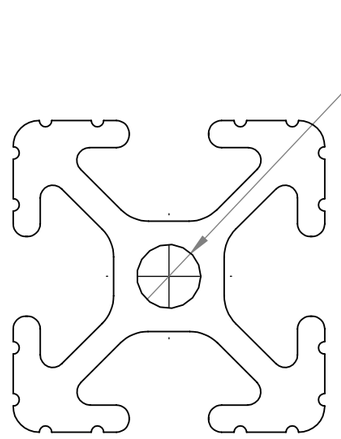

5:1 Scale Image

This part can be purchased from McMaster Carr, Part # 47065T412. The piece is needs to be cut to the specified length, and only one side needs to be tapped for the connection with the top plate.

Ghaemi Group	DO NOT SCALE DRAWING
Drawn By: Rafat Jami	MATERIAL: Anodized Aluminum
Name of Part: Support Leg # 47065T412	UNLESS OTHERWISE SPECIFIED: DIMENSIONS ARE: INCHES [mm] TOLERANCES: 0.002 in
	SCALE:1:5 | SHEET 22 OF 30

Machining Required

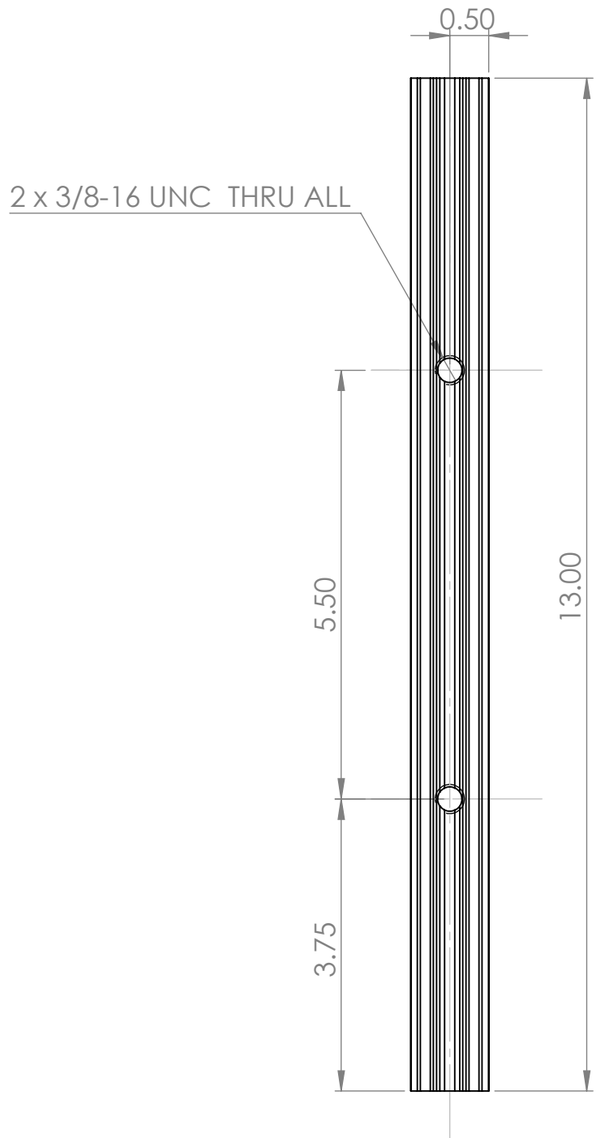

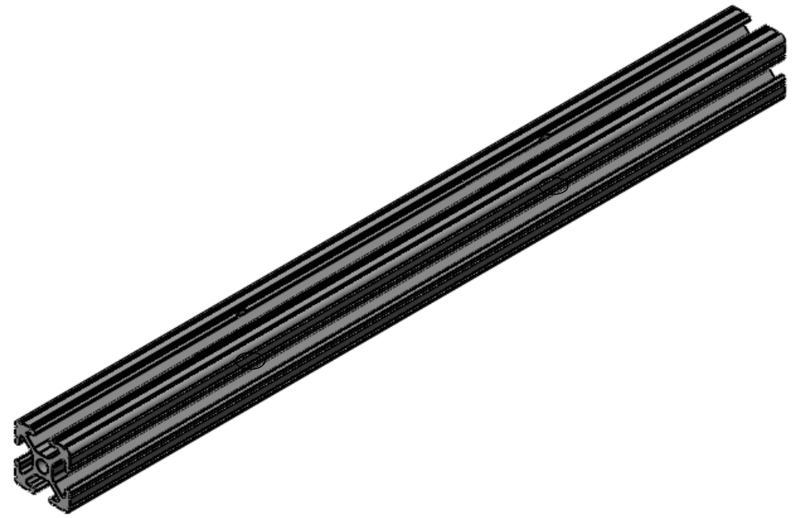

This piece can be purchased from McMaster Carr,
Part # 47065T209. It needs to be cut to the correct length indicated.
The two tapped holes need to be added for the knobs to be placed.

Ghaemi Group	DO NOT SCALE DRAWING
Drawn By: Rafat Jami	MATERIAL: Anodized Aluminum
Name of Part: Truss # 47065T209	UNLESS OTHERWISE SPECIFIED: DIMENSIONS ARE: INCHES [mm] TOLERANCES: 0.002 in
	SCALE:1:2 | SHEET 23 OF 30

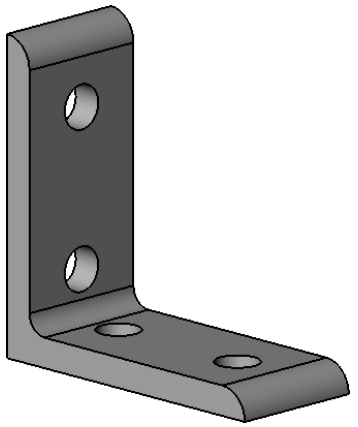

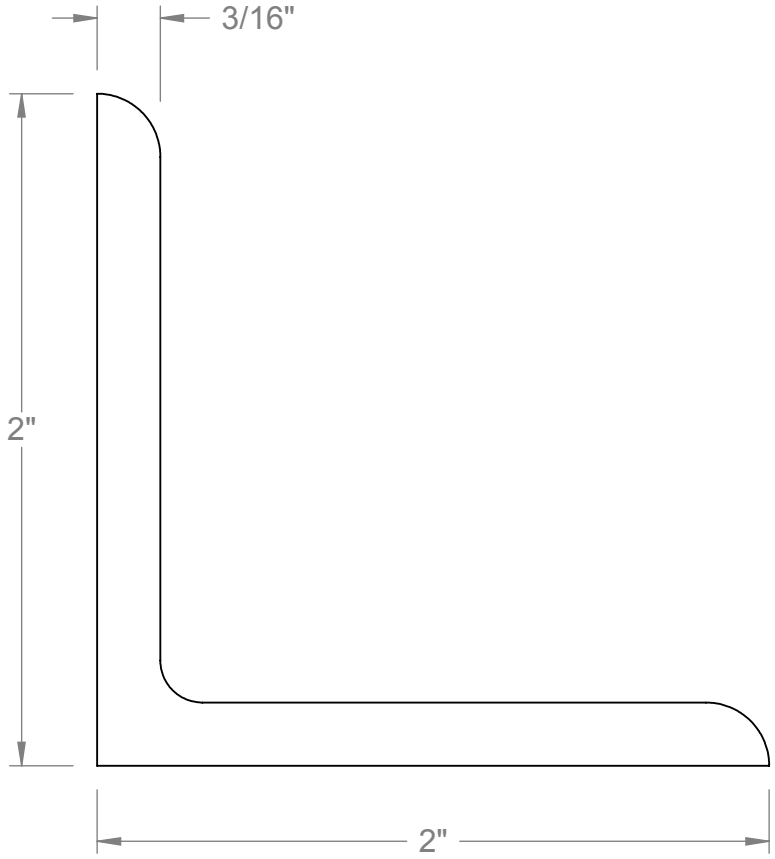

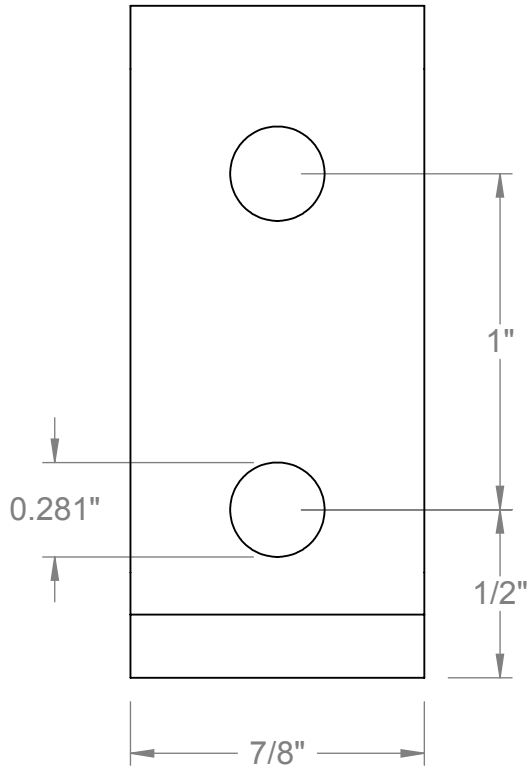

Sheet 24 of 30

McMASTER-CARR® CAD

http://www.mcmaster.com

PART NUMBER **47065T239**

Extended 90° Bracket for Aluminum T-Slotted Framing

ITEM NO.	PART NUMBER	DESCRIPTION	QTY.
1	Custom	Bearing Connection	1
2	8486K591	Inner Cylinder	1
3	Custom	Motor Connection	1

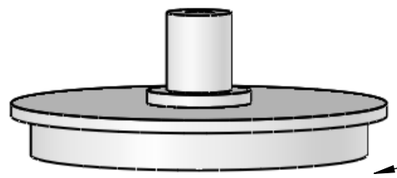

This will be attached with silicon glue and a tight press fit (there will be high torsion here).

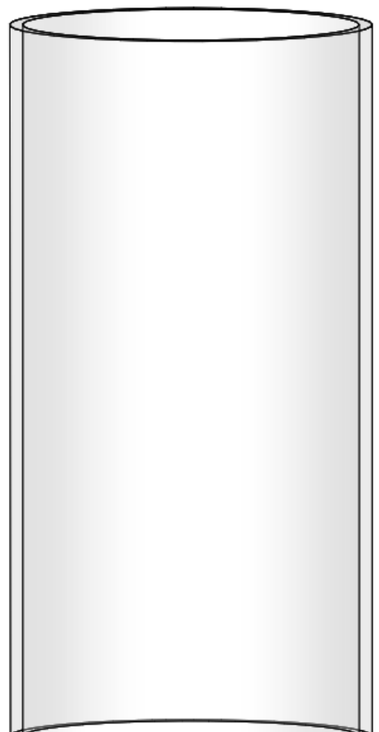

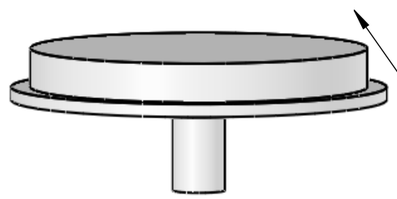

This will be attached with silicon glue and a tight press fit (there will be high torsion here).

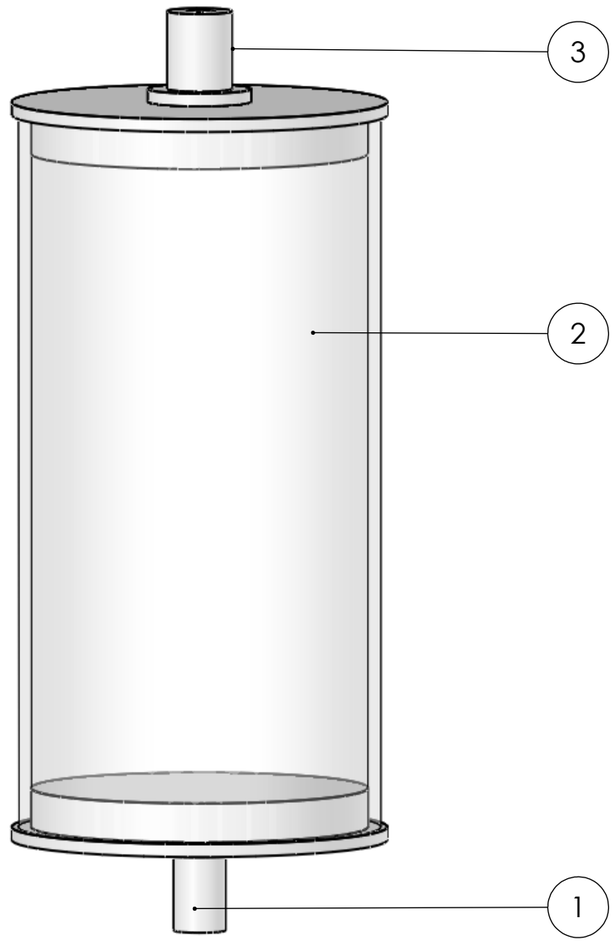

Ghaemi Group	DO NOT SCALE DRAWING
Drawn By: Rafat Jami	MATERIAL: Multiple
Name of Part: Inner Cylinder Subassembly	UNLESS OTHERWISE SPECIFIED: DIMENSIONS ARE: INCHES [mm] TOLERANCES:
SCALE:1:3	SHEET 25 OF 30

Machining Required

The shaft should be a relatively lose fit inside the Bearing (refer to bearing drawing) and the bottom extrusion should be a tight fit with glue inside the Inner cylinder. The inner cylinder has tolerancing based on McMaster Carr, so the specified drawing tolerance may need to be adjusted based on the size of the Inner acrylic shaft that McMaster Carr ships.

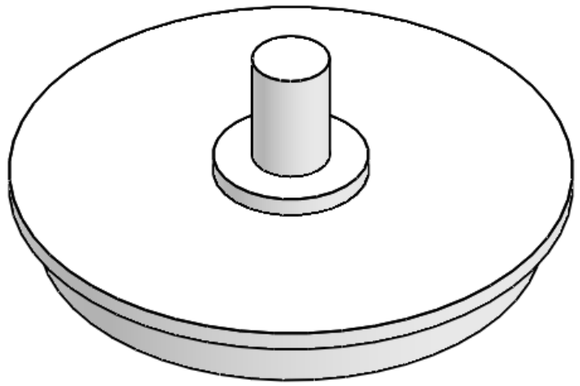

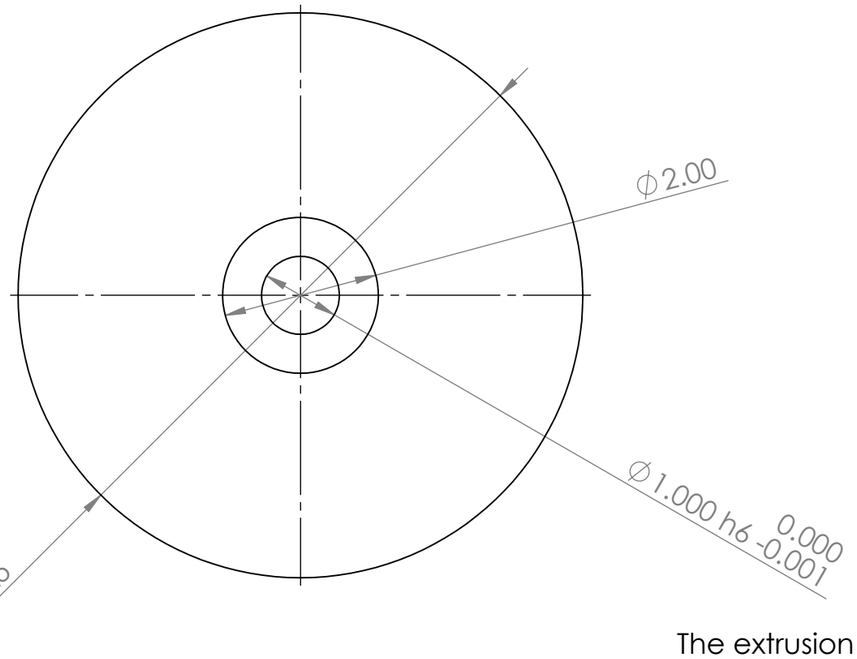

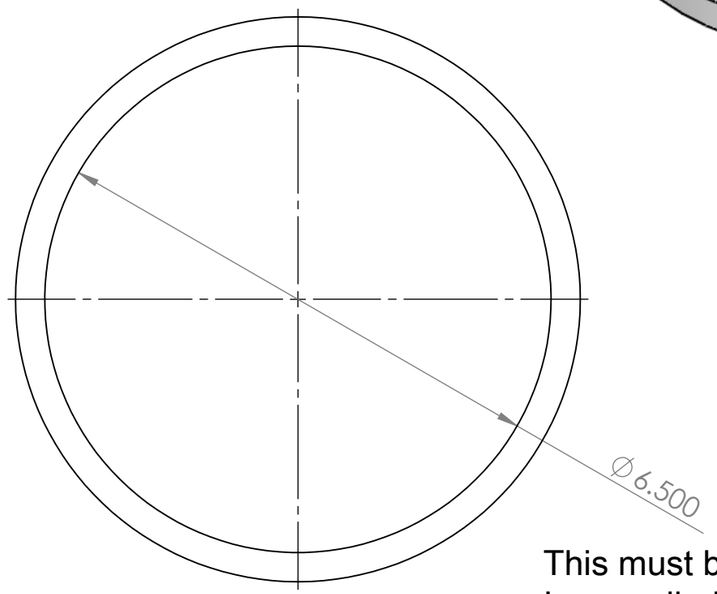

The extrusion into the bearing should be a snug fit but easily removable from the bearing for disasembly when cleaning the device.

This must be a press fit with the Inner cylinder from McMaster Carr. Tolerance must be determined after cylinder is measured due to their tolerances.

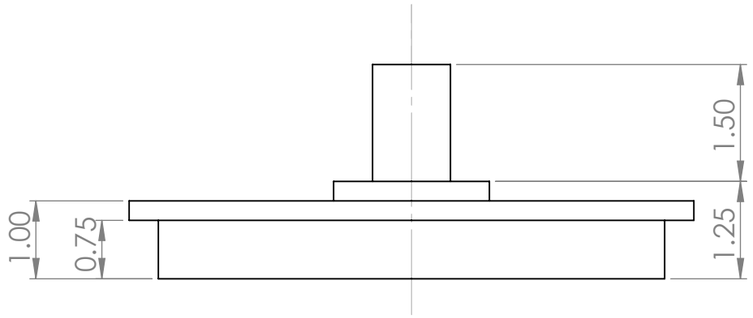

Ghaemi Group	DO NOT SCALE DRAWING
Drawn By: Rafat Jami	MATERIAL: PVC
Name of Part: Bearing Connection	UNLESS OTHERWISE SPECIFIED: DIMENSIONS ARE: INCHES [mm] TOLERANCES: 0.002 in
	SCALE:1:2 SHEET 26 OF 30

Machining Required

Tolerance Based on Inner Cylinder from McMaster Carr, a press fit tolerance is required.

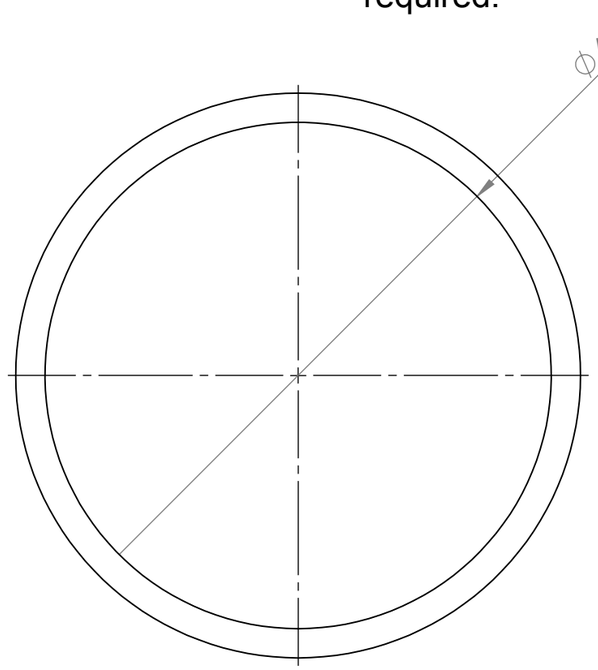

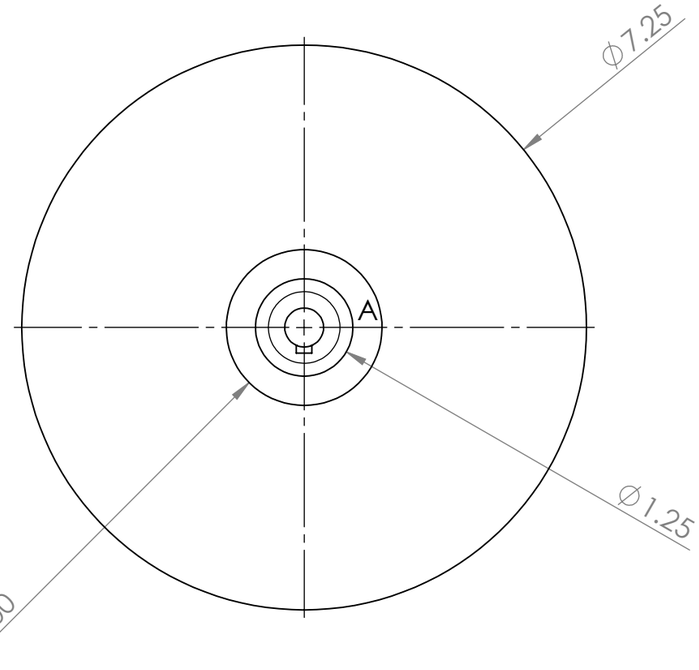

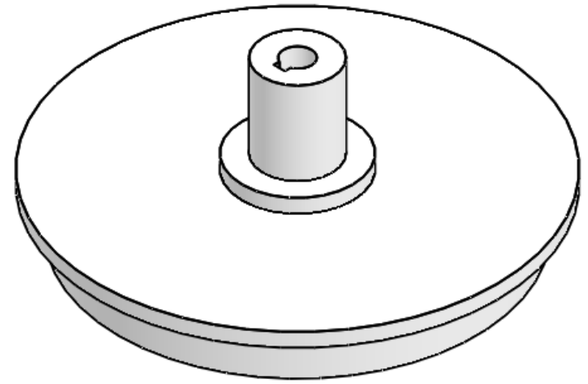

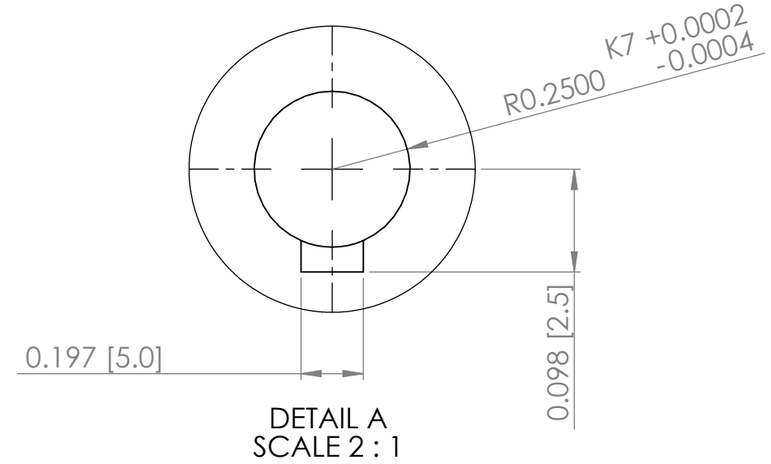

DETAIL A
SCALE 2 : 1

This keyway is meant to connect the motor output with a 5 mm x 5 mm key that is slightly oversized # 92288A120 from McMaster Carr

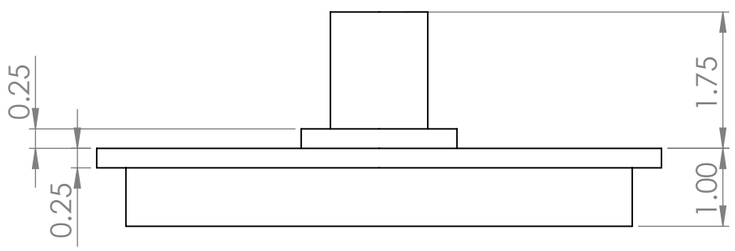

Ghaemi Group	DO NOT SCALE DRAWING
Drawn By: Rafat Jami	MATERIAL: PVC
Name of Part: Motor Connection	UNLESS OTHERWISE SPECIFIED: DIMENSIONS ARE: INCHES [mm] TOLERANCES: 0.002 in
	SCALE:1:2 | SHEET 27 OF 30

Machining Required

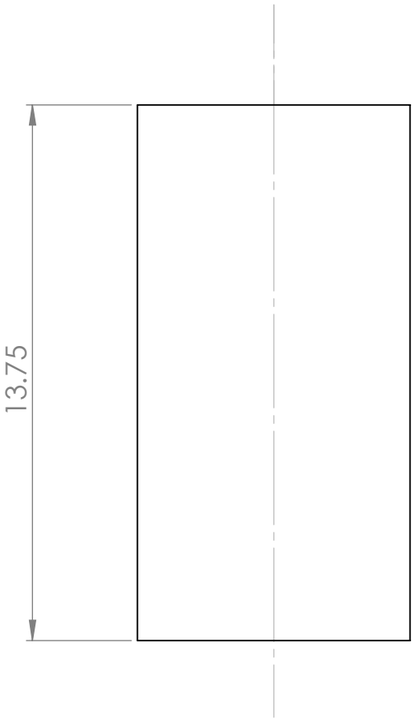

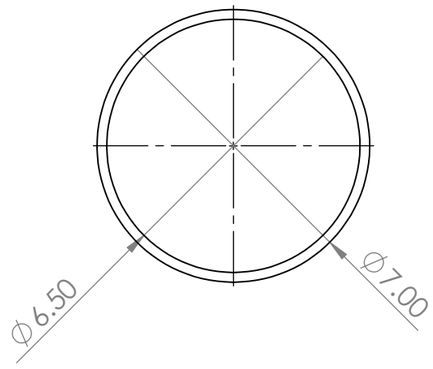

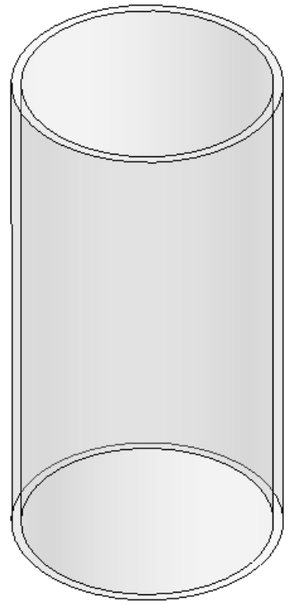

Needs to be turned on a lathe
for consistent inner diameter alignment.

This Part must be purchased from McMaster Carr.
The Part # 8486K591 is , however, the piece needs
to be cut to this custom length.

Ghaemi Group	DO NOT SCALE DRAWING
Drawn By: Rafat Jami	MATERIAL: Clear Cast Acrylic
Name of Part: Inner Cylinder	UNLESS OTHERWISE SPECIFIED: DIMENSIONS ARE: INCHES [mm] TOLERANCES: 0.002 in
SCALE:1:4	SHEET 28 OF 30

Machining Required

ITEM NO.	Description	QTY.
1	Lid	1
2	Lid Exit	2
3	Lid Cap	1

The extruded slits will help this piece fit into the slots of the lid. Easy removability is required.

This will be a snug fit (transitional).

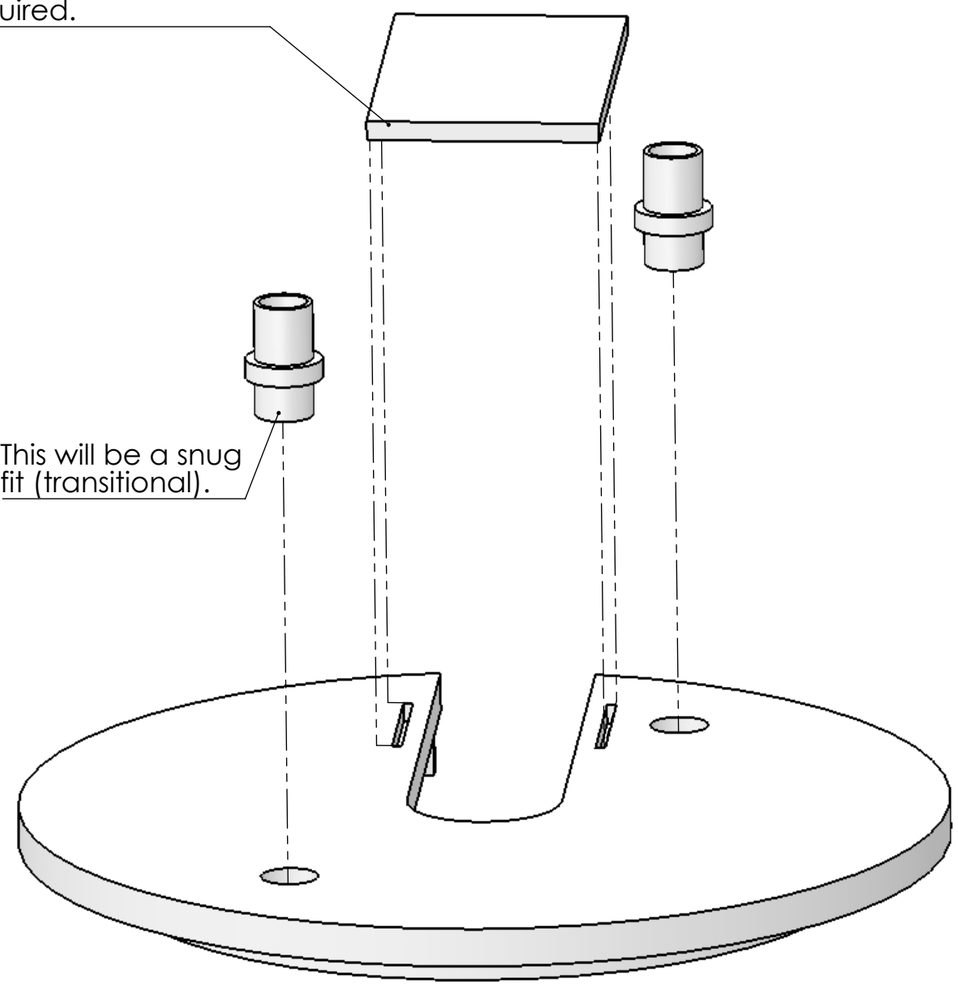

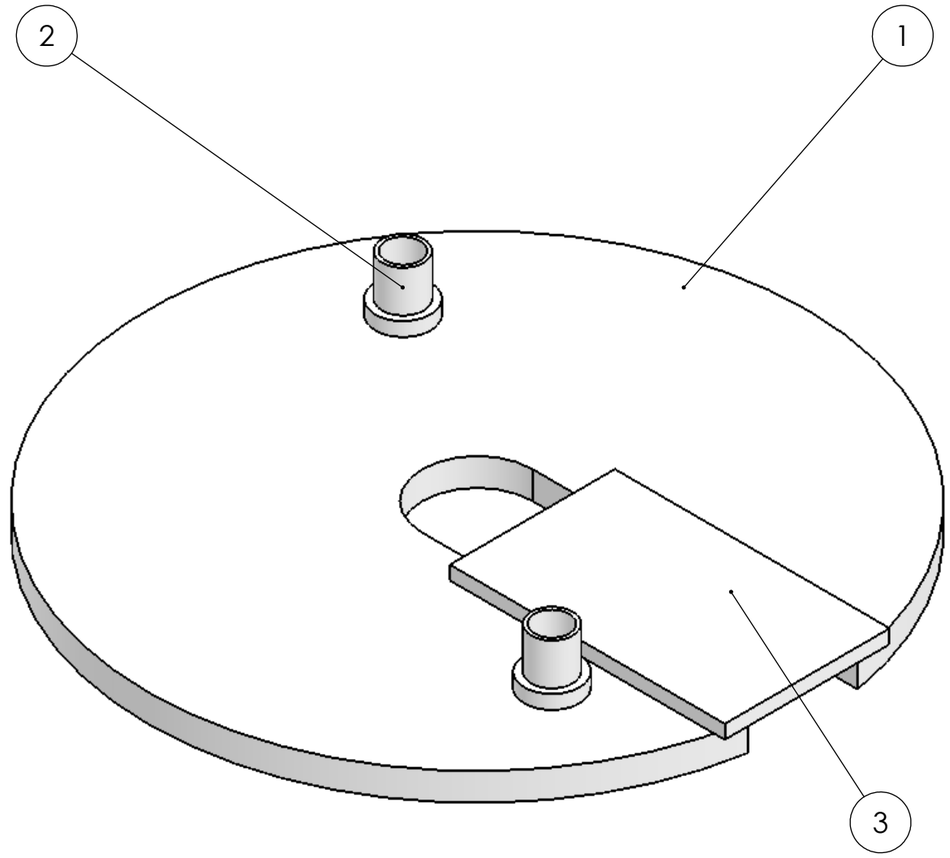

The individual Parts for this assembly will be given to the shop since they are created externally.

Ghaemi Group	DO NOT SCALE DRAWING
Drawn By: Rafat Jami	MATERIAL: Multiple
Name of Part: Lid Subassembly	UNLESS OTHERWISE SPECIFIED: DIMENSIONS ARE: INCHES [mm] TOLERANCES: 0.002 in
SCALE:1:2	SHEET 29 OF 30

Machining Required

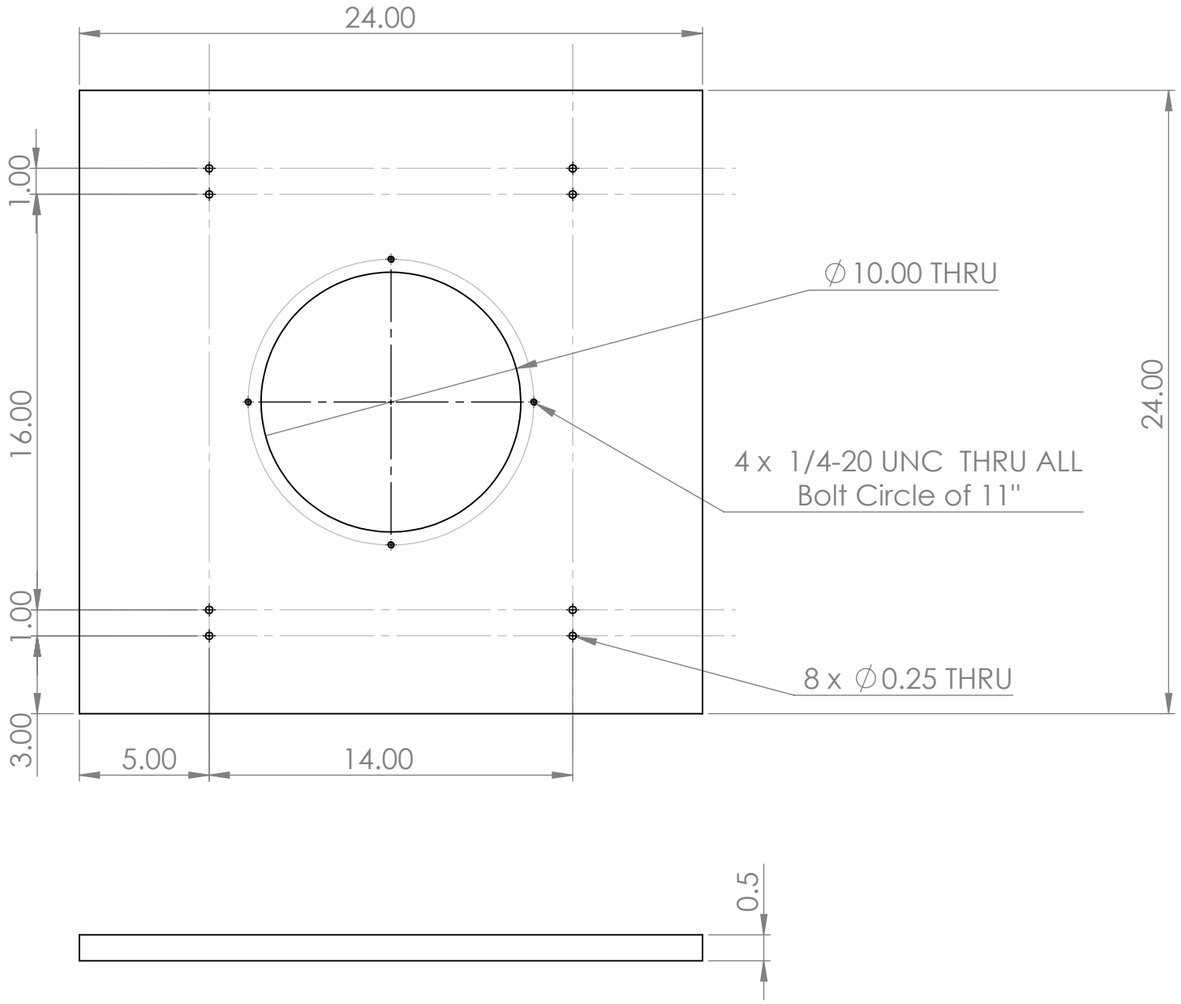

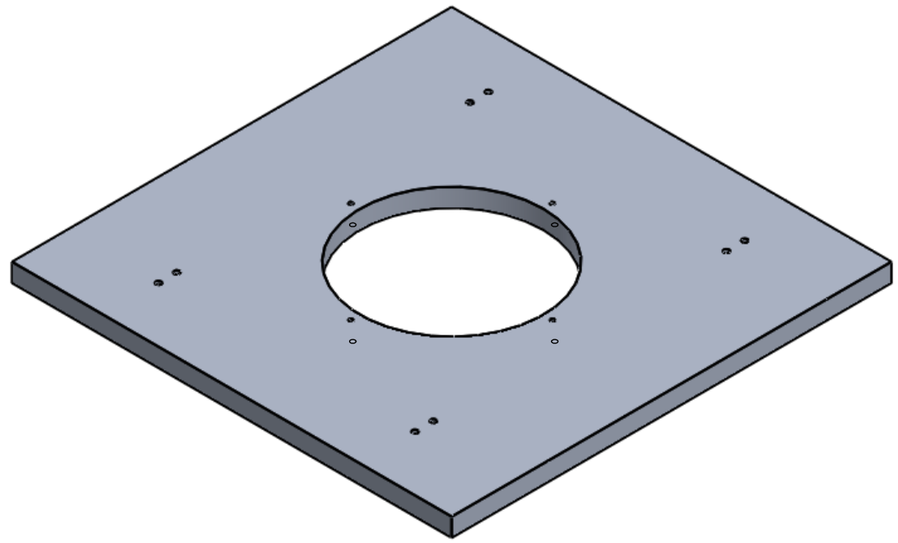

Note: There are also screw holes required to fit it on the metal frame of the table which will be shown to the shop in person since I do not have accurate dimensions of it.

DO NOT SCALE DRAWING	REVISION
Drawn By: Rafat Jami	MATERIAL: 6061 Aluminum
Name of Part: Table Top	UNLESS OTHERWISE SPECIFIED: DIMENSIONS ARE: INCHES [mm] TOLERANCES:
	SCALE:1:6 SHEET 30 OF 30